Engineering catalytic organic-inorganic materials for sensing applications

Pietro Pacchin Tomanin

ORCID ID: 0000-0002-5547-3863

Submitted in total fulfilment of the requirements for the degree of

Doctor of Philosophy

June 2020

School of Chemical and Biomedical Engineering

The University of Melbourne Parkville, Vic 3010, Australia

“Con il tempo, anche le zucche maturano…”

“With time, even pumpkins ripen…”

Wispered by Vittorina Dal Cero to a young Pietro,
Italy, Montagnana, early 2000

Abstract

Nanostructured hybrid organic-inorganic materials are a unique class of materials showing distinctive properties that have attracted high interest due to their diverse applications in the fields of energy, environment and medicine. In particular, hybrid materials are promising candidates for sensing applications due to the tunable chemical, structural and functional properties of the organic and inorganic components. Hence, the engineering of novel nanostructured catalytic organic/inorganic materials provides opportunities for the fabrication of advanced nanodevices for biosensing.

In this thesis, novel hybrid materials have been prepared and their electrocatalytic, catalytic, and optical properties explored. First, nanostructured electrocatalytic microparticles were synthesized in mild conditions and used with an organic binding agent to prepare carbon electrodes applied in the detection of glucose in biologically relevant media. Second, hierarchically structured hybrid particles displaying enzyme-like catalytic activities were synthesized and used to prepare high-throughput micro-reactors for the detection of bioanalytes via a hybrid organic-inorganic cascade reaction. Finally, a natural occurring polysaccharidic nanoparticle, i.e. glycogen, was engineered to impart adhesive functional properties to a hybrid film and used for the coating of various substrates with different chemical composition. These hybrid coatings embedding metal nanoparticles were employed as catalytic and optically active functional interfaces.

Declaration of Authorship

This is to certify that:

I. The thesis comprises only my original work toward the degree of Doctor of Philosophy (PhD) except where indicated in the preface;

II. Due acknowledgement has been made in the text to all other material used;

III. The thesis is fewer than the 100,000 words in length, exclusive of tables, maps, bibliographies and appendices.

Pietro Pacchin Tomanin

Preface

Chapter 3, **Chapter 4**, and **Chapter 5** in this PhD thesis were carried out in collaboration with others. The following paragraphs indicate the nature and proportion of the contribution of the PhD candidate and collaborators.

In this thesis, the following Chapters are presented in the form of:

Chapter 3, published article;

Chapter 4, manuscript in preparation;

Chapter 5, submitted manuscript in revision after peer review.

All authors who provided contributions signed a copy of the co-author authorization form. The forms were submitted to the Melbourne School of Graduate Research along with this thesis.

Chapter 3: Cobalt Phosphate Nanostructures for Non-Enzymatic Glucose Sensing at Physiological pH. (published article)

Pietro Pacchin Tomanin, Pavel V. Cherepanov, Quinn A. Besford, Andrew J. Christofferson, Alessia Amodio, Chris F. McConville, Irene Yarovsky, Frank Caruso, and Francesca Cavalieri, *ACS Applied Materials & Interfaces* 10, no. 49 (2018): 42786-42795.

The PhD candidate is the first author and contributed to more than 75% of the contents in this publication. The candidate reviewed the literature, designed and executed the experimental scientific work, analysed the obtained experimental data, prepared the artwork contents and prepared the manuscript under the supervision of Frank Caruso and Francesca Cavalieri. Pavel V. Cherepanov, Quinn A. Besford and Alessia Amodio contributed to assisting the experimental work design. Andrew J. Christofferson and Irene Yarovsky contributed to performing computational analysis. Chris F. McConville contributed to analysing XPS data. Francesca Cavalieri and Frank Caruso conceived the research project, revised the manuscript critically for important intellectual content and approved the final version to be published.

Chapter 4: Enzyme-Mimicking Hybrid Nanoflowers Enable Sensing of Bioanalytes (manuscript in preparation)

Pietro Pacchin Tomanin, Frank Caruso, and Francesca Cavalieri.

The PhD candidate is the first author and contributed to more than 75% of the contents in this publication, as for literature review, design and execution of experimental work, data analysis, artwork preparation and manuscript writing under the supervision of Frank Caruso and Francesca Cavalieri.

Chapter 5: Nanoengineering Multifunctional Hybrid Interfaces Using Adhesive Glycogen Nanoparticles (in revision following peer review by *Journal of Materials Chemistry B*)

Pietro Pacchin Tomanin, Jiajing Zhou, Alessia Amodio, Rita Cimino, Agata Glab, Frank Caruso, and Francesca Cavalieri. Manuscript submitted in February 2020 to *Journal of Materials Chemistry B*.

The PhD candidate is the first author and contributed to more than 75% of the contents in this publication. The candidate reviewed the literature, designed and executed the experimental scientific work, analysed the obtained experimental data, prepared the artwork contents and prepared the manuscript under the supervision of Frank Caruso and Francesca Cavalieri. Jiajing Zhou contributed to design the experimental work and to synthesize gold nanoparticles. Alessia Amodio contributed to design the experimental work. Rita Cimino contributed to the materials synthesis. Agata Glab contributed to executing degradability studies. Francesca Cavalieri and Frank Caruso conceived the research project, revised the manuscript critically for important intellectual content and approved the final version to be published.

Publications

The following publications and manuscripts have been produced during this PhD candidature.

PhD projects

1. **Pietro Pacchin Tomanin**, Pavel V. Cherepanov, Quinn A. Besford, Andrew J. Christofferson, Alessia Amodio, Chris F. McConville, Irene Yarovsky, Frank Caruso, and Francesca Cavalieri. " Cobalt Phosphate Nanostructures for Non-Enzymatic Glucose Sensing at Physiological pH" *ACS Applied Materials & Interfaces* 10, no. 49 (**2018**): 42786-42795. (published article)
2. **Pietro Pacchin Tomanin**, Jiajing Zhou, Alessia Amodio, Rita Cimino, Agata Glab, Francesca Cavalieri, and Frank Caruso. “Nanoengineering Multifunctional Hybrid Interfaces Using Adhesive Glycogen Nanoparticles” (*Journal of Materials Chemistry B,* manuscript submitted in February 2020)
3. **Pietro Pacchin Tomanin**, Frank Caruso, and Francesca Cavalieri. “Enzyme-Mimicking Hybrid Nanoflowers Enable Sensing of Bioanalytes” (manuscript in preparation)

Other projects

4. Rahim, Md Arifur, Gan Lin, **Pietro Pacchin Tomanin**, Yi Ju, Anders Barlow, Mattias Björnmalm, and Frank Caruso. "Self-Assembly of a Metal–Phenolic Sorbent for Broad-Spectrum Metal Sequestration" *ACS Applied Materials & Interfaces* (2020). (published article)

Presentations

The following presentations were delivered during this PhD candidature:

1. **Pietro Pacchin Tomanin**, F. Cavalieri. “Organic/inorganic hybrid microflowers”, Nanostructured Interfaces and Materials Science Group (NIMS), School of Chemical and Biomedical Engineering, The University of Melbourne, Australia.
2. **Pietro Pacchin Tomanin**, F. Cavalieri. “Shed light on hybrid nanoflowers”, Particulate Fluids Processing Centre (PFPC) Seminar, Oral Presentation, 20th June 2017, The University of Melbourne, Australia.
3. **Pietro Pacchin Tomanin**, F. Cavalieri. “Ultrasound-responsive PVA micro-bubbles for the controlled degradation of soft scaffolds”, Particulate Fluids Processing Centre (PFPC) Seminar, Oral Presentation, 3rd July 2018, The University of Melbourne, Australia.
4. **Pietro Pacchin Tomanin**, F. Cavalieri. “Nanostructured organic, inorganic and hybrid materials for biosensing and biomedical applications”, Research group of Wendel Alves, Oral Presentation, 22nd August 2018, Federal University of ABC, Brazil.
5. **Pietro Pacchin Tomanin**, F. Cavalieri. Various oral presentations during the period 2016-2019, Nanostructured Interfaces and Materials Science Group (NIMS), School of Chemical and Biomedical Engineering, The University of Melbourne, Australia.
6. **Pietro Pacchin Tomanin**. “Engineering catalytic organic/inorganic materials for sensing applications”, PhD Completion Seminar, 4th December 2019, oral presentation, The University of Melbourne, Australia.
7. **Pietro Pacchin Tomanin**, J. Zhou, A. Amodio, R. Cimino, A. Glab, F. Cavalieri, F. Caruso. “Nanoengineering multifunctional hybrid interfaces using adhesive glycogen nanoparticles”, Convergent Bio-Nano Science & Technology (CBNS) Nodes meeting, Oral presentation, 14th February 2020, Monash University, Melbourne, Victoria, Australia.

Acknowledgements

I would like to express my utmost gratitude to everyone that assisted me with the preparation of this thesis and with whom this PhD-chapter of my life has been possible and memorable.

My appreciation to Dr Francesca Cavalieri, who helped, guided, and had faith in my scientific capabilities. Thanks for having provided significant and delightful scientific collaborations, helping me learning personal and professional skills that will shape my future self and having the patience and perseverance in developing my scientific research career. Moreover, thank for having assisted my research with crucial scientific discussions, revisions, and feedback.

My sincere gratitude to Prof Frank Caruso, who allowed me to freely pursue my PhD, encouraged my unique research, provided extraordinary scientific facilities and collaborations, and welcomed me to be part of his Nanostructured Interfaces and Materials Sciences (NIMS) group. Thanks for having assembled such an exceptional international research team composed of people with profound intellects and big hearts.

Many thanks also to my former committee chair, Prof. David E. Dunstan, and my actual committee chair, Dr Gabriel da Silva, who assisted in my PhD journey with significant scientific discussions, with time spent in evaluating my scientific work, and with valuable feedback.

My obligations to my close collaborators, whom aided and promoted my scientific research with valuable contributions in joint projects, Dr Alessia Amodio, Dr Andrew J. Christoffersons, Dr Jiajing Zhou, Dr Md Arifur Rahim, Dr Pavel V. Cherepanov, and Dr Quinn A Besford. I am especially in debt to them for keeping me on track and supporting myself in surmount periods of crisis cheering me up.

I was honoured to had over the years marvellous colleagues, visitors and friends which whom I shared deeply joyful moments, Dr Tomoya Suma, Dr Alessia Weiss, Dr Nadja Bertleff-Zieschang, Dr Mattias Björnmalm, Dr Yi Ju, Dr Ka Fung Noi, Dr Jiwei Cui, Dr Yunlu Dai, Dr Danzi Song, Dr Marcin Wojnilowicz, Dr Shuaijun Pan, Dr Christina Cortez-Jugo, Dr Ting Yi Wang, Dr Wenjie Zhang, Dr Alessandro Bertucci, Dr Gyeongwon Yun, Dr Joseph J. Richardson, Dr Matthew Faria, Dr Samantha L. Kristufek, Dr René Lafleur, Jingqu Chen, Ewa Czuba- Wojnilowicz, Agata Glab, Yiyuan Han, Yingjie Hu, Shiyao Li, Gan Lin, Zhixing Lin, Yutian ma, Yijiao Qu, Jiaying Song, Wanjun Xu, Mehmet Can Zeybek, Qizhi Zhong, Dr Marco Cassani, Dr Soraia Fernandes, Marco Savioli, Dr Sukhvir Kaur Bhangu, Paula Cevaal, Rita Cimino, Liviana Mummolo, Denzil Furtado, Lei Huang, Prof. Noritaka Kato and family, Nicolas, Kate Reidy, Fabiana, Federico, Jenny Peng, Alex Duan, Dr Srinivas Mettu, Anna, Abdalla, Anika Printz, Ece Ergir, Petra Burilová, and Sahar Talebi. A special thanks to my colleagues and friends from my Brazilian exchange that made my experience memorable, Prof. Wendel Alves, Dr Bárbara Bianca, Rodrigo Silva Nascimento Mancini, Sandra Valéria, Wallace Pereira, Karina Argüello, Érick Hannud, Davi Ramalho Bruno Toriba, and Felipe Da Silva Branco.

Furthermore thanks to Dr Andrew J. Mitchell, Paul Brannon, and Tian Zheng from the Materials Characterisation and Fabrication Platform (MCFP) facility for helpful advice and constructive scientific discussions.

Honourable mentions to the NIMS administrative staffs: Marc Riemer, Melanie Hutchins, Maryline Chee, Catherine Eyre, Jenny Tran, and Steve Spoljaric for assisting me with paperwork, for proofreading my manuscripts, and for the technical management of the laboratories during my PhD.

Moreover, I also deeply thank my climbing and housemates crews, which whom I shared many exciting experiences, the old dude, Anthony Claxton, Petey Mason, Will Ashton, Annie Paras, Frazer Neill Baker, Jan Kabátek, and Davide, as well as Josefine Berg Bring, Juraj Hronec, Lars van Breemen, Leonie Glitz, Luis Barri, Milou Scheeren, Nicky Hugens, Akane Matsumoto, Simone Luijckx, and Rosa Smeet.

Importantly, the people mentioned above (and to whoever I had missed my sincere apology) become friends over the years. With these, I have vivid beautiful memories that contributed to making this chapter of my life memorable and for whom I have been immensely fortunate to have around me.

I also would like to specially acknowledge the funding from The University of Melbourne that allowed me to finance this journey: Melbourne Research Scholarship (MRS) and FAPESP-SPRINT scholarship (grant number: 2016-2018/50188-4) as for the University of Melbourne-São Paulo Research Foundation.

Last but not the least, there are no words to express how thankful, beholden, and grateful I am to my family: mom Giovanna, grandma Vittorina, aunty Laura, and my beloved partner in life Flora. Their endless support and encouragement gave me the enthusiasm, determination, and ambition to pursue, sustain, and complete this PhD degree. I am in great indebt with them to have been always there standing by my side during the joyful and dreadful times. In particular, I am grateful to Flora that, like no one else, she went out of her way to do her best for us. I dedicate this thesis to my family.

Table of Contents

Abstract...v

Declaration of Authorship vi

Preface..vii

Publications...ix

Presentations...x

Acknowledgements...xi

Table of Contents xiv

List of Figures...xviii

Chapter 1 - Introduction..1-1

1.1 Introduction to hybrid materials 1-2
1.2 Natural hybrid materials 1-4
1.3 History of hybrid materials..1-6
1.4 Modern synthetic hybrid materials..1-8
  1.4.1 Inorganic building blocks 1-9
  1.4.2 Organic building blocks..1-10
  1.4.3 Clay- and zeolite-based hybrid materials...............................1-11
  1.4.4 Coordination complex-based hybrid materials............................1-13
  1.4.5 Phenolic building block-based hybrid materials.........................1-16
  1.4.6 Nanoflowers-based hybrid materials 1-21
  1.4.7 Gold nanoparticle layers-based hybrid materials........................1-25
  1.4.8 Glycogen building block-based hybrid materials 1-28
1.5 Applications of hybrid materials..1-34
  1.5.1 Industrial applications of hybrid materials............................1-35
  1.5.2 Nanoflower-based biosensors 1-36

1.5.3 Gold nanoparticle-based biosensors 1-39
1.6 Scope of the thesis 1-43
1.7 References 1-45

Chapter 2 - Experimental Details 2-71

2.1 Cobalt phosphate nanostructures for non-enzymatic glucose sensing at physiological pH 2-72
2.1.1 Reagents and chemicals 2-72
2.1.2 Instrumentation 2-72
2.1.3 Synthesis of CPNs 2-73
2.1.4 Electrode Preparation 2-74
2.1.5 Electrochemical Measurements 2-75
2.1.6 Computational Details 2-75
2.2 Enzyme-mimicking hybrid nanoflowers enables sensing of bio-analytes 2-77
2.2.1 Materials 2-77
2.2.2 Synthesis of Dextran sulfate-copper phosphate nanoflowers 2-77
2.2.3 Characterization of hybrid nanoflowers 2-78
2.2.4 Preparation of D-NF functionalized microreactors 2-79
2.2.5 Catalytic activity and H_2O_2 sensing 2-79
2.2.6 Glucose detection via hybrid cascade reaction 2-80
2.3 Nanoengineering multifunctional hybrid interfaces using adhesive glycogen nanoparticles 2-81
2.3.1 Materials 2-81
2.3.2 Synthesis and materials preparation 2-82
2.3.2.1 Synthesis of L-PG 2-82
2.3.2.2 Preparation of fluorescent labeled L-PG 2-83
2.3.2.3 Synthesis of dodecane-conjugated phytoglycogen (DD-PG) 2-83
2.3.2.4 Synthesis of gold nanoparticles (AuNPs) 2-83

2.3.2.5 Preparation of L-PG metal nanoparticle hybrid coatings on glass 2-84
2.3.2.6 Preparation of PS microparticles coated with L-PG and AuNPs 2-84
2.3.2.7 Preparation of inner-coated PP tubes with L-PG and AuNPs 2-85
2.3.3 Instrumentation 2-85
2.3.4 Characterization 2-87
2.3.4.1 Attenuated total reflectance Fourier transform infrared (ATR-FTIR) spectroscopy 2-87
2.3.4.2 UV–Vis spectroscopy 2-87
2.3.4.3 Dynamic light scattering (DLS): hydrodynamic diameter and ζ-potential 2-87
2.3.4.4 Atomic force microscopy (AFM) 2-88
2.3.4.5 Contact angle measurements 2-88
2.3.4.6 Cytotoxicity assay 2-89
2.3.4.7 Degradation of PG and L-PG nanoparticles by β-amylase 2-89
2.3.4.8 Stability of L-PG coatings on glass substrates 2-90
2.3.4.9 Quartz crystal microbalance with dissipation 2-91
2.3.4.10 Differential interference contrast microscopy 2-91
2.3.4.11 Transmission electron microscopy (TEM) 2-92
2.3.4.12 Scanning electron microscopy (SEM) and energy-dispersive X-ray (EDX) spectroscopy 2-92
2.3.4.13 Scanning helium ion microscopy (HIM) 2-92
2.3.4.14 Stability of L-PG/AuNP hybrid coatings on glass substrates 2-93
2.3.4.15 Catalytic evaluation of AuNPs in L-PG/AuNP-coated 15 mL polypropylene (PP) tubes 2-93
2.3.4.16 AuNP stability in modified 15 mL PP tubes 2-94

2.3.4.17 Surface-enhanced Raman scattering (SERS) sensing using L-PG/AgNP hybrid coatings........................2-94

Chapter 3 - Cobalt Phosphate Nanostructures for Non-Enzymatic Glucose Sensing at Physiological pH 3-96

3.1 Manuscript main text 3-97
3.2 Supplementary Information 3-107

Chapter 4 - Enzyme-Mimicking Hybrid Nanoflowers Enable Sensing of Bioanalytes 4-120

4.1 Manuscript main text 4-121
  4.1.1 Abstract..4-121
  4.1.2 Introduction 4-121
  4.1.3 Results and discussions 4-123
    4.1.3.1 Synthesis and characterization of dextran sulfate-copper phosphate hybrid nanoflowers.................4-123
    4.1.3.2 Preparation of D-NF functionalized surfaces 4-130
    4.1.3.3 Non-enzymatic activity and kinetics of D-NF........4-131
    4.1.3.4 Detection of H_2O_2 via fluorometric assay.............4-134
    4.1.3.5 Detection of glucose via hybrid cascade reaction.4-135
  4.1.4 Conclusions 4-137
  4.1.5 References 4-138
4.2 Supplementary Information 4-141

Chapter 5 - Nanoengineering Multifunctional Hybrid Interfaces Using Adhesive Glycogen Nanoparticles 5-148

5.1 Manuscript main text 5-149
  5.1.1 Abstract..5-149
  5.1.2 Introduction 5-151
  5.1.3 Results and Discussion 5-154
    5.1.3.1 Synthesis and characterization of L-PG 5-154
    5.1.3.2 Preparation and characterization of L-PG films....5-156

5.1.3.3 Characterization of L-PG/metal nanoparticles hybrid films 5-159
5.1.3.4 Catalytic and SERS properties of hybrid LbL assemblies 5-162
5.1.4 Conclusions 5-164
5.1.5 Acknowledgements 5-165
5.1.6 Notes and references 5-166
5.2 Supplementary Information 5-168

Chapter 6 - Conclusions and Future Prospects 6-180

Appendix 7-185

List of Figures

Chapter 1 - Introduction

Figure 1. Examples of hybrid materials found in nature. a) Venus sponge, b) brittlestar's lens, c) radiolaria, d) vertebrate teeth, e) diatom, f) corals, g) coccolith, h) teeth of chitons, i) kidney stone, j) abalone shell, k) magnetotactic bacteria, and l) teeth of the urchin. Adapted from [19-27] 1-5

Figure 2. Hybrid materials for arts throughout history. a) Prehistoric painting, b) Ancient Mayan drawing and Flemish art made also with, respectively, minerals-clays paste, indigo dye-clay pigment and Prussian Blue. Adapted from [30]. 1-6

Figure 3. Schematic of three different levels of inorganic particles dispersion in a polymeric matrix, characteristic of clay-polymer hybrid materials. Adapted from [87]. 1-12

Figure 4. Functional and chronological classification of porous coordination polymers: a) copper-based framework, b) MOF-5, and c) MIL-53. Adapted from [30]. 1-16

Figure 5. a) Schematic of MPN assembly preparation. TA/Fe^{III} thin film and hollow capsules: b) planar (photographs), c) spherical, and d) ellipsoidal (DIC images). MPN assembly with various metals: e) capsules obtained using TA and Al^{III}, V^{III}, Cr^{III}, Mn^{II}, Fe^{III}, Co^{II}, Ni^{II}, and Cu^{II} (DIC images, scale bar 5 µm), and the corresponding f) high-angle annular dark-field spectra (scale bar 1 µm). MPN assembly with various ligands: photographs of the capsule dispersions colours of g) GA/Fe^{III}, h) PG/Fe^{III}, and i) PC/Fe^{III}. j) GA/Fe^{III} coatings on several substrates. k) UV-Vis spectra of GA and GA/Fe^{III} capsules, and p) AFM image of dried GA/Fe^{III} capsules. Adapted from [133] 1-20

Figure 6. Metallogels based on tannic acid and titanium. a-e) Gelation of TA-Ti^{IV}, f) shape persistence, g) adhesive, h) co-gelation (multiwalled carbon nanotubes), and i) crystallization (HKUST-1) properties of TA-Ti^{IV} gels. Adapted from [133]. 1-21

Figure 7. a) Schematic of the proposed synthetic formation mechanism of organic-inorganic nanoflowers through four main steps: coordination of metal ions via functional groups in the organic component, co-precipitation, self-assembly of inorganic crystals and organic molecules, and anisotropic growth until structure completion. SEM images of protein-inorganic nanoflowers with different morphologies prepared with BSA and copper phosphate, using a BSA concentration of b) 0.5, c)

0.02, and d) 0.1 mg mL^{-1}. e) Commonly used characterization techniques, inner circle, and corresponding analysed properties, outer circle, for the studied of hybrid nanoflowers. f) Advanced biotechnological applications of organic-inorganic nanoflowers. Adapted from [179, 184, 186, 188] 1-24

Figure 8. Depiction of assembly methods to prepare gold nanoparticle layers. a) Spin- and dip-coating via layer-by-layer strategy, and b) by template coating with pre-functionalized surfaces with self-assembled and self-organized DNA strands following conjugation with gold nanoparticles. Adapted from [223] 1-28

Figure 9. A) Depiction of the biological production of Glycogen from uridine diphosphate glucose to hyperbranched polysaccharidic nanoparticle via enzymatic synthesis. Transmission electron microscopy (TEM) images of several types of glycogens having different structural properties from various sources, as B) rat liver, C) rabbit liver, D) slipper limpet, and E) human skeletal muscles. F) Examples of schematics relative to synthetic reactions for the modification of the glycogen repeating unit. Adapted from [254, 260]. 1-32

Figure 10. Depiction illustrating the assembly process of glycogen-AuNP hybrid materials and the photograph showing the colours of the different solutions as a function of the glycogen/AuNP ratio. Adapted from [254, 280]. 1-33

Figure 11. Examples of advanced technological applications of hybrid materials. Adapted from [4]. 1-34

Figure 12. Examples of nanoflowers in biosensing applications. a) The chemical equation of glucose sensing via a two-step enzymatic cascade reaction and b) depiction of the cascade reaction using HRP/GOx-$Cu_3(PO_4)_2$ nanoflowers. c) Schematic of the assembly process of hybrid ConA/GOx-$CaHPO_4$ hybrid nanoflowers and d) corresponding nanoflowers-based immunosensing of E. coli. Adapted from [195, 301]. 1-39

Figure 13. a) An overview of biotechnological applications and b-h) specific biosensing applications of hybrid materials based on gold nanoparticles layers. b) SERS-active substrates composed of gold nanoparticles resulting in c) enhanced SERS intensities signals. d) Depiction of ELISA-enhancing substrates and e) improved signals in an immunoassay targeting CEA. f) Schematic of acetylthiocholine sensing via an electrochemical-active modified electrode with gold nanoparticle layers and acethylcholinesterase, g) amperometric response upon addition of the analyte, and h) AFM image of the modified electrode. Adapted from [223, 318, 327, 343]. 1-42

Chapter 3 - Cobalt Phosphate Nanostructures for Non-Enzymatic Glucose Sensing at Physiological pH

Figure 1. (a) Schematic illustration of the proposed mechanism for CPN formation. (b,c) SEM and (d,e) TEM images of the CPNs at various magnification. (f) EDX spectrum, (g,h,i) highresolution Co 2p (g), P 2p (h), and O1s (i) XPS spectra, (j) XRD spectrum, and (k) ATR-FTIR spectrum of the CPNs (the inset in (k) shows a magnified portion of spectrum in the range of 1300–370 cm−1)……………….……….3-99

Figure 2. (a) Schematic representation of the preparation of the glassy carbon electrode and screen-printed electrode, the experimental setup used for the electrochemical characterizations, and measurements performed in the electrolyte composed of human serum and PBS. WE, working electrode; CE, counter electrode; RE, reference electrode. (b) CV cycles (30) of the CPNs in a N2-saturated PBS electrolyte (10 mM, pH 7.4) at a scan rate of 20 mV/s. The inset shows a plot of the peak current density value at 0.65 V vs Ag/AgCl as a function of the cycle number. (c) CVs of the CPNs in PBS buffer (10 mM, pH 7.4) at different scan rates: 20, 25, 30, 35, 40, 50, and 60 mV/s. The inset shows a plot of the oxidation (Ox) and reduction (Red) peaks current densities as a function of the square root of the scan rate. (d) CVs of the CPNs in 5 mM K3Fe(CN)6/0.1 M KCl supporting electrolyte at different scan rates from 20 to 270 mV/s. The inset shows a plot of the peak current of the Fe(CN)6 3-/Fe(CN)6 4- redox couple as a function of the square root of the scan rate. Dashed arrows indicate the potential sweep direction. All current density data are normalized by the ESA……………………………………………………………………3-100

Figure 3. (a) Proposed electrochemical oxidation of Glu to gluconolactone at the electrode interface. (b) CVs of the CPN-modified electrode in PBS buffer (10 mM, pH 7.4) at a scan rate of 20 mV/s in the absence (black line) and presence (blue lines) of 30 mM Glu, respectively. The dashed line represents the CV of the GCE (bare electrode) obtained under the same experimental conditions. The inset shows a magnification of the potential region from 0.5 to 0.7 V (vs Ag/AgCl) with the presence of 10, 20, and 30 mM Glu (full profiles shown in Figure S5). (c) Chronoamperometric responses of the CPN in PBS buffer (10 mM, pH 7.4) to successive additions of Glu at an applied potential of 0.65 V (vs Ag/AgCl) and (d) the calibration curve based on the triplicate CA experiments. (e) Amperometric responses of the CPNs at 0.65 V (vs Ag/AgCl) to the addition of Glu (5 mM) in PBS electrolyte (10 mM, pH 7.4), followed by additions of interfering agents lactose (LA, 1.5 μM), galactose (GA, 1.5 μM), ascorbic acid (AA, 30 μM), and dopamine (DP, 0.14 nM), and second addition of Glu (5 mM). (f) Cyclic amperometric responses of CPN-modified GCE in 0, 5, and 30 mM Glu; the CPN-modified GCE was washed with water after each

measurement. Note that all current data have been normalized by the ESA and are not apparent current densities……………………………3-101

Figure 4. Energetically favorable Glu binding configurations and energies: (a) (100), (b) (111), and (c) (211) surfaces. Solid orange lines indicate coordination bonds and dotted black lines indicate hydrogen bonding. Cobalt, phosphorous, oxygen, carbon, and hydrogen are represented as blue, purple, red, grey, and white spheres, respectively………………………………………………………………3-103

Figure 5. (a) Calibration curves with the relative fittings based on the chronoamperometric response of the CPN-modified SPE in the electrolyte composed of HS diluted with PBS (10 mM, pH 7.4) to the successive addition of Glu at an applied potential of 0.65 V (vs Ag/AgCl) (the raw data prior to fitting are shown in Figure S13). (b) Consecutive CVs of the CPNs in a 33 mM Glu HS 5% v/v in PBS electrolyte after activation. The inset shows the changes in the current density at 0.65 V (vs Ag/AgCl) as the cycle number is increased from 1 to 200. All current density data are normalized by the ESA……………………………...3-104

Figure S1. Scanning electron microscopy (SEM) images of commercial Co3(PO4)2 powder at various magnifications……………………………………………………..………3-108

Figure S2. SEM image of the cobalt phosphate nanostructures (CPN) sample showing the region of interest on which energy-dispersive X-ray spectroscopy (EDX) was conducted and associated EDX data. (The EDX pattern is shown in Figure 1f.)…………………………………...3-109

Figure S3. X-ray photoelectron spectroscopy survey spectrum of the CPN……………………………………………………………………………3-110

Figure S4. Cyclic voltammograms of the CPN-modified glassy carbon electrode (GCE) measured in PBS electrolyte at different pHs and a scan rate of 20 mV s^{-1} ………………………………………………………3-110

Figure S5. CVs of the CPN-modified electrode in PBS buffer (10 mM, pH 7.4) recorded at a scan rate of 20 mV/s in the absence (black line) and presence (blue lines) of 10, 20, and 30 mM Glu, respectively. The dashed line represents the CV of the GCE (bare electrode) obtained under the same experimental conditions. In (a) and (b), the reported current densities are normalized against the geometrical area and the real surface area of the electrode, respectively……………………...3-111

Figure S6. Chronoamperometric response of the CPN to the addition of 5 mM of glucose (Glu) in a 0 mM Glu PBS electrolyte. A constant applied potential of 0.65 V was used…………………………………3-111

Figure S7. Chronoamperometric responses of the CPN-modified GCE in PBS buffer (10 mM, pH 7.4) to successive addition of Glu at an applied potential of 0.65 V (vs Ag/AgCl). The data of three successive experiments (exp) conducted using the same prepared electrode are shown. The data were used to construct the calibration curve in Figure 3d……………………………………………………………………………3-112

Figure S8. Chronoamperometric responses of Co3(PO4)2 powder-modified GCE in PBS buffer (10 mM, pH 7.4) to successive addition of Glu at an applied potential of 0.65 V (vs Ag/AgCl). The data of three successive experiments performed using the same electrode are shown. The data were used to construct the calibration curve in Figure S9……………………………………………………………………………3-112

Figure S9. Calibration curve based on CA experiments performed in triplicate (Figure S8)……………………………………………………3-113

Figure S10. Amperometric responses of the CPN-modified GCE to addition of 5 mM Glu in PBS electrolyte as a function of the electrolyte temperature……………………………………………………………...3-113

Figure S11. Relaxed slabs of cobalt phosphate: (a) (100), (b) (111), and (c) (211) surfaces. Cobalt, phosphorous, and oxygen are represented as blue, purple, and red spheres, respectively. Cobalt atoms that coordinate to glucose are highlighted in yellow…………………………………………………………………....3-114

Figure S12. Screen-printed electrode modified with the CPN……..3-116

Figure S13. Chronoamperometric responses of the CPN-modified SPE in PBS electrolyte (10 mM, pH 7.4) containing 1, 2, 5, and 10% v/v of HS to successive addition of Glu at an applied potential of 0.65 V (vs Ag/AgCl). The corresponding calibration curves with the relative fittings are displayed in Figure 5a……………………………………………...3-117

Figure S14. Sensitivity and limit of detection (LOD) of the CPN-modified SPE in PBS buffer as a function of concentration of human serum (HS) based on data from Figure 5a…………………………………………3-118

Chapter 4 - Enzyme-Mimicking Hybrid Nanoflowers Enable Sensing of Bioanalytes

Figure 1. a) Schematic illustration of the preparation of dextran sulfate-copper phosphate hybrid nanoflowers and b) the nanoflowers-based platform for the detection of hydrogen peroxide............................4-124

Figure 2. Characterization of hybrid dextran sulfate-copper phosphate nanoflowers. a) SEM and b) TEM images of the D-NF with, in the respective inserts, high magnification images. c) FT-IR spectra of pure copper phosphate, DS and hybrid D-NF. d) EDX spectrum and, in the insert, mapping, of the D-NF. 4-125

Figure 3. SEM images of the hybrid nanoflowers growth at a) 30, b) 60, c) 90 and d) 180 min from the start of the crystallization reaction. Scale bars reported are the same in all the figures. 4-127

Figure 4. Non-enzymatic peroxidase-like catalytic activities of hybrid nanoflowers. a) Catalytic kinetics regarding the oxidation of OPD to DAP by H_2O_2 or D-NF alone and with the co-presence of H_2O_2 and D-NF. b) Emission spectra of the solutions after kinetic completion with an excitation wavelength of 410 nm. c) Emission spectra, and photos in the insert, of the solutions incubated in functionalized wells upon addition of different H_2O_2 concentrations (from 0 to 7 mM) in PBS buffer. d) Calibration lines representing the extended and, in the insert, linear concentration ranges of H_2O_2 against emission intensities at 566 nm…………………………………………………………………………4-133

Figure 5. a) Schematic depicting the sensing of glucose via a hybrid enzymatic/non-enzymatic cascade reaction. b) Excitation and emission fluorescence spectra of samples with a combination of OPD, GOx, Glu and D-NF in PBS after incubation for 120 min at 37 °C. c) Calibration lines representing the extended and, in the insert, linear concentration ranges of Glu vs. emission intensities at 536 nm. 4-137

Figure S1. XRD spectra of D-NF and the copper phosphate as the reference. 4-141

Figure S2. Thermal gravimetric analysis of the D-NF. 4-141

Figure S3. SEM images of particles prepared as the controls. Particles synthesized as: a-b) pure copper phosphates without the presence of organic molecules, and c-d) with the presence of dextran at a concentration of 0.83 mg mL^{-1} are represented by low and high magnification SEM images. 4-142

Figure S4. Optical microscope images in liquid state of a) D-NF, b) pure copper phosphate NF, and c) Dextran-NF. 4-143

Figure S5. SEM images of D-NF prepared at different concentrations of PBS. Hybrid nanoflowers synthesized with a PBS concentration of a) 0.5 X, b) 2 X, c) 5 X and d) 10 X are represented by low and high magnification SEM images. 4-143

Figure S6. SEM images of D-NF prepared with different concentrations of Cu^{2+} ions. Hybrid nanoflowers synthesized with a Cu^{2+} ions concentration of a) 2.5, b) 5, c) 10, d) 40 and e) 160 mM are represented by low and high magnification SEM images. 4-144

Figure S7. SEM images of D-NF prepared at different pH. Hybrid nanoflowers synthesized at pH of a) 5.4, b) 6.4, c) 8.4, d) 9.4 and e) 10.4 are represented by low and high magnification SEM images. The same scale bars were used for all the images. 4-145

Figure S8. SEM images of D-NF prepared with different concentrations of DS. Hybrid nanoflowers synthesized with a DS concentration of a) 0.08, b) 0.17, c) 0.4, d) 1.7, e) 4.2 and f) 8.3 mg mL^{-1} are represented by low and high magnification SEM images. 4-145

Figure S9. SEM images of D-NF assembled at the functional polystyrene interface of TC plates at a) low, b) medium, and c) high magnifications.. 4-146

Figure S10. Catalytic reaction rates of the OPD oxidation in microreactors with the presence of H_2O_2 and D-NF and control experiments with the presence of only H_2O_2 or D-NF. Included, are the linear fit of the data. The data are relative to Figure 4a.................. 4-146

Chapter 5 - Nanoengineering Multifunctional Hybrid Interfaces Using Adhesive Glycogen Nanoparticles

Table Of Content Graphic. Amphiphilic phytoglycogen nanoparticles are used as building blocks for engineering multifunctional hybrid films with catalytic and sensing properties. 5-150

Fig. 1. (a) Schematic of the L-PG assembly on a substrate and (b) co-assembly of metal nanoparticles on the L-PG layer to obtain hybrid surfaces via LbL assembly suitable for catalysis and sensing applications. 5-154

Fig. 2. Characterization and coating properties of L-PG. (a) ATR-FTIR spectra of PG and L-PG and (b) dry-state AFM image and corresponding height profile of L-PG. (c) Water contact angles of the bare, PG-, and L-PG-coated substrates. Dry-state AFM images and corresponding height profiles of (d) PG- and (e) L-PG-coated glass substrates (scale bar 2 µm). (f) Emission intensities of fluorescently labeled L-PG coatings on glass substrates after incubation in different chemical and biochemical environments. Error bars represent standard deviations. 5-155

Fig. 3. Characterization of hybrid L-PG LbL assemblies with metal nanoparticles. (a) UV–Vis spectra of glass substrates coated with one bilayer of L-PG/AuNP, L-PG/AgNP and L-PG/PtNP (purple, yellow and

grey lines, respectively) and three bilayers of sequentially assembled L-PG/AuNP, L-PG/AgNP, and L-PG/PtNP (red line) and corresponding photograph (inset) of glass substrates coated with various layers of L-PG and metal nanoparticles (Au, Ag, Pt, and Au–Ag–Pt). (b) QCM-D frequency profile of an L-PG/AuNP LbL assembly on a gold chip obtained by sequential deposition of L-PG (blue arrow) and AuNPs (red arrow). (c) Dry-state AFM film thickness profile as a function of the L-PG/AuNP bilayer number and corresponding AFM images of the first and fourth bilayers (insets). (d) LSPR absorbance of glass substrates with 1 bilayer of L-PG/AuNPs after incubation in various chemical environments. (e) Photographs of L-PG/AuNP LbL assemblies on various substrates (scale bar 1 cm)... 5-158

Fig. 4. PS microparticles coated with L-PG and L-PG/AuNP LbL assemblies. (a, f, k) Differential interference contrast (DIC) microscopy, (b, g, l) TEM, and (c, h, m) SEM images, and (d, i, n) C and (e, j, o) Au EDX mapping of bare PS microparticles (a–e), L-PG-coated PS microparticles (f–j), and 3-bilayer L-PG/AuNP-coated PS microparticles (k–o). Scale bars: DIC (10 μm), TEM (2 μm) and inset (100 nm), and SEM and EDX (3 μm)... 5-161

Fig. 5. Catalysis and sensing applications of L-PG/metal nanoparticles LbL assemblies. (a) UV–Vis spectra of MB recorded during its degradation via $NaBH_4$ in a 3-bilayer L-PG/AuNP-coated PP tube and photograph (inset) of the functionalized tube. (b) $NaBH_4$-mediated MB degradation kinetics in 1-, 3-, and 5-bilayer L-PG/AuNP-coated PP tubes. (c) Comparison of the amount of AuNPs leached from a 3-bilayer L-PG/AuNP-coated PP tube and the total amount of AuNPs originally deposited in the same tube. (d) SERS spectra of a 3-bilayer L-PG/AgNP-coated glass as a function of different concentrations of CV……….. 5-164

Figure S1: PG functionalization reaction with lipoic acid to obtain L-PG via Steglich esterification. 5-168

Figure S2: H-NMR spectra of L-PG and PG. The thin red line is a magnification of the lipoate peaks from 3.4 to 0.5 ppm. 5-169

Table S1: Chemical modification reactions of PG into L-PG.......... 5-169

Figure S3: UV–vis spectra of L-PG and PG. 5-170

Figure S4: DLS hydrodynamic diameter populations of L-PG and PG………….. 5-170

Figure S5: Photographs of water droplets on bare, PG-, and L-PG-coated substrates; the contact angle values are given in Figure 2c. Scale bar: 2 μm. 5-171

Figure S6: Cytotoxicity studies of PG and L-PG. 5-171

Figure S7: Enzymatic degradation of PG and L-PG. 5-172

Figure S8: (a) PG functionalization reaction with dodecanoic acid to obtain DD-PG via Steglich esterification and (b) H-NMR spectra of DD-PG with magnification of the peaks corresponding to the dodecane moiety from 2.5 to 0.5 ppm. 5-173

Figure S9: Dry-state AFM image and corresponding height profile of DD-PG-coated glass substrates (scale bar = 2 μm). 5-174

Figure S10: (a) UV–Vis spectra of glass substrates coated with increasing number of L-PG/AuNP bilayers. (b) Localized surface plasmon resonance absorbance profile at 545 nm as a function of the bilayer number. 5-174

Figure S11: UV–Vis spectra of glasses coated with increasing number of (a) L-PG/AgNP and (c) L-PG/PtNP bilayers with corresponding absorbances at (b) 415 nm and (d) 600 nm as a function of the bilayer number. 5-175

Figure S12: (a) UV–Vis spectra of glass substrates coated with L-PG/AuNP, DD-PG/AuNP, PG/AuNP assemblies or AuNPs alone and (b) corresponding absorbances at 545 nm. 5-176

Figure S13: QCM-D dissipation profile of an L-PG/AuNP LbL assembly on gold chip obtained upon sequential deposition of L-PG (blue arrow) and AuNPs (red arrow); the corresponding QCM-D frequency profile is shown in Figure 3b. 5-176

Figure S14: Root mean square (RMS) roughness of dry films as a function of the L-PG/AuNP bilayer number. 5-177

Figure S15: HIM images of L-PG/AuNP LbL assembly on glass with the final layer as L-PG (left) and AuNP (right). 5-177

Figure S16: Photographs of L-PG/AuNP assembly on (a) polyether ether ketone and (b) Viton. 5-178

Figure S17: Degradation kinetics of MB via $NaBH_4$ on a bare PP tube and L-PG-coated PP tube. Both reaction systems do not contain AuNPs. 5-179

Figure S18: SERS signal intensity at 1615 cm^{-1} as a function of the concentration of the crystal violet (CV) solution; the corresponding SERS intensity profiles are shown in Figure 5d. 5-179

Chapter 1

Introduction

This chapter will provide an overview of hybrid materials, their natural origin, and history. Relevant examples of hybrid nanostructures and their synthetic preparation will be discussed.

Moreover, the chapter will review the literature on current industrial applications of hybrid materials and several significant research studies on the use of hybrid materials for biosensing applications.

1.1 Introduction to hybrid materials

Novel technologies generate an immense demand for new and functional materials. Often, established materials as metals, ceramics and polymers do not possess all the properties required for developing new technological applications. However, combinations of these compounds into hybrid materials, display superior properties than their single component counterpart, enabling their uses in advanced applications. For this reason, in the last decades, organic-inorganic hybrid materials attracted immense interests in both industry and academia.[1-6] These materials are obtained via organic, organometallic, supramolecular, intercalation, and polymeric chemical reactions at relatively low temperature and atmospheric pressure in aqueous or organic solvents.[7-8] By using these techniques, is possible to combine in one single material two, or more, inorganic, organic, and biological components at the molecular level to obtain hybrid materials with unique chemical, physical, colloidal, and functional properties. Functional hybrid materials can be prepared in different forms including thin films, coatings, fibres, powders, foams, gels, and monoliths with nano-to-macro complex structures and chemical compositions. These materials can be processed by soft chemical engineering strategies, as dip-, spin-, spray-coatings, electrospinning, templating, extrusion, aerosol processing, and 3D printing.[9-12]. Inorganic particles, fibres and lamellae can be incorporated into an organic matrix to prepare composites with improved mechanical properties. Inorganic microfiber-reinforced polymers are one example of widely applied hybrid materials endowed with lightweight and robust structures. When the inorganic and organic components are manipulated at the nanoscale, novel properties can emerge.

Organic-inorganic hybrid materials are multicomponent compounds in which at least one of the organic and inorganic part reside in the micro-or nanometre domain.[13] The final properties of a hybrid material arise from the single constituent parts, as well as from their synergistic interactions through the organic-inorganic materials interface.[14] The nature and energy of these interactions play a crucial role in tailoring the hybrid materials properties, such as mechanical, optical, chemical, catalytic, and functional properties. Hybrids belong to two main classes, class I and class II, where the organic and inorganic parts are interacting via weak bonds (van der Waals, hydrogen bonds, or electrostatic bonds), or strong bonds (covalent or ionocovalent), respectively.

The research on hybrid materials is highly interdisciplinary, at the crossroad of physics, chemistry, biology, and materials science, interacting with disparate scientific areas and opening new exciting opportunities both in fundamental and applied science, as well as tremendous opportunities for industrial applications. Multidisciplinary teams of engineers, scientists, ceramists, and physicists experts in the fields of solid-state, surface, coordination, polymer, and molecular chemistry merged driven by environmental awareness and economical challenges to develop emerging hybrid nanomaterials by using safe, and cost-effective synthetic strategies including biomimetic and bioinspired approaches.[15] Biomimetic and bioinspired materials, which a hold high level of organizations and dynamic structures featured in biological systems, have not only the advantage of being prepared in environmentally friendly conditions, but also present unique functional characteristics, as adaptivity, self-reparation, hierarchical controlled structures, biological compatibility, and recyclability.[16-17] To have a comprehensive understanding of this class of organic-inorganic hybrid materials an overview of the naturally occurring hybrid materials is first presented in the next section.

1.2 Natural hybrid materials

Nature designed and produced hybrid material long before the humankind gave a name to this concept. Developing biological materials, Nature accomplished a variety of architectures, materials, and systems, from the most simple to the most complex organisms, through crossbreeding and hybridization.[18] For instance, complex hierarchical biomineral nanocomposites assembled via biomineralization, as shellfish shells, shells, nacre, coccolith, bones, exoskeletons, ivory, teeth, diatoms, magnetotactic bacteria, radiolaria, and ferritin, are encountered ubiquitously in nature.

These are hybrid materials composed of biopolymers, like proteins and polysaccharides, interacting at the nanoscale with a variety of inorganic compounds, including calcium phosphate, calcium carbonate, calcium oxalate, iron oxide, silica, and many others (Figure 1a-l).[19-27] The properties of these highly integrated intelligent systems are a compromise of disparate functions, like density, permeability, colour, as well as flexible vs. rigid mechanical characteristics. These functional properties of these natural materials are obtained as a result of the topological and structural organization at all scales, from the molecular to the millimetre scales.[28-29] For instance, unique mechanical properties of hybrids in some crustaceans are achieved because the organic-inorganic components hierarchical organization allow the system to be stimuli-responsive to external stresses at all the different scales.[26] Typically, inorganic materials have good mechanical properties that provide structural integrity to the natural material, whereas organic materials act as a binder, bridging the inorganic parts. Nature, through time and evolution, selected the appropriate material and optimized its hierarchical organization for specific functions.

Nature produces, via biomineralization, a vast variety of materials with different shapes, chemical composition, and disparate functionality, in mild synthetic conditions, such as aqueous environment, neutral pH, ambient temperature and pressure. It is therefore of crucial importance to mimic Nature to prepare materials in such conditions. The interface-controlled growth of hybrid materials in the biomineralization process results in diverse shapes and morphologies relying only on a few different building blocks. Furthermore, the hierarchical organization of these building blocks is obtained via self-assembly mechanisms from the nanometre to the millimetre scale. The function and performance of the resulting hybrid materials depend on the levels of complexity of the assembled components.

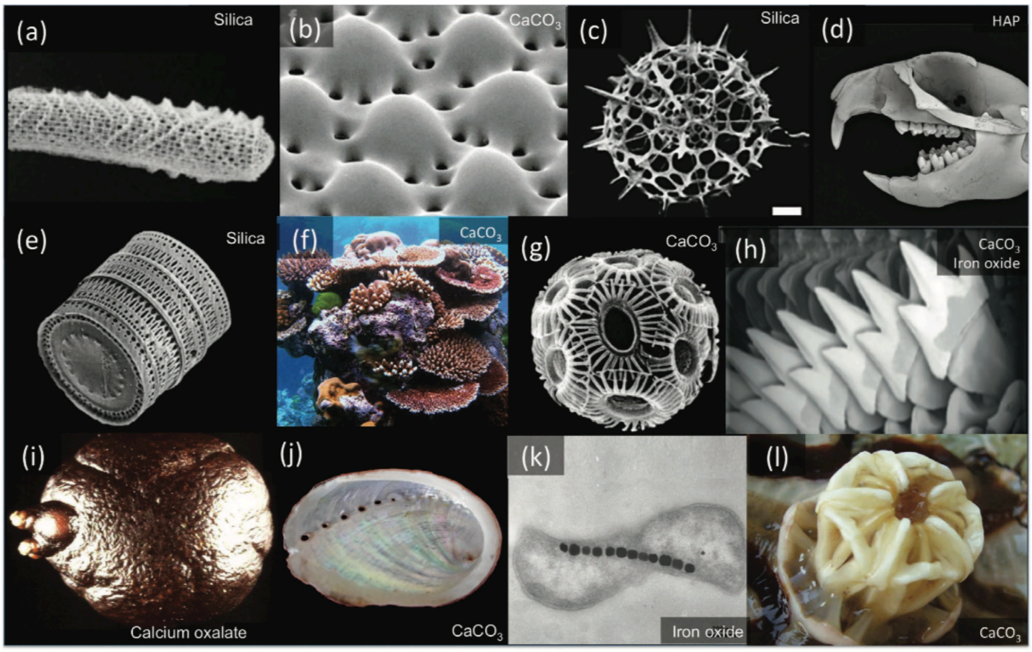

Figure 1. Examples of hybrid materials found in nature. a) Venus sponge, b) brittlestar's lens, c) radiolaria, d) vertebrate teeth, e) diatom, f) corals, g) coccolith, h) teeth of chitons, i) kidney stone, j) abalone shell, k) magnetotactic bacteria, and l) teeth of the urchin. Adapted from [19-27].

1.3 History of hybrid materials

The first example of organic-inorganic material is based on clays.[30] These materials were spontaneously formed in Nature back during the origin of life some 3.8 Ga years ago.[31] The intercalation of organic species into colloidal phyllosilicates was driven by different mechanisms relying on weak interactions such as hydrogen bonding, electrostatic bonds and van der Waals forces.[32] Clays, having some unique properties such as adsorption capacity, high surface area, charge density and interlayer acidity, exhibit catalytic activity on diverse organic molecular species.[33-36] Weak organic-inorganic interactions allow the adsorption-transformation-desorption of organic molecules into the inorganic component, making clays a "molecular replicator". The "clay hypothesis" suggests that during the early period of Earth these hybrid materials concentrate prebiotic organic molecules and catalysed the formation of chiral complex systems, playing a crucial role in the development of life.[37]

Figure 2. Hybrid materials for arts throughout history. a) Prehistoric painting, b) Ancient Mayan drawing and Flemish art made also with, respectively, minerals-clays paste, indigo dye-clay pigment and Prussian Blue. Adapted from [30].

Man-made hybrid organic-inorganic appeared millions of years later. The first hybrid materials dating back to 13000 BC were found in prehistoric paintings in Lascaux's cave (Figure 2a).[30, 38] These materials were hybrid nanocomposites composed of iron oxide, clays and organic components such as fat, urine, saliva and blood. Iron oxide was the pigment, whereas the mixing of clays and organic materials gives binding materials with different rheological properties, allowing the hybrid materials deposition on diverse substrates, this is known as "fingers painting".

In ancient China around 1500 years ago sticky rice soup, lime and other mortar ingredients were used to be mixed to form one of the first organic-inorganic mortars ever made.[39] Amylopectin, found in the soup, was combined with the inorganic components to form biocomposites with novel remarkable mechanical properties used in important buildings, such as the Great Wall.[40] In Central America, during the pre-Spanish period, Mayan populations used to mix the indigo natural dye with a microporous clay, palygorskite, to prepare a long-lasting hybrid pigment called Maya Blue (Figure 2b).[41] In these materials, the inorganic matrix host in its open-channel structure the organic dye and preserve its properties in harsh conditions such as extreme pH, UV irradiation and thermal treatment up to 200 °C.[42] As a result, the colour of Maya Blue used in handworks was preserved over the centuries against atmospheric and biological agents, such as humidity and microorganisms.[43] More recently, in Europe at the beginning of the 18th century, the first purely synthetic coordination compound was discovered out by chance by Diesbach and Dippel: Prussian Blue.[44] The hybrid blue pigment was cheaper and easier to prepare than the other blue pigments available at the time, making it a novel material with an immense commercial impact.[45] For this reason, the synthetic method was hidden for almost 20 years from its first discovery. A beautiful example of early use of this pigment is on the Entombment of Christ by

Pieter van der Werff (1709), for the sky and Mary's veil (Figure 2c). It was only nearly 300 years later, in 1977, and after the advances in crystallography characterizations that Prussian Blue was fully characterized to be a cubic structure in which Fe(II) and Fe(III) alternating octahedra are connected via organic cyanide ligands.[46]

More recently starting from the 17th century, thanks to advances in the field of chemistry, another type of hybrid compound was introduced with monumental impact in modern society: silicon and organosilicon based materials. Pioneering works were done by J. B. van Helmont, J. J. Berzelius,[47] C. Friedel and J. M. Crafts[48] in the discovery and research of silicon and organosilicon precursors, such as silicon halides, alkoxides, and hydrides, and several synthetic methods for the preparation of organic-inorganic compounds characterized by carbon-silicon bonds. In the 40s, massive industrial advancements were done based on the research of F. S. Kipping[49] on silicones driven by the technological demand of military products for World War II. After the conflict, numerous industries, as Dupont, BASF and 3M, developed the silicon and non-silicon based materials, boosting the research of hybrids materials for commercial and scientific applications.

1.4 Modern synthetic hybrid materials

Recent synthetic hybrid materials are composed of numerous organic and inorganic compounds using many synthetic procedures. In the next paragraphs, a literature review of the different organic and inorganic building blocks composing hybrid materials, as well as present hybrid structures based on diverse materials, their synthetic preparations and their applications will be discussed.

1.4.1 Inorganic building blocks

Inorganic structures have distinctive characteristics such as size, size distribution, shape, dimensions, elemental composition, charge, oxidation state, allotropes, and crystallinity.[50-51] Many different inorganic materials are a good candidate for the preparation of hybrid structures, for instance, pure metal clusters and nanoparticles, chalcogenides, oxides, carbonates, phosphates, nitrides, silicon-based materials or clays.[52-53]

Metal clusters and nanoparticles are agglomerates of elements consisting of pure metals or metal mixture, for example, gold, silver and platinum nanoparticles.[54] Commonly, the surface of metal clusters can be functionalized to lower their surface energy to preserve their colloidal stability and to enhance their compatibility with the organic component at the interface.[55] For instance, gold nanoparticles display an increasing affinity toward carboxyl, phosphine and thiol moieties, in this order, and therefore molecules having these functional groups will be a suitable ligand for the capping of the structures.[56-57]

Oxides and transition metal oxides are an interesting class of materials because of their unique magnetic, electronic and catalytic properties.[58-59] Examples of these materials are silica particles and transition metal (Fe, Cu, Co) oxide particles.[60-62] Although the presence of oxygen in silicate-based materials allows their functionalization via covalent bonds with a variety of molecules, such as derivatives of trichlorosilanes bearing different functional groups, for transition metal-based materials, instead, functionalization is carried via electrostatic and coordination interactions or hydrogen bonding.[57] Examples of moieties are carboxylates, sulfonates, phosphates for anionic groups, and ammonium moieties for cationic groups.

1.4.2 Organic building blocks

Organic molecules have many different properties like molecular weight, size, hydrophilic-hydrophobic domains, functional groups, charges, and functionalities.[63] Examples of organic materials are small molecules, natural and synthetic polymers as well as biological active biomacromolecules like proteins or enzymes.[64]

Small organic molecules can modify inorganic materials being physically trapped in cavities or covalently connected to the inorganic structure.[65-66] Usually, mild conditions for the preparation of hybrid materials need to be used to assure the stability of the organic molecules. Functional groups need to be present in molecules to enhance the compatibility toward the inorganic component. Carboxylic, catechol and aromatic moieties are examples of functional groups that can favourably interact with inorganic components via chelation, covalent bonds, electron transfers and electrostatic π-cation interactions.[67-69]

Synthetic and natural polymers such as synthetic block copolymers, proteins nucleic acids and polysaccharides were also used for the preparation of hybrid materials.[70] Enhanced compatibility between the organic and inorganic components arises from either hydrophilic or hydrophobic functional groups present on the polymeric chains. In particular, dendrimers are highly branched monodisperse macromolecules with unique physical and chemical properties.[71] These properties derive from the peripheral functional groups and the internal cavities within the nanostructure. The good control over their size and chemical functional groups, candidate this structure as interesting building blocks for hybrid materials.[72]

Particle-like structures as colloids composed of physically or chemically cross-linked organic molecules were also used as building blocks for hybrid materials.[73] Their properties such as size range, size distribution, and chemical composition can be controlled to prepare ideal building blocks for specific applications.[74] Importantly with organic colloids, is possible to achieve a fine control on their interfacial properties such as surface chemical composition and charge in aqueous environments.[75]

1.4.3 Clay- and zeolite-based hybrid materials

Clay-based hybrid materials are composed by different kind of aluminium phyllosilicates or 2D-like materials and a variety of organic compounds, from small molecules to polymers.[76-77]

Initially, hybrid materials based on layered clays were prepared exchanging the clays interlayer inorganic cations by organic cations.[78] Many organic compounds with different functionality, such negatively charged carboxyl groups or positively charged amines, were intercalated in layered and fibrous clays such as smectite, kaolinite, sepiolite and palygorskite.[79] Moreover, alkaline layered silicates, transition metal chalcogenides, titanates, molybdates, lamellar phosphates and phosphonates have been employed as an alternative of clays for the preparation of 2D-like hybrid materials following similar intercalation processes.[80-82] Due to their versatility, clay-based hybrid materials have found broad industrial applications.[36, 83] In research fields, these materials have been initially applied as additives, fillers, rheological agents, sorbents and recently in biotechnology as advanced material for vaccines carriers.[84-85] In industrial fields, organoclays are produced in the tens of thousands of tons around the world for large-scale applications such as pollutant or oil spill adsorbents, asphalts rheological agents and in bioactive materials as supports for pesticides and enzymes.

When polymers are used clay-polymer nanocomposites are obtained (Figure 3).[86-87] The pioneering work made by Fukushima et al. on polyamide-intercalated inorganic composites paved the way for the development of materials with enhanced properties and functionalities derived from the clay component.[88-89] In these materials, excellent mechanical and thermal properties are achieved along with novel functionality as electric and ionic conductivity for the applications in membranes and sensing.[13, 90] Moreover, organic components can be covalently bonded to the clay structure via acid treatment and subsequent grafting with organosilanes, epoxides or isocyanates, obtaining a material with similarity to silicones but having a planar structural arrangement.[91-93] Other than small molecules and polymers, hybrid clay-based materials were prepared with carbonaceous materials as graphene, carbon nanotubes and graphite nanoplates.[94-95] These hybrids show good mechanical properties and electrical conductivities, as well as the low-cost of production.[96] Finally, biohybrids are assembled by using biological components as the organic part in the hybrid material.[80] Interesting examples are materials based on phospholipids intercalated in clays for the immobilizations of enzymes[97] and viral particles modified clays for the delivery of vaccines.[84]

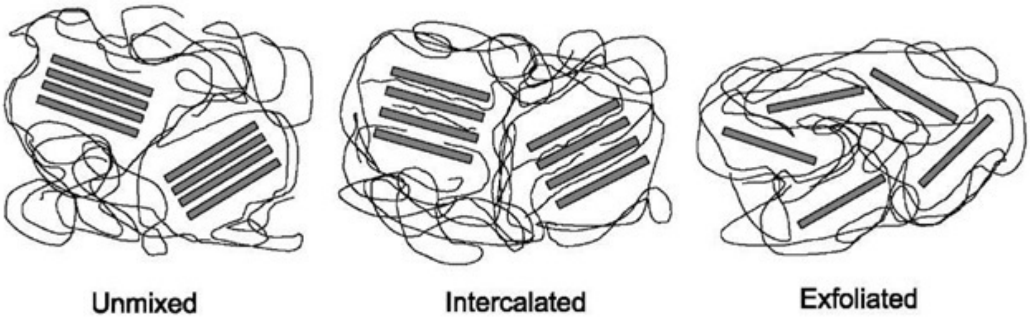

Figure 3. Schematic of three different levels of inorganic particles dispersion in a polymeric matrix, characteristic of clay-polymer hybrid materials. Adapted from [87].

Zeolites are composed of hydrated aluminosilicates with alkaline earth elements that, differently from clays, are connected by silica and alumina tetrahedra forming a 3D crystalline porous structure. The microcavities act as molecular sieves and so zeolites found applications in separation, purification and catalysis. The discovery of zeolites dates back to the 18th century when A. F. Cronstedt first discovered this minerals.[98-99] It is only in the 40s that zeolites started to be studied extensively by R. M. Barrer and R. M. Milton and applied to industrial applications as separation, purification and, due to their acidic-basic properties, catalysis.[100-102] However, inorganic zeolites had a limited number of structures and cavity sizes, limiting their potential applications. To overcome this, organic cations were employed as templating agents for the synthesis of hybrid zeolites replacing inorganic cations, obtaining, therefore, a large variety of structures, pore sizes and acidity.[103] Different organic molecules as alkylammonium,[104] quaternary ammonium anions[105] and trispyrrolidinium[106] were used for the preparation of hybrid zeolites. These structures were successfully applied for the separation of hydrocarbons and the catalysis of shape-specific molecules at high temperature.[107]

1.4.4 Coordination complex-based hybrid materials

The study of hybrid materials based on organic linkers connected to metal ions date back the 18th century since the discovery of Prussian Blue. The development of hybrid materials composed of polymers coordinating metals was introduced by the USA government in the 50s to develop novel materials with advanced mechanical and thermal properties for aerospace applications.[108-109] One of the first examples of coordination polymer materials were developed by Saito in the 50s, which prepared hybrids based on Copper (I) coordinated by organic molecules bearing cyanide moieties to form an extended a 3D network.[110] Subsequently, in the 70s, the group of C. E. Carraher Jr studied new synthetic routes, investigated different organic linkers and expanded the pool of metal ions for the preparation of organic-coordinated hybrid materials.[111] At that time, the structural and crystallographic characterizations of these materials were at their infancy because of the lack in the advancement of these techniques. A better understanding of the structural properties of these hybrid materials came in the 80s thanks to the work done by R. Robson, which had both expertise in coordination chemistry and crystallography. With new insights on the hybrids structural aspects, it was possible to achieve novel designs of extended 3D networks with controlled structure.[112] In the late 80s, Hoskin and Robson prepared a porous coordination polymer material based on copper with extended dimensions.[113] This organic framework had cavities that could potentially be freed to host different compounds. Upon removal of the solvent, however, the framework collapsed, making this material unusable. This and other similar materials belonged to the first-generation of coordination hybrids (Figure 4a).[114] The second-generation of coordination hybrids started during the 90s,[115] with the advancement of metal-organic frameworks (MOF) developed by the pioneering works of O.M. Yaghi, S. Kitagawa and G. Ferey. These materials had controlled rigid structures, porosity, excellent thermal and chemical stability and high surface area that could withstand the exchange of guests molecules without collapsing (Figure 4b).[116] One of the most famous examples in the Yaghi's family is the so-called MOF-5, which is a porous hybrid material based on octahedral zinc acetate building blocks linked by 1,4-benzenedicarboxylate molecules.[117] Other MOF were prepared changing the organic ligand length and functionality, obtaining materials with different properties.[118] MOF prepared with different divalent metal cations and ligands were synthesized by Kitagawa that displayed, as in the case for the CPL-1, channelled structures.[119] Using different organic ligand, a series of channel sizes, shapes and chemical environments could be achieved for the synthesis of materials applied for the adsorption of small molecules or the preparation of polymer-interpenetrated composite materials.[120-121] The third-generation of coordination hybrids took place with the work done by Ferey that expanded the metal pool of choice to trivalent and rare earth elements.[122-124] Advanced characterization techniques, such as NMR and computational modelling, were used for the design of functional MOF with unique properties as magnetic, thermal stability and sorption capacities.[125] MOF as the MIL-53 exhibited dynamic properties as the contraction and swelling of the framework depending on the absence/presence of water vapour (Figure 4c).[126-127] These smart materials, showing reversible responsiveness caused by an external trigger, were widely studied since the 2000s.[128] Nowadays, MOF and other porous coordination polymers are receiving enormous interests thanks to the advanced applications that these materials can fulfil.[129] Overall, a new revolution in the field of hybrid porous materials has started and so it did the transition toward real applications in disparate fields, such as catalysis, separation, nanomedicine, storage and sensing.[130-132]

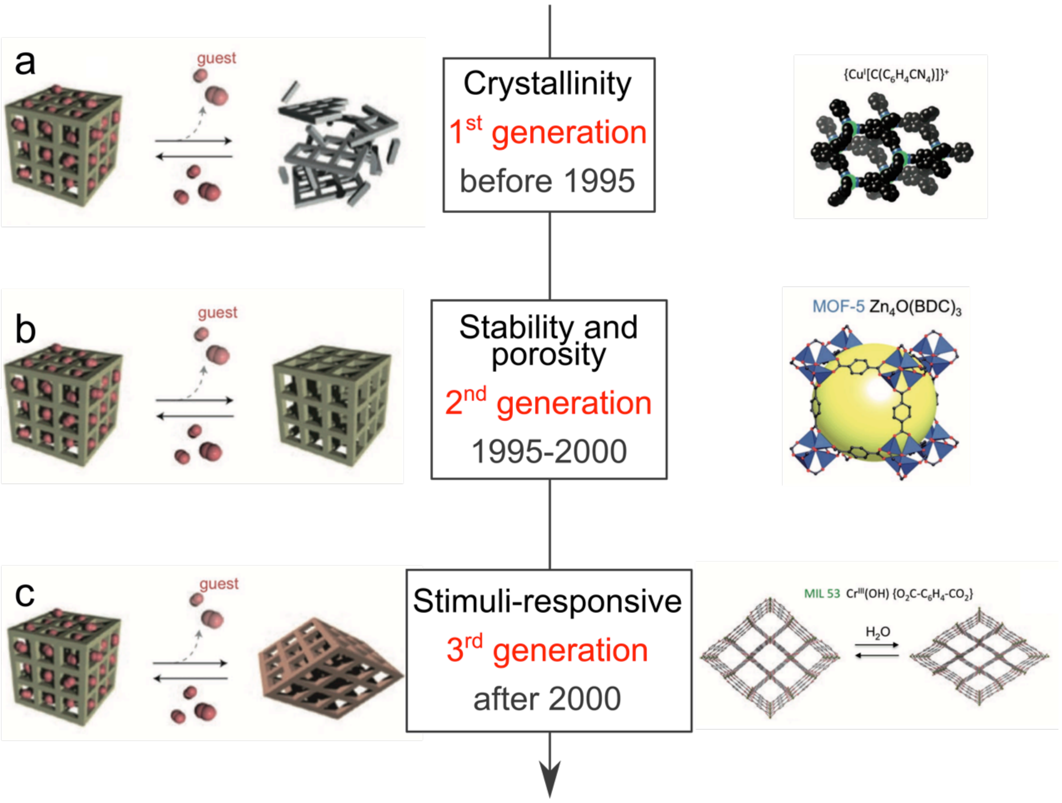

Figure 4. Functional and chronological classification of porous coordination polymers: a) copper-based framework, b) MOF-5, and c) MIL-53. Adapted from [30].

1.4.5 Phenolic building block-based hybrid materials

Phenolic-based materials have long been used in basic applications as inks, coatings and tannings.[133] Recently, hybrid smart materials have been prepared from phenolic building blocks and metal ions via coordination chemistry to produce stimuli-responsive,[134] antibacterial,[135] chemical-resistant[136] and nanostructured[137] materials for advanced nanotechnology, nanomedicine and environmental applications.[133] Phenolic compounds have unique adhesive, antibacterial, antioxidant and metal-chelating properties. Phenolic materials are prepared via synthetic methods as well as found in nature, in plants and animals.[138]

They have different functions including protection against ultraviolet light and reactive oxygen species, colouring and flavouring, transportation of iron in cells, and imparting adhesion to several marine organisms.[139-141] The understanding of the functional properties of polyphenols led to the tremendous development of phenolic-based materials for the preparation of soft-to-hard and one-to-three dimensional structures as thin films, particles and bulk materials.

Hybrid thin films have been prepared via metal-phenolic networks (MPN) and layer-by-layer (LbL) assemblies.[142-143] MPN were prepared originally by F. Caruso et al. from metal ions, as Fe^{III}, coordinated with multidentate phenolic ligands, as tannic acid (TA) (Figure 5a).[143] These films can be prepared using a variety of substrates regardless of their morphology and chemical compositions, such as inorganic (flat glass, silica and gold colloidal suspension), organic (polymer microparticles), and living systems (mammalian cells and yeast) (Figure 5b).[144-146] Besides, hollow capsules were obtained following a simple synthetic strategy that involved the coating of colloidal particles and successive template removal (Figure 5c and d).[147-148] Further studies reported the use of a variety of metal ions and phenolic ligands, from synthetic or biological origins, for the preparation of hybrid thin films with a multitude of disparate physicochemical properties (Figure 5 e and f). For instance, materials with fluorescence, magnetic resonance and positron emission tomography imaging properties were obtained incorporating metal ions as Eu^{III}, Gd^{III} and Cu^{II}.[147] Moreover, films having different disassembly kinetics and triggers, like pH or competing chemical species, were prepared using a range of phenolic-containing small molecules or polymers (Figure 5g-l).[149-151] Another technique used for the preparation of hybrid thin films is the LbL in the form of spray,[152] microfluidics,[153] continuous,[154] electro-triggered,[155] and vacuum filtration assemblies.[156] These films can be deposited on large substrates, with fine control over the film thickness.

Phenol-based particles in the form of crystalline particles, nanoparticles, micelles and superstructures have been prepared with a wide structural diversity and chemical composition. MOF having phenolic organic molecules have been explored since the 90s for the preparation of crystalline particles.[157] Since then, various phenolic-based MOFs were synthesized using several transition metals, such as Mg^{II}, Mn^{II}, Co^{II}, Ni^{II}, Zr^{IV} and Fe^{III}, and diverse phenolic-containing molecules as natural gallic and ellagic acid, and synthetic digallate and catecholate ligands.[158-160] Phenolic-based hybrid nanoparticles were prepared, for instances, using TA and a polaxamer incorporating ^{89}Zr for positron emission tomography imaging and via metal-phenol coordination of a modified polyethylene glycol (PEG) and Fe^{III} including a Pt prodrug for drug delivery.[161-162] Micelles based on linear copolymer, polyelectrolytes, polymer brushes and branched dendrimers were assembled via metal or boron complexation to obtain responsive nanostructures for drug delivery.[163-164] These smart structures were capable to sense the external environment and release the loaded cargo as a function of pH and concentration of diols. Superstructures composed of a variety of nano- and micro-particles were prepared exploiting metal-phenol coordination interactions.[137] Building blocks were coated with a phenolic film and subsequently mixed with the presence of metal ions to induce their cross-linking to obtain complex hierarchies.[165]

Macroscopic bulk hybrid materials were engineered from phenolic compounds via metal coordination to form gels and elastomers.[166-167] Soft gel materials assembled via non-covalent interactions, as the metal-ligand coordination, found applications in fields from nanomedicine to catalysis. These metallogels integrate specific properties deriving from both the metal, e.g. redox and magnetic, and the dynamic structure of the gel to form stimuli-responsive systems.[168-171] Several examples of metallogels based on natural polyphenols and polyelectrolytes or catechol-modified PEG, and iron oxide nanoparticles, Fe^{III} or other metal ions, were reported having self-healing, stimuli-responsive and mechanical dynamic properties.[172-175] Recently, the direct gelation of the natural phenolic compound TA with the Group IV transition metals Ti^{IV} and Zr^{IV} was reported (Figure 6a-e).[176] These metallogels, prepared under ambient conditions in both organic and aqueous solvents, displayed self-healing, transparency, adhesiveness, electrical and tuneable mechanical properties (Figure 6f and g). In particular, these gels allowed the in situ co-gelation of additives, as carbon nanotubes and inorganic nanoparticles, and the crystallization of organic and inorganic structures, such as active pharmaceutical ingredients and MOF (Figure 6h and i).[176-177] Elastomers having superior mechanical properties were synthesized exploiting metal-catechol interactions for the preparation of materials showing self-healing properties and energy dissipation characteristics.[167, 178]

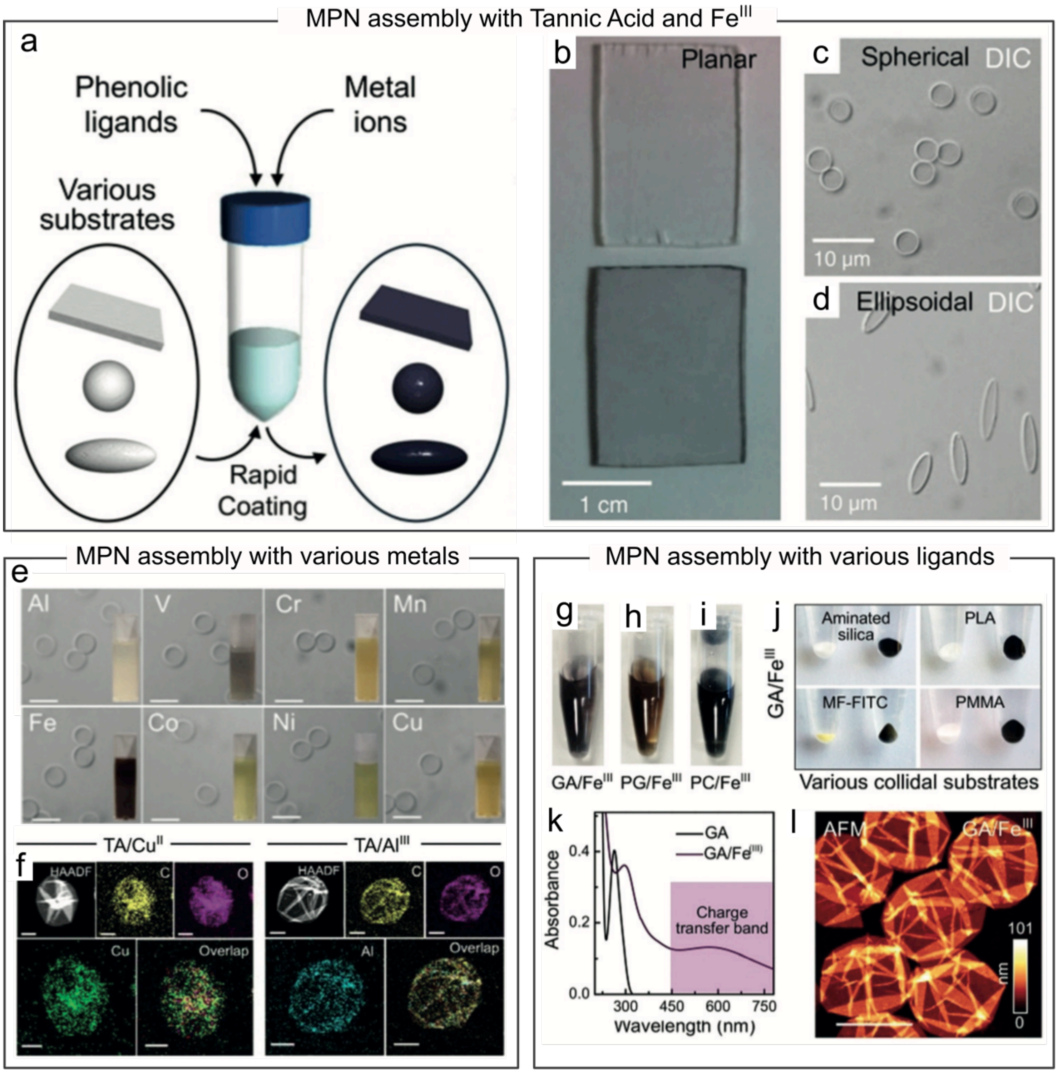

Figure 5. a) Schematic of MPN assembly preparation. TA/Fe^{III} thin film and hollow capsules: b) planar (photographs), c) spherical, and d) ellipsoidal (DIC images). MPN assembly with various metals: e) capsules obtained using TA and Al^{III}, V^{III}, Cr^{III}, Mn^{II}, Fe^{III}, Co^{II}, Ni^{II}, and Cu^{II} (DIC images, scale bar 5 μm), and the corresponding f) high-angle annular dark-field spectra (scale bar 1 μm). MPN assembly with various ligands: photographs of the capsule dispersions colours of g) GA/Fe^{III}, h) PG/Fe^{III}, and i) PC/Fe^{III}. j) GA/Fe^{III} coatings on several substrates. k) UV-Vis spectra of GA and GA/Fe^{III} capsules, and p) AFM image of dried GA/Fe^{III} capsules. Adapted from [133].

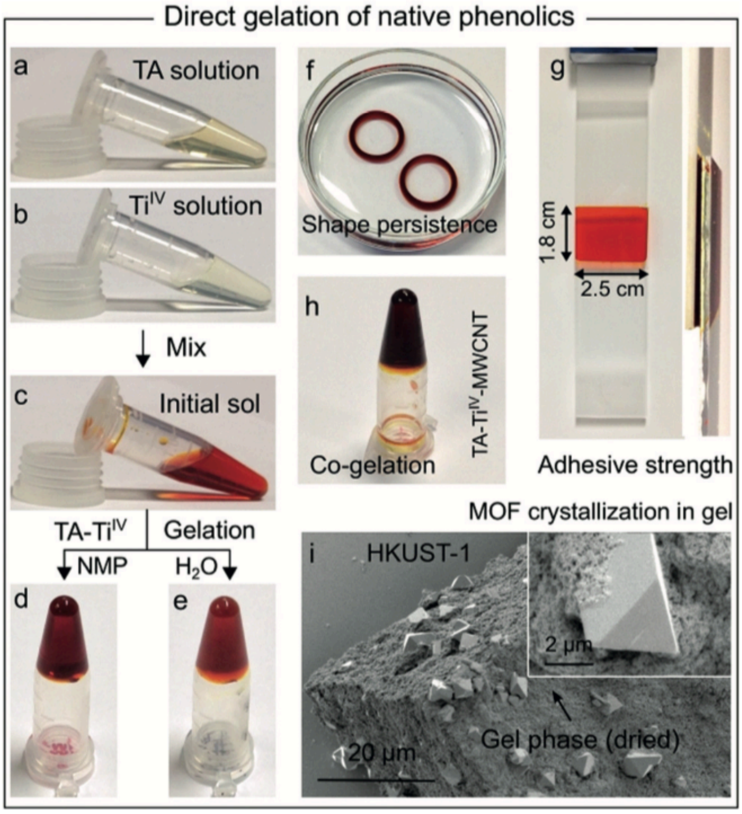

Figure 6. Metallogels based on tannic acid and titanium. a-e) Gelation of TA-Ti^{IV}, f) shape persistence, g) adhesive, h) co-gelation (multiwalled carbon nanotubes), and i) crystallization (HKUST-1) properties of TA-Ti^{IV} gels. Adapted from [133].

1.4.6 Nanoflowers-based hybrid materials

Organic-inorganic nanoflowers are a class of nanostructured flower-like materials self-assembled from biomacromolecules and metal ions. Nanoflowers found widespread interest in nanomedicine, sensing, catalysis and environmental applications.[179-183]

Nanoflowers were prepared for the first time by Zare et al. via a simple one-step precipitation method.[184] These enzyme-containing hybrid materials displayed enhanced enzyme catalytic activity, recyclability, and durability due to the enzyme immobilization effect and the high surface-to-volume ratio of the carriers.[185] Furthermore, organic molecules entrapped in the nanoflowers structure displayed exceptional stability against harsh environments, like high temperatures, organic solvents, and protease catalytic activity.[179] These hierarchically organized porous structures were prepared in mild conditions, e.g. room temperature and aqueous solution, therefore preserving the functionality of biomacromolecules. Remarkably, the enzymatic activities of these nanostructures exceed those reported for covalently attached or physically entrapped enzymes.[186] Nanoflowers were prepared simply adding a copper salt solution to a phosphate buffered saline solution containing the proteins. The self-assembly mechanism begins from the complexation of some functional moieties in the macromolecule (e.g. amide, carboxyl, and thiol groups) with the copper ions via coordination to provide nucleation sites for primary crystals (Figure 7a).[184] The anisotropic and kinetically controlled growth of these primary structures into larger copper phosphate crystals causes separate petals to appear, resulting in the complete formation of branched flower-like architectures. In these structures, the organic component acts as scaffold promoting the crystals nucleation and petals growth, as well as serving as a binder to hold the petals together. The nanoflowers characteristics (e.g. size, surface morphology, chemical composition) can be tuned varying the synthetic conditions, including macromolecules and metal ions nature and concentrations, crystallization time, temperature, pH, and ionic strength (Figure 7b-d).[187]

The physical and chemical properties of nanoflowers are commonly studied via materials science characterization techniques, such as scanning electron microscopy (SEM), transmission electron microscopy (TEM), energy-dispersive X-ray spectroscopy (EDX), X-ray diffraction (XRD) differential scanning calorimetry (DSC), nuclear magnetic resonance spectroscopy (NMR), Fourier-transform infrared spectroscopy (FTIR), and UV–visible spectroscopy (UV-Vis) (Figure 7e).[188] These characterization techniques aim to study the structure, surface morphologies, elemental and functional groups composition, thermal and crystalline properties of the nanoflowers, as well as their catalytic performances.

Further studies proposed other synthetic strategies for the preparation of hybrid nanoflowers to overcome some of the limitations associated with the conventional procedure. For instance, employing sonochemical synthetic strategies, the nanoflowers crystallization time was decreased from a few days down to a few minutes.[189-191] This was achieved simply putting under sonication the PBS solution containing metal ions and biomacromolecules in a laboratory commonly used ultrasound water bath. Moreover, a synthetic method was recently developed to prepare nanoflowers-functionalized substrates aiming to directly grow the hybrid structures on surfaces, such as paper- and fibrous-based membranes.[192-193] This was accomplished directly incubating the PBS solution including metal ions and biomacromolecules with the targeted substrate.

Several biomacromolecules as proteins,[194] enzymes,[195] peptides,[196] amino acids,[197] and antibodies[182, 198] were used in the synthetic procedure to obtain diverse types of nanoflowers. For instance, laccase,[184] lipase,[199] amylase,[200] catalase,[201] α-chymotrypsin,[202] trypsin,[203] alcohol dehydrogenase,[204] glucose oxidase (GOx),[189] horseradish peroxidase (HRP)[187, 205] and several other enzymes were used to prepare hybrid nanoflowers which displayed enhanced catalytic activity and improved recycling capabilities than their free analogue.[206-207]

Copper ions were mainly used for the preparation of hybrid nanoflowers, as well as other divalent metal ions, as Ca^{II}, Mg^{II}, Zn^{II}, Co^{II}, and Fe^{II}.[208-215] Besides the crystal structure and chemical composition of the inorganic matrix composing the nanoflowers, metal ions influence the enzymes encapsulation yield and relative reactivity.[216-217] For instance, β-glucosidase and[216] β-galactosidase[217] catalytic activities were superior in nanoflowers prepared with, respectively, Zn^{II} and Ca^{II}

rather than other divalent metal ions. This could be explained by the higher affinity of different binding sites on diverse biomacromolecules for specific metal ions, as shown with computational studies.[218]

Due to the high complexity and modularity that these hybrid materials have, different applications have been explored, including relevant biotechnological applications in the field of biosensing, biomedicine, catalysis, and environmental remediation (Figure 7f).[186]

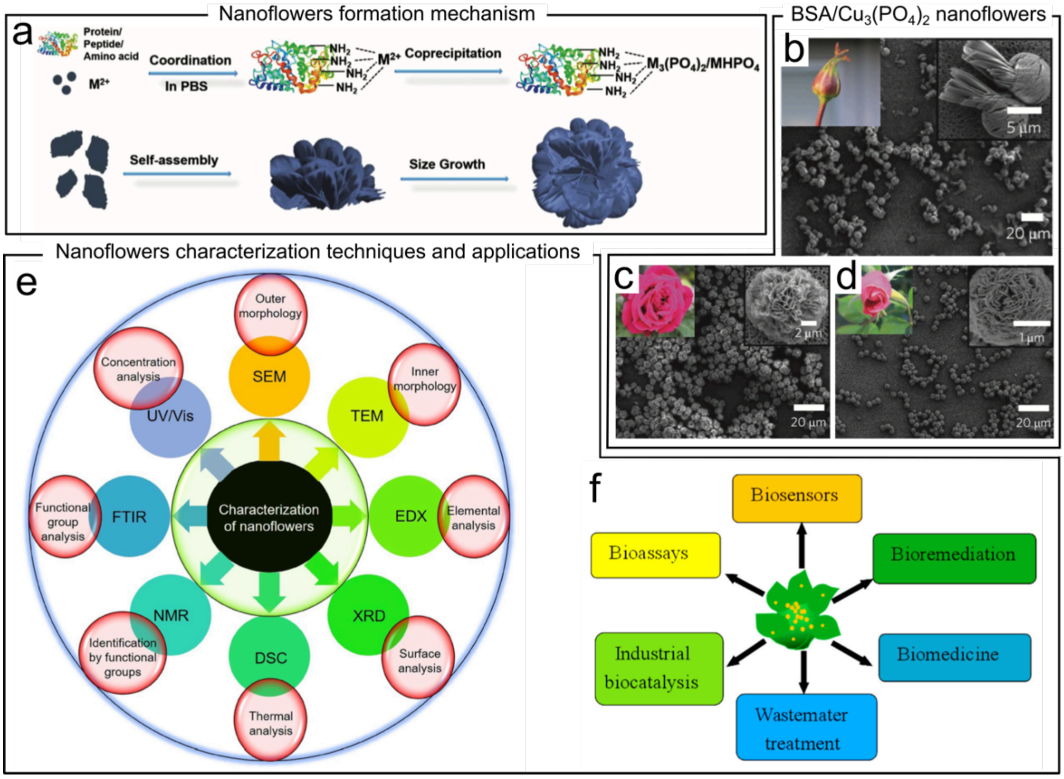

Figure 7. a) Schematic of the proposed synthetic formation mechanism of organic-inorganic nanoflowers through four main steps: coordination of metal ions via functional groups in the organic component, co-precipitation, self-assembly of inorganic crystals and organic molecules, and anisotropic growth until structure completion. SEM images of protein-inorganic nanoflowers with different morphologies prepared with BSA and copper phosphate, using a BSA concentration of b) 0.5, c) 0.02, and d) 0.1 mg mL^{-1}. e) Commonly used characterization techniques, inner circle, and corresponding analysed properties, outer circle, for the studied of hybrid nanoflowers. f) Advanced biotechnological applications of organic-inorganic nanoflowers. Adapted from [179, 184, 186, 188].

1.4.7 Gold nanoparticle layers-based hybrid materials

Metal nanoparticles, and in particular gold nanoparticles, have been extensively studied because of their unique size- and shape-dependent optical, electronic, catalytic and photo-thermal properties, high surface-to-volume ratio, facile functionalization and biocompatibility in fields such as physics, chemistry, biology and materials science for sensing, imaging, drug delivery and cancer therapy.[219-222]

The self-assembly of hybrid structures at the interfaces using gold nanoparticles and organic molecules was reported, obtaining nano- and micro-structured materials used in the biomedical field as biosensors based on surface-enhanced Raman scattering (SERS), enzyme-linked immunosorbent assay (ELISA), and electrochemical technologies.[223] These gold nanoparticle layers (GNPL) hybrid materials are assembled via non-covalent and covalent bonds.[224] Pre-functionalized surfaces can be easily coated with AuNPs simply immersing them in a colloidal solution of the nanoparticles.[225] Multi-layered structures can be prepared by the repetition of the alternating deposition of linking agents and metal nanoparticles. Commonly, these techniques are called by the name of layer-by-layer (LbL) assembly methods.[145] These are usually employed for the coating of interfaces and preparation of layered structures via a multitude of techniques, as dip-, spin-, and spray-coating, to name a few.[156] By the means of these techniques, parameters like the coating thickness, roughness, morphology, order, pores sizes, and functionality can be controlled. For instance, the coating thickness is finely controlled by the number of layers composing the final structure. Moreover, the final properties of a functional hybrid LbL assembled material arise from both the inorganic and organic component, as in the case of lysozyme-AuNPs assemblies were the inorganic GNPLs possess antibacterial properties derive from the presence of the protein.[226]

Coatings, thin films and layered structures based on LbL assemblies relying on non-covalent bonds among their building blocks usually are based on electrostatic interactions, between oppositely charged nanoparticles and polyelectrolytes, and hydrogen bonds. Polyelectrolytes are polymers whose repeating unit carry a charged functional group that in water dissociate making the polymer charged.[227] Coating substrates with polyelectrolytes provide a simple, controllable and versatile method for the preparation of thin-film and functionalized surfaces for the build-up of hybrid LbL assemblies (Figure 8a).[156, 228] Metal nanoparticles are electrically neutral and, for the successful electrostatic LbL assembly, they must be functionally charged in advance. Charged reducing or capping agents used in the preparation of such nanoparticles confer them a net charge and therefore colloidal stability in solution. Different agents produce nanoparticles with different charges. For instance, the use of sodium citrate and glucose provide nanoparticles with a negative charge, whereas using hexadecyl trimethyl ammonium bromide gives positively charged nanoparticles. As an example, non-covalent LbL assemblies were prepared with alternate deposition of positively charged poly(allylamine hydrochloride) and negatively charged sodium citrate-capped gold nanoparticles.[226, 229-230] Another class of non-covalent approaches for the preparation of GNPL rely on hydrogen bonding, in particular in the DNA templated self-assembly (Figure 8b).[231] This technique allows to prepare large-scale spatially controlled patterns of AuNP with nanometre-sized features by the self-assembling of complementary bases in the DNA structure.[232-233] These patterned materials have a homogeneous and controlled spatial distribution of AuNP on the surface, which is beneficial for applications relying on the materials nanoparticles distance-dependent optical and electronic properties, such as nanoelectronic and sensing.[234-235] This is obtained carefully engineering the DNA functional groups, that function as attaching point to the AuNP, and geometry, therefore controlling the intramolecular interactions and the DNA self-assembling via base pairing that rely on hydrogen bonds.[236-237] Briefly, AuNP with covalently attached DNA strands can self assemble on a surface with interparticle distances and geometries dictated by the self-assembly of the DNA structure.[234, 238]

In addition to electrostatically bonded assemblies, covalent interactions between gold nanoparticles and thiols-bearing molecules were used to produce hybrid LbL assemblies.[239] For instance, using 1,9-nonanedithiol as the spacer and linking agents, coatings and multi-layered hybrid structures were prepared on gold substrates using gold nanoparticles. Covalently linked structures show greater stability than non-covalently assembled materials due to the non-dynamic nature of their interactions, which is useful for the preparation of materials applied in catalytic, sensing and environmental applications. Interestingly, covalent-based coatings can be used for the production of patterned GNPL for applications as cell and protein patternings. Substrates are modified with spatial control over the deposition of AuNP via micro-contact printing or transfer printing.[240] This technique involves the transfer of gold nanoparticles from a stamp to a substrate by the means of specific covalent interactions, as the thiol-gold affinity.[241] For example, when a thiol-functionalized substrate is placed in contact with an AuNP-coated patterning stamp, the transferring process of AuNP to the functionalized substrate is driven by the newly formed covalent bonds between the thiols and the AuNP.[242] Moreover, the GNPL can be further modified with biomacromolecules, such as peptides, to promote cell adhesion and proliferation on a spatially controlled patterned area.[243]

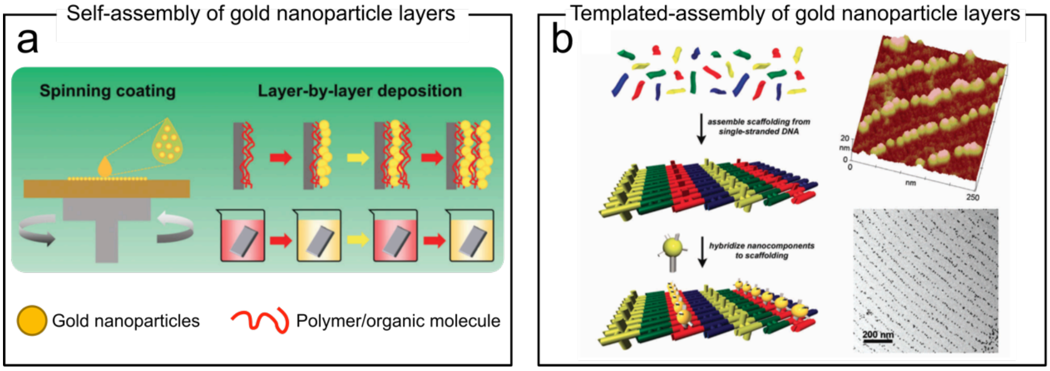

Figure 8. Depiction of assembly methods to prepare gold nanoparticle layers. a) Spin- and dip-coating via layer-by-layer strategy, and b) by template coating with pre-functionalized surfaces with self-assembled and self-organized DNA strands following conjugation with gold nanoparticles. Adapted from [223].

1.4.8 Glycogen building block-based hybrid materials

Natural occurring nanoparticles having multifunctional properties hold great potentials in biomedical and sensing applications,[244] as tissue engineering,[245-247] drug delivery,[248-249] and imaging.[250-251] These nanostructures have been modified to have targeting, drug loading, tracking, and imaging properties, yet maintaining biocompatibility and biodegradability features.[252-253] Contrarily to their synthetic counterparts that require multiple reagents, organic solvents, time and energy-intensive fabrication routes, natural nanoparticles and polymers such as polysaccharides are usually obtained via cost-effective extraction processes directly from natural resources. This allows their possible scale up production and easy research-to-industrial translation.[254] Among the available polysaccharides, glycogen is emerging as a natural building block for assembling nanostructured hybrid biomaterials.

Glycogen was firstly studied in the 19th century when Bernard C. reported the isolation of glycogen from animal livers and its physical and chemical properties.[255-256] Since then, it was found that glycogen nanoparticles exist in most living organisms acting as a vital component of the cellular energy machinery.[257-258] Different methodologies were proposed over the years to extract various types of glycogens with disparate chemical and physical properties from living organisms, such as animals and plants.[259-262] Glycogen acts as a regulator in the blood glucose homeostasis and cellular hydration. As an example, in mammals, glycogen made up to 10% of the hydrated weight of livers and it is present in lower quantity in other organs, like heart, brain and muscles.[263-265] Glycogen is synthesized by the cooperative activity of glycogen synthase, glycogenin, and glycogen-branching enzymes acting on uridine diphosphate glucose as the substrate (Figure 9a).[266] Briefly, glycogenin starts the polymerization leading to 8-12 glucose units linearly linked by an α-D-(1,4) glycosidic bonds, which convert into nanoparticle via branching of the structure, linking other glucose repeating units via α-D-(1,6) glycosidic bonds, and continuing the polymerization and branching sequences.[257, 267-268]

Glycogen is a hyperbranched polysaccharide in the form of spherical soft nanoparticle with high water solubility and molecular weight, made of glucose repeating units linked by linear or branching glycosidic linkages.[254] It has a dendrimer-like architecture of glucose chains and branches randomly linked to form a hyperbranched polymer nanoparticle,[269-272] with a higher density of glucose units in the core than the surface of the particle.[273] Several parameters characterize different types of glycogen from different sources, like particle size, charge, protein content, degradability, molecular weight, water content, degree of branching, and chain ends. Thus, the unique properties of glycogen-based materials are correlated to specific glycogen sources.[254] For example, TEM images of glycogen nanoparticles extracted from rat liver, rabbit liver, slipper limpet, and human skeletal muscles show their different structural properties (Figure 9b-e).[260] These polysaccharidic nanoparticles are easily modified to prepare advanced functional derivatives, which maintain biodegradability and biocompatibility. Chemical modifications are performed via carbohydrate chemistry and biochemistry in both water and organic solvents, at room temperature, under mild conditions, and with nontoxic reagents (Figure 9f). Engineering the chemical, physical, and structural properties of glycogen allow the tuning of hydrophobicity, colloidal stability, toxicity, degradability, and functionality of these nanostructures. For instance, glycogen can be functionalized with several functional groups via simple synthetic chemical routes, as periodate oxidation, reductive amination, oxime formation, esterification, alkylation, and several "click" based chemical reactions.[254] Although several materials were already proposed and used in targeting, drug delivery, and imaging applications,[251, 274-276] only a few reports proposed glycogen as a building block for the preparation of hybrid materials.

Hybrid materials based on organic components and metal nanoparticles hold great potentials in applications in sensing and biomedicine thank the components combined properties.[277] In particular, glycogen-AuNP hybrid materials were prepared with a self-assembly process simply mixing the metal and organic nanoparticles in solution.[278] The plasmon absorption of the AuNP had a redshift and its intensity was a function of the glycogen concentration. This effect was due to the enhanced dielectric constant of the surrounding environment of the AuNP, which aggregated on the surface of glycogen. Interestingly, when AuNP were mixed with other glycans or proteins similar opticals behaviour were not observed, indicating the affinity of glycogen to AuNP.[279] Another synthetic method to prepared glycogen-based hybrid materials was proposed following a bottom-up approach where AuNP were synthesized directly in the presence of glycogen

(Figure 10).[280] A higher concentration of gold ions precursors on the surface of glycogen resulted in an increased number of metal nanoparticles and therefore in a controlled shift of the plasmonic band. Moreover, following a similar procedure, glycogen-silver nanoparticles hybrids were prepared to hold antimicrobial properties.[281] Glycogen-based hybrid materials for drug delivery applications were designed and proposed by Kandimalla et al.[282] In this study, glycogen-AuNP hybrids were used to increase the solubility of the scarcely water-soluble silymarin, enhancing the drug gut permeation and ultimately the drug therapeutic effect in rats. Besides, these hybrids nanomaterials were non-toxic and biocompatible to human erythrocytes. The interesting and highly tunable properties of glycogen combined with the unique electromagnetic properties of inorganic metal nanoparticles make these nanoparticles an enticing potential platform for the preparation of functional advanced hybrid materials.

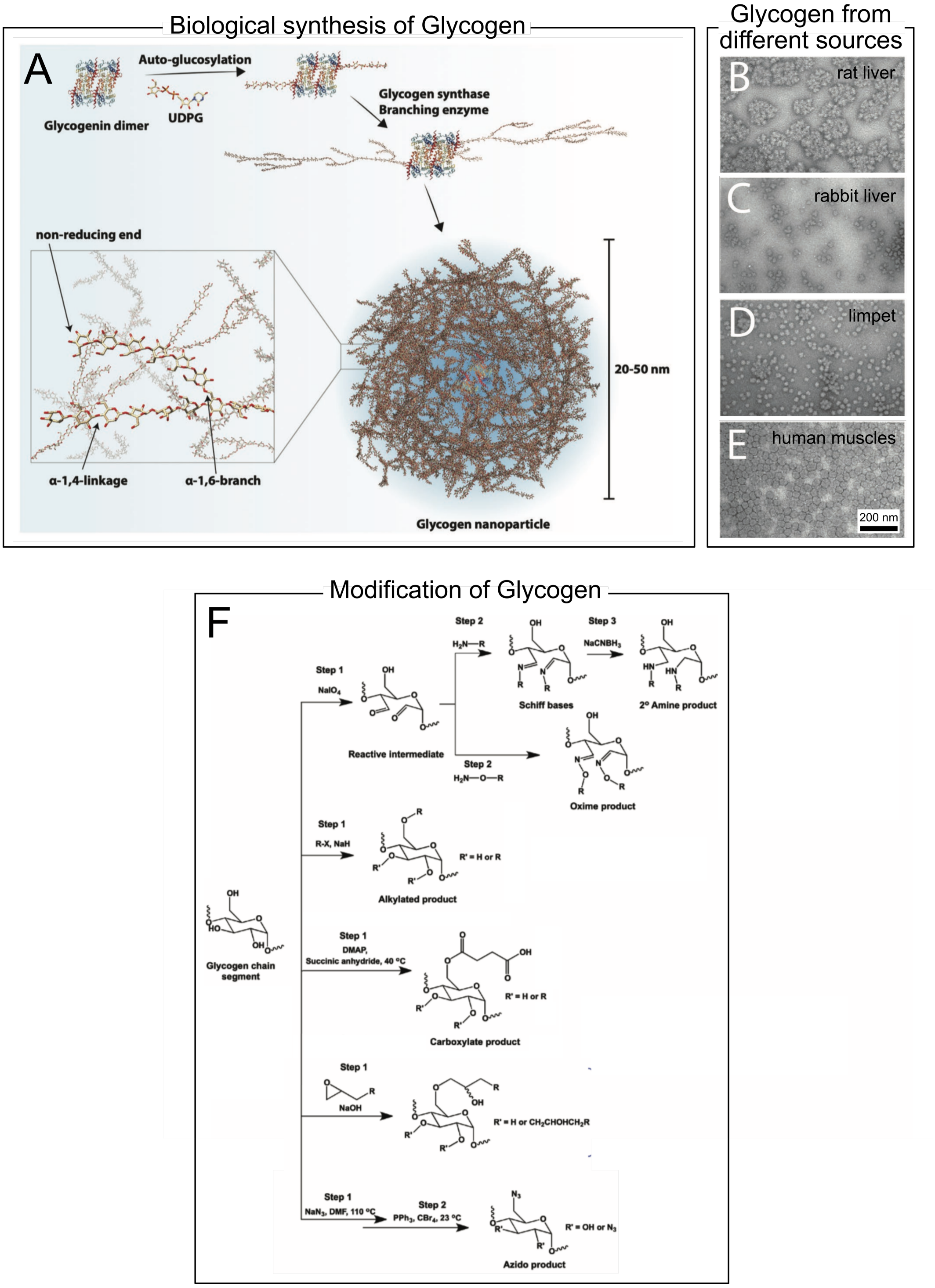

Figure 9. A) Depiction of the biological production of Glycogen from uridine diphosphate glucose to hyperbranched polysaccharidic nanoparticle via enzymatic synthesis. Transmission electron microscopy (TEM) images of several types of glycogens having different structural properties from various sources, as B) rat liver, C) rabbit liver, D) slipper limpet, and E) human skeletal muscles. F) Examples of schematics relative to synthetic reactions for the modification of the glycogen repeating unit. Adapted from [254, 260].

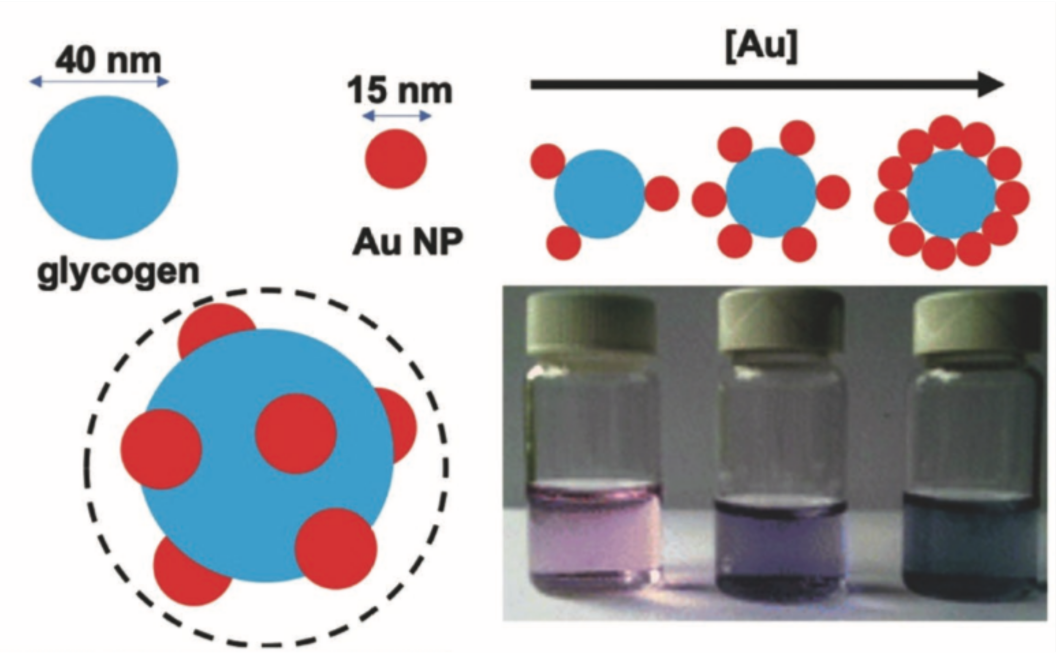

Figure 10. Depiction illustrating the assembly process of glycogen-AuNP hybrid materials and the photograph showing the colours of the different solutions as a function of the glycogen/AuNP ratio. Adapted from [254, 280].

1.5 Applications of hybrid materials

Hybrid materials provide researchers with many opportunities to explore materials for a variety of scientific and industrial applications. Hereon, after an overview of the progress in hybrid technologies, for the scope of this thesis, this section will showcase recent advances of hybrid materials in biomedical and, in particular, sensing applications.[3-4]

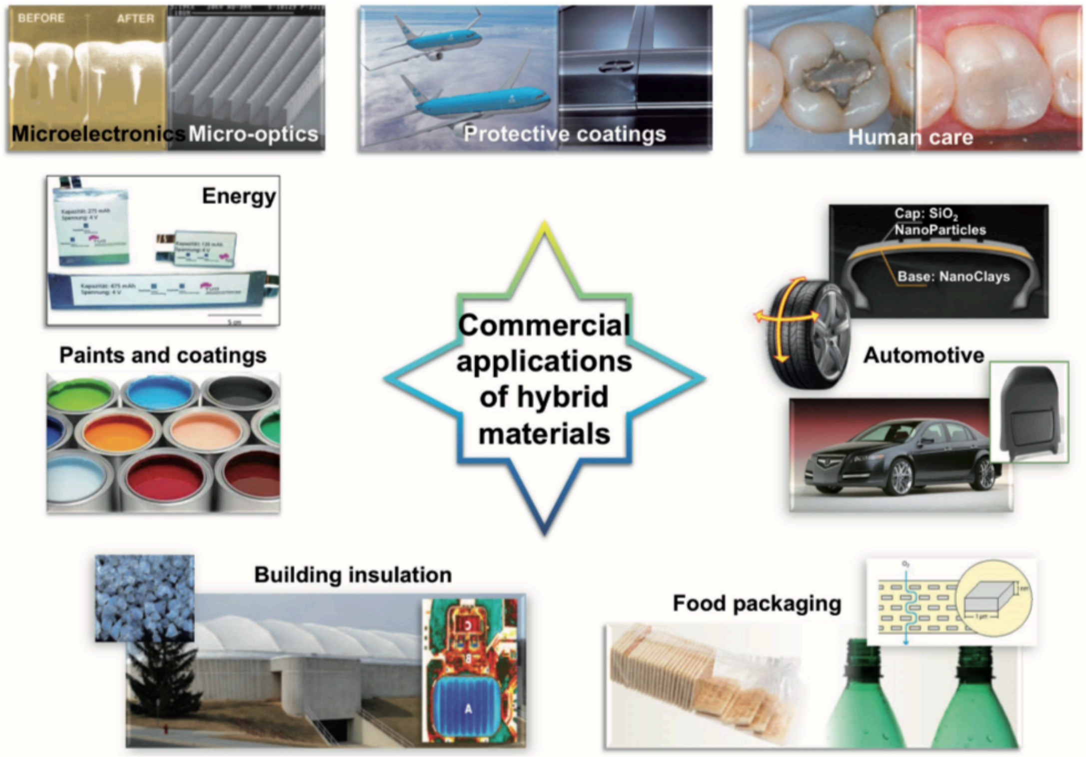

Figure 11. Examples of advanced technological applications of hybrid materials. Adapted from [4].

1.5.1 Industrial applications of hybrid materials

Hybrid nanomaterials have been extensively employed in the last decades in disparate applications, because of their large-scale production and excellent properties (Figure 11).[283-285] Hybrid materials for commercial/industrial applications were successfully applied in the fields of electronics (microprocessor, waveguides), optics (curved lenses, lasers mirrors), smart coatings (self-cleaning, antidust, anticorrosion, anti-scratch), energy (batteries, membranes, hybrid cells, solar cells, fuel cells), environment (catalysis, biosensors, adsorbents), nanomedicine (imaging, drug delivery, coatings, implants), automotive (green tyres, lightweight reinforcement), packaging (textiles, nanocomposites), sport (polymer reinforcement) and construction (paints, organoclays, sealant, woods).[286-289] Moreover, these hybrid materials can be prepared by a great variety of synthetic procedures, including bottom-up, top-down, and advanced processing methodologies such as deposition of thin-film (dip, spin, electrocoating, microfluidic), lithography (nanoimprinting, two-photon absorption, dip-pen), plasma sintering, spray, ion etching, 3D printing and extrusion.[290]

Successful innovative hybrid materials have to be prepared from raw and inexpensive materials and available at the industrial scale. The manufacturing processes of hybrid materials have to be compatible with existing industrial infrastructures, they need to show real added value compared to former materials and they must fulfil safety and regulation requirements.[30]

Factors that can trigger the development and marketing of new hybrid materials can be of regulatory, technical or economic nature. For instance, regulatory constraints on chromates and Ni-based conversion coatings allowed the development of hybrid coatings in aeronautics and automotive applications.[4] These hybrid coatings fulfil not only new regulations but also technical and economical requirements, adding real value to the new material.[3] Moreover, these materials can be processed with already existing automotive technologies, making the transition toward the uses of hybrids easier and less expensive.[291-292]

Overall, the process from the discovery to the industrial production of hybrids is generally long and many factors and actors need to be considered, in addition to scientific work, to successfully bring a material to the market for real applications.

1.5.2 Nanoflower-based biosensors

Recent studies gave significant development of hybrid nanoflowers in the field of sensing applications.[179, 186] Biosensors are detector devices that transduce target biological activities by the means of specific biochemical recognition mechanisms in a quantifiable signal, usually electrical, thermal or optical.[293-296] The unique hierarchical nano-to-micro structures of nanoflowers endow these materials with a large surface area, providing accessible and numerous active sites, improved catalytic activities, capture ability and detection sensitivity properties.

Elegant examples of hybrids for the detection of bioanalytes were designed incorporating multi-enzymes, as GOx and HRP, within the inorganic structure of the nanoflowers (Figure 12a and b).[195, 297] The prepared nanoflowers allowed the multi-step catalysis of an enzymatic cascade reaction in one hybrid system. The cascade reactions involved, first, the oxidation of glucose in the presence of oxygen by GOx with the concomitant production of hydrogen peroxide (H_2O_2), and, then, the oxidation of a chromogen catalysed by the presence of HRP and H_2O_2 (Figure 12a). The colour change was readily monitored via spectroscopic analysis. The vicinity of the two enzymes enhanced the glucose detection sensitivity reducing the diffusion and decomposition of H_2O_2, obtaining, therefore, a multi-enzyme hybrid nanoflowers capable to detect glucose via a colourimetric method with a low limit of detection in the range of fractions of μM (Figure 12b).

Several kinds of hybrid nanoflowers were prepared in combination with a sandwich immunoassay for the sensing of bioanalytes, such as protein biomarkers and pathogens. These systems rely on specific bioanalyte recognitions using recognition probes which trigger a transduced and amplified signal change via signal probes.[298-299] The design of nanoflowers for sandwich biosensing consists of hybrid structures exhibiting two functionalities: the specific capability to bind targeted bioanalyte and the improved enzymatic activity and stability for the amplification of the signal. This adaptable design can host various kind of recognition proteins, as antibodies[198] and streptavidin,[194] as well as signal enzymes, as HRP[300] and β-galactosidase,[217] for the preparation of various protein-enzyme hybrid nanoflowers. Depending on the chosen enzyme, the transduced and amplified signal outputs can be a colourimetric, fluorescent and electrochemical response Nanoflowers, compared to other platforms for the immobilization of functional biomacromolecules, can easily load a greater quantity and simultaneously combine several biomolecules into one hybrid system. Hybrid nanoflowers for the sandwich biosensing were prepared with concanavalin-A (Con A) and GOx incorporated in a calcium hydrogen phosphate structure via a one-pot synthesis in mild conditions (Figure 12c).[301] Con A was used as the recognition unit toward the superficial *E. coli* O-antigen, whereas GOx acted as the transducer and signal amplification unit that catalysed the glucose to gluconic acid reaction causing a decrease in pH, (Figure 12d). The sensor had a linear range of 10-10^6 CFU mL^{-1} and a low LOD of 10 CFU mL^{-1}. Electrochemical signals were also explored to develop electrochemical sensors for the detection of bioanalytes.[212, 302] In particular, in impedimetric immunosensor devices the transduced signal is the increasing resistance of the system, measured via electrochemical impedance spectroscopy (EIS), which is associated with the increasing amount of analytes at the surface of the electrode. For example, a cobalt phosphate nanocomposite was prepared in the presence of an aptamer for the detection of platelet-derived growth factor.[212] The hybrid material was deposited on the surface of an electrode and then incubated in a solution containing the bioanalyte. The protein adsorbed on the electrode surface, via aptamer recognition, increased the system resistance as a function of the protein concentration in solution, with a low LOD of 3.7 pg mL^{-1}.

To expand the potentials of nanoflowers for sensing applications, paper-based, low-cost and portable sensors incorporating these hybrids were developed.[206, 303-305] Cellulose materials supported hybrid structures were prepared via a direct in situ growth of nanoflowers on the paper-liquid interface avoiding additional steps, as purification and drying, and shortening the crystallization time, from days to several minutes, compared to the conventional synthesis. A colourimetric glucose sensor was developed using a functionalized microfluidic paper with manganese phosphate hybrid nanoflowers and GOx.[303] The hybrid material was readily synthesized adding a manganese and phosphate salt solutions in the presence of GOx on the paper interface. The device achieved rapid on-site glucose detection in complex biological samples with a LOD of 0.01 mM.

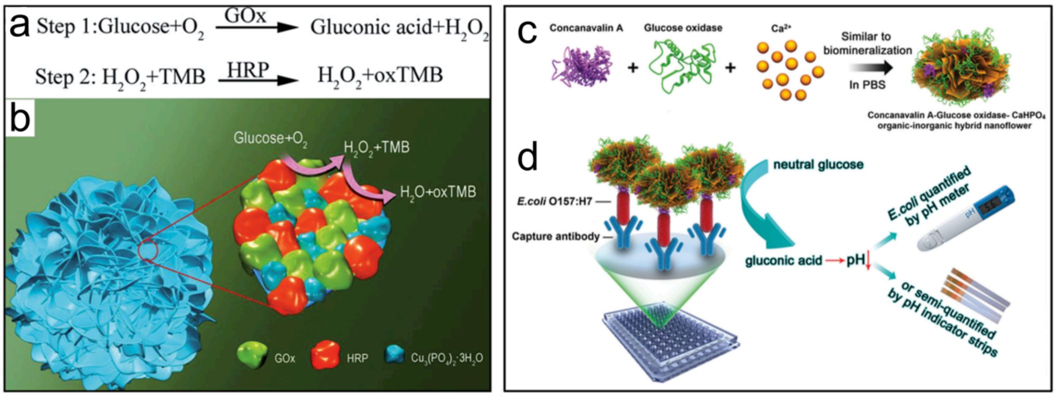

Figure 12. Examples of nanoflowers in biosensing applications. a) The chemical equation of glucose sensing via a two-step enzymatic cascade reaction and b) depiction of the cascade reaction using HRP/GOx-$Cu_3(PO_4)_2$ nanoflowers. c) Schematic of the assembly process of hybrid ConA/GOx-$CaHPO_4$ hybrid nanoflowers and d) corresponding nanoflowers-based immunosensing of E. coli. Adapted from [195, 301].

1.5.3 Gold nanoparticle-based biosensors

Hybrid biosensors made from controlled nanostructured materials greatly benefit from the materials enhanced optical, electrical, morphological, and cargo loading properties.[306-307] SERS-, ELISA- and electrochemical-based sensors with low detection limit and high sensitivity can be developed using GNPL embedded in organic architectures benefiting from the assemblies excellent surface plasmon resonance, surface area, loading capacity, and electron transfer properties (Figure 13a).

SERS is a surface-sensitive technique were Raman scattering from analytes adsorbed on ordered plasmonic rough metal nanostructured interfaces is enhanced by a factor of 10^{12}, allowing the detection of even single molecules.[308] The chemical as well the electromagnetic effects, which are the electron transfer from substrate to the analyte and the excitation of the localized surface plasmon resonance (LSPR), respectively, contribute to the SERS.[309] This technique is useful for the detection of biochemical analytes in biomedical and food applications, and environmental monitoring.[310] Interfaces with excellent SERS activities should have rough and stable surfaces able to immobilize a high quantity of analytes and have strong and homogeneously distributed LSPR to achieve reproducible and uniform SERS signals.[311-312] GNPL present rough surfaces, chemical stability, well-defined and controlled structures, high surface area, and strong interactions between nanoparticles producing LSPR modes, which properties make these structures and ideal material for preparing SERS substrates.[313-314] Moreover, other variables in GNPL can be finely tuned as the nanoparticles size, size distribution, shape, and thickness of the inorganic layer to control the hot spots number and spatial organization, therefore control the SERS sensing properties.[315-318] Several examples of SERS sensors based on GNPL have been successfully proposed for the detection of biomacromolecules, as the proteins BSA and myoglobin,[319-320] the pathogen *S. Typhimurium*,[321] and small molecules, as the antiviral medicine amantadine,[322] antibiotic penicillin,[323] and benzenethiol[318] (Figure 13b and c) with high sensitivities and low detection limits.

The biochemical assay ELISA is based on the specific recognition reaction between an antigen and its specific antibody to detect and quantify the antigen amount in a sample.[324] It is a widespread analytical assay used in clinical analysis and quality controls. The most used and accurate ELISA assay uses the “sandwich” method, in which the sample solution containing the target antigen is incubated on a functionalized substrate with the relative antibody. The recognized and linked antigen on the substrate is then conjugated to another antibody bearing an enzyme, which can be quantified by an enzymatic reaction involving, usually, a colourimetric assay.[325] The immobilization of the antibody on the substrate is of crucial importance for the sensing properties of the assay. Commonly, substrates used in ELISA assay are smooth and flat polystyrene microplates that, due to the two-dimensional interfacial structure, accommodate a limited quantity of antibody at the interface. This negatively affects the assay detection limit, restricting the sensing capability of low concentration biomarkers, such as antigens at initial phases of cancer.[326] GNPL present rough surfaces, high surface area, micro-to-nano architectures, and electron transfer efficiency properties that endow materials with characteristics that greatly benefit ELSA assay. Indeed, these structures have high loading cargo capability, low diffusion hindrance, and enhanced catalytic activity, improving the sensing properties of ELISA assay. For instance, the lysozyme, human serum albumin and fibrinogen proteins absorption on GNPL-modified PS microplates is a few folders higher compared to the unmodified one.[326] Moreover, also the sensitivity of GNPL-modified PS microplates toward the carcinoembryonic antigen in human plasma was increased of 100-folds compared to unmodified plates and the limit of detection halved compared to commercial ELISA kit (Figure 13d and e).[327]

Electrochemical biosensors are based on the conversion of biological information into an easily processed electrical signal, which can be studied via common electrochemical techniques as chronopotentiometry, chronoamperometry, cyclic voltammetry, and electrochemical impedance spectroscopy.[328-329] These techniques are widely explored for biosensing applications due to their fast and reliable results and the possibility to miniaturize the electrochemical sensing device. Sensing properties, as sensitivity and limit of detection, are strictly correlated to the chemical composition and structure of the interface that connects the electrode and the biological sample.[330] The topographies, architectures, and chemical compositions of the electrodes can be controlled by the means of nanotechnology to enhance biosensor detection properties.[331] In electrochemical sensors, GNPL improve bioactive molecules adhesion and bioactivity, enhance stability and promote electron transfer efficiency.[332-333] GNPL electrodes, compared to unmodified electrodes, have an increased loading cargo and electron transfer efficiency that result in improved sensitivity and limit of detection.[223] Usually, electrodes are prepared by the facile self-assembling of antibodies, enzymes, and proteins via LbL methods.[334-336] A variety of biomolecules were successfully detected using immobilized bioactive molecules on electrode surfaces functionalized with GNPL, including antigens such as lipoprotein with apolipoprotein B,[337] human chorionic gonadotropin antigen with anti-human chorionic gonadotrophin,[338] carcinoembryonic antigen with anti-carcinoembryonic antigen,[339] and enzymes as hydrogen peroxide with horseradish peroxidase,[340] glucose with glucose oxidase,[230, 341-342] and acetylthiocholine with acethylcholinesterase (Figure 13f-h).[343]

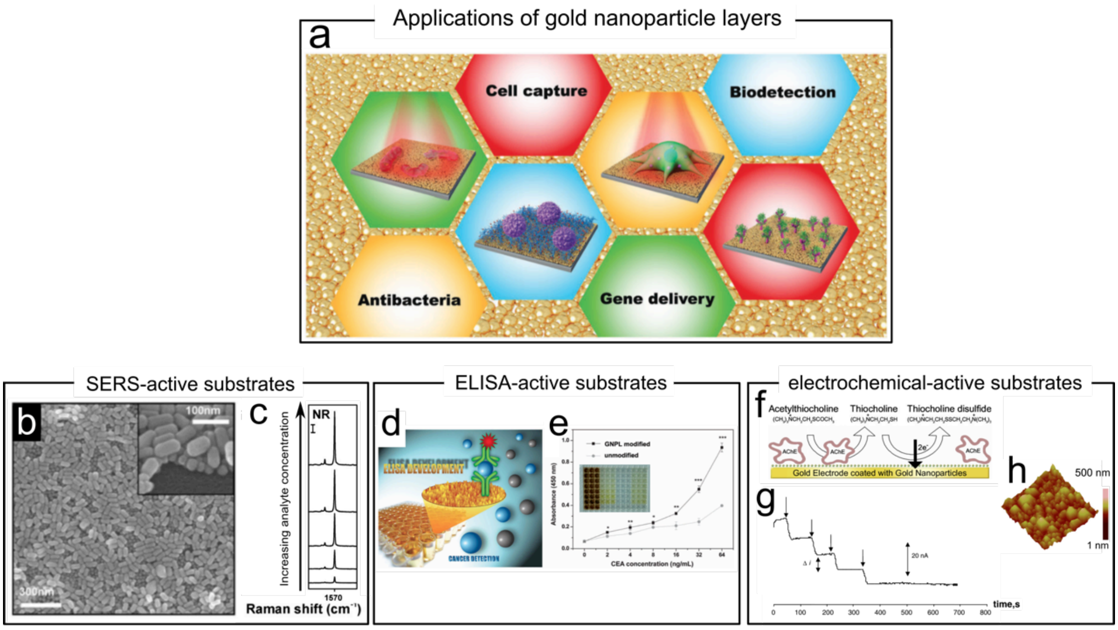

Figure 13. a) An overview of biotechnological applications and b-h) specific biosensing applications of hybrid materials based on gold nanoparticles layers. b) SERS-active substrates composed of gold nanoparticles resulting in c) enhanced SERS intensities signals. d) Depiction of ELISA-enhancing substrates and e) improved signals in an immunoassay targeting CEA. f) Schematic of acetylthiocholine sensing via an electrochemical-active modified electrode with gold nanoparticle layers and acethylcholinesterase, g) amperometric response upon addition of the analyte, and h) AFM image of the modified electrode. Adapted from [223, 318, 327, 343].

1.6 Scope of the thesis

Recent developments in the field of hybrids hold great potentials for their advanced applications as a platform for a range of biomedical-related applications. In particular, the detection properties of sensors based on hybrid structures greatly benefit from the synergistic combination of organic and inorganic components in a single material. However, questions persist regarding the detection properties, synthetic preparation, catalytic activities, and assembly capability of functional hybrid materials for sensing applications. This thesis explores innovative approaches to design advanced hybrid nanostructured materials with electrocatalytic, optical and catalytic properties

Several characterization methods were used for the study of the prepared hybrid materials, as well as the evaluation of their catalytic and sensing properties. **Chapter 2** displays the materials, methods, instruments, techniques and other relevant experimental details used in this thesis.

In **Chapter 3** a non-enzymatic glucose sensor capable of detecting glucose at physiological pH was developed. The electrochemical sensor was prepared modifying a carbon electrode with inks made blending cobalt phosphate nanostructures and a fluorinated binding agent. The cobalt-based material was prepared in mild conditions without the use of toxic chemicals or high temperatures, providing a robust and scalable synthetic method for the preparation of hierarchically organized nanostructures. The modified electrode showed to be electroactive for the oxidation of glucose to gluconolactone due to the presence of cobalt metal ions, which are known for their electrocatalytic properties. Taking advantage of the electrochemical reaction, glucose was detected in PBS and human serum in biological relevant concentrations. Moreover, density functional theory studies gave further insights on the glucose binding to the modified electrode surface.

In **Chapter 4** hybrid nanostructured nanoflowers with enzymatic-like catalytic properties were prepared. These particles were synthesized in mild conditions via a crystallization process of copper phosphate in the presence of the biomacromolecule dextran sulfate.

Structures with different morphologies were obtained varying the synthetic parameters, as the concentration of reagents, pH and the reaction time. It was found that surfaces could be functionalized with these hybrid materials via a simple, one-pot, scalable and robust method to prepare catalytic micro-reactors. These structures displayed a non-enzymatic peroxidase-like catalytic activity toward hydrogen peroxide as substrate. Thus, a hydrogen peroxide sensor was developed using a fluorescent chromogenic substrate. Furthermore, a glucose sensor was prepared taking advantage of a hybrid enzymatic/non-enzymatic cascade reaction achieved combining the enzyme glucose oxidase and the inorganic hybrid particles.

In **Chapter 5** a natural nanoparticle was engineered to prepare, with metal nanoparticles, hybrid functional materials. The organic engineered nanoparticles display adhesive and functional properties for the preparation of thin film on a variety of substrates, regardless of the substrate chemical composition. The coatings were found to be stable in several chemical environments and yet maintain enzymatic degradability. These organic coatings with metal nanoparticles were further used for the tuneable preparation of modular hybrid layer-by-layer assemblies. These hybrid systems, in which the metal nanoparticles maintain catalytic and optical properties, were used for the preparation of catalytic reactors and functional surfaces for sensing applications.

Finally, **Chapter 6** provides the conclusions of the entire scientific work completed during this PhD program, as well as prospective research works that can result from the outcomes of this thesis.

1.7 References

(1) C. Sanchez, K. J. Shea and S. Kitagawa, *Recent progress in hybrid materials science*, *Chemical Society Reviews,* 2011, **40**, 471-472.

(2) C. Sanchez, F. Ribot and B. Lebeau, *Molecular design of hybrid organic-inorganic nanocomposites synthesized via sol-gel chemistry*, *Journal of Materials Chemistry,* 1999, **9**, 35-44.

(3) C. Sanchez, B. Julián, P. Belleville and M. Popall, *Applications of hybrid organic–inorganic nanocomposites*, *Journal of Materials Chemistry,* 2005, **15**, 3559-3592.

(4) C. Sanchez, P. Belleville, M. Popall and L. Nicole, *Applications of advanced hybrid organic–inorganic nanomaterials: from laboratory to market*, *Chemical Society Reviews,* 2011, **40**, 696-753.

(5) J. Livage, M. Henry and C. Sanchez, *Sol-gel chemistry of transition metal oxides*, *Progress in Solid State Chemistry,* 1988, **18**, 259-341.

(6) C. J. Brinker and G. W. Scherer, *Sol-gel science: the physics and chemistry of sol-gel processing*. Academic press: 2013.

(7) B.-L. Su, C. Sanchez and X.-Y. Yang, *Hierarchically structured porous materials: from nanoscience to catalysis, separation, optics, energy, and life science*. John Wiley & Sons: 2012.

(8) L. Merhari, *Hybrid nanocomposites for nanotechnology*. Springer: 2009.

(9) G. J. d. A. Soler-Illia, C. Sanchez, B. Lebeau and J. Patarin, *Chemical strategies to design textured materials: from microporous and mesoporous oxides to nanonetworks and hierarchical structures*, *Chemical Reviews,* 2002, **102**, 4093-4138.

(10) S. Mann, S. L. Burkett, S. A. Davis, C. E. Fowler, N. H. Mendelson, S. D. Sims, D. Walsh and N. T. Whilton, *Sol− gel synthesis of organized matter*, *Chemistry of Materials,* 1997, **9**, 2300-2310.

(11) M. Faustini, D. Grosso, C. Boissière and C. Sanchez, *"Integrative sol–gel chemistry": a nanofoundry for materials science*, *Journal of Sol-Gel Science and Technology,* 2014, **70**, 216-226.

(12) N. Brun, S. Ungureanu, H. Deleuze and R. Backov, *Hybrid foams, colloids and beyond: From design to applications*, *Chemical Society Reviews,* 2011, **40**, 771-788.

(13) B. I. Kharisov, O. V. Kharissova and U. Ortiz-Mendez, *CRC concise encyclopedia of nanotechnology*. CRC Press: 2016.

(14) P. Judeinstein and C. Sanchez, *Hybrid organic–inorganic materials: a land of multidisciplinarity*, *Journal of Materials Chemistry,* 1996, **6**, 511-525.

(15) E. Ruiz-Hitzky, *Functionalizing inorganic solids: towards organic–inorganic nanostructured materials for intelligent and bioinspired systems*, *The chemical record,* 2003, **3**, 88-100.

(16) B. Bhushan, *Biomimetics: bioinspired hierarchical-structured surfaces for green science and technology*. Springer: 2016.

(17) J. Aizenberg, *Crystallization in patterns: a bio‐inspired approach*, *Advanced Materials,* 2004, **16**, 1295-1302.
(18) N. Nassif and J. Livage, *From diatoms to silica-based biohybrids*, *Chemical Society Reviews,* 2011, **40**, 849-859.
(19) C. Sanchez, H. Arribart and M. M. G. Guille, *Biomimetism and bioinspiration as tools for the design of innovative materials and systems*, *Nature materials,* 2005, **4**, 277-288.
(20) J. Aizenberg, J. C. Weaver, M. S. Thanawala, V. C. Sundar, D. E. Morse and P. Fratzl, *Skeleton of Euplectella sp.: structural hierarchy from the nanoscale to the macroscale*, *Science,* 2005, **309**, 275-278.
(21) J. Aizenberg, A. Tkachenko, S. Weiner, L. Addadi and G. Hendler, *Calcitic microlenses as part of the photoreceptor system in brittlestars*, *Nature,* 2001, **412**, 819-822.
(22) Y. Politi and J. C. Weaver, *Built for tough conditions*, *Science,* 2015, **347**, 712-713.
(23) T. Henkel, *Coral Reefs. Nature Education Knowledge 1 (11): 5 Email*, *Coral reefs are one of the most diverse ecosystems on the planet. What are the abiotic and biotic interactions that structure this diverse ecosystem,* 2010.
(24) S. Cassaignon, R. De Maleprade, N. Nassif and J. Livage, *From living light to living materials*, *Materials Today: Proceedings,* 2014, **1**, 209-215.
(25) J. R. Young, S. A. Davis, P. R. Bown and S. Mann, *Coccolith ultrastructure and biomineralisation*, *Journal of structural biology,* 1999, **126**, 195-215.
(26) D. Faivre and T. U. Godec, *From bacteria to mollusks: the principles underlying the biomineralization of iron oxide materials*, *Angewandte Chemie International Edition,* 2015, **54**, 4728-4747.
(27) D. Faivre and D. Schuler, *Magnetotactic bacteria and magnetosomes*, *Chemical Reviews,* 2008, **108**, 4875-4898.
(28) S. Weiner and P. M. Dove, *An overview of biomineralization processes and the problem of the vital effect*, *Reviews in mineralogy and geochemistry,* 2003, **54**, 1-29.
(29) S. Mann, *Biomineralization: principles and concepts in bioinorganic materials chemistry*. Oxford University Press on Demand: 2001; Vol. 5.
(30) M. Faustini, L. Nicole, E. Ruiz‐Hitzky and C. Sanchez, *History of organic–inorganic hybrid materials: prehistory, art, science, and advanced applications*, *Advanced Functional Materials,* 2018, **28**, 1704158.
(31) R. E. Dickerson, *Chemical evolution and the origin of life*, *Scientific American,* 1978, **239**, 70-87.
(32) G. Rogez, C. Massobrio, P. Rabu and M. Drillon, *Layered hydroxide hybrid nanostructures: a route to multifunctionality*, *Chemical Society Reviews,* 2011, **40**, 1031-1058.
(33) A. Brack, *.4 Clay Minerals and the Origin of Life*, *Developments in Clay Science,* 2006, **1**, 379-391.

(34) G. Lailach and G. Brindley, *Specific co-absorption of purines and pyrimidines by montmorillonite (Clay-organic studies XV)*, *Clays and Clay Minerals,* 1969, **17**, 95-100.
(35) J. A. Rausell-Colom and V. Fornés, *Monodimensional fourier analysis of some vermiculite-l-ornithine+ complexes*, *American Mineralogist: Journal of Earth and Planetary Materials,* 1974, **59**, 790-798.
(36) E. Ruiz-Hitzky, *Clay-Organic Interactions: Organoclay complexed and Polymer-Clay Nanocomposites*, *Handbook of layered materials,* 2004, 91-154.
(37) L. E. Orgel, *The origin of life—a review of facts and speculations*, *Trends in Biochemical Sciences,* 1998, **23**, 491-495.
(38) E. Chalmin, M. Menu and C. Vignaud, *Analysis of rock art painting and technology of Palaeolithic painters*, *Measurement Science and Technology,* 2003, **14**, 1590.
(39) K. Zhang, H. Zhang, S. Fang, J. Li, Y. Zheng and B. Zhang, *Textual and Experimental Studies on The Compositions of Traditional C hinese Organic–Inorganic Mortars*, *Archaeometry,* 2014, **56**, 100-115.
(40) F. Yang, B. Zhang and Q. Ma, *Study of sticky rice− lime mortar technology for the restoration of historical masonry construction*, *Accounts of Chemical Research,* 2010, **43**, 936-944.
(41) P. Gómez-Romero and C. Sanchez, *Hybrid materials. Functional properties. From Maya Blue to 21st century materials*, *New Journal of Chemistry,* 2005, **29**, 57-58.
(42) H. Van Olphen, *Maya Blue: a clay-organic pigment?*, *Science,* 1966, **154**, 645-646.
(43) R. J. Gettens, *Maya Blue: an unsolved problem in ancient pigments*, *American Antiquity,* 1962, **27**, 557-564.
(44) G. E. Stahl, *Experimenta, observationes, animadversiones, CCC numero, Chymicae et Physicae, qualium alibi vel nulla, vel rara,... commentatio aut explicatio invenitur... etc*. Haude: 1731.
(45) A. Kraft, *On the discovery and history of Prussian blue*, *Bull. Hist. Chem,* 2008, **33**, 61-67.
(46) H. Buser, D. Schwarzenbach, W. Petter and A. Ludi, *The crystal structure of Prussian blue: Fe4 [Fe (CN) 6] 3. xH2O*, *Inorganic Chemistry,* 1977, **16**, 2704-2710.
(47) J. J. Berzelius, *Atomgewichts-Tabellen: Besonderer Abdruck aus Berzelius Lehrbuch der Chemie*. Vieweg: 1845; Vol. 3.
(48) M. Rueping and B. J. Nachtsheim, *A review of new developments in the Friedel–Crafts alkylation–From green chemistry to asymmetric catalysis*, *Beilstein journal of organic chemistry,* 2010, **6**, 6.
(49) F. Kipping In *Organic derivative of silicon. Preparation of alkylsilicon chlorides*, Proc. Chem. Soc, 1904; p 15.
(50) U. Schubert and N. Hüsing, *Synthesis of inorganic materials*. John Wiley & Sons: 2019.

(51) S. Mann and G. A. Ozin, *Synthesis of inorganic materials with complex form*, *Nature,* 1996, **382**, 313-318.

(52) S. Parola, B. Julián-López, L. D. Carlos and C. Sanchez, *Optical properties of hybrid organic-inorganic materials and their applications*, *Advanced Functional Materials,* 2016, **26**, 6506-6544.

(53) P. Gomez-Romero, *Hybrid organic–inorganic materials—in search of synergic activity*, *Advanced Materials,* 2001, **13**, 163-174.

(54) P. K. Jain, X. Huang, I. H. El-Sayed and M. A. El-Sayed, *Review of some interesting surface plasmon resonance-enhanced properties of noble metal nanoparticles and their applications to biosystems*, *Plasmonics,* 2007, **2**, 107-118.

(55) J. Virkutyte and R. S. Varma, *Green synthesis of metal nanoparticles: biodegradable polymers and enzymes in stabilization and surface functionalization*, *Chemical Science,* 2011, **2**, 837-846.

(56) G. Kickelbick, *Introduction to hybrid materials*, *Hybrid materials,* 2007, **1**, 2.

(57) G. Kickelbick, *Hybrid materials: synthesis, characterization, and applications*. John Wiley & Sons: 2007.

(58) Y. Wang, H. Arandiyan, J. Scott, A. Bagheri, H. Dai and R. Amal, *Recent advances in ordered meso/macroporous metal oxides for heterogeneous catalysis: a review*, *Journal of Materials Chemistry A,* 2017, **5**, 8825-8846.

(59) V. V. Kumar and S. P. Anthony, Antimicrobial studies of metal and metal oxide nanoparticles. In *Surface chemistry of nanobiomaterials*, Elsevier: 2016; pp 265-300.

(60) W. Wu, Q. He and C. Jiang, *Magnetic iron oxide nanoparticles: synthesis and surface functionalization strategies*, *Nanoscale research letters,* 2008, **3**, 397.

(61) G. Ren, D. Hu, E. W. Cheng, M. A. Vargas-Reus, P. Reip and R. P. Allaker, *Characterisation of copper oxide nanoparticles for antimicrobial applications*, *International journal of antimicrobial agents,* 2009, **33**, 587-590.

(62) H. Yang, Y. Hu, X. Zhang and G. Qiu, *Mechanochemical synthesis of cobalt oxide nanoparticles*, *Materials Letters,* 2004, **58**, 387-389.

(63) F. A. Carey and R. J. Sundberg, *Advanced organic chemistry: part A: structure and mechanisms*. Springer Science & Business Media: 2007.

(64) I. Cobo, M. Li, B. S. Sumerlin and S. Perrier, *Smart hybrid materials by conjugation of responsive polymers to biomacromolecules*, *Nature materials,* 2015, **14**, 143-159.

(65) P. Canepa, N. Nijem, Y. J. Chabal and T. Thonhauser, *Diffusion of small molecules in metal organic framework materials*, *Physical Review Letters,* 2013, **110**, 026102.

(66) E. Dugan, Z. Wang, M. Okamura, A. Medina and S. M. Cohen, *Covalent modification of a metal–organic framework with isocyanates:*

probing substrate scope and reactivity, *Chemical Communications,* 2008, 3366-3368.

(67) H. Deng, C. J. Doonan, H. Furukawa, R. B. Ferreira, J. Towne, C. B. Knobler, B. Wang and O. M. Yaghi, *Multiple functional groups of varying ratios in metal-organic frameworks*, *Science,* 2010, **327**, 846-850.

(68) O. Shekhah, J. Liu, R. Fischer and C. Wöll, *MOF thin films: existing and future applications*, *Chemical Society Reviews,* 2011, **40**, 1081-1106.

(69) Q.-L. Zhu and Q. Xu, *Metal–organic framework composites*, *Chemical Society Reviews,* 2014, **43**, 5468-5512.

(70) P. Gómez-Romero and C. Sanchez, *Functional hybrid materials*. John Wiley & Sons: 2006.

(71) F. Vögtle, S. Gestermann, R. Hesse, H. Schwierz and B. Windisch, *Functional dendrimers*, *Progress in Polymer Science,* 2000, **25**, 987-1041.

(72) d. A. Bosman, H. Janssen and E. Meijer, *About dendrimers: structure, physical properties, and applications*, *Chemical Reviews,* 1999, **99**, 1665-1688.

(73) R. B. Thompson, V. V. Ginzburg, M. W. Matsen and A. C. Balazs, *Block copolymer-directed assembly of nanoparticles: Forming mesoscopically ordered hybrid materials*, *Macromolecules,* 2002, **35**, 1060-1071.

(74) H.-B. Fu and J.-N. Yao, *Size effects on the optical properties of organic nanoparticles*, *Journal of the American Chemical Society,* 2001, **123**, 1434-1439.

(75) D. Horn and J. Rieger, *Organic nanoparticles in the aqueous phase—theory, experiment, and use*, *Angewandte Chemie International Edition,* 2001, **40**, 4330-4361.

(76) M. Hun Kim, G. Choi, A. Elzatahry, A. Vinu, Y. Bin Choy and J.-H. Choy, *Review of clay-drug hybrid materials for biomedical applications: administration routes*, *Clays and Clay Minerals,* 2016, **64**, 115-130.

(77) H. Uyama, M. Kuwabara, T. Tsujimoto, M. Nakano, A. Usuki and S. Kobayashi, *Green nanocomposites from renewable resources: plant oil− clay hybrid materials*, *Chemistry of Materials,* 2003, **15**, 2492-2494.

(78) S. B. Hendricks, *Base Exchange of the Clay Mineral Montmorillonite for Organic Cations and its Dependence upon Adsorption due to van der Waals Forces*, *The Journal of Physical Chemistry,* 1941, **45**, 65-81.

(79) D. MacEwan, *Halloysite-organic complexes*, *Nature,* 1946, **157**, 159-160.

(80) E. Ruiz-Hitzky, P. Aranda, M. Darder and M. Ogawa, *Hybrid and biohybrid silicate based materials: molecular vs. block-assembling bottom–up processes*, *Chemical Society Reviews,* 2011, **40**, 801-828.

(81) F. Leroux and J.-P. Besse, *Polymer interleaved layered double hydroxide: a new emerging class of nanocomposites*, *Chemistry of Materials,* 2001, **13**, 3507-3515.
(82) E. Brunet, J. L. Colón and A. Clearfield, *Tailored organic-inorganic materials*. John Wiley & Sons: 2015.
(83) E. Ruiz-Hitzky, P. Aranda, M. Darder and G. Rytwo, *Hybrid materials based on clays for environmental and biomedical applications*, *Journal of Materials Chemistry,* 2010, **20**, 9306-9321.
(84) B. Wicklein, M. Á. Martín del Burgo, M. Yuste, M. Darder, C. E. Llavata, P. Aranda, J. Ortin, G. del Real and E. Ruiz-Hitzky, *Lipid-based bio-nanohybrids for functional stabilisation of influenza vaccines*, *European Journal of Inorganic Chemistry,* 2012, **2012**, 5186-5191.
(85) H. He, L. Ma, J. Zhu, R. L. Frost, B. K. Theng and F. Bergaya, *Synthesis of organoclays: A critical review and some unresolved issues*, *Applied Clay Science,* 2014, **100**, 22-28.
(86) B. K. G. Theng, *Formation and properties of clay-polymer complexes*. Elsevier: 2012.
(87) J. A. Schwarz, C. I. Contescu and K. Putyera, *Dekker encyclopedia of nanoscience and nanotechnology*. CRC press: 2004; Vol. 5.
(88) A. Okada, Y. Fukushima, M. Kawasumi, S. Inagaki, A. Usuki, S. Sugiyama, T. Kurauchi and O. Kamigaito, Composite material and process for manufacturing same. Google Patents: 1988.
(89) Y. Fukushima and S. Inagaki, Synthesis of an intercalated compound of montmorillonite and 6-polyamide. In *Inclusion Phenomena in Inorganic, Organic, and Organometallic Hosts*, Springer: 1987; pp 365-374.
(90) E. Ruiz-Hitzky, P. Aranda, B. Casal and J. C. Galvan, *Nanocomposite materials with controlled ion mobilityk*, *Advanced Materials,* 1995, **7**, 180-184.
(91) M. F. Hernandez and E. R. Hitzky, *Interacción de isocianatos con sepiolita*, *Clay Minerals,* 1979, **14**, 295-305.
(92) E. Ruiz-Hitzky and J. Fripiat, *Organomineral derivatives obtained by reacting organochlorosilanes with the surface of silicates in organic solvents*, *Clays and Clay Minerals,* 1976, **24**, 25-30.
(93) C. W. Lentz, *Silicate minerals as sources of trimethylsilyl silicates and silicate structure analysis of sodium silicate solutions*, *Inorganic Chemistry,* 1964, **3**, 574-579.
(94) A. Gómez-Avilés, M. Darder, P. Aranda and E. Ruiz-Hitzky, *Functionalized carbon–silicates from caramel–sepiolite nanocomposites*, *Angewandte Chemie International Edition,* 2007, **46**, 923-925.
(95) C. Ruiz-García, M. Darder, P. Aranda and E. Ruiz-Hitzky, *Toward a green way for the chemical production of supported graphenes using porous solids*, *Journal of Materials Chemistry A,* 2014, **2**, 2009-2017.

(96) E. Ruiz-Hitzky, M. M. C. Sobral, A. Gómez-Avilés, C. Nunes, C. Ruiz-García, P. Ferreira and P. Aranda, *Clay-graphene nanoplatelets functional conducting composites*, *Advanced Functional Materials,* 2016, **26**, 7394-7405.
(97) B. Wicklein, M. Darder, P. Aranda and E. Ruiz-Hitzky, *Phospholipid–sepiolite biomimetic interfaces for the immobilization of enzymes*, *ACS applied materials & interfaces,* 2011, **3**, 4339-4348.
(98) C. Colella and A. F. Gualtieri, *Cronstedt's zeolite*, *Microporous and Mesoporous Materials,* 2007, **105**, 213-221.
(99) A. F. Cronstedt, *Rön och beskrifning om en obekant bärg art, som kallas Zeolites*. 1756.
(100) J. A. Rabo and M. W. Schoonover, *Early discoveries in zeolite chemistry and catalysis at Union Carbide, and follow-up in industrial catalysis*, *Applied Catalysis A: General,* 2001, **222**, 261-275.
(101) E. M. Flanigen, Zeolites and molecular sieves an historical perspective. In *Studies in Surface Science and Catalysis*, Elsevier: 1991; Vol. 58, pp 13-34.
(102) S. Kulprathipanja, *Zeolites in industrial separation and catalysis*. John Wiley & Sons: 2010.
(103) B. Lok, T. R. Cannan and C. Messina, *The role of organic molecules in molecular sieve synthesis*, *Zeolites,* 1983, **3**, 282-291.
(104) R. M. Barrer, *Zeolites and their synthesis*, *Zeolites,* 1981, **1**, 130-140.
(105) G. T. Kerr, *Chemistry of crystalline aluminosilicates. III. The synthesis and properties of zeolite ZK-5*, *Inorganic Chemistry,* 1966, **5**, 1539-1541.
(106) S. L. Lawton and W. J. Rohrbaugh, *The framework topology of ZSM-18, a novel zeolite containing rings of three (Si, Al)-O species*, *Science,* 1990, **247**, 1319-1322.
(107) S. Mintova, N. H. Olson, V. Valtchev and T. Bein, *Mechanism of zeolite A nanocrystal growth from colloids at room temperature*, *Science,* 1999, **283**, 958-960.
(108) R. M. Izatt, *Macrocyclic and Supramolecular Chemistry: How Izatt-Christensen Award Winners Shaped the Field*. John Wiley & Sons: 2016.
(109) A. S. Abd-El-Aziz, C. E. Carraher Jr, C. U. Pittman Jr and M. Zeldin, *Macromolecules Containing Metal and Metal-Like Elements, Volume 5: Metal-Coordination Polymers*. John Wiley & Sons: 2005; Vol. 17.
(110) Y. Kinoshita, I. Matsubara, T. Higuchi and Y. Saito, *The crystal structure of bis (adiponitrilo) copper (I) nitrate*, *Bulletin of the Chemical Society of Japan,* 1959, **32**, 1221-1226.
(111) Y. Pei, M. Verdaguer, O. Kahn, J. Sletten and J. P. Renard, *Ferromagnetic transition in a bimetallic molecular system*, *Journal of the American Chemical Society,* 1986, **108**, 7428-7430.

(112) B. Hoskins and R. Robson, *Design and construction of a new class of scaffolding-like materials comprising infinite polymeric frameworks of 3D-linked molecular rods. A reappraisal of the zinc cyanide and cadmium cyanide structures and the synthesis and structure of the diamond-related frameworks [N (CH3) 4][CuIZnII (CN) 4] and CuI [4, 4', 4'', 4'''-tetracyanotetraphenylmethane] BF4. xC6H5NO2*, *Journal of the American Chemical Society,* 1990, **112**, 1546-1554.

(113) B. F. Hoskins and R. Robson, *Infinite polymeric frameworks consisting of three dimensionally linked rod-like segments*, *Journal of the American Chemical Society,* 1989, **111**, 5962-5964.

(114) S. Kitagawa and M. Kondo, *Functional micropore chemistry of crystalline metal complex-assembled compounds*, *Bulletin of the Chemical Society of Japan,* 1998, **71**, 1739-1753.

(115) D. Venkataraman, G. B. Gardner, S. Lee and J. S. Moore, *Zeolite-like behavior of a coordination network*, *Journal of the American Chemical Society,* 1995, **117**, 11600-11601.

(116) J. L. Rowsell and O. M. Yaghi, *Metal–organic frameworks: a new class of porous materials*, *Microporous and Mesoporous Materials,* 2004, **73**, 3-14.

(117) H. Li, M. Eddaoudi, M. O'Keeffe and O. M. Yaghi, *Design and synthesis of an exceptionally stable and highly porous metal-organic framework*, *Nature,* 1999, **402**, 276-279.

(118) M. Eddaoudi, J. Kim, N. Rosi, D. Vodak, J. Wachter, M. O'Keeffe and O. M. Yaghi, *Systematic design of pore size and functionality in isoreticular MOFs and their application in methane storage*, *Science,* 2002, **295**, 469-472.

(119) M. Kondo, T. Okubo, A. Asami, S. i. Noro, T. Yoshitomi, S. Kitagawa, T. Ishii, H. Matsuzaka and K. Seki, *Rational synthesis of stable channel‐like cavities with methane gas adsorption properties:[{Cu2 (pzdc) 2 (L)} n](pzdc= pyrazine‐2, 3‐dicarboxylate; L= a pillar ligand)*, *Angewandte Chemie International Edition,* 1999, **38**, 140-143.

(120) R. Kitaura, S. Kitagawa, Y. Kubota, T. C. Kobayashi, K. Kindo, Y. Mita, A. Matsuo, M. Kobayashi, H.-C. Chang and T. C. Ozawa, *Formation of a one-dimensional array of oxygen in a microporous metal-organic solid*, *Science,* 2002, **298**, 2358-2361.

(121) T. Kitao, Y. Zhang, S. Kitagawa, B. Wang and T. Uemura, *Hybridization of MOFs and polymers*, *Chemical Society Reviews,* 2017, **46**, 3108-3133.

(122) D. Riou and G. Férey, *Hybrid open frameworks (MIL-n). Part 3 Crystal structures of the HT and LT forms of MIL-7: a new vanadium propylenediphosphonate with an open-framework. Influence of the synthesis temperature on the oxidation state of vanadium within the same structural type*, *Journal of Materials Chemistry,* 1998, **8**, 2733-2735.

(123) F. Serpaggi and G. Férey, *Hybrid open frameworks (MIL-n). Part 4 Synthesis and crystal structure of MIL-8, a series of lanthanide glutarates with an open framework,[Ln (H 2 O)] 2 [O 2 C (CH 2) 3 CO 2] 3· 4H 2 O*, *Journal of Materials Chemistry,* 1998, **8**, 2737-2741.

(124) C. Livage, C. Egger, M. Nogues and G. Férey, *Hybrid open frameworks (MIL-n). Part 5 Synthesis and crystal structure of MIL-9: a new three-dimensional ferrimagnetic cobalt (II) carboxylate with a two-dimensional array of edge-sharing Co octahedra with 12-membered rings*, *Journal of Materials Chemistry,* 1998, **8**, 2743-2747.

(125) G. Férey, C. Mellot-Draznieks, C. Serre, F. Millange, J. Dutour, S. Surblé and I. Margiolaki, *A chromium terephthalate-based solid with unusually large pore volumes and surface area*, *Science,* 2005, **309**, 2040-2042.

(126) G. Férey and C. Serre, *Large breathing effects in three-dimensional porous hybrid matter: facts, analyses, rules and consequences*, *Chemical Society Reviews,* 2009, **38**, 1380-1399.

(127) C. Serre, F. Millange, C. Thouvenot, M. Nogues, G. Marsolier, D. Louër and G. Férey, *Very Large Breathing Effect in the First Nanoporous Chromium (III)-Based Solids: MIL-53 or CrIII (OH)⍰{O2C− C6H4− CO2}⍰{HO2C− C6H4− CO2H} x⍰ H2O y*, *Journal of the American Chemical Society,* 2002, **124**, 13519-13526.

(128) K. S. Min and M. P. Suh, *Silver (I)− polynitrile network solids for anion exchange: anion-induced transformation of supramolecular structure in the crystalline state*, *Journal of the American Chemical Society,* 2000, **122**, 6834-6840.

(129) G. Maurin, C. Serre, A. Cooper and G. Férey, *The new age of MOFs and of their porous-related solids*, *Chemical Society Reviews,* 2017, **46**, 3104-3107.

(130) M. Clemente-León, E. Coronado, C. Martí-Gastaldo and F. M. Romero, *Multifunctionality in hybrid magnetic materials based on bimetallic oxalate complexes*, *Chemical Society Reviews,* 2011, **40**, 473-497.

(131) K. K. Tanabe and S. M. Cohen, *Postsynthetic modification of metal–organic frameworks—a progress report*, *Chemical Society Reviews,* 2011, **40**, 498-519.

(132) G. Férey, C. Serre, T. Devic, G. Maurin, H. Jobic, P. L. Llewellyn, G. De Weireld, A. Vimont, M. Daturi and J.-S. Chang, *Why hybrid porous solids capture greenhouse gases?*, *Chemical Society Reviews,* 2011, **40**, 550-562.

(133) M. A. Rahim, S. L. Kristufek, S. Pan, J. J. Richardson and F. Caruso, *Phenolic building blocks for the assembly of functional materials*, *Angewandte Chemie International Edition,* 2019, **58**, 1904-1927.

(134) X.-W. Peng, L.-X. Zhong, J.-L. Ren and R.-C. Sun, *Highly effective adsorption of heavy metal ions from aqueous solutions by*

macroporous xylan-rich hemicelluloses-based hydrogel, *Journal of Agricultural and Food Chemistry,* 2012, **60**, 3909-3916.

(135) S. Pan, A. K. Kota, J. M. Mabry and A. Tuteja, *Superomniphobic surfaces for effective chemical shielding*, *Journal of the American Chemical Society,* 2013, **135**, 578-581.

(136) D. Payra, M. Naito, Y. Fujii and Y. Nagao, *Hydrophobized plant polyphenols: self-assembly and promising antibacterial, adhesive, and anticorrosion coatings*, *Chemical Communications,* 2016, **52**, 312-315.

(137) J. Guo, B. L. Tardy, A. J. Christofferson, Y. Dai, J. J. Richardson, W. Zhu, M. Hu, Y. Ju, J. Cui and R. R. Dagastine, *Modular assembly of superstructures from polyphenol-functionalized building blocks*, *Nature nanotechnology,* 2016, **11**, 1105.

(138) S. Quideau, D. Deffieux, C. Douat-Casassus and L. Pouységu, *Plant polyphenols: chemical properties, biological activities, and synthesis*, *Angewandte Chemie International Edition,* 2011, **50**, 586-621.

(139) R. J. Stewart, J. C. Weaver, D. E. Morse and J. H. Waite, *The tube cement of Phragmatopoma californica: a solid foam*, *Journal of Experimental Biology,* 2004, **207**, 4727-4734.

(140) A. Soto-Vaca, A. Gutierrez, J. N. Losso, Z. Xu and J. W. Finley, *Evolution of phenolic compounds from color and flavor problems to health benefits*, *Journal of Agricultural and Food Chemistry,* 2012, **60**, 6658-6677.

(141) H. Lee, S. M. Dellatore, W. M. Miller and P. B. Messersmith, *Mussel-inspired surface chemistry for multifunctional coatings*, *Science,* 2007, **318**, 426-430.

(142) T. Shutava, M. Prouty, D. Kommireddy and Y. Lvov, *pH responsive decomposable layer-by-layer nanofilms and capsules on the basis of tannic acid*, *Macromolecules,* 2005, **38**, 2850-2858.

(143) H. Ejima, J. J. Richardson, K. Liang, J. P. Best, M. P. van Koeverden, G. K. Such, J. Cui and F. Caruso, *One-step assembly of coordination complexes for versatile film and particle engineering*, *Science,* 2013, **341**, 154-157.

(144) J. H. Park, K. Kim, J. Lee, J. Y. Choi, D. Hong, S. H. Yang, F. Caruso, Y. Lee and I. S. Choi, *A cytoprotective and degradable metal–polyphenol nanoshell for single-cell encapsulation*, *Angewandte Chemie International Edition,* 2014, **53**, 12420-12425.

(145) J. J. Richardson, J. Cui, M. Björnmalm, J. A. Braunger, H. Ejima and F. Caruso, *Innovation in layer-by-layer assembly*, *Chemical Reviews,* 2016, **116**, 14828-14867.

(146) T. Park, J. Y. Kim, H. Cho, H. C. Moon, B. J. Kim, J. H. Park, D. Hong, J. Park and I. S. Choi, *Artificial spores: Immunoprotective nanocoating of red blood cells with supramolecular ferric ion-tannic acid complex*, *Polymers,* 2017, **9**, 140.

(147) J. Guo, Y. Ping, H. Ejima, K. Alt, M. Meissner, J. J. Richardson, Y. Yan, K. Peter, D. Von Elverfeldt and C. E. Hagemeyer, *Engineering*

multifunctional capsules through the assembly of metal–phenolic networks, *Angewandte Chemie International Edition,* 2014, **53**, 5546-5551.

(148) M. Björnmalm, J. Cui, N. Bertleff-Zieschang, D. Song, M. Faria, M. A. Rahim and F. Caruso, *Nanoengineering particles through template assembly*, *Chemistry of Materials,* 2017, **29**, 289-306.

(149) M. A. Rahim, K. Kempe, M. Müllner, H. Ejima, Y. Ju, M. P. Van Koeverden, T. Suma, J. A. Braunger, M. G. Leeming and B. F. Abrahams, *Surface-confined amorphous films from metal-coordinated simple phenolic ligands*, *Chemistry of Materials,* 2015, **27**, 5825-5832.

(150) J. Guo, H. Sun, K. Alt, B. L. Tardy, J. J. Richardson, T. Suma, H. Ejima, J. Cui, C. E. Hagemeyer and F. Caruso, *Boronate–Phenolic Network Capsules with Dual Response to Acidic pH and cis-Diols*, *Advanced healthcare materials,* 2015, **4**, 1796-1801.

(151) N. Bertleff-Zieschang, M. A. Rahim, Y. Ju, J. A. Braunger, T. Suma, Y. Dai, S. Pan, F. Cavalieri and F. Caruso, *Biofunctional metal–phenolic films from dietary flavonoids*, *Chemical Communications,* 2017, **53**, 1068-1071.

(152) J. H. Park, S. Choi, H. C. Moon, H. Seo, J. Y. Kim, S.-P. Hong, B. S. Lee, E. Kang, J. Lee and D. H. Ryu, *Antimicrobial spray nanocoating of supramolecular Fe (III)-tannic acid metal-organic coordination complex: applications to shoe insoles and fruits*, *Scientific reports,* 2017, **7**, 1-7.

(153) B. J. Kim, S. Han, K. B. Lee and I. S. Choi, *Biphasic supramolecular self-assembly of ferric ions and tannic acid across interfaces for nanofilm formation*, *Advanced Materials,* 2017, **29**, 1700784.

(154) M. A. Rahim, M. Björnmalm, N. Bertleff-Zieschang, Q. Besford, S. Mettu, T. Suma, M. Faria and F. Caruso, *Rust-mediated continuous assembly of metal–phenolic networks*, *Advanced Materials,* 2017, **29**, 1606717.

(155) C. m. Maerten, L. Lopez, P. Lupattelli, G. Rydzek, S. Pronkin, P. Schaaf, L. Jierry and F. Boulmedais, *Electrotriggered confined self-assembly of metal–polyphenol nanocoatings using a morphogenic approach*, *Chemistry of Materials,* 2017, **29**, 9668-9679.

(156) J. J. Richardson, M. Björnmalm and F. Caruso, *Technology-driven layer-by-layer assembly of nanofilms*, *Science,* 2015, **348**, aaa2491.

(157) C. Wunderlich, R. Weber and G. Bergerhoff, *On iron gallic ink*, *Zeitschrift fur Anorganische und Allgemeine Chemie,* 1991, **598**, 371-376.

(158) G. Mouchaham, L. Cooper, N. Guillou, C. Martineau, E. Elkaïm, S. Bourrelly, P. L. Llewellyn, C. Allain, G. Clavier and C. Serre, *A robust infinite zirconium phenolate building unit to enhance the chemical stability of Zr MOFs*, *Angewandte Chemie International Edition,* 2015, **54**, 13297-13301.

(159) L. Cooper, T. Hidalgo, M. Gorman, T. Lozano-Fernández, R. Simón-Vázquez, C. Olivier, N. Guillou, C. Serre, C. Martineau and F. Taulelle, *A biocompatible porous Mg-gallate metal–organic framework as an antioxidant carrier*, *Chemical Communications,* 2015, **51**, 5848-5851.
(160) L. Cooper, N. Guillou, C. Martineau, E. Elkaim, F. Taulelle, C. Serre and T. Devic, *ZrIV coordination polymers based on a naturally occurring phenolic derivative*, *European Journal of Inorganic Chemistry,* 2014, **2014**, 6281-6289.
(161) X. Wang, J. Yan, D. Pan, R. Yang, L. Wang, Y. Xu, J. Sheng, Y. Yue, Q. Huang and Y. Wang, *Polyphenol–Poloxamer Self‐Assembled Supramolecular Nanoparticles for Tumor NIRF/PET Imaging*, *Advanced healthcare materials,* 2018, **7**, 1701505.
(162) Y. Dai, J. Guo, T. Y. Wang, Y. Ju, A. J. Mitchell, T. Bonnard, J. Cui, J. J. Richardson, C. E. Hagemeyer and K. Alt, *Self‐Assembled Nanoparticles from Phenolic Derivatives for Cancer Therapy*, *Advanced healthcare materials,* 2017, **6**, 1700467.
(163) S. Wu, R. Qi, H. Kuang, Y. Wei, X. Jing, F. Meng and Y. Huang, *pH‐Responsive Drug Delivery by Amphiphilic Copolymer through Boronate–Catechol Complexation*, *ChemPlusChem,* 2013, **78**, 175-184.
(164) Y. Li, W. Xiao, K. Xiao, L. Berti, J. Luo, H. P. Tseng, G. Fung and K. S. Lam, *Well‐defined, reversible boronate crosslinked nanocarriers for targeted drug delivery in response to acidic pH values and cis‐diols*, *Angewandte Chemie International Edition,* 2012, **51**, 2864-2869.
(165) L. Sun, C. Wang and L. Wang, *A kind of coordination complex cement for the self-assembly of superstructure*, *ACS nano,* 2018, **12**, 4002-4009.
(166) N. M. Sangeetha and U. Maitra, *Supramolecular gels: Functions and uses*, *Chemical Society Reviews,* 2005, **34**, 821-836.
(167) J. Li, H. Ejima and N. Yoshie, *Seawater-assisted self-healing of catechol polymers via hydrogen bonding and coordination interactions*, *ACS applied materials & interfaces,* 2016, **8**, 19047-19053.
(168) A. Y.-Y. Tam and V. W.-W. Yam, *Recent advances in metallogels*, *Chemical Society Reviews,* 2013, **42**, 1540-1567.
(169) P. Dastidar, S. Ganguly and K. Sarkar, *Metallogels from coordination complexes, organometallic, and coordination polymers*, *Chemistry–An Asian Journal,* 2016, **11**, 2484-2498.
(170) M. Martínez-Calvo, O. Kotova, M. E. Möbius, A. P. Bell, T. McCabe, J. J. Boland and T. Gunnlaugsson, *Healable luminescent self-assembly supramolecular metallogels possessing lanthanide (Eu/Tb) dependent rheological and morphological properties*, *Journal of the American Chemical Society,* 2015, **137**, 1983-1992.
(171) J. H. Kim, J. Y. Oh, J. M. Lee, Y. C. Jeong, S. H. So, Y. S. Cho, S. Nam, C. R. Park and S. J. Yang, *Macroscopically interconnected*

hierarchically porous carbon monolith by metal-phenolic coordination as an sorbent for multi-scale molecules, *Carbon,* 2018, **126**, 190-196.

(172) N. Holten-Andersen, M. J. Harrington, H. Birkedal, B. P. Lee, P. B. Messersmith, K. Y. C. Lee and J. H. Waite, *pH-induced metal-ligand cross-links inspired by mussel yield self-healing polymer networks with near-covalent elastic moduli*, *Proceedings of the National Academy of Sciences,* 2011, **108**, 2651-2655.

(173) P. S. Yavvari, S. Pal, S. Kumar, A. Kar, A. K. Awasthi, A. Naaz, A. Srivastava and A. Bajaj, *Injectable, self-healing chimeric catechol-Fe (III) hydrogel for localized combination cancer therapy*, *ACS Biomaterials Science & Engineering,* 2017, **3**, 3404-3413.

(174) Q. Li, D. G. Barrett, P. B. Messersmith and N. Holten-Andersen, *Controlling hydrogel mechanics via bio-inspired polymer–nanoparticle bond dynamics*, *ACS nano,* 2016, **10**, 1317-1324.

(175) M. Krogsgaard, A. Andersen and H. Birkedal, *Gels and threads: mussel-inspired one-pot route to advanced responsive materials*, *Chemical Communications,* 2014, **50**, 13278-13281.

(176) M. A. Rahim, M. Björnmalm, T. Suma, M. Faria, Y. Ju, K. Kempe, M. Müllner, H. Ejima, A. D. Stickland and F. Caruso, *Metal–phenolic supramolecular gelation*, *Angewandte Chemie International Edition,* 2016, **55**, 13803-13807.

(177) M. A. Rahim, Y. Hata, M. Björnmalm, Y. Ju and F. Caruso, *Supramolecular metal–phenolic gels for the crystallization of active pharmaceutical ingredients*, *Small,* 2018, **14**, 1801202.

(178) C. Kim, H. Ejima and N. Yoshie, *Non-swellable self-healing polymer with long-term stability under seawater*, *RSC Advances,* 2017, **7**, 19288-19295.

(179) Y. Liu, X. Ji and Z. He, *Organic–inorganic nanoflowers: from design strategy to biomedical applications*, *Nanoscale,* 2019, **11**, 17179-17194.

(180) H. Zhang, L.-Y. Guo, J. Jiao, X. Xin, D. Sun and S. Yuan, *Ionic self-assembly of polyoxometalate–dopamine hybrid nanoflowers with excellent catalytic activity for dyes*, *ACS Sustainable Chemistry & Engineering,* 2017, **5**, 1358-1367.

(181) S. K. Patel, S. V. Otari, J. Li, D. R. Kim, S. C. Kim, B.-K. Cho, V. C. Kalia, Y. C. Kang and J.-K. Lee, *Synthesis of cross-linked protein-metal hybrid nanoflowers and its application in repeated batch decolorization of synthetic dyes*, *Journal of Hazardous materials,* 2018, **347**, 442-450.

(182) Y. Liu, M. Du, J. Zhu, X. Hu, X. Ji and Z. He, *Three-Dimensional Immunosensing Platform Based on a Hybrid Nanoflower for Sensitive Detection of α-Fetoprotein and Enterovirus 71*, *ACS Applied Nano Materials,* 2018, **1**, 4964-4971.

(183) J. Han, P. Luo, L. Wang, C. Li, Y. Mao and Y. Wang, *Construction of magnetic nanoflower biocatalytic system with enhanced enzymatic*

performance by biomineralization and its application for bisphenol A removal, *Journal of Hazardous materials,* 2019, **380**, 120901.

(184) J. Ge, J. Lei and R. N. Zare, *Protein–inorganic hybrid nanoflowers*, *Nature nanotechnology,* 2012, **7**, 428-432.

(185) X. Wu, M. Hou and J. Ge, *Metal–organic frameworks and inorganic nanoflowers: a type of emerging inorganic crystal nanocarrier for enzyme immobilization*, *Catalysis Science & Technology,* 2015, **5**, 5077-5085.

(186) J. Cui and S. Jia, *Organic–inorganic hybrid nanoflowers: A novel host platform for immobilizing biomolecules*, *Coordination Chemistry Reviews,* 2017, **352**, 249-263.

(187) B. Somturk, M. Hancer, I. Ocsoy and N. Özdemir, *Synthesis of copper ion incorporated horseradish peroxidase-based hybrid nanoflowers for enhanced catalytic activity and stability*, *Dalton Transactions,* 2015, **44**, 13845-13852.

(188) M. Bilal, M. Asgher, S. Z. H. Shah and H. M. Iqbal, *Engineering enzyme-coupled hybrid nanoflowers: The quest for optimum performance to meet biocatalytic challenges and opportunities*, *International Journal of Biological Macromolecules,* 2019.

(189) M. Chung, T. L. Nguyen, T. Q. N. Tran, H. H. Yoon, I. T. Kim and M. I. Kim, *Ultrarapid sonochemical synthesis of enzyme-incorporated copper nanoflowers and their application to mediatorless glucose biofuel cell*, *Applied Surface Science,* 2018, **429**, 203-209.

(190) B. S. Batule, K. S. Park, M. I. Kim and H. G. Park, *Ultrafast sonochemical synthesis of protein-inorganic nanoflowers*, *International journal of nanomedicine,* 2015, **10**, 137.

(191) M. Chung, Y. J. Jang and M. I. Kim, *Convenient colorimetric detection of cholesterol using multi-enzyme co-incorporated organic–inorganic hybrid nanoflowers*, *Journal of nanoscience and nanotechnology,* 2018, **18**, 6555-6561.

(192) M. Li, M. Luo, F. Li, W. Wang, K. Liu, Q. Liu, Y. Wang, Z. Lu and D. Wang, *Biomimetic copper-based inorganic–protein nanoflower assembly constructed on the nanoscale fibrous membrane with enhanced stability and durability*, *The Journal of Physical Chemistry C,* 2016, **120**, 17348-17356.

(193) M. Ariza-Avidad, A. Salinas-Castillo and L. Capitán-Vallvey, *A 3D µPAD based on a multi-enzyme organic–inorganic hybrid nanoflower reactor*, *Biosensors and Bioelectronics,* 2016, **77**, 51-55.

(194) Y. Liu, J. Chen, M. Du, X. Wang, X. Ji and Z. He, *The preparation of dual-functional hybrid nanoflower and its application in the ultrasensitive detection of disease-related biomarker*, *Biosensors and Bioelectronics,* 2017, **92**, 68-73.

(195) J. Sun, J. Ge, W. Liu, M. Lan, H. Zhang, P. Wang, Y. Wang and Z. Niu, *Multi-enzyme co-embedded organic–inorganic hybrid nanoflowers: synthesis and application as a colorimetric sensor*, *Nanoscale,* 2014, **6**, 255-262.

(196) Z. Zhao, J. Zhang, M. Wang, Z. Wang, L. Wang, L. Ma, X. Huang and Z. Li, *Structure advantage and peroxidase activity enhancement of deuterohemin-peptide–inorganic hybrid flowers*, *RSC Advances,* 2016, **6**, 104265-104272.
(197) Z.-F. Wu, Z. Wang, Y. Zhang, Y.-L. Ma, C.-Y. He, H. Li, L. Chen, Q.-S. Huo, L. Wang and Z.-Q. Li, *Amino acids-incorporated nanoflowers with an intrinsic peroxidase-like activity*, *Scientific reports,* 2016, **6**, 22412.
(198) T. Wei, D. Du, M.-J. Zhu, Y. Lin and Z. Dai, *An improved ultrasensitive enzyme-linked immunosorbent assay using hydrangea-like antibody–enzyme–inorganic three-in-one nanocomposites*, *ACS applied materials & interfaces,* 2016, **8**, 6329-6335.
(199) C. Ke, Y. Fan, Y. Chen, L. Xu and Y. Yan, *A new lipase–inorganic hybrid nanoflower with enhanced enzyme activity*, *RSC Advances,* 2016, **6**, 19413-19416.
(200) L.-B. Wang, Y.-C. Wang, R. He, A. Zhuang, X. Wang, J. Zeng and J. Hou, *A new nanobiocatalytic system based on allosteric effect with dramatically enhanced enzymatic performance*, *Journal of the American Chemical Society,* 2013, **135**, 1272-1275.
(201) J. Shi, S. Zhang, X. Wang, C. Yang and Z. Jiang, *Preparation and enzymatic application of flower-like hybrid microcapsules through a biomimetic mineralization approach*, *Journal of Materials Chemistry B,* 2014, **2**, 4289-4296.
(202) Y. Yin, Y. Xiao, G. Lin, Q. Xiao, Z. Lin and Z. Cai, *An enzyme–inorganic hybrid nanoflower based immobilized enzyme reactor with enhanced enzymatic activity*, *Journal of Materials Chemistry B,* 2015, **3**, 2295-2300.
(203) Z. Lin, Y. Xiao, L. Wang, Y. Yin, J. Zheng, H. Yang and G. Chen, *Facile synthesis of enzyme–inorganic hybrid nanoflowers and their application as an immobilized trypsin reactor for highly efficient protein digestion*, *RSC Advances,* 2014, **4**, 13888-13891.
(204) F. López-Gallego and L. Yate, *Selective biomineralization of Co 3 (PO 4) 2-sponges triggered by His-tagged proteins: efficient heterogeneous biocatalysts for redox processes*, *Chemical Communications,* 2015, **51**, 8753-8756.
(205) Z. Lin, Y. Xiao, Y. Yin, W. Hu, W. Liu and H. Yang, *Facile synthesis of enzyme-inorganic hybrid nanoflowers and its application as a colorimetric platform for visual detection of hydrogen peroxide and phenol*, *ACS applied materials & interfaces,* 2014, **6**, 10775-10782.
(206) L. Zhu, L. Gong, Y. Zhang, R. Wang, J. Ge, Z. Liu and R. N. Zare, *Rapid detection of phenol using a membrane containing laccase nanoflowers*, *Chemistry–An Asian Journal,* 2013, **8**, 2358-2360.
(207) Z. Zhang, Y. Zhang, L. He, Y. Yang, S. Liu, M. Wang, S. Fang and G. Fu, *A feasible synthesis of Mn3 (PO4) 2@ BSA nanoflowers and its application as the support nanomaterial for Pt catalyst*, *Journal of Power Sources,* 2015, **284**, 170-177.

(208) R. Ye, C. Zhu, Y. Song, J. Song, S. Fu, Q. Lu, X. Yang, M.-J. Zhu, D. Du and H. Li, *One-pot bioinspired synthesis of all-inclusive protein–protein nanoflowers for point-of-care bioassay: detection of E. coli O157: H7 from milk*, *Nanoscale,* 2016, **8**, 18980-18986.
(209) J. Cui, Y. Zhao, R. Liu, C. Zhong and S. Jia, *Surfactant-activated lipase hybrid nanoflowers with enhanced enzymatic performance*, *Scientific reports,* 2016, **6**, 27928.
(210) B. Zhang, P. Li, H. Zhang, L. Fan, H. Wang, X. Li, L. Tian, N. Ali, Z. Ali and Q. Zhang, *Papain/Zn 3 (PO 4) 2 hybrid nanoflower: preparation, characterization and its enhanced catalytic activity as an immobilized enzyme*, *RSC Advances,* 2016, **6**, 46702-46710.
(211) X. Wang, J. Shi, Z. Li, S. Zhang, H. Wu, Z. Jiang, C. Yang and C. Tian, *Facile one-pot preparation of chitosan/calcium pyrophosphate hybrid microflowers*, *ACS applied materials & interfaces,* 2014, **6**, 14522-14532.
(212) L. He, S. Zhang, H. Ji, M. Wang, D. Peng, F. Yan, S. Fang, H. Zhang, C. Jia and Z. Zhang, *Protein-templated cobaltous phosphate nanocomposites for the highly sensitive and selective detection of platelet-derived growth factor-BB*, *Biosensors and Bioelectronics,* 2016, **79**, 553-560.
(213) Y. Guo, S. Li, Y. Wang and S. Zhang, *Diagnosis–Therapy integrative systems based on magnetic RNA nanoflowers for Co-drug delivery and targeted therapy*, *Analytical Chemistry,* 2017, **89**, 2267-2274.
(214) B. Zhang, P. Li, H. Zhang, H. Wang, X. Li, L. Tian, N. Ali, Z. Ali and Q. Zhang, *Preparation of lipase/Zn3 (PO4) 2 hybrid nanoflower and its catalytic performance as an immobilized enzyme*, *Chemical Engineering Journal,* 2016, **291**, 287-297.
(215) I. Ocsoy, E. Dogru and S. Usta, *A new generation of flowerlike horseradish peroxides as a nanobiocatalyst for superior enzymatic activity*, *Enzyme and Microbial Technology,* 2015, **75**, 25-29.
(216) S. K. Patel, R. K. Gupta, V. Kumar, P. Mardina, R. Lestari, V. C. Kalia, M.-S. Choi and J.-K. Lee, *Influence of metal ions on the immobilization of β-glucosidase through protein-inorganic hybrids*, *Indian journal of microbiology,* 2019, **59**, 370-374.
(217) Y. Liu, B. Wang, X. Ji and Z. He, *Self-assembled protein-enzyme nanoflower-based fluorescent sensing for protein biomarker*, *Analytical and bioanalytical chemistry,* 2018, **410**, 7591-7598.
(218) S. Escobar, S. Velasco-Lozano, C.-H. Lu, Y.-F. Lin, M. Mesa, C. Bernal and F. López-Gallego, *Understanding the functional properties of bio-inorganic nanoflowers as biocatalysts by deciphering the metal-binding sites of enzymes*, *Journal of Materials Chemistry B,* 2017, **5**, 4478-4486.
(219) D. Quesada-González and A. Merkoçi, *Nanomaterial-based devices for point-of-care diagnostic applications*, *Chemical Society Reviews,* 2018, **47**, 4697-4709.

(220) J. Mu, J. Lin, P. Huang and X. Chen, *Development of endogenous enzyme-responsive nanomaterials for theranostics*, *Chemical Society Reviews,* 2018, **47**, 5554-5573.

(221) E.-K. Lim, T. Kim, S. Paik, S. Haam, Y.-M. Huh and K. Lee, *Nanomaterials for theranostics: recent advances and future challenges*, *Chemical Reviews,* 2015, **115**, 327-394.

(222) D. A. Giljohann, D. S. Seferos, W. L. Daniel, M. D. Massich, P. C. Patel and C. A. Mirkin, *Gold nanoparticles for biology and medicine*, *Angewandte Chemie International Edition,* 2010, **49**, 3280-3294.

(223) J. Wu, Y. Qu, Q. Yu and H. Chen, *Gold nanoparticle layer: a versatile nanostructured platform for biomedical applications*, *Materials Chemistry Frontiers,* 2018, **2**, 2175-2190.

(224) S. Biswas, X. Liu, J. W. Jarrett, D. Brown, V. Pustovit, A. Urbas, K. L. Knappenberger Jr, P. F. Nealey and R. A. Vaia, *Nonlinear chiro-optical amplification by plasmonic nanolens arrays formed via directed assembly of gold nanoparticles*, *Nano Letters,* 2015, **15**, 1836-1842.

(225) Y. Jiang, Z. Wang, X. Yu, F. Shi, H. Xu, X. Zhang, M. Smet and W. Dehaen, *Self-assembled monolayers of dendron thiols for electrodeposition of gold nanostructures: toward fabrication of superhydrophobic/superhydrophilic surfaces and pH-responsive surfaces*, *Langmuir,* 2005, **21**, 1986-1990.

(226) B. Zhou, Y. Li, H. Deng, Y. Hu and B. Li, *Antibacterial multilayer films fabricated by layer-by-layer immobilizing lysozyme and gold nanoparticles on nanofibers*, *Colloids and Surfaces B: Biointerfaces,* 2014, **116**, 432-438.

(227) D. A. Mortimer, *Synthetic polyelectrolytes—a review*, *Polymer International,* 1991, **25**, 29-41.

(228) F.-X. Xiao, M. Pagliaro, Y.-J. Xu and B. Liu, *Layer-by-layer assembly of versatile nanoarchitectures with diverse dimensionality: a new perspective for rational construction of multilayer assemblies*, *Chemical Society Reviews,* 2016, **45**, 3088-3121.

(229) C. Jiang, S. Markutsya, H. Shulha and V. V. Tsukruk, *Freely suspended gold nanoparticle arrays*, *Advanced Materials,* 2005, **17**, 1669-1673.

(230) F. N. Crespilho, M. E. Ghica, M. Florescu, F. C. Nart, O. N. Oliveira Jr and C. M. Brett, *A strategy for enzyme immobilization on layer-by-layer dendrimer–gold nanoparticle electrocatalytic membrane incorporating redox mediator*, *Electrochemistry Communications,* 2006, **8**, 1665-1670.

(231) V. V. Thacker, L. O. Herrmann, D. O. Sigle, T. Zhang, T. Liedl, J. J. Baumberg and U. F. Keyser, *DNA origami based assembly of gold nanoparticle dimers for surface-enhanced Raman scattering*, *Nature communications,* 2014, **5**, 3448.

(232) H. Yan, S. H. Park, G. Finkelstein, J. H. Reif and T. H. LaBean, *DNA-templated self-assembly of protein arrays and highly conductive nanowires*, *Science,* 2003, **301**, 1882-1884.

(233) Z. Li, J. Wang, Y. Li, X. Liu and Q. Yuan, *Self-assembled DNA nanomaterials with highly programmed structures and functions*, *Materials Chemistry Frontiers,* 2018, **2**, 423-436.
(234) J. Sharma, R. Chhabra, Y. Liu, Y. Ke and H. Yan, *DNA-templated self-assembly of two-dimensional and periodical gold nanoparticle arrays*, *Angewandte Chemie International Edition,* 2006, **45**, 730-735.
(235) S. Shiraishi, L. Yu, Y. Akiyama, G. Wang, T. Kikitsu, K. Miyamura, T. Takarada and M. Maeda, *Folding of Nanoparticle Chains into 2D Arrays: Structural Change of DNA-Functionalized Gold Nanoparticle Assemblies*, *Advanced Materials Interfaces,* 2018, **5**, 1800189.
(236) A. V. Pinheiro, D. Han, W. M. Shih and H. Yan, *Challenges and opportunities for structural DNA nanotechnology*, *Nature nanotechnology,* 2011, **6**, 763.
(237) M. R. Jones, K. D. Osberg, R. J. Macfarlane, M. R. Langille and C. A. Mirkin, *Templated techniques for the synthesis and assembly of plasmonic nanostructures*, *Chemical Reviews,* 2011, **111**, 3736-3827.
(238) C. A. Mirkin, R. L. Letsinger, R. C. Mucic and J. J. Storhoff, *A DNA-based method for rationally assembling nanoparticles into macroscopic materials*, *Nature,* 1996, **382**, 607-609.
(239) C. Xue, M. Gao, Y. Xue, L. Zhu, L. Dai, A. Urbas and Q. Li, *Building 3D layer-by-layer graphene–gold nanoparticle hybrid architecture with tunable interlayer distance*, *The Journal of Physical Chemistry C,* 2014, **118**, 15332-15338.
(240) S. K. Abkenar, A. Tufani, G. O. Ince, H. Kurt, A. Turak and C. W. Ow-Yang, *Transfer printing gold nanoparticle arrays by tuning the surface hydrophilicity of thermo-responsive poly N-isopropylacrylamide (pNIPAAm)*, *Nanoscale,* 2017, **9**, 2969-2973.
(241) N. Kim, H. Kang, J. H. Lee, S. Kee, S. H. Lee and K. Lee, *Highly conductive all-plastic electrodes fabricated using a novel chemically controlled transfer-printing method*, *Advanced Materials,* 2015, **27**, 2317-2323.
(242) Y.-L. Loo, R. L. Willett, K. W. Baldwin and J. A. Rogers, *Interfacial chemistries for nanoscale transfer printing*, *Journal of the American Chemical Society,* 2002, **124**, 7654-7655.
(243) H.-L. Gou, J.-J. Xu, X.-H. Xia and H.-Y. Chen, *Air plasma assisting microcontact deprinting and printing for gold thin film and PDMS patterns*, *ACS applied materials & interfaces,* 2010, **2**, 1324-1330.
(244) C. J. Cheng, G. T. Tietjen, J. K. Saucier-Sawyer and W. M. Saltzman, *A holistic approach to targeting disease with polymeric nanoparticles*, *Nature reviews Drug discovery,* 2015, **14**, 239-247.
(245) P. Matricardi, C. Di Meo, T. Coviello, W. E. Hennink and F. Alhaique, *Interpenetrating polymer networks polysaccharide hydrogels for drug delivery and tissue engineering*, *Advanced drug delivery reviews,* 2013, **65**, 1172-1187.

(246) J.-K. F. Suh and H. W. Matthew, *Application of chitosan-based polysaccharide biomaterials in cartilage tissue engineering: a review*, *Biomaterials,* 2000, **21**, 2589-2598.
(247) A. Kumar, K. M. Rao and S. S. Han, *Application of xanthan gum as polysaccharide in tissue engineering: A review*, *Carbohydrate Polymers,* 2018, **180**, 128-144.
(248) M. I. Giannotti, O. Esteban, M. Oliva, M. F. García-Parajo and F. Sanz, *pH-responsive polysaccharide-based polyelectrolyte complexes as nanocarriers for lysosomal delivery of therapeutic proteins*, *Biomacromolecules,* 2011, **12**, 2524-2533.
(249) Y. Huang, H. Hu, R.-Q. Li, B. Yu and F.-J. Xu, *Versatile types of MRI-visible cationic nanoparticles involving pullulan polysaccharides for multifunctional gene carriers*, *ACS applied materials & interfaces,* 2016, **8**, 3919-3927.
(250) S. Zhou, H. Dou, Z. Zhang, K. Sun, Y. Jin, T. Dai, G. Zhou and Z. Shen, *Fluorescent dextran-based nanogels: efficient imaging nanoprobes for adipose-derived stem cells*, *Polymer Chemistry,* 2013, **4**, 4103-4112.
(251) M. Wojnilowicz, A. Glab, A. Bertucci, F. Caruso and F. Cavalieri, *Super-resolution imaging of proton sponge-triggered rupture of endosomes and cytosolic release of small interfering RNA*, *ACS nano,* 2018, **13**, 187-202.
(252) Q. Sun, Z. Zhou, N. Qiu and Y. Shen, *Rational design of cancer nanomedicine: nanoproperty integration and synchronization*, *Advanced Materials,* 2017, **29**, 1606628.
(253) Z. Cheng, A. Al Zaki, J. Z. Hui, V. R. Muzykantov and A. Tsourkas, *Multifunctional nanoparticles: cost versus benefit of adding targeting and imaging capabilities*, *Science,* 2012, **338**, 903-910.
(254) Q. A. Besford, F. Cavalieri and F. Caruso, *Glycogen as a Building Block for Advanced Biological Materials*, *Advanced Materials,* 2019, 1904625.
(255) F. G. Young, *Claude Bernard and the discovery of glycogen*, *British medical journal,* 1957, **1**, 1431.
(256) W. J. Whelan and M. P. Cameron, *Control of Glycogen Metabolism. Consulting Editor, WJ Whelan... Editor for the Ciba Foundation, Margaret P. Cameron, Etc.[With Plates.]*. J. & A. Churchill: 1964.
(257) P. J. Roach, A. A. Depaoli-Roach, T. D. Hurley and V. S. Tagliabracci, *Glycogen and its metabolism: some new developments and old themes*, *Biochemical Journal,* 2012, **441**, 763-787.
(258) S. G. Ball and M. K. Morell, *From bacterial glycogen to starch: understanding the biogenesis of the plant starch granule*, *Annual review of plant biology,* 2003, **54**, 207-233.
(259) V. Gopinath, S. Saravanan, A. Al-Maleki, M. Ramesh and J. Vadivelu, *A review of natural polysaccharides for drug delivery*

applications: Special focus on cellulose, starch and glycogen, *Biomedicine & Pharmacotherapy,* 2018, **107**, 96-108.

(260) J.-H. Ryu, J. Drain, J. H. Kim, S. McGee, A. Gray-Weale, L. Waddington, G. J. Parker, M. Hargreaves, S.-H. Yoo and D. Stapleton, *Comparative structural analyses of purified glycogen particles from rat liver, human skeletal muscle and commercial preparations*, *International Journal of Biological Macromolecules,* 2009, **45**, 478-482.

(261) B. Deng, M. A. Sullivan, J. Li, X. Tan, C. Zhu, B. L. Schulz and R. G. Gilbert, *Molecular structure of glycogen in diabetic liver*, *Glycoconjugate Journal,* 2015, **32**, 113-118.

(262) M. A. Sullivan, S. T. Aroney, S. Li, F. J. Warren, J. S. Joo, K. S. Mak, D. I. Stapleton, K. S. Bell-Anderson and R. G. Gilbert, *Changes in glycogen structure over feeding cycle sheds new light on blood-glucose control*, *Biomacromolecules,* 2014, **15**, 660-665.

(263) R. F. King, B. Jones and J. P. O'Hara, *The availability of water associated with glycogen during dehydration: a reservoir or raindrop?*, *European journal of applied physiology,* 2018, **118**, 283-290.

(264) Q. A. Besford, M. A. Sullivan, L. Zheng, R. G. Gilbert, D. Stapleton and A. Gray-Weale, *The structure of cardiac glycogen in healthy mice*, *International Journal of Biological Macromolecules,* 2012, **51**, 887-891.

(265) A. M. Brown, *Brain glycogen re‐awakened*, *Journal of Neurochemistry,* 2004, **89**, 537-552.

(266) M. S. Gentry, J. J. Guinovart, B. A. Minassian, P. J. Roach and J. M. Serratosa, *Lafora disease offers a unique window into neuronal glycogen metabolism*, *Journal of Biological Chemistry,* 2018, **293**, 7117-7125.

(267) P. J. Roach, *Glycogen and its metabolism*, *Current molecular medicine,* 2002, **2**, 101-120.

(268) M. M. Adeva-Andany, M. González-Lucán, C. Donapetry-García, C. Fernández-Fernández and E. Ameneiros-Rodríguez, *Glycogen metabolism in humans*, *BBA clinical,* 2016, **5**, 85-100.

(269) Q. A. Besford, X.-Y. Zeng, J.-M. Ye and A. Gray-Weale, *Liver glycogen in type 2 diabetic mice is randomly branched as enlarged aggregates with blunted glucose release*, *Glycoconjugate Journal,* 2016, **33**, 41-51.

(270) D. Konkolewicz, O. Thorn-Seshold and A. Gray-Weale, *Models for randomly hyperbranched polymers: Theory and simulation*, *The Journal of chemical physics,* 2008, **129**, 054901.

(271) D. Konkolewicz, A. A. Gray‐Weale and R. G. Gilbert, *Molecular weight distributions from size separation data for hyperbranched polymers*, *Journal of Polymer Science Part A: Polymer Chemistry,* 2007, **45**, 3112-3115.

(272) D. Konkolewicz, S. Perrier, D. Stapleton and A. Gray‐Weale, *Modeling highly branched structures: Description of the solution*

structures of dendrimers, polyglycerol, and glycogen, *Journal of Polymer Science Part B: Polymer Physics,* 2011, **49**, 1525-1538.

(273) P. Zhang, S. S. Nada, X. Tan, B. Deng, M. A. Sullivan and R. G. Gilbert, *Exploring glycogen biosynthesis through Monte Carlo simulation*, *International Journal of Biological Macromolecules,* 2018, **116**, 264-271.

(274) S. A. Engelberth, N. Hempel and M. Bergkvist, *Chemically modified dendritic starch: a novel nanomaterial for siRNA delivery*, *Bioconjugate Chemistry,* 2015, **26**, 1766-1774.

(275) Q. A. Besford, M. Wojnilowicz, T. Suma, N. Bertleff-Zieschang, F. Caruso and F. Cavalieri, *Lactosylated glycogen nanoparticles for targeting prostate cancer cells*, *ACS applied materials & interfaces,* 2017, **9**, 16869-16879.

(276) M. Wojnilowicz, Q. A. Besford, Y.-L. Wu, X. J. Loh, J. A. Braunger, A. Glab, C. Cortez-Jugo, F. Caruso and F. Cavalieri, *Glycogen-nucleic acid constructs for gene silencing in multicellular tumor spheroids*, *Biomaterials,* 2018, **176**, 34-49.

(277) S. Wang, Y. Kang, L. Wang, H. Zhang, Y. Wang and Y. Wang, *Organic/inorganic hybrid sensors: A review*, *Sensors and Actuators B: Chemical,* 2013, **182**, 467-481.

(278) M. Xiang, X. Xu, D. Li, F. Liu, N. Li and K. Li, *Selective enhancement of resonance light-scattering of gold nanoparticles by glycogen*, *Talanta,* 2008, **76**, 1207-1211.

(279) M. Xiang, X. Xu, F. Liu, N. Li and K.-A. Li, *Gold Nanoparticle Based Plasmon Resonance Light-Scattering Method as a New Approach for Glycogen− Biomacromolecule Interactions*, *The Journal of Physical Chemistry B,* 2009, **113**, 2734-2738.

(280) D. K. Božanić, A. S. Luyt, L. V. Trandafilović and V. Djoković, *Glycogen and gold nanoparticle bioconjugates: controlled plasmon resonance via glycogen-induced nanoparticle aggregation*, *RSC Advances,* 2013, **3**, 8705-8713.

(281) D. K. Božanić, S. Dimitrijević-Branković, N. Bibić, A. Luyt and V. Djoković, *Silver nanoparticles encapsulated in glycogen biopolymer: Morphology, optical and antimicrobial properties*, *Carbohydrate Polymers,* 2011, **83**, 883-890.

(282) R. Kandimalla, S. Dash, A. C. Bhowal, S. Kalita, N. C. Talukdar, S. Kundu and J. Kotoky, *Glycogen–gold nanohybrid escalates the potency of silymarin*, *International journal of nanomedicine,* 2017, **12**, 7025.

(283) J.-M. Oh, D.-H. Park and J.-H. Choy, *Integrated bio-inorganic hybrid systems for nano-forensics*, *Chemical Society Reviews,* 2011, **40**, 583-595.

(284) J. Le Bideau, L. Viau and A. Vioux, *Ionogels, ionic liquid based hybrid materials*, *Chemical Society Reviews,* 2011, **40**, 907-925.

(285) A. Leonard, P. Dandoy, E. Danloy, G. Leroux, C. F. Meunier, J. C. Rooke and B.-L. Su, *Whole-cell based hybrid materials for green energy*

production, environmental remediation and smart cell-therapy, *Chemical Society Reviews,* 2011, **40**, 860-885.

(286) H. Schmidt, *Considerations about the sol-gel process: From the classical sol-gel route to advanced chemical nanotechnologies*, *Journal of Sol-Gel Science and Technology,* 2006, **40**, 115.

(287) P. Gómez-Romero and C. Sanchez, *Hybrid materials, functional applications. An introduction*, *Functional hybrid materials,* 2004, 1-14.

(288) R. K. Gupta, E. Kennel and K.-J. Kim, *Polymer nanocomposites handbook*. CRC press: 2009.

(289) M. Guglielmi, G. Kickelbick and A. Martucci, *Sol-gel nanocomposites*. Springer: 2014.

(290) C. SANCHEZ, *Functional hybrid materials*, *Journal of material chemistry,* 2005, **15**.

(291) M. Zheludkevich, I. M. Salvado and M. Ferreira, *Sol–gel coatings for corrosion protection of metals*, *Journal of Materials Chemistry,* 2005, **15**, 5099-5111.

(292) D. Wang and G. P. Bierwagen, *Sol–gel coatings on metals for corrosion protection*, *Progress in Organic Coatings,* 2009, **64**, 327-338.

(293) G. Hernandez-Vargas, J. E. Sosa-Hernández, S. Saldarriaga-Hernandez, A. M. Villalba-Rodríguez, R. Parra-Saldivar and H. Iqbal, *Electrochemical biosensors: A solution to pollution detection with reference to environmental contaminants*, *Biosensors,* 2018, **8**, 29.

(294) T. Rasheed, M. Bilal, F. Nabeel, H. M. Iqbal, C. Li and Y. Zhou, *Fluorescent sensor based models for the detection of environmentally-related toxic heavy metals*, *Science of the Total Environment,* 2018, **615**, 476-485.

(295) T. Rasheed, C. Li, M. Bilal, C. Yu and H. M. Iqbal, *Potentially toxic elements and environmentally-related pollutants recognition using colorimetric and ratiometric fluorescent probes*, *Science of the Total Environment,* 2018, **640**, 174-193.

(296) A. D. McNaught and A. Wilkinson, *Compendium of chemical terminology*. Blackwell Science Oxford: 1997; Vol. 1669.

(297) Z. Li, Y. Zhang, Y. Su, P. Ouyang, J. Ge and Z. Liu, *Spatial co-localization of multi-enzymes by inorganic nanocrystal–protein complexes*, *Chemical Communications,* 2014, **50**, 12465-12468.

(298) M. Giovanni, M. I. Setyawati, C. Y. Tay, H. Qian, W. S. Kuan and D. T. Leong, *Electrochemical quantification of Escherichia coli with DNA nanostructure*, *Advanced Functional Materials,* 2015, **25**, 3840-3846.

(299) J. Ye, Y. Chen and Z. Liu, *A boronate affinity sandwich assay: an appealing alternative to immunoassays for the determination of glycoproteins*, *Angewandte Chemie International Edition,* 2014, **53**, 10386-10389.

(300) Y. Li, G. Xie, J. Qiu, D. Zhou, D. Gou, Y. Tao, Y. Li and H. Chen, *A new biosensor based on the recognition of phages and the signal amplification of organic-inorganic hybrid nanoflowers for discriminating*

and quantitating live pathogenic bacteria in urine, *Sensors and Actuators B: Chemical,* 2018, **258**, 803-812.

(301) R. Ye, C. Zhu, Y. Song, Q. Lu, X. Ge, X. Yang, M. J. Zhu, D. Du, H. Li and Y. Lin, *Bioinspired synthesis of all‐in‐one organic–inorganic hybrid nanoflowers combined with a handheld pH meter for on‐site detection of food pathogen*, *Small,* 2016, **12**, 3094-3100.

(302) Z. Zhang, Y. Zhang, R. Song, M. Wang, F. Yan, L. He, X. Feng, S. Fang, J. Zhao and H. Zhang, *Manganese (II) phosphate nanoflowers as electrochemical biosensors for the high-sensitivity detection of ractopamine*, *Sensors and Actuators B: Chemical,* 2015, **211**, 310-317.

(303) W. Li, S. Lu, S. Bao, Z. Shi, Z. Lu, C. Li and L. Yu, *Efficient in situ growth of enzyme-inorganic hybrids on paper strips for the visual detection of glucose*, *Biosensors and Bioelectronics,* 2018, **99**, 603-611.

(304) Y. Liu, G. Mao, W. Wang, S. Tian, X. Ji, M. Liu and Z. He, *In situ synthesis of photoluminescence-quenching nanopaper for rapid and robust detection of pathogens and proteins*, *Chemical Communications,* 2019, **55**, 2660-2663.

(305) X. Zhu, J. Huang, J. Liu, H. Zhang, J. Jiang and R. Yu, *A dual enzyme–inorganic hybrid nanoflower incorporated microfluidic paper-based analytic device (μPAD) biosensor for sensitive visualized detection of glucose*, *Nanoscale,* 2017, **9**, 5658-5663.

(306) J. Tian, Z. Zhao, A. Kumar, R. I. Boughton and H. Liu, *Recent progress in design, synthesis, and applications of one-dimensional TiO 2 nanostructured surface heterostructures: a review*, *Chemical Society Reviews,* 2014, **43**, 6920-6937.

(307) S. Zhang, R. Geryak, J. Geldmeier, S. Kim and V. V. Tsukruk, *Synthesis, assembly, and applications of hybrid nanostructures for biosensing*, *Chemical Reviews,* 2017, **117**, 12942-13038.

(308) T. Yaseen, H. Pu and D.-W. Sun, *Functionalization techniques for improving SERS substrates and their applications in food safety evaluation: A review of recent research trends*, *Trends in food science & technology,* 2018, **72**, 162-174.

(309) J. Chen, L. Guo, B. Qiu, Z. Lin and T. Wang, *Application of ordered nanoparticle self-assemblies in surface-enhanced spectroscopy*, *Materials Chemistry Frontiers,* 2018, **2**, 835-860.

(310) S. Schlücker, *Surface‐Enhanced raman spectroscopy: Concepts and chemical applications*, *Angewandte Chemie International Edition,* 2014, **53**, 4756-4795.

(311) Q. Yu, H. Liu and H. Chen, *Vertical SiNWAs for biomedical and biotechnology applications*, *Journal of Materials Chemistry B,* 2014, **2**, 7849-7860.

(312) M. F. Cardinal, E. Vander Ende, R. A. Hackler, M. O. McAnally, P. C. Stair, G. C. Schatz and R. P. Van Duyne, *Expanding applications of SERS through versatile nanomaterials engineering*, *Chemical Society Reviews,* 2017, **46**, 3886-3903.

(313) K. C. Grabar, R. G. Freeman, M. B. Hommer and M. J. Natan, *Preparation and characterization of Au colloid monolayers*, *Analytical Chemistry,* 1995, **67**, 735-743.

(314) Y. Chu, E. Schonbrun, T. Yang and K. B. Crozier, *Experimental observation of narrow surface plasmon resonances in gold nanoparticle arrays*, *Applied Physics Letters,* 2008, **93**, 181108.

(315) M. Suzuki, Y. Niidome, Y. Kuwahara, N. Terasaki, K. Inoue and S. Yamada, *Surface-enhanced nonresonance Raman scattering from size- and morphology-controlled gold nanoparticle films*, *The Journal of Physical Chemistry B,* 2004, **108**, 11660-11665.

(316) A. Wei, B. Kim, B. Sadtler and S. L. Tripp, *Tunable surface-enhanced Raman scattering from large gold nanoparticle arrays*, *ChemPhysChem,* 2001, **2**, 743-745.

(317) N. Félidj, J. Aubard, G. Lévi, J. R. Krenn, G. Schider, A. Leitner and F. Aussenegg, *Enhanced substrate-induced coupling in two-dimensional gold nanoparticle arrays*, *Physical review B,* 2002, **66**, 245407.

(318) M. K. Oh, S. Yun, S. K. Kim and S. Park, *Effect of layer structures of gold nanoparticle films on surface enhanced Raman scattering*, *Analytica Chimica Acta,* 2009, **649**, 111-116.

(319) A. Foti, C. D'Andrea, V. Villari, N. Micali, M. G. Donato, B. Fazio, O. M. Maragò, R. Gillibert, M. Lamy de la Chapelle and P. G. Gucciardi, *Optical aggregation of gold nanoparticles for SERS detection of proteins and toxins in liquid environment: Towards ultrasensitive and selective detection*, *Materials,* 2018, **11**, 440.

(320) M. Shorie, V. Kumar, H. Kaur, K. Singh, V. K. Tomer and P. Sabherwal, *Plasmonic DNA hotspots made from tungsten disulfide nanosheets and gold nanoparticles for ultrasensitive aptamer-based SERS detection of myoglobin*, *Microchimica Acta,* 2018, **185**, 158.

(321) X. Ma, X. Xu, Y. Xia and Z. Wang, *SERS aptasensor for Salmonella typhimurium detection based on spiny gold nanoparticles*, *Food Control,* 2018, **84**, 232-237.

(322) M. Ma, J. Sun, Y. Chen, K. Wen, Z. Wang, J. Shen, S. Zhang, Y. Ke and Z. Wang, *Highly sensitive SERS immunosensor for the detection of amantadine in chicken based on flower-like gold nanoparticles and magnetic bead separation*, *Food and Chemical Toxicology,* 2018, **118**, 589-594.

(323) L. A. Wali, K. K. Hasan and A. M. Alwan, *Rapid and highly efficient detection of ultra-low concentration of penicillin G by gold nanoparticles/porous silicon SERS active substrate*, *Spectrochimica Acta Part A: Molecular and Biomolecular Spectroscopy,* 2019, **206**, 31-36.

(324) S. Zhang, A. Garcia-D'Angeli, J. P. Brennan and Q. Huo, *Predicting detection limits of enzyme-linked immunosorbent assay (ELISA) and bioanalytical techniques in general*, *Analyst,* 2014, **139**, 439-445.

(325) S. Y. Toh, M. Citartan, S. C. Gopinath and T.-H. Tang, *Aptamers as a replacement for antibodies in enzyme-linked immunosorbent assay*, *Biosensors and Bioelectronics,* 2015, **64**, 392-403.

(326) F. Zhou, L. Yuan, H. Wang, D. Li and H. Chen, *Gold nanoparticle layer: a promising platform for ultra-sensitive cancer detection*, *Langmuir,* 2011, **27**, 2155-2158.

(327) F. Zhou, M. Wang, L. Yuan, Z. Cheng, Z. Wu and H. Chen, *Sensitive sandwich ELISA based on a gold nanoparticle layer for cancer detection*, *Analyst,* 2012, **137**, 1779-1784.

(328) L. Wang, Q. Xiong, F. Xiao and H. Duan, *2D nanomaterials based electrochemical biosensors for cancer diagnosis*, *Biosensors and Bioelectronics,* 2017, **89**, 136-151.

(329) L. Rotariu, F. Lagarde, N. Jaffrezic-Renault and C. Bala, *Electrochemical biosensors for fast detection of food contaminants–trends and perspective*, *TRAC Trends in Analytical Chemistry,* 2016, **79**, 80-87.

(330) D. Grieshaber, R. MacKenzie, J. Vörös and E. Reimhult, *Electrochemical biosensors-sensor principles and architectures*, *Sensors,* 2008, **8**, 1400-1458.

(331) Y. Song, Y. Luo, C. Zhu, H. Li, D. Du and Y. Lin, *Recent advances in electrochemical biosensors based on graphene two-dimensional nanomaterials*, *Biosensors and Bioelectronics,* 2016, **76**, 195-212.

(332) S. Guo and E. Wang, *Synthesis and electrochemical applications of gold nanoparticles*, *Analytica Chimica Acta,* 2007, **598**, 181-192.

(333) X. Luo, A. Morrin, A. J. Killard and M. R. Smyth, *Application of nanoparticles in electrochemical sensors and biosensors*, *Electroanalysis: An International Journal Devoted to Fundamental and Practical Aspects of Electroanalysis,* 2006, **18**, 319-326.

(334) L.-P. Lu, S.-Q. Wang and X.-Q. Lin, *Fabrication of layer-by-layer deposited multilayer films containing DNA and gold nanoparticle for norepinephrine biosensor*, *Analytica Chimica Acta,* 2004, **519**, 161-166.

(335) B.-Y. Wu, S.-H. Hou, F. Yin, J. Li, Z.-X. Zhao, J.-D. Huang and Q. Chen, *Amperometric glucose biosensor based on layer-by-layer assembly of multilayer films composed of chitosan, gold nanoparticles and glucose oxidase modified Pt electrode*, *Biosensors and Bioelectronics,* 2007, **22**, 838-844.

(336) B.-Y. Wu, S.-H. Hou, F. Yin, Z.-X. Zhao, Y.-Y. Wang, X.-S. Wang and Q. Chen, *Amperometric glucose biosensor based on multilayer films via layer-by-layer self-assembly of multi-wall carbon nanotubes, gold nanoparticles and glucose oxidase on the Pt electrode*, *Biosensors and Bioelectronics,* 2007, **22**, 2854-2860.

(337) G. Jie, B. Liu, H. Pan, J.-J. Zhu and H.-Y. Chen, *CdS nanocrystal-based electrochemiluminescence biosensor for the detection of low-density lipoprotein by increasing sensitivity with gold nanoparticle amplification*, *Analytical Chemistry,* 2007, **79**, 5574-5581.

(338) R. Chai, R. Yuan, Y. Chai, C. Ou, S. Cao and X. Li, *Amperometric immunosensors based on layer-by-layer assembly of gold nanoparticles and methylene blue on thiourea modified glassy carbon electrode for determination of human chorionic gonadotrophin*, *Talanta,* 2008, **74**, 1330-1336.
(339) C.-Y. Tsai, T.-L. Chang, C.-C. Chen, F.-H. Ko and P.-H. Chen, *An ultra sensitive DNA detection by using gold nanoparticle multilayer in nano-gap electrodes*, *Microelectronic Engineering,* 2005, **78**, 546-555.
(340) X.-L. Luo, J.-J. Xu, Q. Zhang, G.-J. Yang and H.-Y. Chen, *Electrochemically deposited chitosan hydrogel for horseradish peroxidase immobilization through gold nanoparticles self-assembly*, *Biosensors and Bioelectronics,* 2005, **21**, 190-196.
(341) Y. Du, X.-L. Luo, J.-J. Xu and H.-Y. Chen, *A simple method to fabricate a chitosan-gold nanoparticles film and its application in glucose biosensor*, *Bioelectrochemistry,* 2007, **70**, 342-347.
(342) Y. Wang, W. Wei, X. Liu and X. Zeng, *Carbon nanotube/chitosan/gold nanoparticles-based glucose biosensor prepared by a layer-by-layer technique*, *Materials Science and Engineering: C,* 2009, **29**, 50-54.
(343) O. Shulga and J. R. Kirchhoff, *An acetylcholinesterase enzyme electrode stabilized by an electrodeposited gold nanoparticle layer*, *Electrochemistry Communications,* 2007, **9**, 935-940.

Chapter 2

Experimental Details

Chapter 2 reports the materials, methods, instruments, techniques and other experimental details used in this thesis.

2.1 Cobalt Phosphate Nanostructures for Non-Enzymatic Glucose Sensing at Physiological pH

2.1.1 Reagents and chemicals

Cobalt(II) nitrate hexahydrate ($Co(NO_3)_2 \cdot 6H_2O$, ≥97%, CAS no. 10026-22-9) was purchased from Baker. PBS tablets, Nafion 117 solution (CAS no. 31175-20-9), cobalt(II) phosphate hydrate ($Co_3(PO_4)_2 \cdot xH_2O$, CAS no. 10294-50- 5), potassium ferricyanide(III) ($K_3Fe(CN)_6$, CAS no. 13746-66-2), and HS from human male AB plasma were purchased from Sigma-Aldrich. D-Glucose (CAS no. 50-99-7) was purchased from AnalR. Potassium chloride (KCl, CAS no. 7440-09-7) was purchased from Chem-Supply. All the chemicals were used as received. High-purity (Milli-Q) water with a resistivity of 18.2 MΩ cm was obtained from an inline Millipore RiOs/origin water purification system.

2.1.2 Instrumentation

X-ray photoelectron spectroscopy (XPS) spectra were acquired using an Axis Ultra X-ray photoelectron spectrometer (Kratos Analytical, UK), equipped with a 165 mm concentric hemispherical electron energy analyzer and a monochro- mated Al Kα incident X-ray source (1486.6 eV). Survey (wide) scans were recorded in the binding energy range of 0−1200 eV, with 1.0 eV steps, a dwell time of 100 ms, and an analyzer pass energy of 160 eV. Multiplex (narrow) high-resolution spectra were recorded with a pass energy of 20 eV, 0.05 eV steps, and a dwell time of 250 ms, resulting in an energy resolution (ΔE/E) of ~300 meV. The base pressure in the analysis chamber during data collection was 1−2 × 10^{-9} mbar, and these data were processed using the software CasaXPS. All binding energies were calibrated using the C 1s level of adventitious carbon at 285.0 eV. Fourier transform infrared (FTIR) spectra were obtained on a TENSOR II (Bruker) attenuated total reflectance FTIR (ATR−FTIR) spectrometer and analyzed using the software OPUS 7.8. The number of scans was 64. A minimum resolution of 4 cm^{-1} and the absorbance/transmittance mode were used. Scanning electron microscopy (SEM) images were obtained on a Teneo VolumeScope (FEI) microscope. Transmission electron microscopy (TEM) was conducted on a Tecnai Spirit (FEI) microscope operating at 120 kV. Energy-dispersive X-ray spectroscopy (EDX) was performed on a 20 mm^2 X-Max SDD instrument (Oxford Instruments) equipped with the software AZtec 3.2. X-ray diffraction (XRD) data were collected using a D8 ADVANCE X-ray diffractometer (Bruker) with Ni-filtered Cu Kα radiation (1.54 Å). Data were collected between 5° and 85° 2θ, with a step size of 0.02° and a scan rate of 1.0 s per step. An anti- scatter blade was used to reduce the diffracted background intensity at low angles. An incident beam divergence of 1.0° was used with a 2.5° soller slit in the diffracted beam. The sample was spun at 15 rpm. Generally, unless otherwise specified, the data from the characterizations were exported to the software OriginPro 8.5 for further analysis.

2.1.3 Synthesis of CPNs

An aqueous $Co(NO_3)_2 \cdot 6H_2O$ solution (100 μL, 1.2M) was added to PBS (20mL, 1mM, pH7.4) in a 50mL tube with simultaneous vortexing, which was continued for 5 s after addition, followed by static incubation at 23 °C overnight. For the scale-up of the synthesis, an aqueous $Co(NO_3)_2 \cdot 6H_2O$ solution (10 mL, 1.2 M) was added to PBS (2 L, 1 mM, pH 7.4) in a 2 L glass beaker with vigorous stirring, which was continued for 5 s after addition, followed by static aging at 23 °C overnight. The precipitate was then collected, washed 5 times by centrifugation (67g, 5 min) and resuspension in water, and finally resuspended in water (40 mL) and stored at 4 °C for further characterization. SEM and TEM samples were prepared by dropcasting the aqueous suspension on a silicon wafer and a carbon grid, respectively, followed by drying in air. XPS, XRD, and FTIR samples were prepared by drying the aqueous suspension in a vacuum desiccator prior to analysis.

2.1.4 Electrode preparation

A glassy carbon electrode (GCE, 3 mm in diameter) was first polished with a 0.05 µm alumina slurry. The polished GCE was then rinsed with water and ethanol, and allowed to dry in air. A CPN suspension (10 mg/mL) in 10% (v/v) Nafion in ethanol was prepared and vortexed to obtain a homogeneous suspension. On the center of the GCE, the prepared suspension (10 µL) was dropcasted and allowed to dry in air. Similarly, a screen- printed electrode (SPE, 3 mm in diameter) was modified by dropcasting a 10 mg/mL CPN suspension (10 µL) in 10% (v/v) Nafion in water and allowed to dry in air. A total mass of 0.1 mg of CPNs was deposited on the GCE or SPE to achieve complete surface coverage of the working electrode (WE). A bare GCE electrode for control measurements was prepared following the aforementioned procedure without the use of CPNs, thereby resulting in an electrode coated with Nafion only. For comparison, GCE was also modified with $Co_3(PO_4)_2$ powder following the aforementioned protocol. Graphite SPE chips that were produced in the Laboratory of Biosensors and Nanomachines at the University of Rome, Tor Vergata, were used. Briefly, the electrodes were printed using a 245 DEK (Weymouth, UK) screen-printing machine and graphite- (LOCTITE EDAG PF-407A) and silver-based (LOCTITE EDAG PF-410) conductive inks and a gray dielectric paste insulating ink. The inks were printed on a polyester flexible film (Autostat HT5). Each graphite SPE chip contained three separate printed portions that served as the working (carbon-based ink), the reference (silver-based ink), and the counter electrode (CE) (carbon-based ink). The diameter of the WE was 3 mm, which resulted in an apparent geometric area of 7.07 mm^2.

2.1.5 Electrochemical measurements

Cyclic voltammetry (CV) and chronoamperometry (CA) measurements were performed on a MM510 potentiostat/galvanostat (Materials Mates Italia S.r.l.) using the software VoltaScope 5.4. Electrochemical measurements involving the GCE were conducted in a three-electrode electrochemical cell composed of a glassy carbon WE (3 mm diameter), a platinum wire as the CE, and a Ag/AgCl reference electrode (RE). Electrochemical measurements involving the SPE were performed on the SPE described above. The supporting electrolyte, unless specified otherwise, was a N_2-saturated 10 mM PBS solution (pH 7.4) that was thoroughly mixed by a magnetic stirrer. The pH of the electrolyte was adjusted, when needed, with 1 M NaOH solution.

2.1.6 Computational details

The X-ray crystal structure of $Co_3(PO_4)_2$ was obtained based on the most likely cobalt phosphate stoichiometry determined from the XRD pattern of the CPNs and cleaved to form the (100), (111), and (211) surfaces. For the (111) and (211) surfaces, oxygen positions were adjusted to preserve the tetrahedral phosphate geometry. Each slab consisted of two layers, with x × y dimensions of 16.72 × 8.79, 9.77 × 12.13, and 17.47 × 12.13 Å^2 for the (100), (111), and (211) surfaces, respectively. Increasing the number of layers or replicating the unit cell in the x or y dimension did not affect the Glu binding energies significantly. A vacuum spacer of at least 20 Å in the z-direction was added, and the model surfaces were subsequently relaxed, generating surface structures corresponding to different possibilities of surface cobalt coordination. Following surface relaxation, the geometry of the bottom layer of the slabs was frozen for the surface−Glu binding energy calculations. For the free Glu structural optimization, a single Glu molecule was placed in the center of a 20 × 20 × 20 Å^3 box, and only the gamma point was sampled. For the adsorption calculations, a variety of initial orientations of Glu on the relaxed surfaces were constructed, with an O1(Glu)−cobalt initial distance of ~2.5 Å. All calculations were performed using the Vienna Ab initio simulation package and the generalized gradient approximation (GGA) Perdew−Burke−Ernzerhof exchange correlation functional. The projector augmented wave (PAW) method was used with the Blöchl all-electron, frozen-core PAW pseudopotentials. A 5 × 5 × 1 Monkhorst−Pack k-point mesh for sampling the Brillouin zone and a cutoff energy of 500 eV were applied, and spin polarization was included. A dipole correction was applied to minimize polarization effects because of slab asymmetry. The Hubbard U parameter (GGA + U) for the electron correlation of the d states in cobalt ions was used with a value of 3.5 eV. A convergence criterion of 0.01 eV/Å was employed for the geometry optimizations.

2.2 Enzyme-Mimicking Hybrid Nanoflowers Enables Sensing of Bio-analytes

2.2.1 Materials

Copper sulfate (7758-99-8), phosphate buffered saline tablets, dextran sulfate (9011-18-1), hydrochloric acid (7647-01-0), sodium hydroxide (1310-73-2), o-phenylenediamine (95-54-5), hydrogen peroxide (7722-84-1), glucose oxidase from Aspergillus Niger (9001-37-0), glucose (50-99-7) and Corning 96 well TC-treated plates were purchased from Sigma Aldrich.

The CAS number for each chemical was reported in brackets. All the chemicals were used as received. High-purity (Milli-Q) water with a resistivity of 18.2 MΩ cm was obtained from an inline Millipore RiOs/origin water purification system.

2.2.2 Synthesis of dextran sulfate-copper phosphate nanoflowers

In a typical synthesis of hybrid Dextran Sulfate-copper phosphate nanoflowers (D-NF), 500 µL of phosphate buffered saline (PBS, 1 X, pH 7.4) with a dextran sulfate (DS) concentration of 1 mg mL^{-1} was quickly added under vortex mixing to 100 µL of a $CuSO_4$ aqueous solution (120 mM) in a 2.2 mL PS vial. The solution was then mixed by vortex for 60 s and subsequently incubated statically overnight at room temperature (25 °C). At 30 min of incubation, the solution turned from transparent to opaque, indicating the nucleation and growth of micrometre-sized nanoflowers. After overnight incubation, the blue precipitate was washed via centrifugation and re-suspension with water for at least five times, then dried under vacuum at room temperature. To study the reaction synthetic parameters, nanoflowers preparations were carried systematically changing one variable at a time, namely PBS, DS, $CuSO_4$ concentrations and pH. The final chemical concentrations of a 1 X PBS solution is defined as 137 mM NaCl, 10 mM Na_2HPO_4/NaH_2PO_4, and 2.7 mM KCl at pH 7.4.

2.2.3 Characterization of hybrid nanoflowers

Transmission electron microscopy (TEM) images were acquired using a Tecnai Spirit (FEI, USA) instrument with an operating voltage of 120 kV. Scanning electron microscopy (SEM) images and energy-dispersive X-ray spectroscopy (EDX) spectra and mapping were acquired with a FlexSEM 1000 (Hitachi, Japan) benchtop SEM equipped with a Quantax 80 (Bruker, USA) EDX system. Typically, images and spectra of uncoated samples were recorded using a beam voltage of 15 kV, operating in SEM pressure mode and with an acquisition time of 5 min. Attenuated total reflectance Fourier-transform infrared spectroscopy (ATR-FTIR) spectra were obtained on a TENSOR II (Bruker) ATR−FTIR spectrometer and analyzed using the software OPUS 7.8. The number of scans was 64 with a minimum resolution of 4 cm^{-1}. The fluorescence emission and excitation spectra were recorded on a Infinite M200 microplate reader (Tecan, Switzerland) spectrophotometer and analysed using the software i-control. The samples for X-ray diffraction (XRD) analysis were ground in a mortar and pestle under ethanol, smeared onto a glass slide, allowed to dry overnight in air and then analysed as a randomly orientated sample. Diffraction data were collected using a Bruker D8 Advance X-ray diffractometer with Ni-filtered Cu kα radiation (1.54 Å). Data were collected between 5 and 85° 2θ, with a step size of 0.02° and a scan rate of 1.0 s per step. An anti-scatter blade was used to reduce the diffracted background intensity at low angles. An incident beam divergence of 1.0° was used with a 2.5° soller slit in the diffracted beam. The sample was spun at 15 revolutions per minute. Phase identification was completed using Diffrac.EVA V4.1 software with the ICDD PDF4+ 2018 database. Thermal gravimetric analysis (TGA) was performed using an alumina crucible in a TGA Netzsch TG 209F1 Libra at a heating rate of 4 °C min^{-1} from 30 to 600 °C in air.

2.2.4 Preparation of D-NF functionalized microreactors

To prepare a 96 well plate coated with D-NF, a similar synthetic procedure described for the preparation of D-NF was executed. In a 15 mL PS vial, 5000 µL of phosphate buffered saline (PBS, 1X pH 7.4) with a dextran sulfate (DS) concentration of 1 mg mL^{-1} was quickly added under vortex mixing to 1000 µL of a $CuSO_4$ aqueous solution (240 mM), continuing then the mixing by vortex for 60 s. Solution aliquots (300 µL) were then added to each well of a 96 well plate and subsequently incubated statically overnight at room temperature (25 °C). The functionalized wells were washed rinsing with water and stored under water at room temperature (25 °C) until further use.

2.2.5 Catalytic activity and H_2O_2 sensing

The non-enzymatic peroxidase-like activity of the hybrid nanoflowers was studied using OPD as substrate. In each D-NF coated well, 100 µL of OPD solution (0.3 mM), 100 µL of PBS (3X pH 6.5) and 100 µL of H_2O_2 (15 mM) were incubated under gentle mixing, recording the solution fluorescence emission intensity in real-time every 5 min for a total of 45 min. Fluorescence emission intensities at 566 nm were recorded using an excitation wavelength of 410 nm. There was no need to separate the nanoflowers from the solution since the catalytic substrate remained attached to the bottom of the well during the reaction. H_2O_2 detection was performed in the same experimental conditions as described before varying the final H_2O_2 concentration from 0 to 7 mM. For control experiments, solutions composed of a) OPD in PBS with the presence of D-NF and b) OPD and H_2O_2 in PBS without the presence of D-NF were incubated as previously described and their fluorescence emissions recorded over time.

2.2.6 Glucose detection via hybrid cascade reaction

The detection of glucose was performed in 96 D-NF coated well plate. In each well, 100 µL of OPD solution (0.3 mM), 100 µL of PBS (3X pH 6.5) with different concentrations of glucose and 100 µL of glucose oxidase (100 U mL^{-1}) were incubated under gentle mixing at 37 °C. After 120 min of incubation, the solutions fluorescence emission intensities at 536 nm were recorded using an excitation wavelength of 444 nm.

2.3 Nanoengineering Multifunctional Hybrid Interfaces Using Adhesive Glycogen Nanoparticles

2.3.1 Materials

Phytoglycogen derived from sweet corn (PG) was purchased from Glysantis. Acetic acid glacial, anhydrous dimethyl sulfoxide (DMSO) (≥99.9%), ammonium molybdate, β-amylase from barley, copper(II) sulfate pentahydrate, crystal violet (CV), deuterium oxide, dialysis tubing cellulose membrane (14 kDa cutoff), fetal bovine serum, glutathione (GSH), gold(III) chloride hydrate, hydrochloric acid, lipoic acid (LA), methylene blue, nitric acid, Parafilm M, phosphate buffered saline (PBS) tablets, platinum nanopowder (<50 nm), polyethylene terephthalate (PET) film, polymethylmethacrylate (PMMA) film, polypropylene (PP) film, polystyrene (PS) film, PTFE film, AgNPs (20 nm), sodium acetate, sodium arsenate dibasic pentahydrate, sodium bicarbonate, sodium borohydride, sodium carbonate, sodium citrate, sodium dodecyl sulfate (SDS), sodium potassium tartrate tetrahydrate, sodium sulfate, sulfuric acid, thiazolyl blue tetrazolium bromide (MTT), and *N*-(3-dimethylaminopropyl)-*N′*-ethylcarbodiimide hydrochloride (EDC-HCl) were purchased from Sigma-Aldrich. Cover glass slips were purchased from Knittel Glass. PMMA slides were purchased from Caplugs Evergreen. 4-(Dimethylamino)pyridine (DMAP) was purchased from Fluka. Alexa Fluor 488 NHS Ester and Dulbecco's modified Eagle medium were purchased from Thermo Fisher Scientific. Dodecanoic acid was purchased from Alfa Aesar. Hydrogen peroxide, ethanol (EtOH), and *n*-hexane were purchased from Chem-Supply. A PS particle suspension (3.2 μm) was purchased from MicroParticles. PP conical tubes (15 mL) were purchased from Corning. Nickel foam was purchased from American Elements. PS cuvettes were purchased from Greiner Bio-One. PTFE and polyurethane tubes were purchased from ATA Scientific. All the chemicals were used as received. High-purity (Milli-Q) water with a resistivity of 18.2 MΩ cm was obtained from an inline Millipore RiOs/origin water purification system.

2.3.2 Synthesis and materials preparation

2.3.2.1 Synthesis of L-PG

To modify PG with a degree of functionalization of 2% (LA/glucose mol/mol), PG (200 mg, 1.23 mmol glucose unit) was dissolved in 8 mL anhydrous DMSO under an inert atmosphere of nitrogen. LA (30.6 mg, 0.12 eq.), DMAP (45.2 mg, 0.3 eq.), and EDC-HCl (28.4 mg, 0.12 eq.), each dissolved in 4 mL anhydrous DMSO, were sequentially added dropwise to the above solution under stirring. The system was allowed to react for 72 h under nitrogen gas flux. Then, HCl (1.2 M, 0.31 mL, 0.3 eq.) was slowly added to neutralize DMAP. The product was purified by dialysis (14 kDa cutoff) against acidic Milli-Q water (2 L, pH 4 using HCl) for 2 days and neutral Milli-Q water for one day, and freeze-dried to finally obtain L-PG (yield 180 mg, 90%). The degree of functionalization of modified glycogen was determined by NMR spectroscopy. ^{1}H-NMR (400 MHz, D_2O, 50 °C) δ (ppm): 5.36 (0.98, H-aα), 4.97 (0.02, H-aβ), 4.30–3.32 (6.53, H-b, c, d, e, f), 3.31–3.20 (0.02, H-k, m), 2.62–2.4 (0.07, H-g), 2.08–1.94 (0.03, H-l), 1.87–1.19 (0.13, H-h, i, j). The degree of functionalization was calculated by dividing the peaks integral relative to the lipoate peaks (δ (ppm): 3.31–1.19) by the peaks integral of H-aα and H-aβ (δ (ppm): 5.60–4.80) to 100.

2.3.2.2 Preparation of fluorescent labeled L-PG

Lipoate-conjugated phytoglycogen (L-PG; 2 mg) was dispersed in carbonate buffer (1 mL, 10 mM, pH 9.2). To this dispersion, AF488NHS solution (30 µL, 1 mg $\mathrm{mL^{-1}}$ in dimethyl sulfoxide (DMSO)) was added and the resulting solution was mixed overnight. Excess fluorophore was removed using an illustra Nap 10 Sephadex column (GE Healthcare Life Sciences), and the resulting product was freeze-dried to generate L-PG@AF488.

2.3.2.3 Synthesis of dodecane-conjugated phytoglycogen (DD-PG)

DD-PG was prepared using the same synthesis procedure as that used for preparing L-PG, with the exception that dodecanoic acid (0.06 eq.) was used instead of lipoic acid. The degree of functionalization of modified glycogen, as determined by NMR spectroscopy, was 1% (dodecanoic moieties/glucose mol/mol).

2.3.2.4 Synthesis of gold nanoparticles (AuNPs)

AuNPs of 14 nm in diameter were prepared by citrate reduction of $HAuCl_4$ in aqueous phase. Typically, a sodium citrate (102 mg) water solution (2 mL) was rapidly injected into a boiling aqueous $HAuCl_4$ solution (30 mg in 200 mL water) under vigorous stirring. After boiling for 15 min, the solution was cooled to room temperature. The colloidal suspension was stored at 4 °C in the dark until further use.

2.3.2.5 Preparation of L-PG metal nanoparticle hybrid coatings on glass

Circular glass substrates (diameter of 10 mm) were functionalized with L-PG and Au, Ag and Pt metal nanoparticles. First, the substrates were cleaned with EtOH and water and placed on a planar surface. To prepare the first layer, an L-PG dispersion (0.4 mL, 0.1 mg mL^{-1}) was deposited on the glass. After incubation for 10 min, the glass was rinsed with water. To prepare the second layer of metal nanoparticles, 0.4 mL of a Au (0.06 mg mL^{-1}), Ag (0.02 mg mL^{-1}), or Pt (0.1 mg mL^{-1}) colloidal dispersion was added and the system was incubated for another 10 min. The glass was then washed with water to obtain one bilayer on one side of the substrate. To prepare multilayered or multi-elements systems, the process was repeated as many times as required with the appropriate metal nanoparticles. When the appropriate number of bilayers was obtained, the glass was dried with a N_2 gun. For control experiments, unmodified PG was used with AuNPs following the abovementioned procedure. The glass substrates were directly incubated with AuNPs in the absence of L-PG following the same procedure.

2.3.2.6 Preparation of PS microparticles coated with L-PG and AuNPs

A dispersion of 3.2 µm PS particles (0.3 mL, 1 mg mL^{-1}) was washed via centrifugation and redispersion with water three times (2000 rcf, 2 min). After each centrifugation, sonication in an ultrasound bath was performed for 5 s to disperse the particles in solution. During the last wash, the dispersion was diluted with water to 0.3 mL and added via pipetting to an L-PG solution (0.2 mL, 0.1 mg mL^{-1}). After gentle mixing for 3 min, a further three washes as previously described were performed. In the last wash, the dispersion was diluted to 0.3 mL to obtain a 1 mg mL^{-1} L-PG-coated PS microparticle dispersion. To this dispersion, 0.5 mL of AuNP colloidal suspension was added by pipetting and the solution was gently mixed for 3 min. The colloidal dispersion was then washed three times as previously described and finally diluted to 0.3 mL to obtain a 1 mg mL^{-1} PS microparticles coated with one L-PG/AuNP bilayer. The assembly cycle was repeated as many times as required, with the last layer composed of AuNP after each cycle.

2.3.2.7 Preparation of inner-coated PP tubes with L-PG and AuNPs

To prepare an inner-coated 15 mL PP tube via layer-by-layer (LbL) assembly, an L-PG solution (2 mL, 0.1 mg mL^{-1}) was introduced into the PP tube and vortexed for 3 min, followed by washing with water. Then, a AuNP colloidal suspension (2 mL, 0.06 mg mL^{-1}) was introduced into the tube, vortexed for 3 min, and washed with water, producing a 1-bilayer inner-coated PP tube. To obtain systems with more bilayers, the steps were repeated several times as required. The obtained functionalized vials were used fresh for the catalysis experiments.

2.3.3 Instrumentation

Attenuated total reflectance Fourier transform infrared (ATR-FTIR) spectra were obtained on a TENSOR II (Bruker) ATR−FTIR spectrometer. UV–vis absorbance spectra were recorded on a SPECORD 250 PLUS (Analytik Jena, Germany) spectrophotometer or an Infinite M200 microplate reader (Tecan, Switzerland). Dynamic light scattering (DLS) hydrodynamic diameter and ζ-potential were measured using a Zetasizer Nano-ZS instrument (Malvern Instruments, Malvern, UK). Atomic force microscopy (AFM) experiments were performed on a JPK NanoWizard II BioAFM instrument. Contact angle experiments were performed on an optical contact angle tensiometer (DataPhysics) using the sessile drop method. Cell viability was evaluated via a standard MTT assay protocol using MDA-MB-231 cells. The rate of glycogen particle degradation by β-amylase was determined using the Somogyi–Nelson assay. The chemical stability of the L-PG coatings was studied via fluorescence analysis using a Fluorolog spectrofluorometer (Jobin Yvon Horiba). Quartz crystal microbalance with dissipation (QCM-D) experiments were performed using a QSense E4 (Biolin Scientific, Sweden) equipped with gold sensor chips (QSX 301 Gold, Biolin Scientific). Differential interference contrast (DIC) microscopy images were recorded using an inverted Olympus IX71 microscope. TEM images were acquired using a Tecnai Spirit (FEI, USA) instrument with an operation voltage of 120 kV. SEM images and EDX spectra and mapping were acquired with a FlexSEM 1000 (Hitachi, Japan) benchtop scanning electron microscope equipped with a Quantax 80 (Bruker, USA) EDX system. Helium ion microscopy images were recorded on an ORION NanoFab (Zeiss, Peabody, USA) using a 25 keV He^+ probe with a current of 0.3 pA. SERS analysis was conducted on a RENISHAW Raman microscope equipped with a He−Ne laser operating at 532 nm.

2.3.4 Characterization

2.3.4.1 Attenuated total reflectance Fourier transform infrared (ATR-FTIR) spectroscopy

ATR-FTIR spectra were obtained on a TENSOR II ATR−FTIR spectrometer (Bruker) and analyzed using the software OPUS 7.8. The number of scans was 64 with a minimum resolution of 4 cm^{-1}.

2.3.4.2 UV–Vis spectroscopy

UV–Vis absorbance spectra were recorded on a SPECORD 250 PLUS spectrophotometer (Analytik Jena, Germany) and analyzed using the software Aspect UV. Solid and liquid samples spectra were recorded using, respectively, a solid sample holder and a reduced volume quartz cuvette with a path length of 1 cm mounted on a standard cell holder. Spectra were acquired with a scan speed of 20 nm s^{-1}. The spectra of PG and L-PG were recorded using a 1 mg mL^{-1} water dispersion.

2.3.4.3 Dynamic light scattering (DLS): hydrodynamic diameter and ζ-potential

The hydrodynamic diameter and ζ-potential of the nanoparticles were measured using a Zetasizer Nano-ZS instrument (Malvern Instruments, Malvern, UK) equipped with a He–Ne ion laser (λ = 633 nm). To evaluate the hydrodynamic diameter based on the scattered intensity, an L-PG or PG suspension (0.1 mL, 1 mg mL^{-1} in water) was analyzed in a micro cuvette (ZEN0040, Malvern Instruments). To evaluate the ζ-potential, a particle suspension (0.8 mL, 3 mg mL^{-1}) in PBS (0.1×, pH 7.4) was analyzed in a capillary cell (DTS1070, Malvern Instruments).

The analysis was performed using a standard operation procedure with automatic attenuation and measurement position, executing 5 runs consisting of at least 10 acquisitions for each sample.

2.3.4.4 Atomic force microscopy (AFM)

AFM experiments were performed on a JPK NanoWizard II BioAFM instrument. Images were obtained in tapping mode using Tap300-G (BudgetSensors, Bulgaria) monolithic silicon cantilevers with a spring constant and resonance frequency of about 40 N m^{-1} and 300 kHz, respectively. For the analysis of single particles, an L-PG aqueous dispersion (40 µL, 1 µg mL^{-1}) was incubated on a freshly gold-sputtered mica substrate (20 nm gold layer) for 60 min, extensively washed with water, and dried with a N_2 gun. Height and thickness values were averaged over 250 single nanoparticles. For the thickness and roughness analysis of the films, glass substrates were first cleaned with EtOH and water and then completely immersed in a 0.1 mg mL^{-1} PG, DD-PG or L-PG solution for 10 min. The glass slides were then rinsed with water several times to remove all excess and unbound polymer, and dried with a N_2 gun to obtain PG-, DD-PG- or L-PG-functionalized glass substrates. Scratches were made using a metallic doctor blade. Films thicknesses and roughness were analyzed (at least 20 different profiles for each sample) using the JPK SPM image processing software.

2.3.4.5 Contact angle measurements

For the contact angle measurements, substrates were incubated in a 0.1 mg mL^{-1} L-PG or PG water solution for 30 min at 21 °C, then rinsed with water to remove excess polymer. Excess water was removed by blowing the sample with a N_2 gun. Uncoated substrates were used as the control. Contact angle experiments were performed using H_2O (3 µL) at 21 °C on an optical contact angle tensiometer (DataPhysics) using the sessile drop method. The substrates were placed in the contact angle instrument window analysis. The drop shape was fitted using the elliptic method. The contact angle values and standard deviations were calculated based on the left and right contact angles of at least 15 different drops per sample.

2.3.4.6 Cytotoxicity assay

Cell viability was evaluated via a standard thiazolyl blue tetrazolium bromide (MTT) assay protocol. Cells (MDA-MB-231) were plated on a 96-well plate (Costar 3596, Corning, USA) with a seeding density of 10^4 cells per well in Dulbecco's modified Eagle medium (100 µL) with 10% fetal bovine serum. After 24 h, L-PG nanoparticles were added to the culture media (final concentrations as reported) and the systems were incubated for 24 h. Then, MTT reagent was added and after 4 h, the resulting formazan crystals were dissolved in DMSO. The cell viability was determined by absorbance measurements at 554 and 670 nm (as reference) with an Infinite M200 microplate reader (Tecan, Switzerland).

2.3.4.7 Degradation of PG and L-PG nanoparticles by β-amylase

The rate of glycogen particle hydrolysis by β-amylase was determined using the Somogyi–Nelson assay adjusted for a microtiter plate.[1] For the assay, a PG or L-PG solution (25 µL, 2 mg mL^{-1}) in 16 mM sodium acetate buffer (pH 4.8) was treated with β-amylase solution in H_2O (25 µL, 1 U mg^{-1}) for 20 min, 1 h, 2 h, or 24 h on a 96-well plate (Costar 3596, Corning, MA, USA); the experiments were performed in triplicates. After the incubation, the working solution was added (50 µL), the plate was covered and heated in a water bath at 95 °C for 20 min. Then, the plate was cooled to room temperature, and the arsenomolybdate color reagent was added (50 µL) into each well, followed by incubation for 1.5 h for complete color development. The absorbance was measured at 750 nm with an Infinite M200 microplate reader. To prepare the working solution, sodium potassium tartrate tetrahydrate (1.2 g), sodium carbonate (2.4 g), sodium bicarbonate (1.6 g), and sodium sulfate (14.4 g) were dissolved in water, and the resulting solution was diluted to 80 mL to obtain stock Solution I. Copper sulfate pentahydrate (0.4 g) and sodium sulfate (3.6 g) were dissolved in water, and the resulting solution was diluted to 20 mL to obtain stock Solution II. The solutions were stored separately to prevent copper oxidation.[2] Four parts of Solution I and one part of Solution II were freshly mixed to prepare the working solution before analysis. To prepare the color reagent, ammonium molybdate (2.5 g) was dissolved in water (45 mL) and concentrated sulfuric acid (2.1 mL). Sodium arsenate dibasic pentahydrate (0.3 g) was dissolved in water (2.5 mL) and mixed with the ammonium molybdate solution. The reagent was incubated at 37 °C for 24–48 h and stored in a brown bottle.[3]

References:

(1) Y. Shao and A. H.-M. Lin, *Food Chem.,* 2018, **240**, 898.
(2) M. Somogyi, *J. Biol. Chem.,* 1952, **195**, 19.
(3) N. Nelson, *J. biol. Chem.,* 1944, **153**, 375.

2.3.4.8 Stability of L-PG coatings on glass substrates

The chemical stability of the L-PG coatings was studied via fluorescence analysis. First, square-shaped glass slides were cleaned with ethanol (EtOH) and water and then completely immersed in a 0.1 mg mL^{-1} AF488-labeled L-PG solution for 10 min. Then, the functionalized glass substrates were rinsed with water several times to remove all excess and unbound polymer. The prepared glass substrates were then separately incubated for 60 min in several solutions: H_2O, 10 mM phosphate-buffered saline (PBS; pH 7.4), 1 M HCl, 1 M HNO_3, 1 M H_2O_2, 10 mM glutathione (GSH), 17 mM sodium dodecyl sulfate (SDS), EtOH, and 0.5 U mL^{-1} β-amylase (in 8 mM acetate buffer, pH 4.8). Following incubation, each glass slide was rinsed with water and dried with a N_2 gun. The fluorescence emission intensities were recorded by mounting the samples on a solid-state sample holder in a Fluorolog instrument (Jobin Yvon Horiba). Emissions intensities were recorded at a wavelength of 515 nm using an excitation wavelength of 488 nm (slit aperture 5). The data were recorded using the software FluorEssence.

2.3.4.9 Quartz crystal microbalance with dissipation (QCM-D)

QCM-D experiments were performed using a QSense E4 (Biolin Scientific, Sweden) equipped with a peristaltic pump. Before the measurements, gold sensor chips (QSX 301 Gold, Biolin Scientific) were cleaned with piranha solution, rinsed with Milli-Q water, dried with a N_2 gun and sterilized with a UV/ozone treatment (Bioforce Nanoscience, UV.TC.EU.003, USA) for 20 min.

2.3.4.10 Differential interference contrast (DIC) microscopy

DIC microscopy images were recorded using an inverted Olympus IX71 microscope.

2.3.4.11 Transmission electron microscopy (TEM)

For TEM analysis of the bare, L-PG- and L-PG/AuNP-coated PS microparticles, the corresponding water dispersion was dropped onto an ozone-cleaned copper grid and allowed to dry in air overnight. TEM images were acquired using a Tecnai Spirit (FEI, USA) instrument with an operation voltage of 120 kV.

2.3.4.12 Scanning electron microscopy (SEM) and energy-dispersive X-ray (EDX) spectroscopy

For SEM and EDX analysis, the sample-containing copper grid prepared for TEM analysis was attached onto a carbon tape and analyzed as is. SEM images and EDX spectra and mapping were acquired with a FlexSEM 1000 benchtop scanning electron microscope (Hitachi, Japan) equipped with a Quantax 80 EDX system (Bruker, USA). Typically, images and spectra of samples were recorded using a beam voltage of 15 kV, operating in SEM pressure mode and with an acquisition time of 5 min.

2.3.4.13 Scanning helium ion microscopy (HIM)

HIM was performed on an ORION NanoFab (Zeiss, Peabody, USA) using a 25 keV He^+ probe with a current of 0.3 pA, and the image was obtained using an Everhart–Thornley-type secondary electron detector. The sample was mounted on a 45° holder and the stage tilted by a further 30° to give a final viewing angle of 75°.

2.3.4.14 Stability of L-PG/AuNP hybrid coatings on glass substrates

To assess the chemical stability of the L-PG/AuNP hybrid coatings, square-shaped glass slides were first cleaned with EtOH and water and then completely immersed in a 0.1 mg mL^{-1} L-PG solution for 10 min. The functionalized glass substrates were then rinsed with water several times to remove all excess and unbound polymer. The L-PG-coated substrates were then completely immersed in a AuNP colloidal suspension for 10 min and subsequently rinsed with water to obtain 1 bilayer coating of L-PG/AuNP on each side. The prepared glass slides were then separately incubated for 60 min in several solutions: H_2O, 10 mM PBS (pH 7.4), 1 M HCl, 1 M HNO_3, 10 mM $NaBH_4$, 1 M H_2O_2, *n*-hexane, EtOH, 17 mM SDS, and 10 mM GSH. After that, each glass slide was washed with water and dried with a N_2 gun. The UV–vis spectrum of each glass slide was recorded from 350 to 800 nm.

2.3.4.15 Catalytic evaluation of AuNPs in L-PG/AuNP-coated 15 mL polypropylene (PP) tubes

PP tubes functionalized with an inner coating of L-PG/AuNPs were used to perform the decoloration of methylene blue (MB; blue solution) to leucomethylene blue (LMB; colorless solution) via $NaBH_4$ in the presence of catalyst AuNPs. In a typical reaction, 5 mL of a 0.025 mM MB and 10 mM $NaBH_4$ solution were introduced into the tube and vortexed for 45 min. At intervals of 5 min, aliquots (0.3 mL) were withdrawn. The UV–vis spectra of the aliquots were measured using a plate reader in the range of 450 to 750 nm, with a recording interval of 2 nm. To obtain the kinetics graph, the absorbance intensity at 664 nm was recorded for each sample and plotted against the reaction time.

2.3.4.16 AuNP stability in modified 15 mL PP tubes

A 3-bilayer L-PG/AuNP-functionalized PP tube was prepared as described before, with AuNPs as the last layer. After each addition of AuNP solution, the supernatant was withdrawn and the UV–vis spectra were acquired. A 10 mM $NaBH_4$ solution (2 mL) was incubated by vortexing in the prepared tube for 45 min. At intervals of 5 min, aliquots (0.3 mL) were withdrawn. The aliquots were analyzed via UV–vis spectroscopy. To calculate the concentration (mM) of AuNPs in the supernatant, the following formula was used: OD@400nm:1.2 = 0.5 mM:x mM (where OD is the optical density).

2.3.4.17 Surface-enhanced Raman scattering (SERS) sensing using L-PG/AgNP hybrid coatings

A 3-bilayer L-PG/AgNP glass substrate was prepared as described before, with AgNPs as the last layer. Liquid samples at different concentrations of crystal violet were loaded onto the functionalized substrate and the SERS intensity was then measured with a RENISHAW Raman microscope equipped with a He−Ne laser operating at 532 nm. The laser spot size was 5 μm, focused by a 50× lens. Single scans were run with an integration time of 15 s using a grating of 1800 lines mm^{-1} from 300 to 1800 cm^{-1}. The acquired data were processed with the WIRE 2.0 software.

Chapter 3

Cobalt Phosphate Nanostructures for Non-Enzymatic Glucose Sensing at Physiological pH

This Chapter has been published as:

Pacchin Tomanin, P., Cherepanov, P.V., Besford, Q.A., Christofferson, A.J., Amodio, A., McConville, C.F., Yarovsky, I., Caruso, F. and Cavalieri, F., **2018**. Cobalt phosphate nanostructures for non-enzymatic glucose sensing at physiological pH. *ACS applied materials & interfaces*, *10*(49), pp.42786-42795.

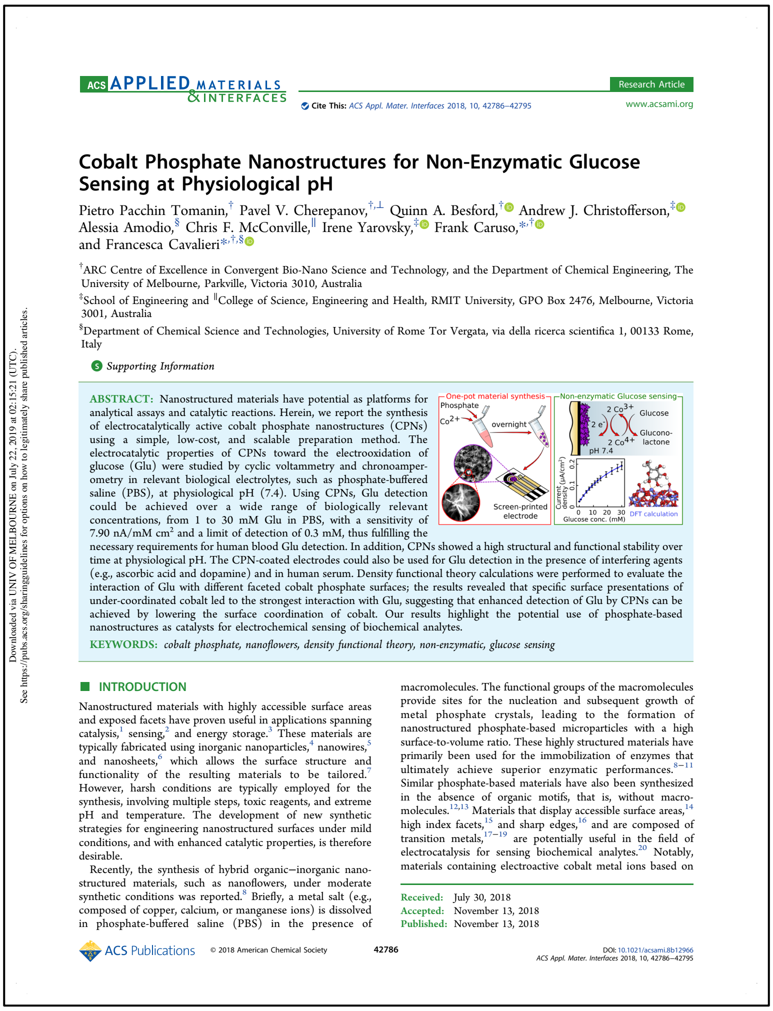

ACS APPLIED MATERIALS & INTERFACES
Research Article
Cite This: *ACS Appl. Mater. Interfaces* 2018, 10, 42786−42795
www.acsami.org

Cobalt Phosphate Nanostructures for Non-Enzymatic Glucose Sensing at Physiological pH

Pietro Pacchin Tomanin,[†] Pavel V. Cherepanov,[†,⊥] Quinn A. Besford,[†] Andrew J. Christofferson,[‡] Alessia Amodio,[§] Chris F. McConville,[‖] Irene Yarovsky,[‡] Frank Caruso,[*,†] and Francesca Cavalieri[*,†,§]

[†]ARC Centre of Excellence in Convergent Bio-Nano Science and Technology, and the Department of Chemical Engineering, The University of Melbourne, Parkville, Victoria 3010, Australia

[‡]School of Engineering and [‖]College of Science, Engineering and Health, RMIT University, GPO Box 2476, Melbourne, Victoria 3001, Australia

[§]Department of Chemical Science and Technologies, University of Rome Tor Vergata, via della ricerca scientifica 1, 00133 Rome, Italy

Supporting Information

ABSTRACT: Nanostructured materials have potential as platforms for analytical assays and catalytic reactions. Herein, we report the synthesis of electrocatalytically active cobalt phosphate nanostructures (CPNs) using a simple, low-cost, and scalable preparation method. The electrocatalytic properties of CPNs toward the electrooxidation of glucose (Glu) were studied by cyclic voltammetry and chronoamperometry in relevant biological electrolytes, such as phosphate-buffered saline (PBS), at physiological pH (7.4). Using CPNs, Glu detection could be achieved over a wide range of biologically relevant concentrations, from 1 to 30 mM Glu in PBS, with a sensitivity of 7.90 nA/mM cm^2 and a limit of detection of 0.3 mM, thus fulfilling the necessary requirements for human blood Glu detection. In addition, CPNs showed a high structural and functional stability over time at physiological pH. The CPN-coated electrodes could also be used for Glu detection in the presence of interfering agents (e.g., ascorbic acid and dopamine) and in human serum. Density functional theory calculations were performed to evaluate the interaction of Glu with different faceted cobalt phosphate surfaces; the results revealed that specific surface presentations of under-coordinated cobalt led to the strongest interaction with Glu, suggesting that enhanced detection of Glu by CPNs can be achieved by lowering the surface coordination of cobalt. Our results highlight the potential use of phosphate-based nanostructures as catalysts for electrochemical sensing of biochemical analytes.

KEYWORDS: *cobalt phosphate, nanoflowers, density functional theory, non-enzymatic, glucose sensing*

INTRODUCTION

Nanostructured materials with highly accessible surface areas and exposed facets have proven useful in applications spanning catalysis,[1] sensing,[2] and energy storage.[3] These materials are typically fabricated using inorganic nanoparticles,[4] nanowires,[5] and nanosheets,[6] which allows the surface structure and functionality of the resulting materials to be tailored.[7] However, harsh conditions are typically employed for the synthesis, involving multiple steps, toxic reagents, and extreme pH and temperature. The development of new synthetic strategies for engineering nanostructured surfaces under mild conditions, and with enhanced catalytic properties, is therefore desirable.

Recently, the synthesis of hybrid organic−inorganic nanostructured materials, such as nanoflowers, under moderate synthetic conditions was reported.[8] Briefly, a metal salt (e.g., composed of copper, calcium, or manganese ions) is dissolved in phosphate-buffered saline (PBS) in the presence of macromolecules. The functional groups of the macromolecules provide sites for the nucleation and subsequent growth of metal phosphate crystals, leading to the formation of nanostructured phosphate-based microparticles with a high surface-to-volume ratio. These highly structured materials have primarily been used for the immobilization of enzymes that ultimately achieve superior enzymatic performances.[8−11] Similar phosphate-based materials have also been synthesized in the absence of organic motifs, that is, without macromolecules.[12,13] Materials that display accessible surface areas,[14] high index facets,[15] and sharp edges,[16] and are composed of transition metals,[17−19] are potentially useful in the field of electrocatalysis for sensing biochemical analytes.[20] Notably, materials containing electroactive cobalt metal ions based on

Received: July 30, 2018
Accepted: November 13, 2018
Published: November 13, 2018

DOI: 10.1021/acsami.8b12966
ACS Appl. Mater. Interfaces 2018, 10, 42786−42795

3.1 Manuscript main text

ACS APPLIED MATERIALS & INTERFACES
Research Article
Cite This: ACS Appl. Mater. Interfaces 2018, 10, 42786−42795
www.acsami.org

Cobalt Phosphate Nanostructures for Non-Enzymatic Glucose Sensing at Physiological pH

Pietro Pacchin Tomanin,[†] Pavel V. Cherepanov,[†,⊥] Quinn A. Besford,[†] Andrew J. Christofferson,[‡] Alessia Amodio,[§] Chris F. McConville,[∥] Irene Yarovsky,[‡] Frank Caruso,[*,†] and Francesca Cavalieri[*,†,§]

[†]ARC Centre of Excellence in Convergent Bio-Nano Science and Technology, and the Department of Chemical Engineering, The University of Melbourne, Parkville, Victoria 3010, Australia

[‡]School of Engineering and [∥]College of Science, Engineering and Health, RMIT University, GPO Box 2476, Melbourne, Victoria 3001, Australia

[§]Department of Chemical Science and Technologies, University of Rome Tor Vergata, via della ricerca scientifica 1, 00133 Rome, Italy

Supporting Information

ABSTRACT: Nanostructured materials have potential as platforms for analytical assays and catalytic reactions. Herein, we report the synthesis of electrocatalytically active cobalt phosphate nanostructures (CPNs) using a simple, low-cost, and scalable preparation method. The electrocatalytic properties of CPNs toward the electrooxidation of glucose (Glu) were studied by cyclic voltammetry and chronoamperometry in relevant biological electrolytes, such as phosphate-buffered saline (PBS), at physiological pH (7.4). Using CPNs, Glu detection could be achieved over a wide range of biologically relevant concentrations, from 1 to 30 mM Glu in PBS, with a sensitivity of 7.90 nA/mM cm^2 and a limit of detection of 0.3 mM, thus fulfilling the necessary requirements for human blood Glu detection. In addition, CPNs showed a high structural and functional stability over time at physiological pH. The CPN-coated electrodes could also be used for Glu detection in the presence of interfering agents (e.g., ascorbic acid and dopamine) and in human serum. Density functional theory calculations were performed to evaluate the interaction of Glu with different faceted cobalt phosphate surfaces; the results revealed that specific surface presentations of under-coordinated cobalt led to the strongest interaction with Glu, suggesting that enhanced detection of Glu by CPNs can be achieved by lowering the surface coordination of cobalt. Our results highlight the potential use of phosphate-based nanostructures as catalysts for electrochemical sensing of biochemical analytes.

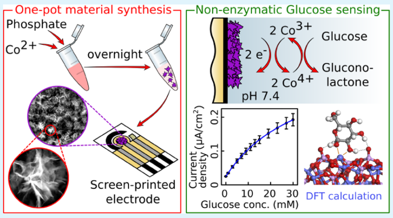

KEYWORDS: *cobalt phosphate, nanoflowers, density functional theory, non-enzymatic, glucose sensing*

INTRODUCTION

Nanostructured materials with highly accessible surface areas and exposed facets have proven useful in applications spanning catalysis,[1] sensing,[2] and energy storage.[3] These materials are typically fabricated using inorganic nanoparticles,[4] nanowires,[5] and nanosheets,[6] which allows the surface structure and functionality of the resulting materials to be tailored.[7] However, harsh conditions are typically employed for the synthesis, involving multiple steps, toxic reagents, and extreme pH and temperature. The development of new synthetic strategies for engineering nanostructured surfaces under mild conditions, and with enhanced catalytic properties, is therefore desirable.

Recently, the synthesis of hybrid organic−inorganic nanostructured materials, such as nanoflowers, under moderate synthetic conditions was reported.[8] Briefly, a metal salt (e.g., composed of copper, calcium, or manganese ions) is dissolved in phosphate-buffered saline (PBS) in the presence of macromolecules. The functional groups of the macromolecules provide sites for the nucleation and subsequent growth of metal phosphate crystals, leading to the formation of nanostructured phosphate-based microparticles with a high surface-to-volume ratio. These highly structured materials have primarily been used for the immobilization of enzymes that ultimately achieve superior enzymatic performances.[8−11] Similar phosphate-based materials have also been synthesized in the absence of organic motifs, that is, without macromolecules.[12,13] Materials that display accessible surface areas,[14] high index facets,[15] and sharp edges,[16] and are composed of transition metals,[17−19] are potentially useful in the field of electrocatalysis for sensing biochemical analytes.[20] Notably, materials containing electroactive cobalt metal ions based on

Received: July 30, 2018
Accepted: November 13, 2018
Published: November 13, 2018

DOI: 10.1021/acsami.8b12966
ACS Appl. Mater. Interfaces 2018, 10, 42786−42795

phosphates,[13] phosphides,[20] nitrites,[21] and oxides[18] have recently shown promise for their use in electrochemical applications, such as water splitting,[22] energy storage,[13] and sensing.[23]

Particularly, the development of accurate, inexpensive, and stable glucose (Glu) detection devices is an expanding field, where the key goal is to reduce costs associated with the measurements, ultimately leading to increased patient compliance for patients diagnosed with metabolic diseases, such as diabetes. A variety of methods have been developed for Glu sensing and include processes based on enzymatic reactions,[24−26] Glu-specific conjugation chemistry,[27] supramolecular recognition,[28] and direct electrochemical oxidation.[29,30] Commercial methods used for the detection of blood Glu level involve enzymatic sensors. However, these enzymatic sensors have drawbacks in terms of material cost,[31] measurement variability with temperature, pH, humidity, interfering chemical species, and enzyme stability.[32] These disadvantages have thus generated interest in developing non-enzymatic Glu sensors. Examples of non-enzymatic systems developed to date are based on noble metals,[33,34] alloys,[35] transition metals,[21,36] and hybrid organic−inorganic structures comprising carbon nanotubes[37] and graphene.[38] However, despite these recent developments, several problems remain to be addressed relative to the high cost of the component materials, the complexity of the fabrication method, the specificity of the sensor to the analyte, and the limit and range of detection. Importantly, the poor performance of existing non-enzymatic sensors in detecting Glu at near-biological conditions, such as in an aqueous buffer at physiological pH, has limited the use of non-enzymatic Glu-sensing systems in real-life applications.[23,39−43]

Herein, we have developed a low-cost and scalable one-pot approach to fabricate electrocatalytically active cobalt phosphate nanostructures (CPNs) under mild synthetic conditions. The CPNs are amorphous, exhibit high surface areas, and can catalyze the electrooxidation of Glu in aqueous buffer at physiological pH. Upon coating an electrode with CPNs, the electrooxidation of Glu can be quantified as a function of Glu concentration—the CPN-coated electrode can achieve a wide range of detection between 1 and 30 mM Glu in aqueous buffer (PBS), with a sensitivity of 7.90 nA/mM cm^2 at 5 mM of Glu based on the electroactive surface area (ESA) and a limit of detection (LOD) of 0.3 mM [signal-to-noise ratio (S/N) = 3]. In addition, the CPN-coated electrode exhibits high stability with time and can detect Glu in the presence of common interfering agents [ascorbic acid (AA) and dopamine (DP)] and in human serum (HS). Density functional theory (DFT) calculations were performed to investigate the interaction between Glu and the surface of the CPN sensor. The results show that the interaction of CPNs with Glu is because of the presentation of under-coordinated cobalt atoms at the interface of the CPN material. Our results highlight the potential use of CPNs for the electrochemical detection of biochemical analytes.

■ EXPERIMENTAL METHODS

Reagents and Chemicals. Cobalt(II) nitrate hexahydrate ($Co(NO_3)_2{\cdot}6H_2O$, ≥97%, CAS no. 10026-22-9) was purchased from Baker. PBS tablets, Nafion 117 solution (CAS no. 31175-20-9), cobalt(II) phosphate hydrate ($Co_3(PO_4)_2{\cdot}xH_2O$, CAS no. 10294-50-5), potassium ferricyanide(III) ($K_3Fe(CN)_6$, CAS no. 13746-66-2), and HS from human male AB plasma were purchased from Sigma-Aldrich. D-Glucose (CAS no. 50-99-7) was purchased from AnalR. Potassium chloride (KCl, CAS no. 7440-09-7) was purchased from Chem-Supply. All the chemicals were used as received. High-purity (Milli-Q) water with a resistivity of 18.2 MΩ cm was obtained from an inline Millipore RiOs/origin water purification system.

Instrumentation. X-ray photoelectron spectroscopy (XPS) spectra were acquired using an Axis Ultra X-ray photoelectron spectrometer (Kratos Analytical, UK), equipped with a 165 mm concentric hemispherical electron energy analyzer and a monochromated Al Kα incident X-ray source (1486.6 eV). Survey (wide) scans were recorded in the binding energy range of 0−1200 eV, with 1.0 eV steps, a dwell time of 100 ms, and an analyzer pass energy of 160 eV. Multiplex (narrow) high-resolution spectra were recorded with a pass energy of 20 eV, 0.05 eV steps, and a dwell time of 250 ms, resulting in an energy resolution ($\Delta E/E$) of ~300 meV. The base pressure in the analysis chamber during data collection was $1-2 \times 10^{-9}$ mbar, and these data were processed using the software CasaXPS. All binding energies were calibrated using the C 1s level of adventitious carbon at 285.0 eV. Fourier transform infrared (FTIR) spectra were obtained on a TENSOR II (Bruker) attenuated total reflectance FTIR (ATR−FTIR) spectrometer and analyzed using the software OPUS 7.8. The number of scans was 64. A minimum resolution of 4 cm^{-1} and the absorbance/transmittance mode were used. Scanning electron microscopy (SEM) images were obtained on a Teneo VolumeScope (FEI) microscope. Transmission electron microscopy (TEM) was conducted on a Tecnai Spirit (FEI) microscope operating at 120 kV. Energy-dispersive X-ray spectroscopy (EDX) was performed on a 20 mm^2 X-Max SDD instrument (Oxford Instruments) equipped with the software AZtec 3.2. X-ray diffraction (XRD) data were collected using a D8 ADVANCE X-ray diffractometer (Bruker) with Ni-filtered Cu Kα radiation (1.54 Å). Data were collected between 5° and 85° 2θ, with a step size of 0.02° and a scan rate of 1.0 s per step. An anti-scatter blade was used to reduce the diffracted background intensity at low angles. An incident beam divergence of 1.0° was used with a 2.5° soller slit in the diffracted beam. The sample was spun at 15 rpm. Generally, unless otherwise specified, the data from the characterizations were exported to the software OriginPro 8.5 for further analysis.

Synthesis of CPNs. An aqueous $Co(NO_3)_2{\cdot}6H_2O$ solution (100 μL, 1.2 M) was added to PBS (20 mL, 1 mM, pH 7.4) in a 50 mL tube with simultaneous vortexing, which was continued for 5 s after addition, followed by static incubation at 23 °C overnight. For the scale-up of the synthesis, an aqueous $Co(NO_3)_2{\cdot}6H_2O$ solution (10 mL, 1.2 M) was added to PBS (2 L, 1 mM, pH 7.4) in a 2 L glass beaker with vigorous stirring, which was continued for 5 s after addition, followed by static aging at 23 °C overnight. The precipitate was then collected, washed 5 times by centrifugation (67g, 5 min) and resuspension in water, and finally resuspended in water (40 mL) and stored at 4 °C for further characterization. SEM and TEM samples were prepared by dropcasting the aqueous suspension on a silicon wafer and a carbon grid, respectively, followed by drying in air. XPS, XRD, and FTIR samples were prepared by drying the aqueous suspension in a vacuum desiccator prior to analysis.

Electrode Preparation. A glassy carbon electrode (GCE, 3 mm in diameter) was first polished with a 0.05 μm alumina slurry. The polished GCE was then rinsed with water and ethanol, and allowed to dry in air. A CPN suspension (10 mg/mL) in 10% (v/v) Nafion in ethanol was prepared and vortexed to obtain a homogeneous suspension. On the center of the GCE, the prepared suspension (10 μL) was dropcasted and allowed to dry in air. Similarly, a screen-printed electrode (SPE, 3 mm in diameter) was modified by dropcasting a 10 mg/mL CPN suspension (10 μL) in 10% (v/v) Nafion in water and allowed to dry in air. A total mass of 0.1 mg of CPNs was deposited on the GCE or SPE to achieve complete surface coverage of the working electrode (WE). A bare GCE electrode for control measurements was prepared following the aforementioned procedure without the use of CPNs, thereby resulting in an electrode coated with Nafion only. For comparison, GCE was also modified with $Co_3(PO_4)_2$ powder following the aforementioned protocol. Graphite SPE chips that were produced in the Laboratory of

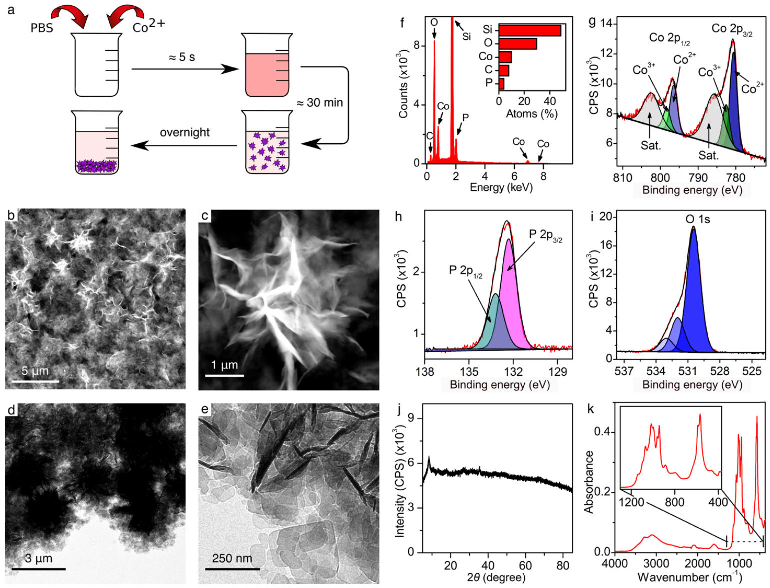

Figure 1. (a) Schematic illustration of the proposed mechanism for CPN formation. (b,c) SEM and (d,e) TEM images of the CPNs at various magnification. (f) EDX spectrum. High-resolution Co 2p (g), P 2p (h), and O 1s (i) XPS spectra, (j) XRD spectrum, and (k) ATR−FTIR spectrum of the CPNs (the inset in (k) shows a magnified portion of spectrum in the 1300−370 cm^{-1} range).

Biosensors and Nanomachines at the University of Rome, Tor Vergata, were used. Briefly, the electrodes were printed using a 245 DEK (Weymouth, UK) screen-printing machine and graphite- (LOCTITE EDAG PF-407A) and silver-based (LOCTITE EDAG PF-410) conductive inks and a gray dielectric paste insulating ink. The inks were printed on a polyester flexible film (Autostat HT5). Each graphite SPE chip contained three separate printed portions that served as the working (carbon-based ink), the reference (silver-based ink), and the counter electrode (CE) (carbon-based ink). The diameter of the WE was 3 mm, which resulted in an apparent geometric area of 7.07 mm^2.

Electrochemical Measurements. Cyclic voltammetry (CV) and chronoamperometry (CA) measurements were performed on a MM510 potentiostat/galvanostat (Materials Mates Italia S.r.l.) using the software VoltaScope 5.4. Electrochemical measurements involving the GCE were conducted in a three-electrode electrochemical cell composed of a glassy carbon WE (3 mm diameter), a platinum wire as the CE, and a Ag/AgCl reference electrode (RE). Electrochemical measurements involving the SPE were performed on the SPE described above. The supporting electrolyte, unless specified otherwise, was a N_2-saturated 10 mM PBS solution (pH 7.4) that was thoroughly mixed by a magnetic stirrer. The pH of the electrolyte was adjusted, when needed, with 1 M NaOH solution.

Computational Details. The X-ray crystal structure[44] of $Co_3(PO_4)_2$ was obtained based on the most likely cobalt phosphate stoichiometry determined from the XRD pattern of the CPNs and cleaved to form the (100), (111), and (211) surfaces. For the (111) and (211) surfaces, oxygen positions were adjusted to preserve the tetrahedral phosphate geometry. Each slab consisted of two layers, with $x \times y$ dimensions of 16.72 × 8.79, 9.77 × 12.13, and 17.47 × 12.13 $Å^2$ for the (100), (111), and (211) surfaces, respectively. Increasing the number of layers or replicating the unit cell in the x or y dimension did not affect the Glu binding energies significantly. A vacuum spacer of at least 20 Å in the z-direction was added, and the model surfaces were subsequently relaxed, generating surface structures corresponding to different possibilities of surface cobalt coordination. Following surface relaxation, the geometry of the bottom layer of the slabs was frozen for the surface−Glu binding energy calculations. For the free Glu structural optimization, a single Glu molecule was placed in the center of a 20 × 20 × 20 $Å^3$ box, and only the gamma point was sampled. For the adsorption calculations, a variety of initial orientations of Glu on the relaxed surfaces were constructed, with an O1(Glu)−cobalt initial distance of ~2.5 Å. All calculations were performed using the Vienna Ab initio simulation package[45] and the generalized gradient approximation (GGA) Perdew−Burke−Ernzerhof[46] exchange correlation functional. The projector augmented wave (PAW) method[47] was used with the Blöchl all-electron, frozen-core PAW pseudopotentials.[48] A 5 × 5 × 1 Monkhorst−Pack[49] k-point mesh for sampling the Brillouin zone and a cutoff energy of 500 eV were applied, and spin polarization was included. A dipole correction was applied to minimize polarization effects because of slab asymmetry. The Hubbard U parameter (GGA + U)[50] for the electron correlation of the d states in cobalt ions was used with a value of 3.5 eV.[51] A convergence criterion of 0.01 eV/Å was employed for the geometry optimizations.

■ RESULT AND DISCUSSION

Preparation and Characterization of CPNs. CPNs were synthesized using a one-pot crystallization method in water at neutral pH and 23 °C. Briefly, $Co(NO_3)_2{\cdot}6H_2O$ solution was added to PBS while mixing for 5 s. The resulting solution was then incubated statically overnight (Figure 1a). After ca. 30 min following the addition of $Co(NO_3)_2{\cdot}6H_2O$, the solution turned from a transparent pale red to an opaque dispersion. After aging overnight, a dark purple precipitate formed at the bottom of the flask, leaving an almost transparent supernatant. These observations suggest that the Co^{2+} ions are involved in the formation of the solid precipitate. The morphology of the precipitate was characterized by SEM and TEM. The SEM images in Figure 1b,c reveal the open flower-like network of the CPNs. The flower-like structures were about 3 μm in diameter and were composed of smaller sub-unit nanosheets that had a thickness of about 20 nm and a width of about 100

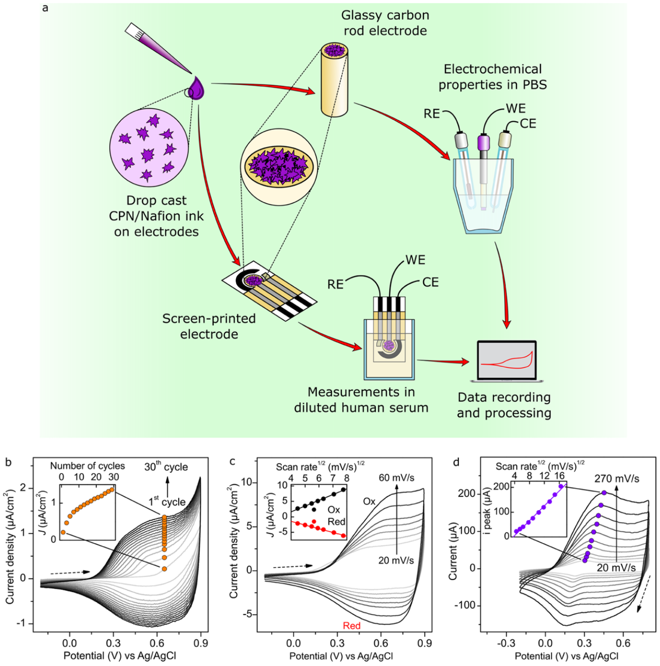

Figure 2. (a) Schematic representation of the preparation of GCE and SPE, the experimental setup used for the electrochemical characterization, and measurements performed in the electrolyte composed of HS and PBS. (b) CV cycles (30) of the CPNs in a N_2-saturated PBS electrolyte (10 mM, pH 7.4) at a scan rate of 20 mV/s. The inset shows a plot of the peak current density value at 0.65 V vs Ag/AgCl as a function of the cycle number. (c) CVs of CPNs in PBS buffer (10 mM, pH 7.4) at different scan rates: 20, 25, 30, 35, 40, 50, and 60 mV/s. The inset shows a plot of the oxidation (Ox) and reduction (Red) peak current densities as a function of the square root of the scan rate. (d) CVs of CPNs in 5 mM $K_3Fe(CN)_6$/0.1 M KCl supporting electrolyte at different scan rates from 20 to 270 mV/s. The inset shows a plot of the peak current of the $Fe(CN)_6^{3-}/Fe(CN)_6^{4-}$ redox couple as a function of the square root of the scan rate. Dashed arrows indicate the potential sweep direction. All current density data are normalized by the ESA.

nm. The TEM images in Figure 1d,e indicate that the distribution of the nanosheets was denser at the core than in the outer layer of the particles. The spatially organized length of the network spans from the nano- to the microscale, providing both exposed facets and a high surface-to-volume ratio. In contrast, $Co_3(PO_4)_2$ powder is composed of aggregates of sheets with thickness and lateral dimensions of around 400 nm and 4 μm, respectively (Figure S1). These dimensions are significantly larger than the dimensions of the prepared CPNs.

The EDX and XPS analyses of the CPNs, shown in Figure 1f–i, reveal the presence of the elements Co, P, and O in the sample. In addition, EDX analysis indicates a bulk Co/P ratio of 1:0.4 (Figure S2), whereas the XPS analysis shows a surface Co/P ratio of 1:6 (Figure S3). The surface composition determined from XPS data of the Co and P 2p levels was calculated taking into account the relative sensitivity factors. Hence, we conclude that the composition of CPNs is nonhomogeneous.

The XPS survey spectrum in Figure S3 shows the presence of a prominent O 1s peak and characteristic core-level peaks of Co and P. The Co 2p XPS spectra (Figure 1g) displayed Co $2p_{3/2}$ and Co $2p_{1/2}$ peaks, with each peak consisting of contributions from Co^{2+} and Co^{3+}, respectively, observed at 780.6 and 782.6 eV for the Co $2p_{3/2}$ peak and at 796.5 and 789.3 eV for the Co $2p_{1/2}$ peak. In addition, two broad satellite (Sat.) features were observed at 780.6 and 782.6 eV. The intensity of the satellite features appears to be enhanced, indicating a contribution from the presence of $Co(OH)_2$ and phosphate species on the surface.[52] As shown in Figure 1h, two peaks, P $2p_{3/2}$ and P $2p_{1/2}$, were also present in the P 2p region at 132.3 and 133.2 eV, respectively. These peaks are consistent with the characteristic binding energies of tetrahedral (PO_4) groups.[53] The O 1s peak could be resolved into three components, with the main core-level oxygen line at 530.5 eV and two satellites at 532.0 and 533.0 eV. Although the assignment of these satellites features is controversial in the literature, the peak at 533.0 eV could be attributed to OH species present in small quantities of cobalt hydroxide, whereas the peak at 532.0 eV could be assigned to the presence of a layer of loosely bound oxygen at the surface of the CPNs. As the core-binding energies relative to Co 2p and O 1s of cobalt oxides and hydroxides are in the same range as those of cobalt phosphate, we suggest that the surface of CPNs constitutes a combination of Co^{2+} and Co^{3+} as oxo/hydroxo and phosphate species, however, with the latter phosphate species believed to be more predominant in line with the Co/P ratio of 1:6 determined by XPS.[54]

The typical XRD pattern of the CPNs in Figure 1j indicates that the sample is not crystalline. The XRD pattern could be matched to the $Co_3(PO_4)_2 \cdot H_2O$ phase. The ATR–FTIR spectrum of the CPNs in Figure 1k displayed peaks at around

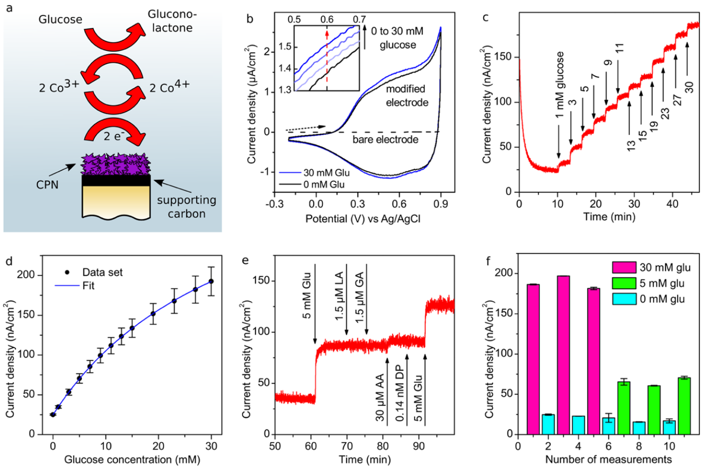

Figure 3. (a) Proposed electrochemical oxidation of Glu to gluconolactone at the electrode interface. (b) CVs of the CPN-modified electrode in PBS buffer (10 mM, pH 7.4) at a scan rate of 20 mV/s in the absence (black line) and presence (blue lines) of 30 mM Glu, respectively. The dashed line represents the CV of the GCE (bare electrode) obtained under the same experimental conditions. The inset shows a magnification of the potential region from 0.5 to 0.7 V (vs Ag/AgCl) with the presence of 10, 20, and 30 mM Glu (full profiles shown in Figure S5). (c) Chronoamperometric responses of the CPN in PBS buffer (10 mM, pH 7.4) to successive additions of Glu at an applied potential of 0.65 V (vs Ag/AgCl) and (d) the calibration curve based on the triplicate CA experiments. (e) Amperometric responses of CPNs at 0.65 V (vs Ag/AgCl) to the addition of Glu (5 mM) in PBS electrolyte (10 mM, pH 7.4), followed by additions of interfering agents LA (1.5 μM), GA (1.5 μM), AA (30 μM), and DP (0.14 nM), and second addition of Glu (5 mM). (f) Cyclic amperometric responses of CPN-modified GCE in 0, 5, and 30 mM Glu; the CPN-modified GCE was washed with water after each measurement. Note that all current data have been normalized by the ESA and are not apparent current densities.

580 cm^{-1} and in the 3500−2500 and 1200−900 cm^{-1} regions. The broad absorption in the region from 3500 to 2500 cm^{-1} and the weak peak at 1607 cm^{-1} were assigned to the vibration of the OH groups, suggesting the presence of water of crystallization and hydroxyl groups within the structure.[55] The vibration frequencies present in the region from 1200 to 900 cm^{-1} are characteristic of phosphate groups.[56] The two overlapping intense peaks at 567 and 586 cm^{-1} are characteristic of the stretching vibrations of the metal−oxygen bond.[57] The morphological properties of the CPNs suggest the potential use of this material as an electrocatalyst.

Electrochemical Characterization of CPNs. A schematic illustration of the preparation of electrode surfaces with CPNs and the setup used for the electrochemical studies is shown in Figure 2a. Briefly, a suspension of CPNs was dropcast on the GCE and electrochemically characterized using a three-electrode cell with PBS as the supporting electrolyte. A SPE that was prepared in a similar manner was used for the detection of Glu in HS. The SPE was selected because of its small size, as this would allow for low-volume measurements. In addition, the SPE device is portable and disposable. The dropcasting technique, which is a common and widespread approach for preparing electrodes, was selected as it allows for a fast and facile deposition.

CV and CA experiments were conducted to characterize the electrochemical properties of the CPN electrode. Figure 2b shows the first 30 consecutive CV cycles of CPNs obtained at a scan rate of 20 mV/s and in the potential range from −0.2 to 0.9 V. After the first few cycles, broad reduction and oxidation peaks were observed in the potential region of 0.35−0.65 V. These two peaks were respectively assigned to the oxidation and reduction of the Co ions. The inset in Figure 2b displays the oxidation current response of CPNs at 0.65 V over the 30 CV cycles run; a gradual increase in current was observed as the cycle number increased. This upward trend can potentially be explained by the migration of anions to the electrode surface, which counterbalance the electrostatic charge from the oxidized Co cations and subsequently penetrate the CPNs with successive CV cycles, thereby generating and expanding percolation pathways within the catalyst, leading to an increase in the ESA.[58] As the abovementioned process enhances the electrochemical response of the CPN, 30 CV cycles were run as an activation step.

Figure 2c displays the CV cycles of the CPN electrode in PBS at various scanning rates ranging from 20 to 60 mV/s. Faster scanning rates resulted in an increase in both anodic and cathodic peak currents, suggesting a limiting process in the Co^{3+}/Co^{4+} redox reaction. The inset in Figure 2c shows the linear relationship between the peak currents and the square root of the scan rate at neutral pH, indicating that the Co^{3+}/Co^{4+} redox reaction is a diffusion-controlled process.[59] The fitting values are reported in Table S1.

The effective surface area of the activated CPN-modified GCE was measured via CV at varying scan rates of 20−270 mV/s in a non-mixed 5 mM $K_3Fe(CN)_6$ and 0.1 M KCl supporting electrolyte by the ferri-/ferrocyanide redox couple method (Figure 2d).[60] The inset in Figure 2d shows the relationship between the peak current associated with the $Fe(CN)_6^{3-}/Fe(CN)_6^{4-}$ pair and the square root of the scan rate. This relationship can be described by eq 1

$$i_{\text{peak}} = 268\,600An^{3/2}D^{1/2}Cv^{1/2} \qquad (1)$$

where i_{peak} (A) is the peak current, A (cm^2) is the effective surface area, n (1) is the number of electrons transferred in the process, D (7.3×10^{-6} cm^2/s) is the diffusion coefficient of

$Fe(CN)_6^{3-}$ at 25 °C,[61] C (5×10^{-6} mol cm^{-3}) is the concentration of $Fe(CN)_6^{3-}$, and ν (V/s) is the scan rate. The slope of the plot in the inset of Figure 2d was used to calculate the effective surface area, A, using eq 1. The calculated effective surface area of the CPN-modified GCE was 46.63 cm^2, which is about 660 times larger than the geometrical area of the electrode ($\approx 7 \times 10^{-2}$ cm^2).

To elucidate the electrochemical properties of CPNs, several CV cycles in PBS at different pHs at a scanning rate of 20 mV/s in the potential region from −0.2 to 0.9 V were performed (Figure S4). At pH 10.5, an overall increase in the magnitude of the current density was observed with the most pronounced oxidation and reduction peaks observed at, respectively, 0.30 and 0.65, and 0.15 and 0.50 V. These peaks could be attributed to the reduction/oxidation of Co^{2+}/Co^{3+} and Co^{3+}/Co^{4+} redox couples, respectively.[23,36,62,63]

Non-Enzymatic Detection of Glucose. The electrocatalytic properties of CPNs were examined toward applications involving physiological pH, such as the detection of Glu. Considering that Glu can be oxidized to gluconolactone at a neutral pH via a two-electron electrochemical reaction[64] and that the Co^{4+} ions may act as oxidizing species,[36] we propose that the prepared CPN material can catalyze the electrochemical oxidation of Glu (Figure 3a), which can be described by eqs 2 and 3

$$2Co^{3+} \rightarrow 2Co^{4+} + 2e^- \tag{2}$$

$$2Co^{4+} + C_6H_{12}O_6(\text{glucose}) \rightarrow 2Co^{3+} + C_6H_{10}O_6(\text{gluconolactone}) + 2H^+ \tag{3}$$

Therefore, electrooxidation of Glu on CPNs for the non-enzymatic detection of Glu at physiological pH was investigated. Figure 3b compares the CVs of the CPN electrode and the bare GCE recorded in 0 and 30 mM Glu solutions (0, 10, 20, and 30 mM partially shown in inset) prepared in N_2-saturated PBS (10 mM, pH 7.4), as supporting electrolyte, at a scan rate of 20 mV/s in the potential region from −0.2 to 0.9 V, where the current density for this and all subsequent profiles are normalized by the ESA. The full CV profiles of the CPNs in various Glu solutions normalized by both the geometric area and the ESA of the electrode are shown in Figure S5. A noticeable Glu concentration-dependent increase in the anodic peak current was observed in the 0.3−0.8 V range, which corresponds to the electrooxidation of Glu. The oxidation of Glu in PBS at pH 7.4 could be related to the formation of the electroactive Co^{4+} species. In contrast, the bare GCE (dashed line in Figure 3b) shows negligible current density and no apparent pair of redox peaks owing to the absence of electroactive species in the potential range from −0.2 to 0.9 V at all Glu solution concentrations studied.

To evaluate the concentration-dependent electrochemical response of CPNs further, CA profiles in PBS electrolyte containing various amounts of Glu (Figure 3c) were recorded at an applied potential of 0.65 V. A stepwise increase in current density upon addition of Glu at increasing concentrations was observed until a stable current density was achieved; 90% of the steady-state current density was achieved in 37 s (Figure S6). No current density drift was observed after consecutively running the CA experiments three times, using the same CPN-modified GCE for a total of 240 min (Figure S7), thus highlighting the stability and longevity of CPNs. Figure 3d shows the calibration curve that was constructed from the triplicate CA experiments. Interestingly, we observed an increase in the magnitude of the standard deviation in moving toward higher glucose concentrations, which may correspond to an increase in the variability of detection as CPNs approach the upper concentration limit of glucose.

The sensitivity of the CPN-modified GCE was 7.90 nA/mM cm^2 at a Glu concentration of 5 mM based on the ESA, and the LOD was 0.3 mM based on S/N = 3. Both the Glu detection range, tested up to 30 mM, and the LOD fulfill the requirements for Glu detection in human blood.[65] It is particularly interesting that CPNs can catalyze the electrooxidation of Glu at physiological pH. In contrast, most of the existing cobalt-based catalysts that are used for non-enzymatic sensing of Glu require strongly alkaline conditions.[23,39,41,42] Furthermore, although some other metal phosphate systems (e.g., $Ni_3(PO_4)_2$-based materials[66]) have shown greater sensitivity for glucose detection than our currently reported materials, the detection range was investigated below the typical glucose concentration of human blood (i.e., <1 mM), and measurements were also performed in strongly alkaline conditions (1 M NaOH solutions).

Figure S8 shows the amperometric responsiveness of commercial $Co_3(PO_4)_2$ powder-based electrode for the electrooxidation of Glu. A similar trend to CPNs was observed in terms of a stepwise increase in current density as the Glu concentration is increased. Figure S9 shows the calibration curve that was constructed from the triplicate CA experiments. The powder displayed a LOD of 0.4 mM (S/N = 3) and a sensitivity of 4.53 nA/mM cm^2 at a Glu concentration of 5 mM based on the ESA, which is 43% lower than that of CPNs. The results suggest that the CPN-improved sensitivity is because of the increased ESA as a result of the smaller dimensions and the spatial organization of the CPN building blocks when compared with the $Co_3(PO_4)_2$ powder. The sensitivity and LOD were calculated, respectively, using eqs S2 and S3, and the fitting values are listed in Table S2.

Selectivity of CPNs in Physiological Contexts. For accurate Glu determination in biological contexts, it is important for the material to exhibit selectivity toward Glu in the presence of other sugars and other oxidizable species in the human blood at their respective concentrations. Therefore, the selectivity of CPNs toward Glu was studied in the presence of other sugars, such as lactose (LA) and galactose (GA), and other readily oxidizable species, such as AA and DP, at their physiological concentrations.[67−70] Figure 3e shows the CA profiles recorded at 0.65 V with successive additions of Glu (5 mM), LA (1.5 μM), GA (1.5 μM), AA (30 μM), DP (0.14 nM), and Glu (5 mM) to PBS (10 mM, pH 7.4) electrolyte under stirring. An increase in current density of about 50 nA/cm^2 was observed upon first addition of 5 mM Glu. In contrast, a significantly smaller increase in current (<10%) was observed upon subsequent addition of AA, and the increase in current was negligible following subsequent addition of LA, GA, and DP. The increase in current density (about 35 nA/cm^2) observed after the second addition of Glu shows that CPNs are still responsive to Glu, and their activity is not compromised by the interfering agents. These results suggest that CPNs are still capable of Glu sensing under the given experimental conditions.

Moreover, CPNs exhibit high tolerance against Cl^- poisoning considering that the experiments were conducted in PBS, which contains a high concentration of NaCl (137

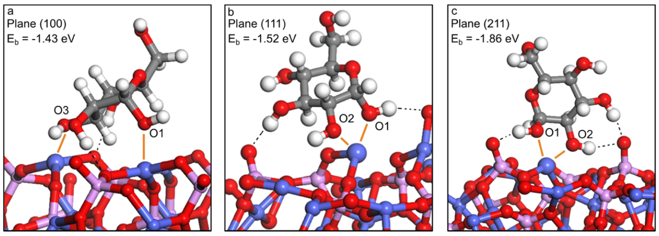

Figure 4. Energetically favorable Glu binding configurations and energies: (a) (100), (b) (111), and (c) (211) surfaces. Solid orange lines indicate coordination bonds and dotted black lines indicate hydrogen bonding. Cobalt, phosphorous, oxygen, carbon, and hydrogen are represented as blue, purple, red, gray, and white spheres, respectively.

mM). It is known that chloride ions can poison non-enzymatic Glu sensors based on precious metals and alloys.[35,36,71]

Reusability of CPNs. The feasibility of reusing the same material (sensor) for multiple measurements is advantageous toward reducing costs and environmental impact. To demonstrate that the CPN-modified GCE can be reused multiple times, amperometric responses at 0.65 V were recorded in 0, 5, and 30 mM Glu PBS electrolyte; the electrode was washed with water after each measurement. Figure 3f shows that the current densities at the Glu concentrations studied were sustained across the multiple measurements performed, thus confirming that the CPN-modified GCE can effectively be reused after simple cleaning with water for reliable Glu sensing.

Thermostability of CPNs. To study the Glu-sensing properties of CPNs as a function of the electrolyte temperature, CA experiments were performed in triplicate as a function of temperature in 5 mM Glu PBS supporting electrolyte at a constant potential of 0.65 V. As observed in Figure S10, the current density was dependent on the temperature. The current density increased steadily with an increase in temperature up to 30 °C and increased more steeply with further increases in temperature to 50 °C. From the electrochemical current densities at 30 and 50 °C, the calculated Glu concentrations (Table S2, fit 1) were, respectively, about 1 and 34 mM higher than the actual Glu concentration (5 mM). The concentration of Glu detected using CPNs was consistent in the temperature range of 23−30 °C. Considering that, in general, the detection of Glu is performed within the temperature range of 23−30 °C, CPNs are suitable for general use as a Glu sensor material. However, if a more precise detection of Glu is needed, the effect of the temperature has to be taken into account, especially at temperatures higher than 30 °C.

Calculations of the Interactions between the Cobalt Phosphate Surface and Glucose. We next investigated the mechanism of interaction between Glu and the CPN surface. To examine binding orientations of Glu on CPN surfaces, DFT calculations were performed. Relaxed surfaces of (100), (111), and (211) facets of $Co_3(PO_4)_2$ provided a variety of possible cobalt coordination scenarios. The relaxed (100) surface presented cobalt in a 3-coordinate trigonal configuration, with a surface cobalt−cobalt distance of ∼6 Å. The relaxed (111) and (211) surfaces presented cobalt in a variety of 3-, 4-, and 5-coordinate geometries, with surface cobalt−cobalt distances of 3−4 Å (Figure S11).

For the 3-coordinate Co arising from the relaxed (100) surface, the most energetically favorable binding of Glu was found to occur via the coordination of O1 to one Co atom at a distance of 2.10 Å and coordination of O3 to a second surface Co atom at a distance of 2.14 Å (Figure 4a). The binding energy of this configuration was calculated as −1.42 eV (Table S3).

The most energetically favorable binding determined on the (111) surface was that between O1 and O2 of Glu and 3-coordinate cobalt, with oxygen−cobalt distances of 2.06 and 2.17 Å, respectively (Figure 4b). The binding energy for this configuration was −1.52 eV. In contrast to the (100) surface, Glu binding on the (111) surface induced significant surface reconstruction upon binding, increasing the distance between the chelated cobalt and one of the phosphate oxygens from 2.06 to 2.31 Å.

Similar to the (111) surface, optimal Glu binding on the (211) surface was with a 3-coordinate cobalt adjacent to a 4-coordinate cobalt, and the O1 and O2 oxygens of Glu chelated the cobalt with oxygen−Glu distances of 2.02 and 2.04 Å, respectively (Figure 4c). However, the presence of an uncoordinated phosphate oxygen within 3 Å of the Glu O1 distinguishes the binding of Glu on the (211) surface from that observed on the (111) surface. It can be suggested that the electrooxidation of Glu is coupled to the proton transfer from the O1 hydroxyl group to the uncoordinated phosphate oxygen. On the basis of the calculations, this configuration exhibits the strongest binding with a binding energy of −1.86 eV. Glu binding configurations involving 4-coordinate and 5-coordinate cobalt on the (111) and (211) surfaces were generally less favorable, with binding energies of approximately −0.3 eV.

Though the results show an increase in binding strength with increasing facet index, it can be suggested that the key requirement for strong Glu binding and electrooxidation is the involvement of the distorted trigonal 3-coordinate geometry of cobalt on the surface, edge, or vertex, where the O1 and O2 of Glu can chelate, regardless of the facet, neighboring uncoordinated phosphate oxygens. Interestingly, the most energetically favorable binding is associated with maximizing the number of electrostatic contacts (e.g., coordinate bonds and hydrogen bonds), while minimizing the overall contact area (Table S3). Therefore, we suggest that the under-coordinated Co surface presentation scenarios associated with more highly faceted surfaces offer a greater distribution of electrostatic contacts, ultimately resulting in greater interactions with Glu.

Detection of Glucose in HS. The ability of CPNs to oxidize Glu suggests that they can be applied to biological samples, such as HS. To examine the use of CPNs for the detection of Glu in a complex matrix, such as HS, a SPE (Figure S12) with a dropcasted suspension of CPNs was used.

SPEs are suitable for the sensing of Glu owing to their miniaturized, portable, and disposable nature.[72] Figure 5a shows the calibration curves based on the chronoamperometric responses of CPN-modified SPE upon addition of Glu in separate diluted solutions of HS, namely, HS 1, 2, 5, 10% v/v in PBS, at an applied constant potential of 0.65 V (Figure S13). The error bars in Figure 5a represent the standard deviation of the steady-state current density at a given Glu concentration. The parameters of the fittings are shown in Table S2. The concentrations studied span up to 35 mM Glu, showing the broad detection range of CPNs. However, with an increase in the content of HS in PBS, a decrease in CPN sensitivity and an increase in LOD were observed, possibly owing to the fouling of biochemical species on the electrode surface (Figure S14). Nevertheless, CPNs still show responsiveness toward the electrooxidation of Glu. Surface fouling from proteins, peptides, and lipids present in a biological matrix can inhibit electron transfers on an electrochemically active surface, causing a reduction in analytical performances, such as sensitivity, detection limit, and reproducibility.[73] This surface fouling causes deactivation of the electroactive sites, resulting in the decrease in electrocatalytic current relative to the oxidation of Glu. The stability of CPNs in HS was also examined by recording 200 consecutive CV cycles in a 33 mM Glu HS 5% in PBS (Figure 5b). Throughout the 200 cycles, CPNs showed no apparent decrease in current density at 0.65 V, as shown in the inset of Figure 5b, indicating its long service life and reliability. Future studies will focus on improving the system with various strategies in order to minimize protein, peptide, and lipid fouling. Such strategies can involve the surface coverage of the electrode with antifouling materials, such as polyvinylpyrrolidone or polyethylene glycol, or pre-filtering the HS to remove the fouling substances.

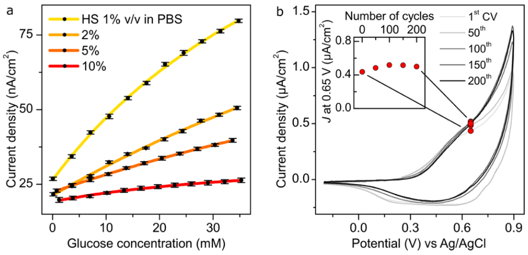

Figure 5. (a) Calibration curves with the relative fittings based on the chronoamperometric response of the CPN-modified SPE in the electrolyte composed of HS diluted with PBS (10 mM, pH 7.4) to the successive addition of Glu at an applied potential of 0.65 V (vs Ag/AgCl) (the raw data prior to fitting are shown in Figure S13). (b) Consecutive CVs of CPNs in a 33 mM Glu HS 5% v/v in PBS electrolyte after activation. The inset shows the changes in the current density at 0.65 V (vs Ag/AgCl) as the cycle number is increased from 1 to 200. All current density data are normalized by the ESA.

■ CONCLUSIONS

We reported the synthesis of electrocatalytically active CPNs using a simple, low-cost, and scalable crystallization method. We investigated the electrocatalytic properties of CPNs for non-enzymatic Glu detection—rod-printed electrodes and SPEs were modified with CPNs for the catalyzed oxidation of Glu in a relevant biological environment, such as PBS electrolyte, at physiological pH of 7.4. The CPNs achieved a wide Glu detection range (from 1 to 30 mM Glu in PBS) with a sensitivity of 7.90 nA/mM cm^2 at 5 mM of Glu (based on the ESA of the electrode) and a LOD of 0.3 mM. The CPN system was stable—no drifts in the current density were observed during the determination of Glu in both PBS and diluted solutions of HS, thus suggesting the longevity and reliability of the CPN system. Additionally, CPNs displayed negligible catalytic activity toward the oxidation of coexisting interfering species, such as LA, GA, AA, and DP, thus demonstrating the specificity of the CPN system toward Glu detection. CPNs were applied in biologically relevant electrolytes, such as diluted solutions of HS in PBS, where CPNs achieved a wide detection range up to 35 mM Glu, with a sensitivity depending on the concentration of HS. DFT calculations suggested that the optimal binding of Glu occurred at under-coordinated cobalt atoms at the surface, edge, or vertex of the nanostructure. Our results suggest the potential application of CPN-modified electrodes for the non-enzymatic detection of Glu under biological conditions.

■ ASSOCIATED CONTENT

Ⓢ Supporting Information

The Supporting Information is available free of charge on the ACS Publications website at DOI: 10.1021/acsami.8b12966.

> EDX data, XPS survey, CV and CA experiments, photograph of SPE, fitting data, and DFT calculations (PDF)

■ AUTHOR INFORMATION

Corresponding Authors

*E-mail: fcaruso@unimelb.edu.au (Frank Caruso).
*E-mail: francesca.cavalieri@unimelb.edu.au (Francesca Cavalieri).

ORCID

Quinn A. Besford: 0000-0002-1779-9176
Andrew J. Christofferson: 0000-0003-0904-6630
Irene Yarovsky: 0000-0002-4033-5150
Frank Caruso: 0000-0002-0197-497X
Francesca Cavalieri: 0000-0001-5391-5069

Present Address

⊥Centre for Advanced 2D Materials, National University of Singapore, Singapore.

Author Contributions

All authors have given approval to the final version of the article.

Funding

This work was supported by the Australian Research Council (ARC) under a Future Fellowship (F. Cavalieri, FT140100873) and a National Health and Medical Research Council Fellowship (F. Caruso, APP1135806). This research was conducted and supported by the ARC Centre of Excellence in Convergent Bio-Nano Science and Technology (project number CE140100036). This work was also supported by a University of Melbourne Establishment Grant (F. Cavalieri).

Notes

The authors declare no competing financial interest.

■ ACKNOWLEDGMENTS

This work was performed in part at the Materials Characterisation and Fabrication Platform (MCFP) at the University of Melbourne and the Victorian Node of the Australian National Fabrication Facility (ANFF). TEM was undertaken at the Biosciences Microscopy Unit, School of Biosciences, University of Melbourne. We thank Roger Curtain from the Bio21 Advanced Microscopy Facility (University of Melbourne) for assistance with SEM, Alex Duan from the Melbourne TrACEES platform (trace analysis for chemical, earth and environmental sciences) for the support and XPS data analysis, and Prof. Francesco Ricci (University of Rome, Tor Vergata) for kindly providing the SPE. This research was undertaken with the assistance of resources and services from the National Computational Infrastructure (NCI), which is supported by the Australian Government.

■ REFERENCES

(1) Zhou, Z.-Y.; Tian, N.; Li, J.-T.; Broadwell, I.; Sun, S.-G. Nanomaterials of High Surface Energy with Exceptional Properties in Catalysis and Energy Storage. *Chem. Soc. Rev.* **2011**, *40*, 4167−4185.

(2) Martinez, C. J.; Hockey, B.; Montgomery, C. B.; Semancik, S. Porous Tin Oxide Nanostructured Microspheres for Sensor Applications. *Langmuir* **2005**, *21*, 7937−7944.

(3) Zhang, Y.-Z.; Wang, Y.; Cheng, T.; Lai, W.-Y.; Pang, H.; Huang, W. Flexible Supercapacitors Based on Paper Substrates: A New Paradigm for Low-Cost Energy Storage. *Chem. Soc. Rev.* **2015**, *44*, 5181−5199.

(4) Awazu, K.; Fujimaki, M.; Rockstuhl, C.; Tominaga, J.; Murakami, H.; Ohki, Y.; Yoshida, N.; Watanabe, T. A Plasmonic Photocatalyst Consisting of Silver Nanoparticles Embedded in Titanium Dioxide. *J. Am. Chem. Soc.* **2008**, *130*, 1676−1680.

(5) Chan, C. K.; Peng, H.; Liu, G.; McIlwrath, K.; Zhang, X. F.; Huggins, R. A.; Cui, Y. High-Performance Lithium Battery Anodes Using Silicon Nanowires. *Nat. Nanotechnol.* **2008**, *3*, 31−35.

(6) Voiry, D.; Yamaguchi, H.; Li, J.; Silva, R.; Alves, D. C. B.; Fujita, T.; Chen, M.; Asefa, T.; Shenoy, V. B.; Eda, G.; Chhowalla, M. Enhanced catalytic activity in strained chemically exfoliated WS_2 nanosheets for hydrogen evolution. *Nat. Mater.* **2013**, *12*, 850−855.

(7) Chen, A.; Peng, X.; Koczkur, K.; Miller, B. Super-Hydrophobic Tin Oxide Nanoflowers. *Chem. Commun.* **2004**, 1964−1965.

(8) Ge, J.; Lei, J.; Zare, R. N. Protein-inorganic hybrid nanoflowers. *Nat. Nanotechnol.* **2012**, *7*, 428−432.

(9) Zhang, Z.; Zhang, Y.; Song, R.; Wang, M.; Yan, F.; He, L.; Feng, X.; Fang, S.; Zhao, J.; Zhang, H. Manganese(II) Phosphate Nanoflowers as Electrochemical Biosensors for the High-Sensitivity Detection of Ractopamine. *Sens. Actuators, B* **2015**, *211*, 310−317.

(10) Wang, L.-B.; Wang, Y.-C.; He, R.; Zhuang, A.; Wang, X.; Zeng, J.; Hou, J. G. A New Nanobiocatalytic System Based on Allosteric Effect with Dramatically Enhanced Enzymatic Performance. *J. Am. Chem. Soc.* **2013**, *135*, 1272−1275.

(11) Kim, K. H.; Jeong, J.-M.; Lee, S. J.; Choi, B. G.; Lee, K. G. Protein-Directed Assembly of Cobalt Phosphate Hybrid Nanoflowers. *J. Colloid Interface Sci.* **2016**, *484*, 44−50.

(12) Luo, Y.-K.; Song, F.; Wang, X.-L.; Wang, Y.-Z. Pure Copper Phosphate Nanostructures with Controlled Growth: A Versatile Support for Enzyme Immobilization. *CrystEngComm* **2017**, *19*, 2996−3002.

(13) Theerthagiri, J.; Thiagarajan, K.; Senthilkumar, B.; Khan, Z.; Senthil, R. A.; Arunachalam, P.; Madhavan, J.; Ashokkumar, M. Synthesis of Hierarchical Cobalt Phosphate Nanoflakes and Their Enhanced Electrochemical Performances for Supercapacitor Applications. *ChemistrySelect* **2017**, *2*, 201−210.

(14) Chen, C.; Kang, Y.; Huo, Z.; Zhu, Z.; Huang, W.; Xin, H. L.; Snyder, J. D.; Li, D.; Herron, J. A.; Mavrikakis, M.; Chi, M.; More, K. L.; Li, Y.; Markovic, N. M.; Somorjai, G. A.; Yang, P.; Stamenkovic, V. R. Highly Crystalline Multimetallic Nanoframes with Three-Dimensional Electrocatalytic Surfaces. *Science* **2014**, *343*, 1339−1343.

(15) Klinkova, A.; Cherepanov, P. V.; Ryabinkin, I. G.; Ho, M.; Ashokkumar, M.; Izmaylov, A. F.; Andreeva, D. V.; Kumacheva, E. Shape-Dependent Interactions of Palladium Nanocrystals with Hydrogen. *Small* **2016**, *12*, 2450−2458.

(16) Klinkova, A.; De Luna, P.; Sargent, E. H.; Kumacheva, E.; Cherepanov, P. V. Enhanced Electrocatalytic Performance of Palladium Nanoparticles with High Energy Surfaces in Formic Acid Oxidation. *J. Mater. Chem. A* **2017**, *5*, 11582−11585.

(17) Popczun, E. J.; Roske, C. W.; Read, C. G.; Crompton, J. C.; McEnaney, J. M.; Callejas, J. F.; Lewis, N. S.; Schaak, R. E. Highly Branched Cobalt Phosphide Nanostructures for Hydrogen-Evolution Electrocatalysis. *J. Mater. Chem. A* **2015**, *3*, 5420−5425.

(18) Dong, X.-C.; Xu, H.; Wang, X.-W.; Huang, Y.-X.; Chan-Park, M. B.; Zhang, H.; Wang, L.-H.; Huang, W.; Chen, P. 3D Graphene-Cobalt Oxide Electrode for High-Performance Supercapacitor and Enzymeless Glucose Detection. *ACS Nano* **2012**, *6*, 3206−3213.

(19) Ji, X.; Zhang, R.; Shi, X.; Asiri, A. M.; Zheng, B.; Sun, X. Fabrication of Hierarchical CoP Nanosheet@Microwire Arrays via Space-Confined Phosphidation toward High-Efficiency Water Oxidation Electrocatalysis under Alkaline Conditions. *Nanoscale* **2018**, *10*, 7941−7945.

(20) Tian, J.; Cheng, N.; Liu, Q.; Xing, W.; Sun, X. Cobalt Phosphide Nanowires: Efficient Nanostructures for Fluorescence Sensing of Biomolecules and Photocatalytic Evolution of Dihydrogen from Water under Visible Light. *Angew. Chem., Int. Ed.* **2015**, *54*, 5493−5497.

(21) Xie, F.; Liu, T.; Xie, L.; Sun, X.; Luo, Y. Metallic Nickel Nitride Nanosheet: An Efficient Catalyst Electrode for Sensitive and Selective Non-Enzymatic Glucose Sensing. *Sens. Actuators, B* **2018**, *255*, 2794−2799.

(22) Liu, T.; Xie, L.; Yang, J.; Kong, R.; Du, G.; Asiri, A. M.; Sun, X.; Chen, L. Self-Standing CoP Nanosheets Array: A Three-Dimensional Bifunctional Catalyst Electrode for Overall Water Splitting in Both Neutral and Alkaline Media. *ChemElectroChem* **2017**, *4*, 1840−1845.

(23) Han, L.; Yang, D.-P.; Liu, A. Leaf-Templated Synthesis of 3D Hierarchical Porous Cobalt Oxide Nanostructure as Direct Electrochemical Biosensing Interface with Enhanced Electrocatalysis. *Biosens. Bioelectron.* **2015**, *63*, 145−152.

(24) Ferri, S.; Kojima, K.; Sode, K. Review of Glucose Oxidases and Glucose Dehydrogenases: A Bird's Eye View of Glucose Sensing Enzymes. *J. Diabetes Sci. Technol.* **2011**, *5*, 1068−1076.

(25) Sun, J.; Ge, J.; Liu, W.; Lan, M.; Zhang, H.; Wang, P.; Wang, Y.; Niu, Z. Multi-enzyme co-embedded organic-inorganic hybrid nanoflowers: synthesis and application as a colorimetric sensor. *Nanoscale* **2014**, *6*, 255−262.

(26) Santana-Jiménez, L.; Márquez-Lucero, A.; Osuna, V.; Estrada-Moreno, I.; Dominguez, R. Naked-Eye Detection of Glucose in Saliva with Bienzymatic Paper-Based Sensor. *Sensors* **2018**, *18*, 1071.

(27) Russell, R. J.; Pishko, M. V.; Gefrides, C. C.; McShane, M. J.; Coté, G. L. A Fluorescence-Based Glucose Biosensor Using Concanavalin A and Dextran Encapsulated in a Poly(ethylene glycol) Hydrogel. *Anal. Chem.* **1999**, *71*, 3126−3132.

(28) Sun, X.; James, T. D. Glucose Sensing in Supramolecular Chemistry. *Chem. Rev.* **2015**, *115*, 8001−8037.

(29) Chen, X.; Tian, X.; Zhao, L.; Huang, Z.; Oyama, M. Nonenzymatic Sensing of Glucose at Neutral pH Values Using a Glassy Carbon Electrode Modified with Graphene Nanosheets and Pt-Pd Bimetallic Nanocubes. *Microchim. Acta* **2014**, *181*, 783−789.

(30) Mei, H.; Wu, W.; Yu, B.; Li, Y.; Wu, H.; Wang, S.; Xia, Q. Non-Enzymatic Sensing of Glucose at Neutral pH Values Using a Glassy Carbon Electrode Modified with Carbon Supported Co@Pt Core-Shell Nanoparticles. *Microchim. Acta* **2015**, *182*, 1869−1875.

(31) Koschinsky, T.; Heinemann, L. Sensors for glucose monitoring: technical and clinical aspects. *Diabetes/Metab. Res. Rev.* **2001**, *17*, 113−123.

(32) Wilson, R.; Turner, A. P. F. Glucose Oxidase: An Ideal Enzyme. *Biosens. Bioelectron.* **1992**, *7*, 165−185.

(33) Yuan, J. H.; Wang, K.; Xia, X. H. Highly Ordered Platinum-Nanotubule Arrays for Amperometric Glucose Sensing. *Adv. Funct. Mater.* **2005**, *15*, 803−809.

(34) Soomro, R. A.; Akyuz, O. P.; Ozturk, R.; Ibupoto, Z. H. Highly Sensitive Non-Enzymatic Glucose Sensing Using Gold Nanocages as Efficient Electrode Material. *Sens. Actuators, B* **2016**, *233*, 230−236.

(35) Sun, Y.; Buck, H.; Mallouk, T. E. Combinatorial Discovery of Alloy Electrocatalysts for Amperometric Glucose Sensors. *Anal. Chem.* **2001**, *73*, 1599−1604.

(36) Ding, Y.; Wang, Y.; Su, L.; Bellagamba, M.; Zhang, H.; Lei, Y. Electrospun Co_3O_4 nanofibers for sensitive and selective glucose detection. *Biosens. Bioelectron.* **2010**, *26*, 542−548.

(37) Premlatha, S.; Sivasakthi, P.; Ramesh Bapu, G. N. K. Electrodeposition of a 3D hierarchical porous flower-like cobalt-MWCNT nanocomposite electrode for non-enzymatic glucose sensing. *RSC Adv.* **2015**, *5*, 74374−74380.

(38) Jiang, D.; Liu, Q.; Wang, K.; Qian, J.; Dong, X.; Yang, Z.; Du, X.; Qiu, B. Enhanced Non-Enzymatic Glucose Sensing Based on Copper Nanoparticles Decorated Nitrogen-Doped Graphene. *Biosens. Bioelectron.* **2014**, *54*, 273−278.

(39) Huang, B.; Wang, Y.; Lu, Z.; Du, H.; Ye, J. One Pot Synthesis of Palladium-Cobalt Nanoparticles over Carbon Nanotubes as a Sensitive Non-Enzymatic Sensor for Glucose and Hydrogen Peroxide Detection. *Sens. Actuators, B* **2017**, *252*, 1016−1025.

(40) Kang, L.; He, D.; Bie, L.; Jiang, P. Nanoporous Cobalt Oxide Nanowires for Non-Enzymatic Electrochemical Glucose Detection. *Sens. Actuators, B* **2015**, *220*, 888−894.

(41) Hoa, L. T.; Chung, J. S.; Hur, S. H. A Highly Sensitive Enzyme-Free Glucose Sensor Based on Co_3O_4 Nanoflowers and 3D Graphene Oxide Hydrogel Fabricated via Hydrothermal Synthesis. *Sens. Actuators, B* **2016**, *223*, 76−82.

(42) Liu, T.; Li, M.; Dong, P.; Zhang, Y.; Guo, L. Design and Facile Synthesis of Mesoporous Cobalt Nitride Nanosheets Modified by Pyrolytic Carbon for the Nonenzymatic Glucose Detection. *Sens. Actuators, B* **2018**, *255*, 1983−1994.

(43) Soomro, R. A.; Ibupoto, Z. H.; Sirajuddin, M. I.; Abro, M. I.; Willander, M. Electrochemical Sensing of Glucose Based on Novel Hedgehog-Like NiO Nanostructures. *Sens. Actuators, B* **2015**, *209*, 966−974.

(44) Anderson, J. B.; Kostiner, E.; Miller, M. C.; Rea, J. R. The crystal structure of cobalt orthophosphate $Co_3(PO_4)_2$. *J. Solid State Chem.* **1975**, *14*, 372−377.

(45) Kresse, G.; Furthmüller, J. Efficient iterative schemes forab initiototal-energy calculations using a plane-wave basis set. *Phys. Rev. B: Condens. Matter Mater. Phys.* **1996**, *54*, 11169−11186.

(46) Perdew, J. P.; Burke, K.; Ernzerhof, M. Generalized Gradient Approximation Made Simple. *Phys. Rev. Lett.* **1996**, *77*, 3865−3868.

(47) Kresse, G.; Joubert, D. From Ultrasoft Pseudopotentials to the Projector Augmented-Wave Method. *Phys. Rev. B: Condens. Matter Mater. Phys.* **1999**, *59*, 1758−1775.

(48) Blöchl, P. E. Projector Augmented-Wave Method. *Phys. Rev. B: Condens. Matter Mater. Phys.* **1994**, *50*, 17953−17979.

(49) Monkhorst, H. J.; Pack, J. D. Special Points for Brillouin-Zone Integrations. *Phys. Rev. B: Solid State* **1976**, *13*, 5188−5192.

(50) Wang, L.; Maxisch, T.; Ceder, G. Oxidation Energies of Transition Metal Oxides within the GGA+U Framework. *Phys. Rev. B: Condens. Matter Mater. Phys.* **2006**, *73*, 195107.

(51) Kim, H.; Park, J.; Park, I.; Jin, K.; Jerng, S. E.; Kim, S. H.; Nam, K. T.; Kang, K. Coordination Tuning of Cobalt Phosphates towards Efficient Water Oxidation Catalyst. *Nat. Commun.* **2015**, *6*, 8253.

(52) Cabrera-German, D.; Gomez-Sosa, G.; Herrera-Gomez, A. Accurate peak fitting and subsequent quantitative composition analysis of the spectrum of Co 2pobtained with Al Kα radiation: I: cobalt spinel. *Surf. Interface Anal.* **2016**, *48*, 252−256.

(53) Biesinger, M. C.; Payne, B. P.; Grosvenor, A. P.; Lau, L. W. M.; Gerson, A. R.; Smart, R. S. C. Resolving Surface Chemical States in XPS Analysis of First Row Transition Metals, Oxides and Hydroxides: Cr, Mn, Fe, Co and Ni. *Appl. Surf. Sci.* **2011**, *257*, 2717−2730.

(54) Sun, Q.-Q.; Wang, M.; Bao, S.-J.; Wang, Y. C.; Gu, S. Analysis of Cobalt Phosphide (CoP) Nanorods Designed for Non-Enzyme Glucose Detection. *Analyst* **2016**, *141*, 256−260.

(55) Dzyuba, E. D.; Shchegrov, L. N.; Pechkovskii, V. V.; Mel'nikova, R. Y. Infrared Absorption Spectra of Disubstituted Cobalt Phosphate. *J. Appl. Spectrosc.* **1970**, *12*, 666−669.

(56) Corbridge, D. E. C.; Lowe, E. J. The Infra-Red Spectra of Inorganic Phosphorus Compounds. Part II. Some Salts of Phosphorus Oxy-Acids. *J. Chem. Soc.* **1954**, 4555−4564.

(57) Tang, C.-W.; Wang, C.-B.; Chien, S.-H. Characterization of Cobalt Oxides Studied by FT-IR, Raman, TPR and TG-MS. *Thermochim. Acta* **2008**, *473*, 68−73.

(58) Acerce, M.; Voiry, D.; Chhowalla, M. Metallic 1T phase MoS_2 nanosheets as supercapacitor electrode materials. *Nat. Nanotechnol.* **2015**, *10*, 313−318.

(59) Kannan, P.; Maiyalagan, T.; Marsili, E.; Ghosh, S.; Niedziolka-Jönsson, J.; Jönsson-Niedziolka, M. Hierarchical 3-dimensional nickel-iron nanosheet arrays on carbon fiber paper as a novel electrode for non-enzymatic glucose sensing. *Nanoscale* **2016**, *8*, 843−855.

(60) Goyal, R. N.; Gupta, V. K.; Chatterjee, S. Voltammetric Biosensors for the Determination of Paracetamol at Carbon Nanotube Modified Pyrolytic Graphite Electrode. *Sens. Actuators, B* **2010**, *149*, 252−258.

(61) Konopka, S. J.; McDuffie, B. Diffusion Coefficients of Ferri- and Ferrocyanide Ions in Aqueous Media, Using Twin-Electrode Thin-Layer Electrochemistry. *Anal. Chem.* **1970**, *42*, 1741−1746.

(62) Yu, H.; Jin, J.; Jian, X.; Wang, Y.; Qi, G.-c. Preparation of Cobalt Oxide Nanoclusters/Overoxidized Polypyrrole Composite Film Modified Electrode and Its Application in Nonenzymatic Glucose Sensing. *Electroanalysis* **2013**, *25*, 1665−1674.

(63) Casella, I. G.; Gatta, M. Study of the Electrochemical Deposition and Properties of Cobalt Oxide Species in Citrate Alkaline Solutions. *J. Electroanal. Chem.* **2002**, *534*, 31−38.

(64) Tominaga, M.; Shimazoe, T.; Nagashima, M.; Taniguchi, I. Electrocatalytic Oxidation of Glucose at Gold Nanoparticle-Modified Carbon Electrodes in Alkaline and Neutral Solutions. *Electrochem. Commun.* **2005**, *7*, 189−193.

(65) Bruen, D.; Delaney, C.; Florea, L.; Diamond, D. Glucose Sensing for Diabetes Monitoring: Recent Developments. *Sensors* **2017**, *17*, 1866.

(66) Padmanathan, N.; Shao, H.; Razeeb, K. M. Multifunctional Nickel Phosphate Nano/Microflakes 3D Electrode for Electrochemical Energy Storage, Nonenzymatic Glucose, and Sweat pH Sensors. *ACS Appl. Mater. Interfaces* **2018**, *10*, 8599−8610.

(67) Arthur, P. G.; Kent, J. C.; Potter, J. M.; Hartmann, P. E. Lactose in Blood in Nonpregnant, Pregnant, and Lactating Women. *J. Pediatr. Gastroenterol. Nutr.* **1991**, *13*, 254−259.

(68) Schadewaldt, P.; Hammen, H.-W.; Loganathan, K.; Bodner-Leidecker, A.; Wendel, U. Analysis of Concentration and ^{13}C enrichment of d-Galactose in Human Plasma. *Clin. Chem.* **2000**, *46*, 612−619.

(69) Sargent, F. A Study of the Normal Distribution of Ascorbic Acid between the Red Cells and Plasma of Human Blood. *J. Biol. Chem.* **1947**, *171*, 471−476.

(70) Ambade, V.; Arora, M. M.; Singh, P.; Somani, B. L.; Basannar, D. Adrenaline, Noradrenaline and Dopamine Level Estimation in Depression : Does it Help? *Med. J. Armed Forces India* **2009**, *65*, 216−220.

(71) Park, S.; Chung, T. D.; Kim, H. C. Nonenzymatic Glucose Detection Using Mesoporous Platinum. *Anal. Chem.* **2003**, *75*, 3046−3049.

(72) Choudhry, N. A.; Kampouris, D. K.; Kadara, R. O.; Jenkinson, N.; Banks, C. E. Next Generation Screen Printed Electrochemical Platforms: Non-Enzymatic Sensing of Carbohydrates Using Copper-(II) Oxide Screen Printed Electrodes. *Anal. Methods* **2009**, *1*, 183−187.

(73) Hanssen, B. L.; Siraj, S.; Wong, D. K. Y. Recent Strategies to Minimise Fouling in Electrochemical Detection Systems. *Rev. Anal. Chem.* **2016**, *35*, 1−28.

3.2 Supplementary Information

Supporting Information

Cobalt Phosphate Nanostructures for Non-Enzymatic Glucose Sensing at Physiological pH

Pietro Pacchin Tomanin,[†] *Pavel V. Cherepanov,*[†,⊥] *Quinn A. Besford,*[†] *Andrew J. Christofferson,*[‡] *Alessia Amodio,*[#] *Chris F. McConville,*[§] *Irene Yarovsky,*[‡] *Frank Caruso,*[*,†] *and Francesca Cavalieri*[*,†,#]

[†]ARC Centre of Excellence in Convergent Bio-Nano Science and Technology, and the Department of Chemical Engineering, The University of Melbourne, Parkville, Victoria 3010, Australia

[‡]School of Engineering, RMIT University, GPO Box 2476, Melbourne, Victoria 3001, Australia

[§]College of Science, Engineering and Health, RMIT University, GPO Box 2476, Melbourne, Victoria 3001, Australia

[#]Department of Chemistry, University of Rome Tor Vergata, Via Della Ricerca Scientifica 1, 00133 Rome, Italy

Present Address

[⊥]Centre for Advanced 2D Materials, National University of Singapore, Singapore.

*Corresponding authors. fcaruso@unimelb.edu.au; francesca.cavalieri@unimelb.edu.au

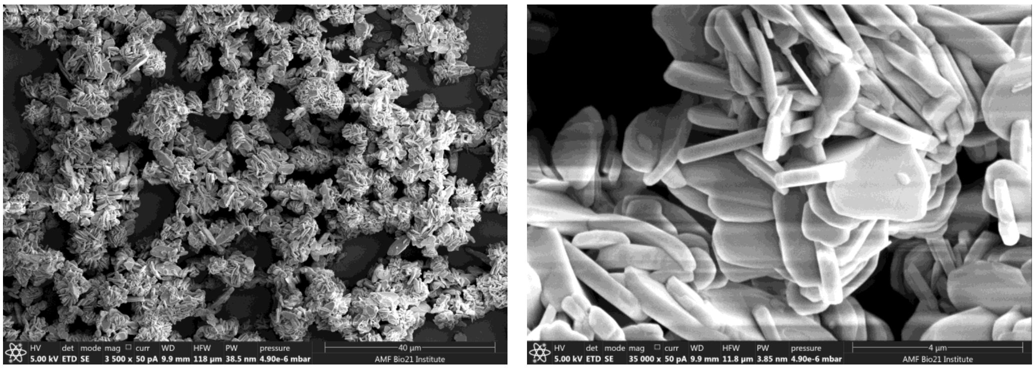

Figure S1. Scanning electron microscopy (SEM) images of commercial $Co_3(PO_4)_2$ powder at various magnifications.

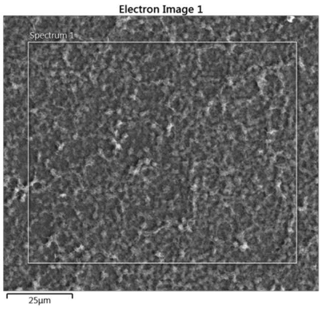

Element	Line type	Apparent concentration	wt%	wt% Sigma	at. %	Standard Label
C	K series	0.02	3.56	0.20	7.84	C Vit
O	K series	0.73	18.02	0.20	29.71	SiO_2
Si	K series	1.52	51.88	0.45	48.72	SiO_2
P	K series	0.16	4.59	0.09	3.91	GaP
Co	K series	0.45	21.95	0.63	9.82	Co
Total			100.00		100.00	

Figure S2. SEM image of the cobalt phosphate nanostructures (CPN) sample showing the region of interest on which energy-dispersive X-ray spectroscopy (EDX) was conducted and associated EDX data. (The EDX pattern is shown in Figure 1f.)

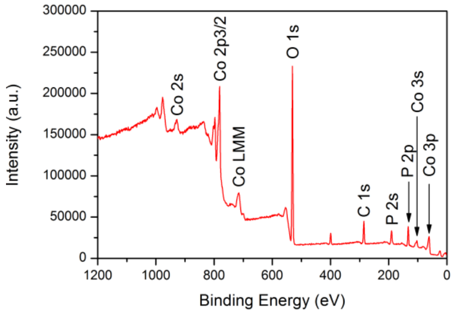

Figure S3. X-ray photoelectron spectroscopy survey spectrum of the CPN.

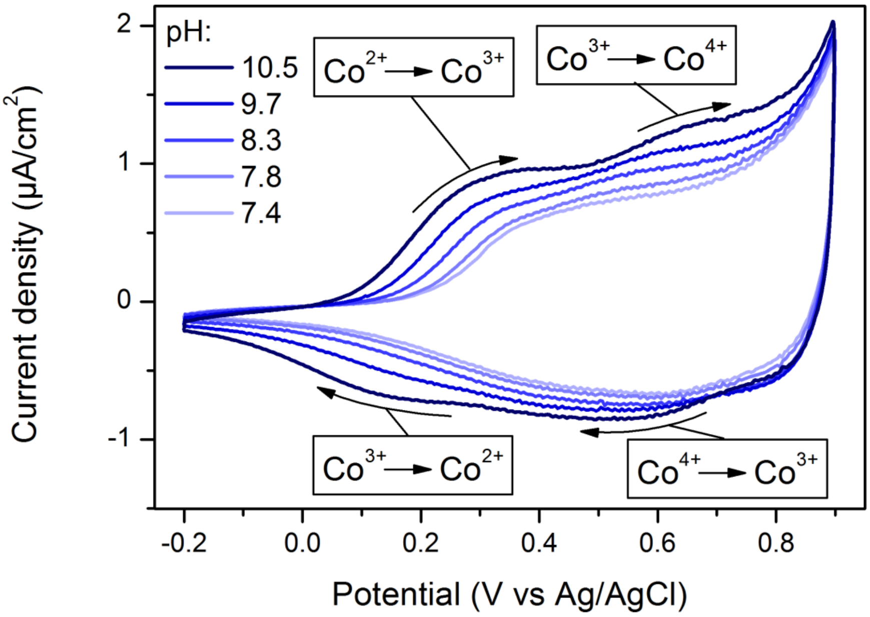

Figure S4. Cyclic voltammograms of the CPN-modified glassy carbon electrode (GCE) measured in PBS electrolyte at different pHs and a scan rate of 20 mV s^{-1}.

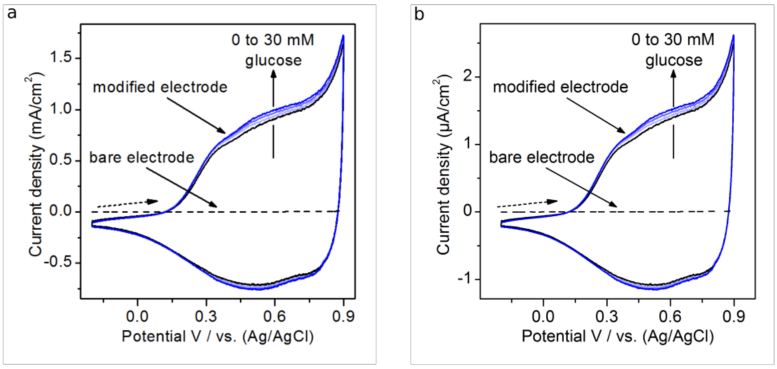

Figure S5. CVs of the CPN-modified electrode in PBS buffer (10 mM, pH 7.4) recorded at a scan rate of 20 mV/s in the absence (black line) and presence (blue lines) of 10, 20, and 30 mM Glu, respectively. The dashed line represents the CV of the GCE (bare electrode) obtained under the same experimental conditions. In (a) and (b), the reported current densities are normalized against the geometrical area and the real surface area of the electrode, respectively.

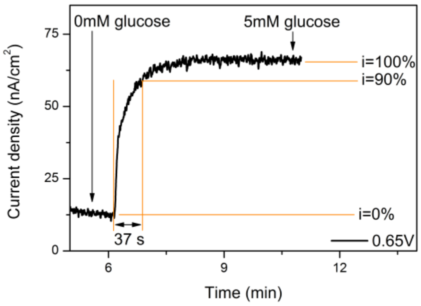

Figure S6. Chronoamperometric response of the CPN to the addition of 5 mM of glucose (Glu) in a 0 mM Glu PBS electrolyte. A constant applied potential of 0.65 V was used.

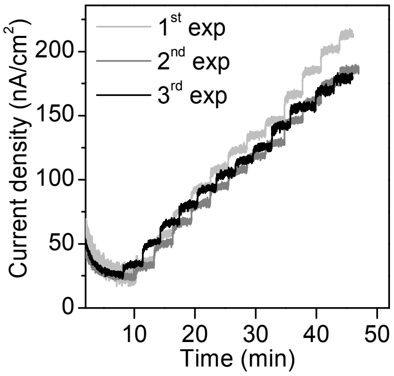

Figure S7. Chronoamperometric responses of the CPN-modified GCE in PBS buffer (10 mM, pH 7.4) to successive addition of Glu at an applied potential of 0.65 V (vs Ag/AgCl). The data of three successive experiments (exp) conducted using the same prepared electrode are shown. The data were used to construct the calibration curve in Figure 3d.

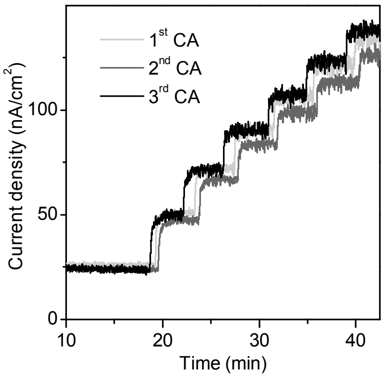

Figure S8. Chronoamperometric responses of $Co_3(PO_4)_2$ powder-modified GCE in PBS buffer (10 mM, pH 7.4) to successive addition of Glu at an applied potential of 0.65 V (vs Ag/AgCl).

The data of three successive experiments performed using the same electrode are shown. The data were used to construct the calibration curve in Figure S9.

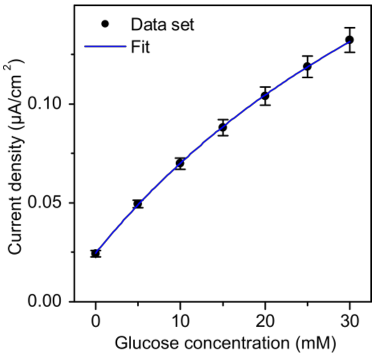

Figure S9. Calibration curve based on CA experiments performed in triplicate (Figure S8).

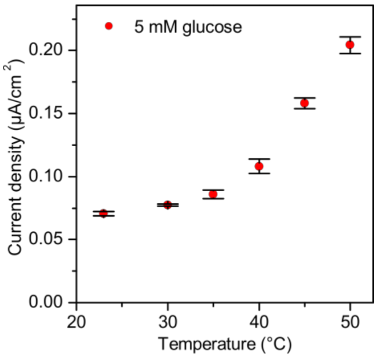

Figure S10. Amperometric responses of the CPN-modified GCE to addition of 5 mM Glu in PBS electrolyte as a function of the electrolyte temperature

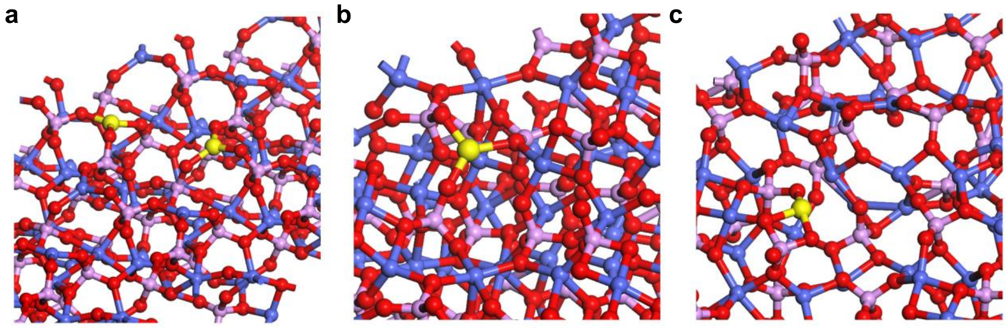

Figure S11. Relaxed slabs of cobalt phosphate: (a) (100), (b) (111), and (c) (211) surfaces. Cobalt, phosphorous, and oxygen are represented as blue, purple, and red spheres, respectively. Cobalt atoms that coordinate to glucose are highlighted in yellow.

Table S1. Parameters Obtained from the Fittings shown in Figure 2c

	intercept (μA/cm^2)	slope ((mV/s)$^{1/2}$ μA/cm^2)	R^2
Oxidation peak current (Ox, black line)	−5.8 ± 0.3	1.86 ± 0.05	0.996
Reduction peak current (Red, red line)	3.4 ± 0.3	−1.21 ± 0.04	0.992

Equation S1 was used to fit the data in Figures 3d and 5a:

$$i = \frac{b+c[Glu]}{1+a[Glu]} \tag{S1}$$

where i (μA/cm^2) is the current density and [Glu] (mM) is the bulk concentration of Glu. The values of the fitting equations are listed in Table S2.

The sensitivity (nA/mM cm^2) was calculated from the tangent of the functions used to fit the 5 mM glucose data in Figure 3d. A glucose concentration of 5 mM was chosen because this concentration is the homeostatic concentration of the analyte in human blood. The derivative of Equation S1, which is described as Equation S2, was used as the fitting equation reported in Figure 3d:

$$\text{Sensitivity} = \frac{\mathrm{d}i}{\mathrm{d}[Glu]} = \frac{(c-ab)}{(a[Glu]+1)^2} \tag{S2}$$

where i (μA/cm^2) is the current density, [Glu] (mM) is the bulk concentration of Glu, and a, b and c are the values of the fitting Equation S1.

The detection limit, or known as limit of detection (LOD), is calculated on the basis of the standard deviation (σ_{sd}) of the blank chronoamperometric current density (PBS with 0 mM of glucose) and the sensitivity (α) as previously calculated at a signal-to-noise ratio of 3, using the Equation S3 as follows:

$$\mathrm{LOD} = 3\sigma_{\mathrm{sd}}/\alpha \tag{S3}$$

Table S2. Parameters from the Fittings Shown in Figures 3d and 5a

fit number	electrode	electrolyte	Figure number	*a*	*b*	*c*	adjusted R^2
1	CPN	PBS	3d	0.0279 ± 0.0005	24.98 ± 0.06	10.96 ± 0.08	0.999
2	CPN	HS 1% v/v in PBS	5a	0.0163 ± 0.0015	26.5 ± 0.4	2.85 ± 0.12	0.999
3	CPN	HS 2% v/v in PBS	5a	0.006 ± 0.002	21.2 ± 0.5	1.17 ± 0.13	0.996
4	CPN	HS 5% v/v in PBS	5a	0.0067 ± 0.0007	22.38 ± 0.09	0.78 ± 0.03	0.999
5	CPN	HS 10% v/v in PBS	5a	0.022 ± 0.005	19.1 ± 0.2	0.79 ± 0.12	0.994
6	$Co_3(PO_4)_2$	PBS	S9	0.01601 ± 0.0009	24.5 ± 0.2	5.7 ± 0.1	0.999

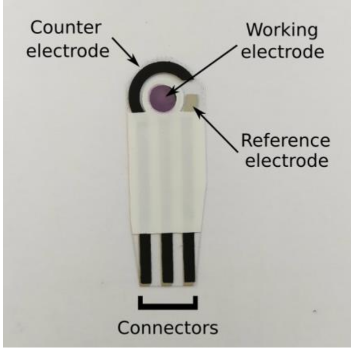

Figure S12. Screen-printed electrode modified with the CPN.

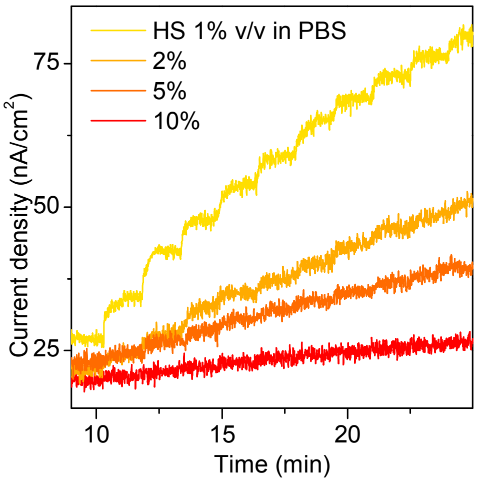

Figure S13. Chronoamperometric responses of the CPN-modified SPE in PBS electrolyte (10 mM, pH 7.4) containing 1, 2, 5, and 10% v/v of HS to successive addition of Glu at an applied potential of 0.65 V (vs Ag/AgCl). The corresponding calibration curves with the relative fittings are displayed in Figure 5a.

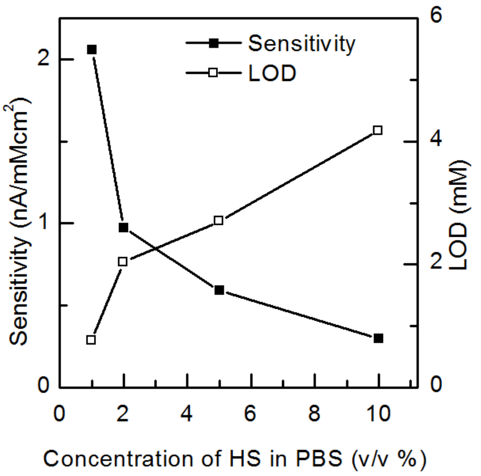

Figure S14. Sensitivity and limit of detection (LOD) of the CPN-modified SPE in PBS buffer as a function of concentration of human serum (HS) based on data from Figure 5a.

Table S3. Total Energies, Binding Energies, Percentage of Glucose Solvent-Accessible Surface Area in Contact with the Cobalt Phosphate Surface, Coordinate Bonds, And Hydrogen Bonds for the (100), (111), And (211) Relaxed Surfaces of Cobalt Phosphate[a]

system	energy (ev)	binding energy (ev)	glucose contact area (%)	coordinate bonds	hydrogen bonds
Glucose	−138.05				
(100) surface	−695.35				
(111) surface	−694.37				
(211) surface	−689.32				
Glucose on (100) surface	−834.82	−1.42	39	2 (different Co)	2
Glucose on (111) surface	−833.95	−1.52	33	2 (same Co)	2
Glucose on (211) surface	−829.22	−1.86	26	2 (same Co)	3

[a] All surfaces comprised 24 cobalt, 16 phosphorous, and 64 oxygen atoms.

Chapter 4

Enzyme-Mimicking Hybrid Nanoflowers Enable Sensing of Bioanalytes

Pietro Pacchin Tomanin[a], Frank Caruso[a], Francesca Cavalieri[b,c]

[a] *ARC Centre of Excellence in Convergent Bio-Nano Science and Technology, and the Department of Chemical Engineering, The University of Melbourne, Parkville, Victoria 3010, Australia. E-mail: fcaruso@unimelb.edu.au*

[b] *School of Science, RMIT University, Melbourne, Victoria 3000, Australia. E-mail: francesca.cavalieri@rmit.edu.au*

[c] *Dipartimento di Scienze e Tecnologie Chimiche, Università di Roma ''Tor Vergata'', via della ricerca scientifica 1, 00133, Rome, Italy. E-mail: francesca.cavalieri@rmit.edu.au*

4.1 Manuscript main text

4.1.1 Abstract

We report the synthesis of dextran sulfate-copper phosphate hybrid nanoflowers (D-NF) with a high surface-to-volume ratio and catalytic properties by a facile and rapid crystallization process in aqueous solution. The D-NF were assembled on surfaces to operate as microreactors. These nanostructured surfaces showed intrinsic non-enzymatic peroxidase-like catalytic activity that was utilized for the detection of hydrogen peroxide (H_2O_2). The limit of detection (LOD, S/N=3) and sensitivity of these catalytic surfaces for H_2O_2 were 35 μM and 28.3±0.6 kcps/mM respectively in PBS (1X, pH 6.5). The D-NF were further combined with glucose oxidase to obtain a glucose-sensing platform via a hybrid enzymatic/non-enzymatic cascade reaction. The glucose sensor showed a LOD of 35 μM and a sensitivity of 1180±70 cps/mM in PBS. Our results revealed the potential of copper phosphate-based nanoflowers as enzyme-mimicking materials for sensing biochemical analytes.

4.1.2 Introduction

Nanoflowers (NF) have attracted an incredibly growing interest in recent years due to their unique properties, advancing the fields of catalysis,[1-2] sensing,[3] and nanomedicine.[4] NF are hybrid materials composed by an organic and inorganic part such as respectively, proteins, polysaccharides, enzymes and various metal phosphate salts.[5-7] These materials exhibit hierarchical structures that span from the micro- to the nano-scale endowing them with a high surface-to-volume ratio. In particular, enzymes-containing nanoflowers exhibit enhanced enzymatic catalytic activity and stability due to the biomolecule immobilization within the organized inorganic architecture.[1]

Despite numerous studies reported the syntheses of functional NF in the last years, some problems in the engineering of these materials remain, limiting their widespread use. Namely, hybrid nanoflowers require costly biomacromolecules, e.g. enzymes, for their synthesis and their catalytic activity is strictly related to the used enzyme. Moreover, nanoflowers have been scarcely applied for the preparation of functional surfaces. To overcome these issues, nanoflowers were prepared using readily available and inexpensive organic molecules as polysaccharides,[8] biosurfactants,[9] amino acids,[10] and proteins[11-12] for environmental and catalytic applications. Furthermore, copper-based nanoflowers displayed catalytic activity via a Fenton-like reaction that involved the metal centre, regardless of the nanoflowers organic composition. Such materials were reported to have non-enzymatic biomimetic peroxidase-like[10, 13] and oxidase-like[11] activity. Recently functional nanoflowers were employed to develop paper-based sensors,[14] graphene-based sorbents[15] and membrane-based catalysts.[16] However, difficulties in obtaining homogeneous hierarchical structures were encountered and laborious multi-steps procedures were required.

Here we report the synthesis of hybrid nanoflowers (D-NF) using dextran sulfate, a readily available polymer, and copper phosphate via a simple and rapid crystallization method in mild conditions. The synthetic parameters as pH, reactants concentrations and reaction time were varied to prepare nanoflowers with different morphologies. A single-step method to functionalize surfaces was developed to prepare catalytic micro-reactors. These structures displayed a non-enzymatic peroxidase-like catalytic activity for the production of hydroxyl radicals from hydrogen peroxide. The functionalized reactors were used as a fluorometric sensor to detect hydrogen peroxide using o-

Phenylenediamine (OPD) as the chromogenic substrate with a LOD of 35 µM (S/N=3). Furthermore, a glucose sensor was engineered combining glucose oxidase and D-NF relying on a hybrid enzymatic/non-enzymatic cascade reaction. The developed sensor allows the detection of glucose at neutral pH with a LOD of 35 µM. Our results highlight the potential of D-NF to assemble functional nanostructured biosensing surface for the detection of biochemical analytes.

4.1.3 Results and discussions

4.1.3.1 Synthesis and characterization of dextran sulfate-copper phosphate hybrid nanoflowers

Dextran sulfate-copper phosphate hybrid nanoflowers, D-NF, were prepared via a simple crystallization method (Figure 1a). In this, PBS (0.5 mL, 1X, pH 7.4) containing DS (1 mg mL^{-1}) was added to 0.1 mL of $CuSO_4$ (120 mM) solution under stirring for 60 s. Then, the solution was incubated statically at 21 °C for 16 h, after which blue precipitates were formed. It is known that copper-containing materials display non-enzymatic peroxidase-like catalytic activity, which involves the conversion of hydrogen peroxide (H_2O_2) to the highly reactive hydroxyl free radical ($^{\bullet}OH$) via a Fenton-like reaction. Based on those assumptions, we hypothesized that the high surface-to-volume ratio and chemical composition of D-NF could be used to design a reusable, high-throughput, fluorometric platform for the rapid and sensitive detection of hydrogen peroxide (Figure 1b).

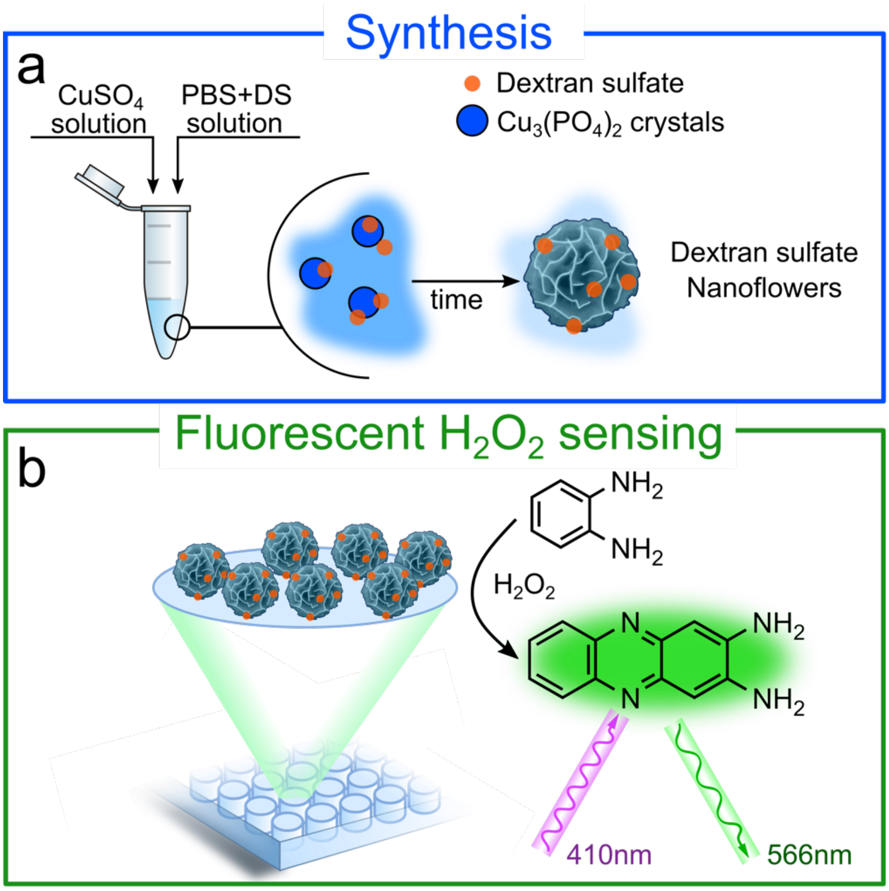

Figure 1. a) Schematic illustration of the preparation of dextran sulfate-copper phosphate hybrid nanoflowers and b) the nanoflowers-based platform for the detection of hydrogen peroxide.

To study the morphologies and investigate the chemical composition of the prepared D-NF, a comprehensive characterization was performed via SEM, TEM, FT-IR, EDX, XRD and TGA (Figure 2 and Figure S1 and S2). The dried D-NF appeared as a fine blue powder, typical colour of copper (II) based materials. Low and high magnification SEM images displayed, respectively, the D-NF homogeneous size distribution of 3.0±0.1 μm in diameter and the hierarchical architecture morphology of the particles, resulting from the nucleation and growth processes of nanosheets (Figure 2a). Low and high magnification TEM images showed, respectively, that the cores of the D-NF were denser than their surface and that their surface was composed by nanosheets of few nanometres in thickness (Figure 2b).

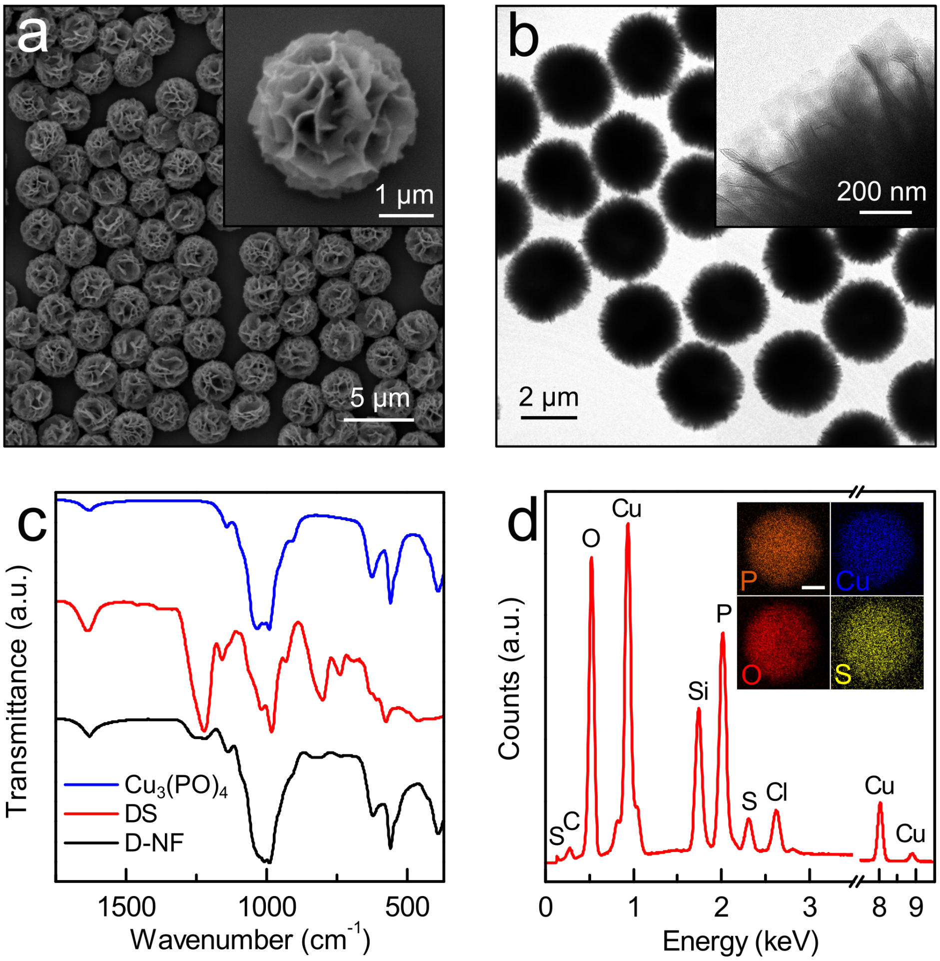

Figure 2. Characterization of hybrid dextran sulfate-copper phosphate nanoflowers. a) SEM and b) TEM images of the D-NF with, in the respective inserts, high magnification images. c) FT-IR spectra of pure copper phosphate, DS and hybrid D-NF. d) EDX spectrum and, in the insert, mapping, of the D-NF.

FT-IR spectroscopy performed on D-NF indicated the presence of P-O and P=O vibrations with intense peaks at 390, 560, 625, 990 and 1035 cm^{-1}, ascribed to the presence of phosphate groups (Figure 2c).[17] Moreover, the FT-IR spectrum of D-NF showed the presence of bands in the regions from 1180 to 1300 cm^{-1} and 680 to 870 cm^{-1} ascribed to the vibrations relative to the sulfate groups in the DS, confirming the presence of DS in the hybrid nanoflowers.[18] EDX spectra and elemental mapping revealed the homogeneous presence of P, Cu, O, and S elements in the D-NF (Figure 2d). The XRD spectrum of the D-NF showed the presence of sharp diffraction peaks and an amorphous background (Figure S1). The peak position and relative intensities matched well with those of copper phosphate hydrate crystal structure (powder diffraction file number 22-0548). The broad peak centred at 20 degrees, instead, was attributed to the presence of amorphous DS within the nanoflowers structure.[19] The XRD analysis confirmed that the hybrid nanoflowers were composed of amorphous DS within a well-crystallized $Cu_3(PO_4)_2$ $3H_2O$ structure. TGA was employed to quantify the weight percentage of DS in the D-NF (Figure S2).[20] The TGA curve showed a weight loss of 8% above 100 °C, which is attributed to water desorption. Subsequently, a weight loss of 12% occurred from 100 to 440 °C due to the decomposition of DS.[21] From 440 to 600 °C there was no further weight loss, indicating that the inorganic component did not further decompose. Taken together the results confirmed the presence of DS within the inorganic nanostructure to form monodisperse, high volume-to-surface ratio and hybrid nanoflowers.

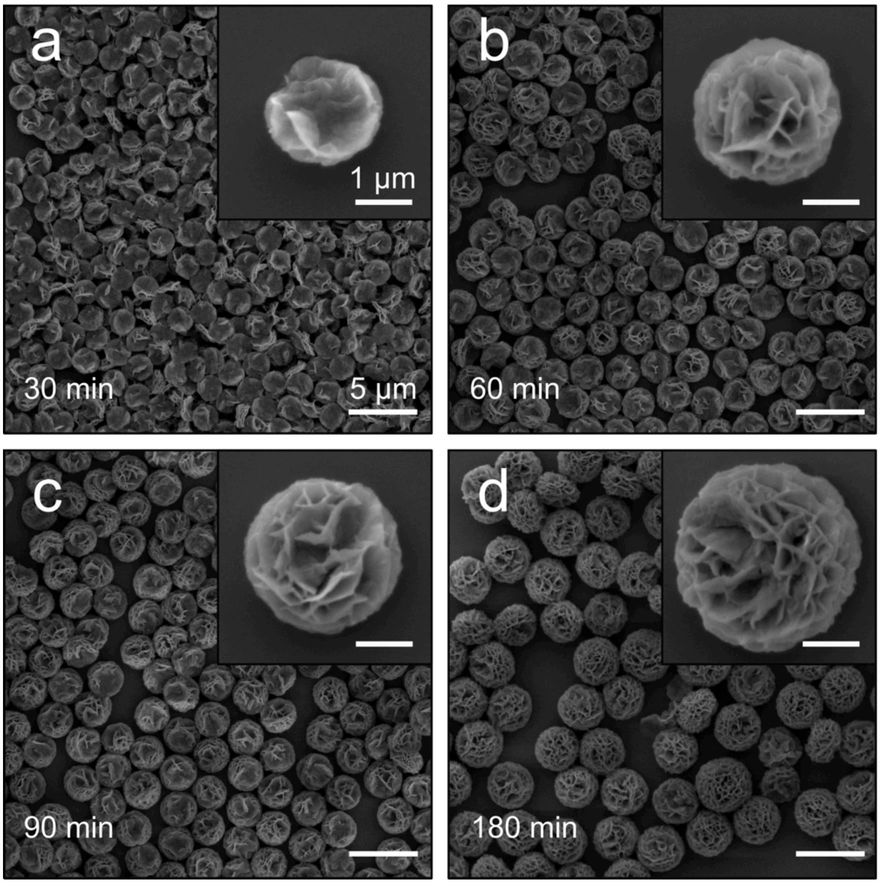

Figure 3. SEM images of the hybrid nanoflowers growth at a) 30, b) 60, c) 90 and d) 180 min from the start of the crystallization reaction. Scale bars reported are the same in all the figures.

To give an insight into the D-NF formation mechanism, different reaction times (30, 60, 90 and 180 min) were set and SEM images were acquired to analyse the surface morphologies of the obtained D-NF (Figure 3). The formation of porous D-NF follows steps of nucleation and growth. At an early reaction stage (30 min), the nucleation of small units of $Cu_3(PO_4)$ along with the complexation of DS with Cu ions, via electrostatic interactions, were observed (Figure 3a). These complexes provided sites for the nucleation of primary crystals. With increasing incubation times (60 and 90 min), kinetically controlled primary crystals grow on the pre-formed structure with the shape of petals, resulting in more petals to appear on the surface of the particles (Figure 3b and c). After 180 min, the anisotropic growth of the petals led to the complete formation of flowerlike spherical structures (Figure 3d). During these steps, DS may promote the nucleation of crystals to form the scaffold for the petals and served as a binder to assemble them into hierarchical structures. To prove this hypothesis and deeply understand the role of DS on the crystallization process of the hybrid nanoflowers, two different control syntheses were executed. First, the influence of the polymeric component during the particle formation was studied. Pure copper phosphates NF were prepared without the use of any organic component. The inorganic nanostructures were formed by large aggregates of several micrometre-sized particles, which were composed of disordered nanosheets assemblies, contrarily to the ordered structure prepared with DS (Figure S3a, b and Figure S4a ,b). We hypothesize that in the absence of the polymer the disorganized nucleation of the primary crystals occurred. Subsequently, the uncontrolled growth of the primary crystals resulted in the formation of large aggregates. Next, we investigated the influence of the chemical composition of the polymer. NF were synthesized using dextran, with a similar molecular weight of DS but lacking negatively charged sulfate groups. We observed that the obtained Dextran-NF were 9±1 mm in diameter, significantly larger than the diameters of D-NF, and showed some degree of aggregation (Figure S3c, d and Figure S4c). The dextran did not lead to a strong interaction between copper ions and the polymer, causing the primary crystals to nucleate differently compared to the case of D-NF. However, the presence of the organic component stabilized the growing particles resulting in the formation of fewer aggregates. It is important to note that in pure copper phosphates NF and Dextran-NF, the building blocks morphologies composing these structures resembled the one described before for the D-NF, suggesting the similar and, however, disordered assembled nature of the crystallization process. These findings indicated the essential role of DS in the crystallization process as the organic component for the nucleation of primary crystals, via the interaction between copper ions and negatively charged sulfate groups, and for the growing of the particles, as the stabilizing agent.

To optimize the final products, the parameters that could influence the crystallization process, such as the concentration of reagents and pH were investigated in details.

D-NF were prepared at different PBS concentrations, from 0.1 X to 10 X (Figure S5). At low PBS salt concentrations of 0.1 X and 0.2 X, no precipitates or particles were found. Defined particles with increasing diameter from 2.8±0.2 to 4.3±0.3 µm and similar surface morphology were achieved using 0.5 X and 2 X PBS (Figure S5a and b). Visible higher reaction yields were obtained with increased PBS concentration, due to the higher content of phosphate ions in the solution. At high PBS salt concentrations of 5 X and 10 X, there was no formation of NF although crystal-like structures in the form of aggregates were formed (Figure S5c and d). This suggests that the low concentration of phosphates does not allow the nucleation and growth of crystals, resulting in the absence of ordered precipitates. Contrarily, at higher concentration of phosphates, aggregates formed from the rapid nucleation of copper phosphates clusters, which did not lead to ordered nanoflowers assemblies.

Moreover, D-NF were synthesized investigating the concentration of copper ions from 2.5 to 160 mM (Figure S6). At the lowest concentration of copper ions of 2.5 mM, aggregated particles were formed showing sparingly petals on the surface resulting in micrometre-sized pores (Figure S6a). Instead, with copper ions concentrations from 5 to 160 mM, dispersed particles were found having diameters from 2 to 6 µm with an increased amount of petals on the surface resulting in a smaller petal-to-petal distance (Figure S6b-e). A noticeable higher yield was achieved with increasing copper ions concentrations.

D-NF were also prepared at different pH from 4.4 to 10.4 (Figure S7). No precipitates were formed at pH 4.4. Particles prepared at pH 5.4 had a low density of petals on the surface, resulting in uncompleted structures (Figure S7a). D-NF synthesized at pH from 6.4 to 10.4 were dispersed particles with a higher density of petals on the surface (Figure S7b-e).

Besides, the formation of D-NF varying the DS concentrations varying from 0.1 to 10 mg mL^{-1} was studied (Figure S8). Aggregated crystal-like structures were observed when the DS concentration was equal or lower than 0.17 mg mL^{-1} (Figure S8a and b), whereas uniform and dispersed flower-like microparticles formed when the DS concentration was equal or higher than 0.4 mg mL^{-1} (Figure S8c-f). The particles prepared with different concentrations of DS displayed similar hierarchical flower-like morphologies. These were composed of lamellae-like building blocks with a thickness of few tens of nanometres, joint together to form particles with an average diameter of around a few micrometres.

These findings indicated that dispersed and homogeneous D-NF could be prepared only within a specific range of pH, PBS, DS and copper ions concentrations. Moreover, D-NF having different morphological properties could be synthesized varying the studied synthetic parameters.

4.1.3.2 Preparation of D-NF functionalized surfaces

The crystallization process for the synthesis of hybrid nanoflowers is influenced by the initial nucleation of primary crystals via the interactions between metal ions and functional moieties, such as the electrostatic interactions between copper cations and negatively functional groups. Taking advantage of these interactions, a coating method was developed for the functionalization of tissue culture-treated polystyrene microplates (TC-plates). The employed TC-plates present on the surface carboxyl functional groups,[17] which could favourably act as the nucleation site for the primary crystals enabling the coating of such surfaces with nanoflowers. TC-plates were prepared via a rapid and scalable crystallization method in which PBS (5 mL, 1X, pH 7.4) containing DS (1 mg ml^{-1}) was added to 1 mL of $CuSO_4$ (240 mM) solution under stirring for 60 s. The solution (0.3 mL) was then injected in a well of a 96 TC-plate and incubated at 21 °C for 16 h. After this time, an opaque blue precipitate was formed at the bottom of the well, whereas the supernatant remained clear. After washing simply by rinsing the functionalized plate with water, the materials deposited on the surface showed a micro-to-nano hierarchical structure and homogeneously coated the well surface (Figure S9a). The coating was composed by D-NF with similar morphologies as described for the preparation of single particles (Figure S9b and c). Rinsing with water could not wash the coating away and its structural integrity was not compromised after several days of soaking in water. The D-NF coating presents a hierarchical structural organization enabling accessible mass transport to the solid-liquid interface and good mechanical and chemical stability in water. For these reasons, functionalized microplates with D-NF coatings were used as reactors for chemical reactions to develop a high throughput sensing platform.

4.1.3.3 Non-enzymatic catalytic activity and kinetics of D-NF

The non-enzymatic peroxidase-like catalytic activities of D-NF were studied using OPD as the substrate (Figure 4). The oxidation of OPD by the hydroxyl radicals deriving from H_2O_2 produces the fluorescent product 2,3-diaminophenazine (DAP) that can be measured via fluorescence spectroscopy. DAP has an absorbance intensity peak at 410 nm and an emission peak at 566 nm which can be used to monitor the reaction in real-time, allowing the monitoring of the catalytic kinetics.

Moreover, fluorescence measurements were taken into consideration instead of absorbance to avoid the contribution of scattering from the immobilized D-NF in functionalized TC-plate wells. To verify this, the fluorescent emission intensities of DAP solutions in unmodified and D-NF coated wells were recorded. The intensities were comparable within the standard deviation, demonstrating that the fluorescence intensities of a DAP solution were not influenced by the presence of a D-NF coating at the bottom of the well (data not shown). When a PBS solution containing (0.1 mM) OPD and (5 mM) H_2O_2 was placed in a D-NF coated well, the emission intensity at 566 nm started to increase reaching a plateau over 30 min. This indicated that the conversion of OPD to DAP started to take place (Figure 4a), highlighting the non-enzymatic peroxidase-like catalytic activity of the hybrid nanoflowers toward hydrogen peroxide as the substrate. The condensation reactions of OPD to DAP followed a pseudo-first-order reaction with different kinetics if D-NF and/or H_2O_2 were present (Figure S10). The pseudo-first-order kinetic hypothesis was validated by the linear trends of the natural logarithm of the fluorescence emission intensities, *Iln*, (which was calculated subtracting the fluorescence intensities from the saturated one) against the time ($R^2>0.99$). Based on these relationships, the reaction rate constants (k) were calculated to be 0.152±0.002, 4.36±0.07 and 122.2±0.4 ms^{-1} when OPD was incubated with H_2O_2 alone, D-NF alone and with the co-presence of H_2O_2 and D-NF. These constants highlighted that H_2O_2 alone could not oxidize OPD and although the presence of just D-NF slightly catalysed the condensation reaction, the highest value of k was obtained with the co-presence of the catalytic substrate and hydrogen peroxide. This highlighted the importance of the co-presence of both D-NF and H_2O_2 at the same time to effectively oxidize the OPD substrate. The D-NF catalytic properties could be attributed to the nanoflowers morphology and chemical composition, in terms of, respectively, high surface-to-volume ratio and the presence of catalytic copper ions, resulting in the enhanced substrate accessibility to active sites (Figure 4b).

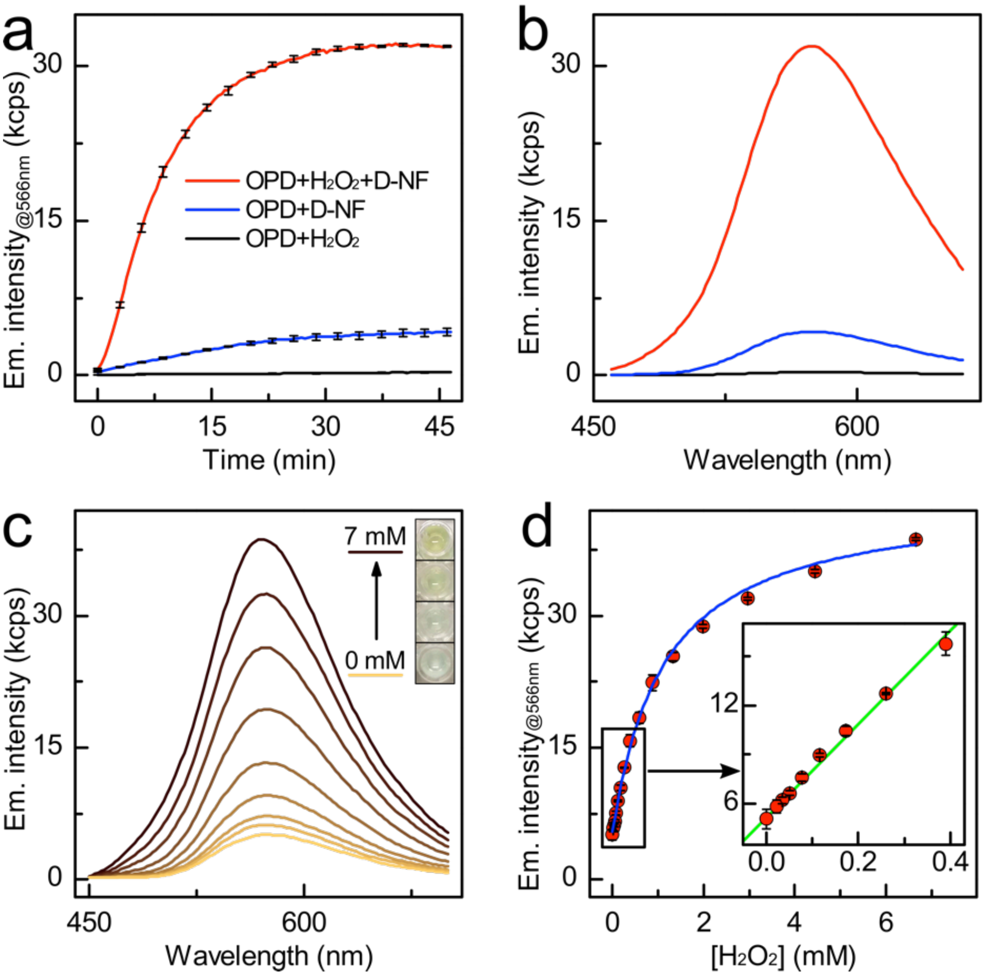

Figure 4. Non-enzymatic peroxidase-like catalytic activities of hybrid nanoflowers. a) Catalytic kinetics regarding the oxidation of OPD to DAP by H_2O_2 or D-NF alone and with the co-presence of H_2O_2 and D-NF. b) Emission spectra of the solutions after kinetic completion with an excitation wavelength of 410 nm. c) Emission spectra, and photos in the insert, of the solutions incubated in functionalized wells upon addition of different H_2O_2 concentrations (from 0 to 7 mM) in PBS buffer. d) Calibration lines representing the extended and, in the insert, linear concentration ranges of H_2O_2 against emission intensities at 566 nm.

4.1.3.4 Detection of hydrogen peroxide via fluorometric assay

As previously described, a fluorometric system based on D-NF and the catalysed condensation reaction of OPD to DAP was developed for the sensing of H_2O_2. To study the quantitative detection of H_2O_2, PBS solutions (1X, pH 6.5) containing different concentrations of H_2O_2 (from 0 to 7 mM) and OPD (0.1 mM) were added to a D-NF modified well and kept under gentle shaking for 45 min at 21 °C (Figure 4c). Upon increasing the concentration of H_2O_2, the colour of the reaction solution gradually changed from colourless to dark yellow. The catalytic activity of D-NF for the oxidation reaction of OPD to DAP was further confirmed by fluorescent measurements. An increase of the emission peak at 566 nm was observed by increasing H_2O_2 concentration (Figure 4d). A linear trend (R^2=0.996) was observed between the emission intensity at 566 nm and the H_2O_2 concentration in the range from 0 to 0.4 mM with a sensitivity of 28.3±0.6 kcps/mM and a LOD of 35 µM (S/N=3). For the extended range from 0 to 7 mM H_2O_2, a non-linear Langmuir-like fit was instead used that matched well with the experimental data (Table S1). This catalytic activity could be attributed to the high surface area and to the morphological spatial organization of the D-NF that enhance the mass transport of OPD from the solution to the catalytic interface and the presence and accessibility of active sites composed of active copper ions exposed to the solution. Importantly, the D-NF coating was found to be stable during the reaction since no particles were observed in the supernatant after the completion of the reaction, indicating the good mechanical stability of the coating.

4.1.3.5 Detection of glucose via a hybrid cascade reactions

H_2O_2 was previously detected in the mM concentration range, which is the concentration of many bio-analytes in biological fluids. For instance, the concentration of glucose (Glu) in the blood is around 5 mM with peaks in diabetic patients from 1 to 30 mM during a day.[22] Interestingly, the limit of detection and detection range of the previously described fluorometric sensing system favourably matched with the physiological glucose concentrations in healthy and diabetic patients. By pairing this non-enzymatic sensing platform to an H_2O_2 producing enzyme, such as glucose oxidase (GOx), a versatile detection platform for the detection and sensing of glucose can be engineered. A system was designed taking advantage of the enzymatic activity of glucose oxidase (GOx) and the non-enzymatic peroxidase-like catalytic activity of D-NF to detect glucose via a hybrid enzymatic/non-enzymatic cascade reaction (Figure 5a). The cascade mechanism of the hybrid system is presented as the following: during the first GOx mediated enzymatic reaction, glucose and oxygen react to form gluconolactone and H_2O_2. In the second non-enzymatic reaction, hydroxyl radicals are produced from H_2O_2 on the D-NF catalytic surface, promoting the condensation reaction of OPD to DAP. This results in a colour change in the solution that can be detected by a fluorometric method. To prove the concept of hybrid cascade reaction, a solution composed of OPD, GOx, Glu in PBS with the presence of D-NF was incubated and its emission and excitation spectra recorded (Figure 5b, black line). For control experiments, two solutions were prepared similarly without the presence of D-NF or Glu (Figure 5b, green and red lines, respectively). When all the components were present, a significant increase of both the excitation and emission spectra intensities were observed, meanwhile weaker intensities were displayed by both control solutions.

The less intense fluorescence intensities of the control experiments that lack the hybrid cascade reaction, indicates the inefficient production of DAP. Conversely, the significant fluorescence signal recorded in the solution consisting of all the components suggests that the cascade reaction effectively promoted the production of DAP, confirming the proposed hybrid cascade reaction mechanism.

Notably, when OPD, GOx and Glu in PBS were incubated in the presence of D-NF with different concentrations of Glu, the emission intensities at 536 nm increased as a function of the initial concentrations of Glu (Figure 5c). A linear trend (R_2=0.976) was observed in the Glu range from 0 to 1 mM with a sensitivity of 1180±70 kcps/mM and a limit of detection of 35 μM (S/N=3). For the fit of the extended range up to 6 mM, a non-linear calibration line was used instead. The range up to 7 mM Glu a non-linear fit was used, matching well with the experimental data (Table S2). Hence, we demonstrated as a proof of concept that with the developed system is possible to detect and quantify the concentration of a biological analyte, glucose, in a physiological relevant solution, as PBS at neutral pH. We envision that this system could be similarly used to detect other biological analytes, like cholesterol, lactic acid, and uric acid via, respectively, cholesterol oxidase, lactate oxidase, and urate oxidase.

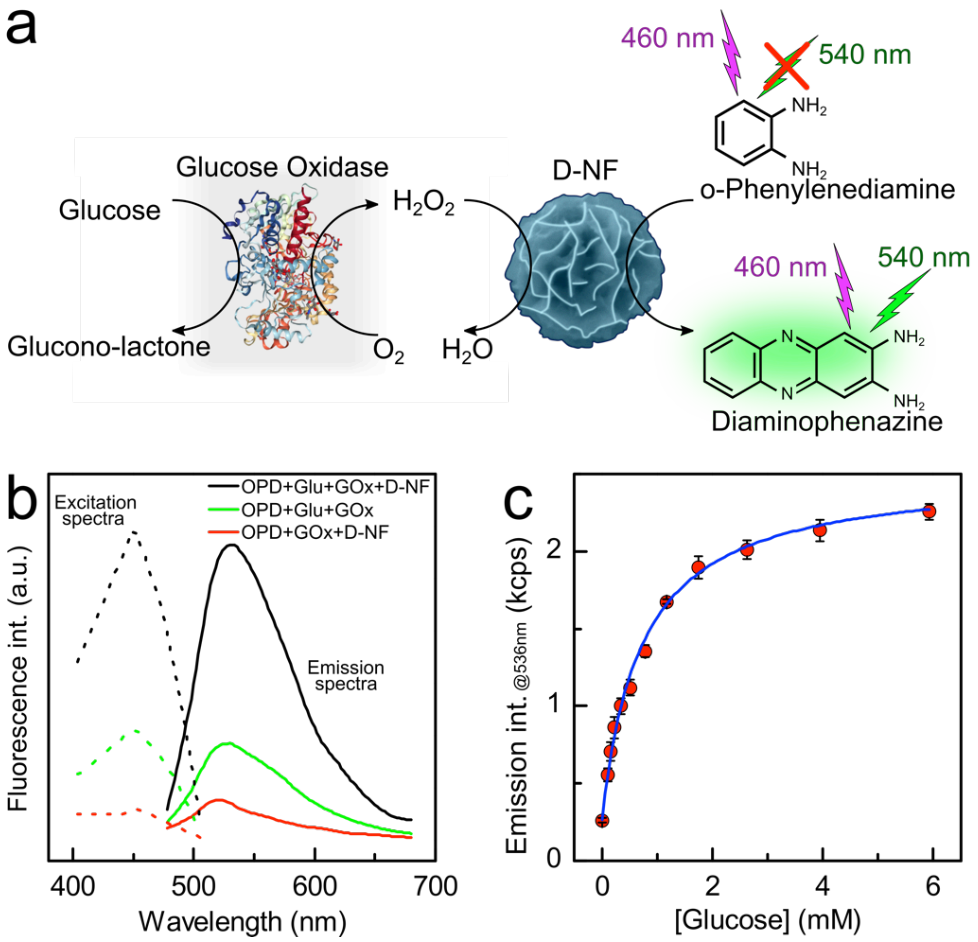

Figure 5. a) Schematic depicting the sensing of glucose via a hybrid enzymatic/non-enzymatic cascade reaction. b) Excitation and emission fluorescence spectra of samples with a combination of OPD, GOx, Glu and D-NF in PBS after incubation for 120 min at 37 °C. c) Calibration lines representing the extended and, in the insert, linear concentration ranges of Glu vs. emission intensities at 536 nm.

4.1.4 Conclusions

We reported the synthesis of dextran sulfate-copper phosphate hybrid nanoflowers via a simple, rapid and low-cost crystallization method. The synthetic parameters were investigated and optimized to prepare monodisperse particles with a high volume-to-surface ratio and hierarchical surface morphology. We developed a facile and scalable coating process of surfaces with D-NF for the preparation of functional microreactors for the detection of H_2O_2 in PBS. This was achieved via the intrinsic non-enzymatic peroxidase-like catalytic activity of the hybrid nanoflowers that, in the presence of H_2O_2, promotes the condensation reaction of OPD to the fluorescent DAP. The proposed sensing system achieved an H_2O_2 linear detection range from 0 to 0.4 mM in PBS with a sensitivity of 28.3±0.6 kcps/mM and a LOD of 35 µM (S/N=3) and a non-linear detection range up to 7 mM. As a proof of concept, the detection of glucose was further performed based on a hybrid cascade reaction via the enzymatic and non-enzymatic activities of GOx and D-NF, respectively. This system showed a linear glucose detection range from 0 to 1 mM in PBS with a sensitivity of 1180±70 kcps/mM and a LOD of 35 µM and a non-linear detection range up to 6 mM. The sensing of H_2O_2 in physiologically relevant media and the possibility to couple a peroxidase-like enzyme, as GOx for the sensing of glucose, to the functional reactor highlighted the potentials of D-NF as catalytic materials for the development of flexible sensing platforms for biomedical and environmental applications.

4.1.5 References

(1) J. Ge, J. Lei and R. N. Zare, *Protein–inorganic hybrid nanoflowers*, *Nature nanotechnology,* 2012, **7**, 428.
(2) Z. Lin, Y. Xiao, L. Wang, Y. Yin, J. Zheng, H. Yang and G. Chen, *Facile synthesis of enzyme–inorganic hybrid nanoflowers and their application as an immobilized trypsin reactor for highly efficient protein digestion*, *RSC Advances,* 2014, **4**, 13888-13891.
(3) J. Sun, J. Ge, W. Liu, M. Lan, H. Zhang, P. Wang, Y. Wang and Z. Niu, *Multi-enzyme co-embedded organic–inorganic hybrid nanoflowers: synthesis and application as a colorimetric sensor*, *Nanoscale,* 2014, **6**, 255-262.
(4) R. Hu, X. Zhang, Z. Zhao, G. Zhu, T. Chen, T. Fu and W. Tan, *DNA nanoflowers for multiplexed cellular imaging and traceable targeted drug delivery*, *Angewandte Chemie International Edition,* 2014, **53**, 5821-5826.

(5) S. W. Lee, S. A. Cheon, M. I. Kim and T. J. Park, *Organic–inorganic hybrid nanoflowers: types, characteristics, and future prospects*, *Journal of nanobiotechnology,* 2015, **13**, 54.

(6) P. Shende, P. Kasture and R. Gaud, *Nanoflowers: The future trend of nanotechnology for multi-applications*, *Artificial cells, nanomedicine, and biotechnology,* 2018, **46**, 413-422.

(7) T. D. Tran and M. I. Kim, *Organic-inorganic hybrid nanoflowers as potent materials for biosensing and biocatalytic applications*, *BioChip Journal,* 2018, **12**, 268-279.

(8) X. Wang, J. Shi, Z. Li, S. Zhang, H. Wu, Z. Jiang, C. Yang and C. Tian, *Facile one-pot preparation of chitosan/calcium pyrophosphate hybrid microflowers*, *ACS applied materials & interfaces,* 2014, **6**, 14522-14532.

(9) J. Jiao, X. Xin, X. Wang, Z. Xie, C. Xia and W. Pan, *Self-assembly of biosurfactant–inorganic hybrid nanoflowers as efficient catalysts for degradation of cationic dyes*, *RSC Advances,* 2017, **7**, 43474-43482.

(10) Z.-F. Wu, Z. Wang, Y. Zhang, Y.-L. Ma, C.-Y. He, H. Li, L. Chen, Q.-S. Huo, L. Wang and Z.-Q. Li, *Amino acids-incorporated nanoflowers with an intrinsic peroxidase-like activity*, *Scientific reports,* 2016, **6**, 22412.

(11) C. Altinkaynak, E. Kocazorbaz, N. Özdemir and F. Zihnioglu, *Egg white hybrid nanoflower (EW-hNF) with biomimetic polyphenol oxidase reactivity: Synthesis, characterization and potential use in decolorization of synthetic dyes*, *International Journal of Biological Macromolecules,* 2018, **109**, 205-211.

(12) J. C. Munyemana, H. He, S. Ding, J. Yin, P. Xi and J. Xiao, *Controlled fabrication of collagen-zinc phosphate hierarchical hybrid nanoflowers via a biomineralization process*, *New Journal of Chemistry,* 2018, **42**, 12824-12829.

(13) B. S. Batule, K. S. Park, S. Gautam, H. J. Cheon, M. I. Kim and H. G. Park, *Intrinsic peroxidase-like activity of sonochemically synthesized protein copper nanoflowers and its application for the sensitive detection of glucose*, *Sensors and Actuators B: Chemical,* 2019, **283**, 749-754.

(14) W. Li, S. Lu, S. Bao, Z. Shi, Z. Lu, C. Li and L. Yu, *Efficient in situ growth of enzyme-inorganic hybrids on paper strips for the visual detection of glucose*, *Biosensors and Bioelectronics,* 2018, **99**, 603-611.

(15) H. Li, J. Hou, L. Duan, C. Ji, Y. Zhang and V. Chen, *Graphene oxide-enzyme hybrid nanoflowers for efficient water soluble dye removal*, *Journal of Hazardous materials,* 2017, **338**, 93-101.

(16) M. Li, M. Luo, F. Li, W. Wang, K. Liu, Q. Liu, Y. Wang, Z. Lu and D. Wang, *Biomimetic copper-based inorganic–protein nanoflower assembly constructed on the nanoscale fibrous membrane with enhanced stability and durability*, *The Journal of Physical Chemistry C,* 2016, **120**, 17348-17356.

(17) M. J. Lerman, J. Lembong, S. Muramoto, G. Gillen and J. P. Fisher, *The evolution of polystyrene as a cell culture material*, *Tissue Engineering Part B: Reviews,* 2018, **24**, 359-372.

4.2 Supplementary Information

Enzyme-Mimicking Hybrid Nanoflowers Enable Sensing of Bioanalytes

Pietro Pacchin Tomanin[a], Frank Caruso[a], Francesca Cavalieri[b,c]

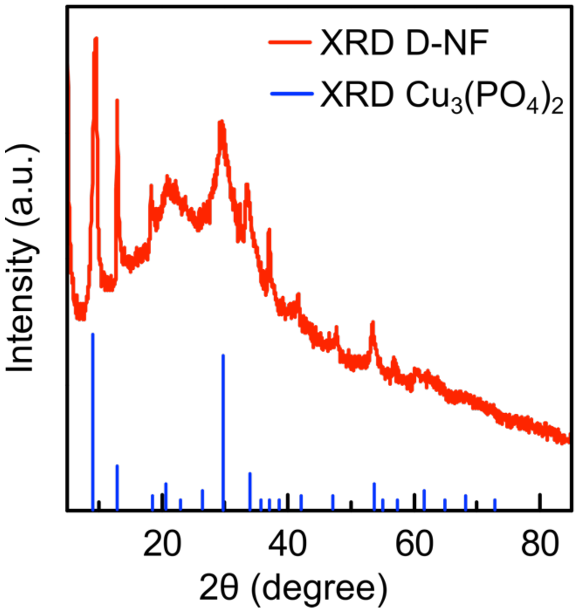

Figure S1. XRD spectra of D-NF and the copper phosphate as the reference.

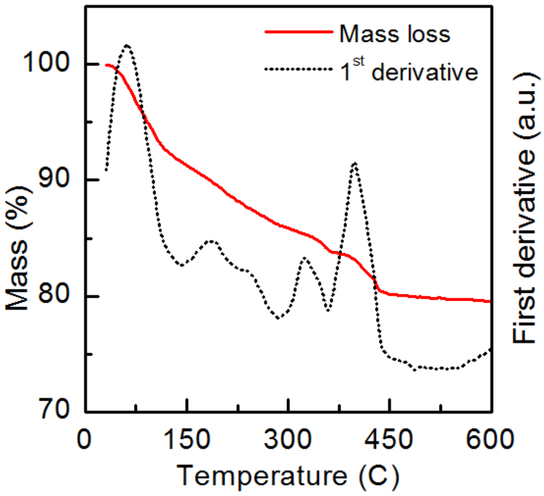

Figure S2. Thermal gravimetric analysis of the D-NF.

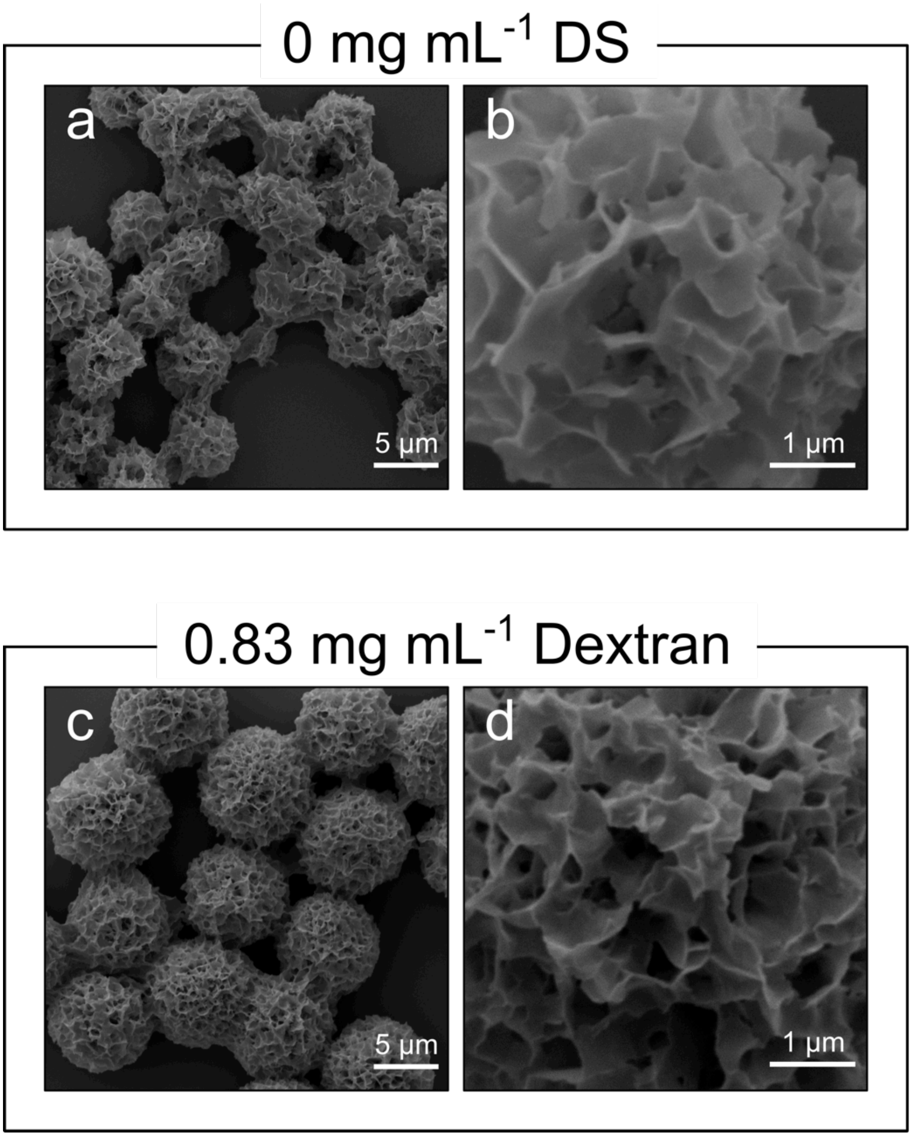

Figure S3. SEM images of particles prepared as the controls. Particles synthesized as: a-b) pure copper phosphates without the presence of organic molecules, and c-d) with the presence of dextran at a concentration of 0.83 mg mL^{-1} are represented by low and high magnification SEM images.

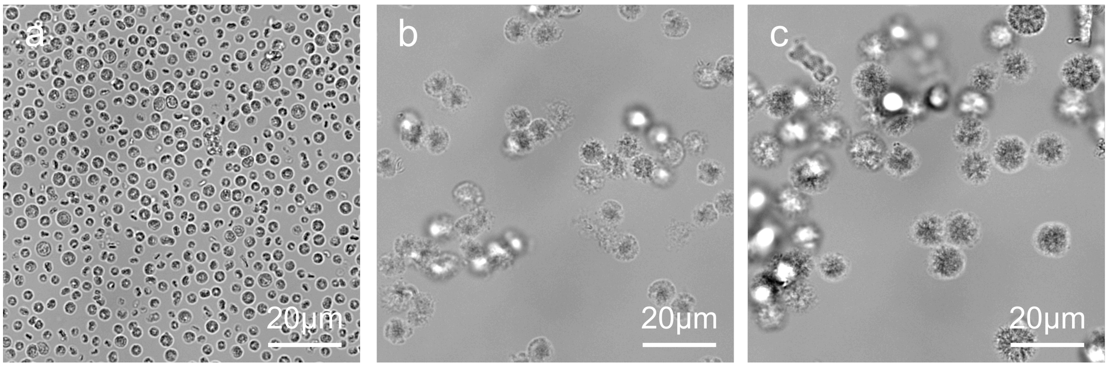

Figure S4. Optical microscope images in liquid state of a) D-NF, b) pure copper phosphate NF, and c) Dextran-NF.

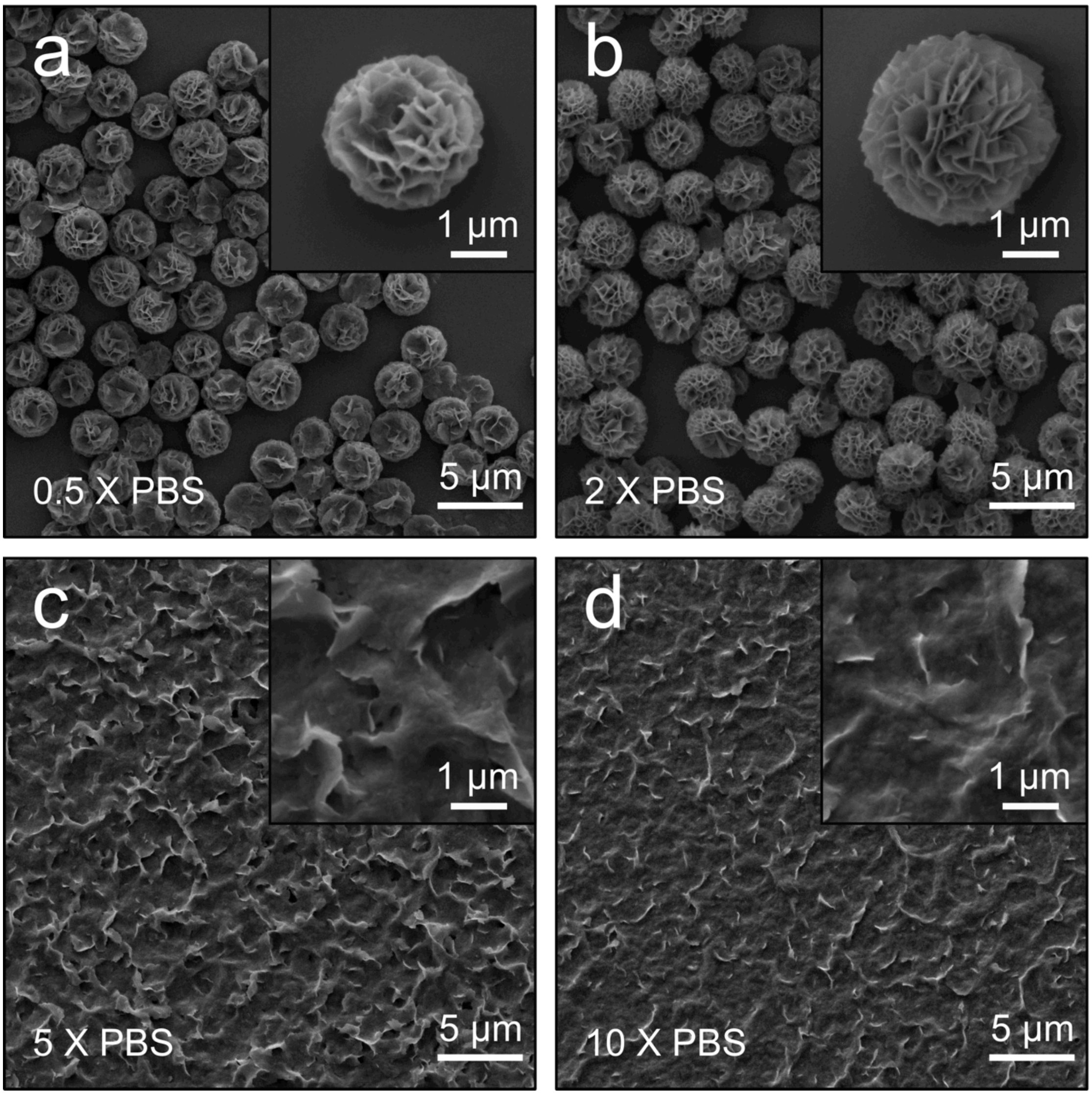

Figure S5. SEM images of D-NF prepared at different concentrations of PBS. Hybrid nanoflowers synthesized with a PBS concentration of a) 0.5 X, b) 2 X, c) 5 X and d) 10 X are represented by low and high magnification SEM images.

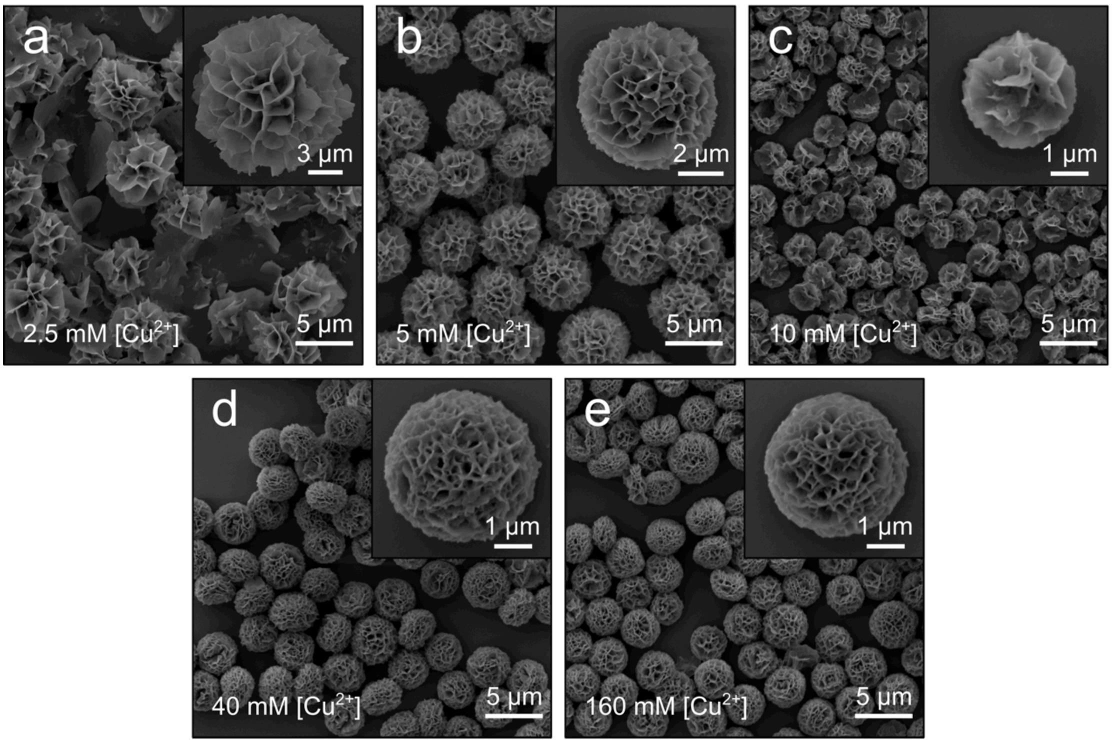

Figure S6. SEM images of D-NF prepared with different concentrations of Cu^{2+} ions. Hybrid nanoflowers synthesized with a Cu^{2+} ions concentration of a) 2.5, b) 5, c) 10, d) 40 and e) 160 mM are represented by low and high magnification SEM images.

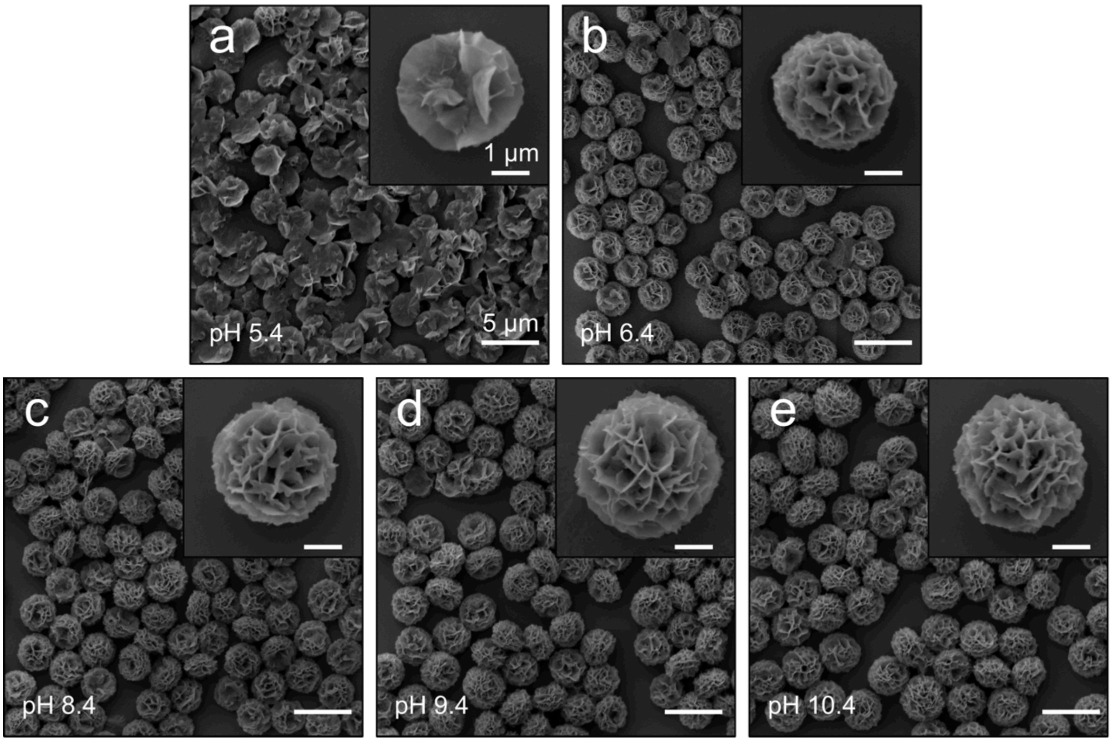

Figure S7. SEM images of D-NF prepared at different pH. Hybrid nanoflowers synthesized at pH of a) 5.4, b) 6.4, c) 8.4, d) 9.4 and e) 10.4 are represented by low and high magnification SEM images. The same scale bars were used for all the images.

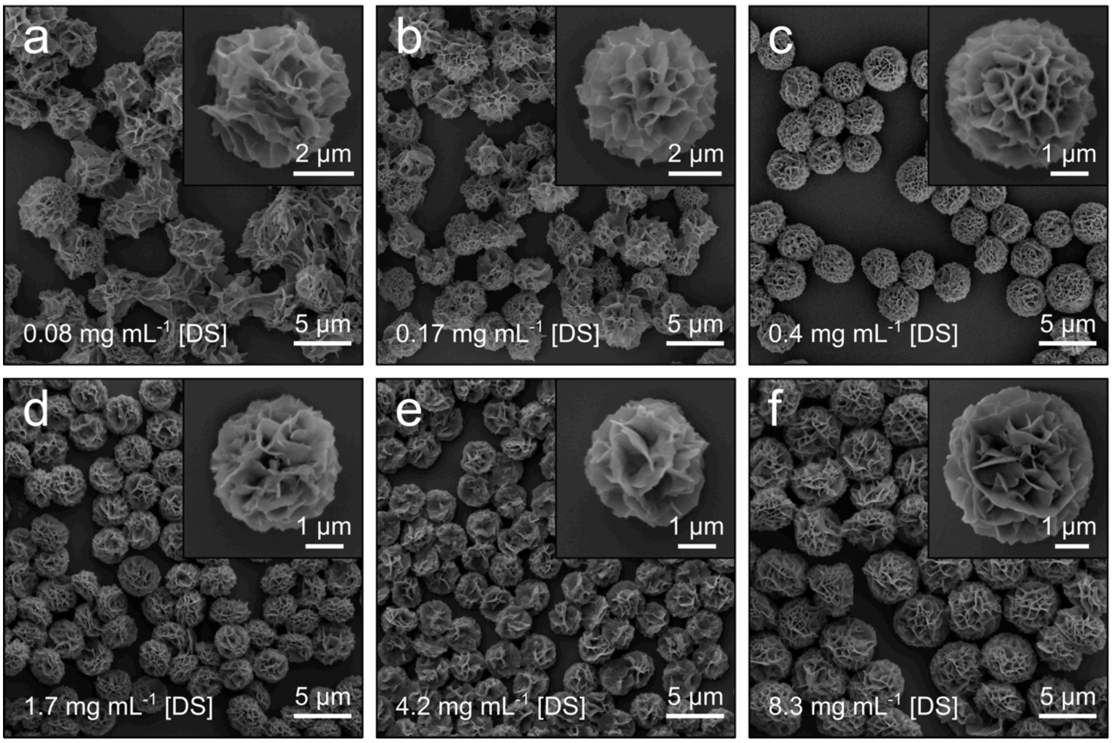

Figure S8. SEM images of D-NF prepared with different concentrations of DS. Hybrid nanoflowers synthesized with a DS concentration of a) 0.08, b) 0.17, c) 0.4, d) 1.7, e) 4.2 and f) 8.3 mg mL^{-1} are represented by low and high magnification SEM images.

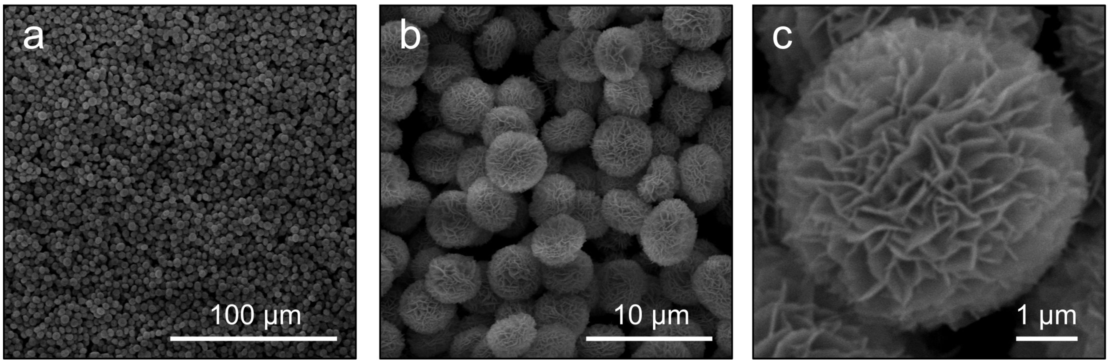

Figure S9. SEM images of D-NF assembled at the functional polystyrene interface of TC plates at a) low, b) medium, and c) high magnifications.

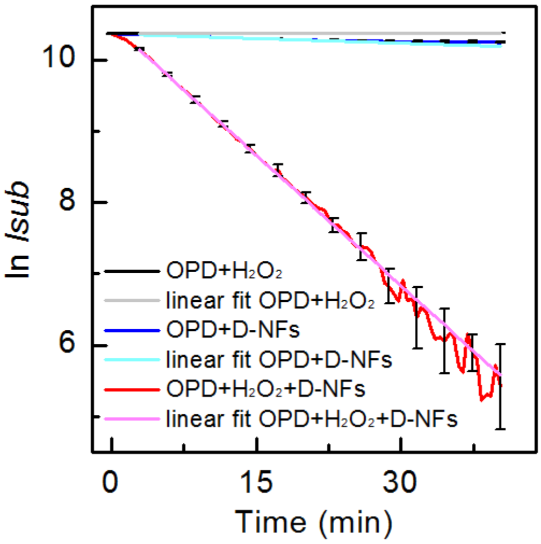

Figure S10. Catalytic reaction rates of the OPD oxidation in microreactors with the presence of H_2O_2 and D-NF and control experiments with the presence of only H_2O_2 or D-NF. Included, are the linear fit of the data. The data are relative to Figure 4a.

Non-linear Langmuir-like equation used for the fitting of the H_2O_2 and Glu sensing extended range in Figure 4d and Figure 5c:

$$y = \frac{(b + cx)}{(1 + ax)}$$

Table S1. Fitting equation parameters relative to the H2O2 sensing represented in Figure 4d.

Variable	Value and standard deviation
a	0.88 ± 0.06
b	5400 ± 300
c	38000 ± 2000
R^2	0.998

Table S2. Fitting equation parameters relative to the Glu sensing represented in Figure 5c.

Variable	Value and standard deviation
a	1.4 ± 0.1
b	260 ± 10
c	3500 ± 200
R^2	0.998

Chapter 5

Nanoengineering Multifunctional Hybrid Interfaces Using Adhesive Glycogen Nanoparticles

Pietro Pacchin Tomanin[a], Jiajing Zhou[a], Alessia Amodio[a], Rita Cimino[a], Agata Glab[a], Francesca Cavalieri[b,c,*], Frank Caruso[a,*]

[a] ARC Centre of Excellence in Convergent Bio-Nano Science and Technology, and the Department of Chemical Engineering, The University of Melbourne, Parkville, Victoria 3010, Australia. E-mail: fcaruso@unimelb.edu.au

[b] School of Science, RMIT University, Melbourne, Victoria 3000, Australia. E-mail: francesca.cavalieri@rmit.edu.au

[c] Dipartimento di Scienze e Tecnologie Chimiche, Università di Roma "Tor Vergata",

via della ricerca scientifica 1, 00133, Rome, Italy. E-mail: francesca.cavalieri@rmit.edu.au

This Chapter has been submitted to *RCS Journal of Materials Chemistry B* as:

Pacchin Tomanin, P., Zhou J., Amodio A., Cimino R., Glab A., Cavalieri F. and Caruso F. **2020.** Nanoengineering multifunctional hybrid interfaces using adhesive glycogen nanoparticles.

5.1 Manuscript main text

5.1.1 Abstract

Multifunctional and biodegradable nanostructured hybrid interfaces based on biopolymers are potentially useful in many applications in catalysis, bioanalytical sensing and nanomedicine. Herein, we report the engineering of multifunctional hybrid films by assembling adhesive biological nanoparticles i.e. lipoate-conjugated phytoglycogen (L-PG). These nano building blocks possess adhesive properties, arising from their amphiphilic nature, and reactive functional disulfide groups. The assembly of L-PG on surfaces enabled the rapid and conformal deposition of a thin film on substrates of varying chemical composition and wettability. The L-PG films showed negligible cytotoxicity and moderate stability under different harsh conditions but displayed enzyme-mediated degradability. In addition, metal nanoparticles were embedded into the L-PG layers to build up multilayered hybrid films. Specifically, Au and Ag nanoparticle-loaded L-PG multilayered films with catalytic and surface-enhanced Raman scattering properties were prepared. Finally, we highlight the versatility of the present approach to engineer multifaceted interfaces for catalysis and sensing applications.

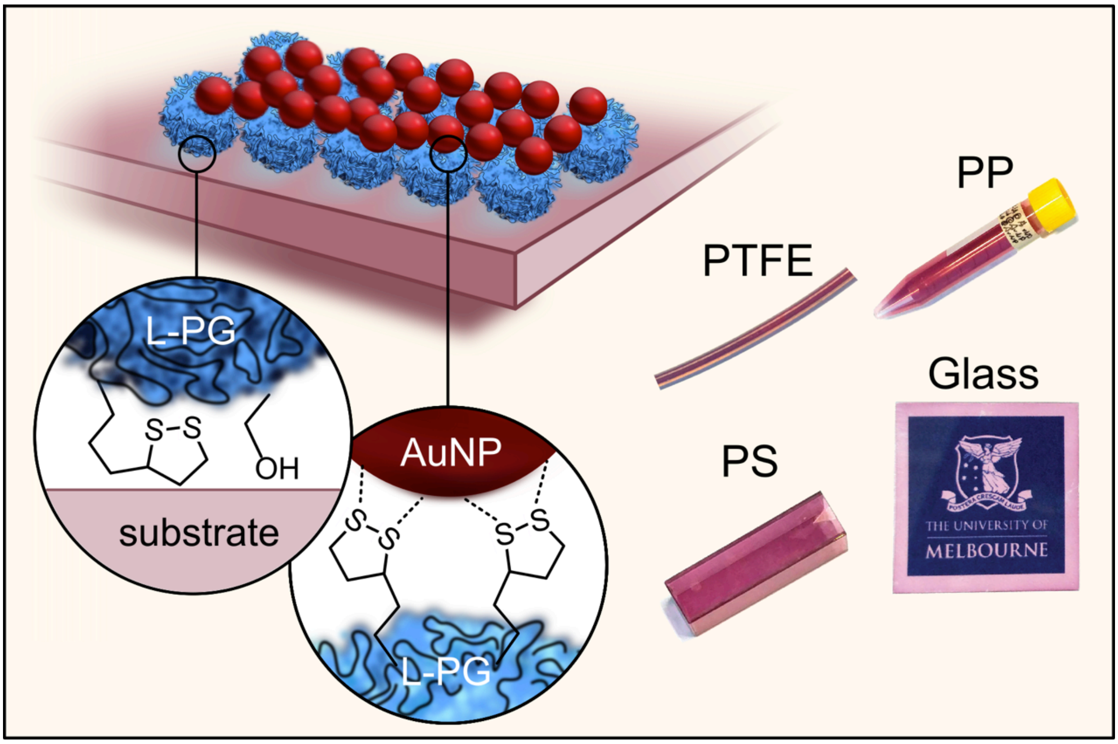

Table Of Content Graphic. Amphiphilic phytoglycogen nanoparticles are used as building blocks for engineering multifunctional hybrid films with catalytic and sensing properties.

5.1.2 Introduction

The engineering of multifunctional nanostructured interfaces has attracted great interest in many interdisciplinary fields including nanomedicine,[1] biosensing,[2] tissue engineering,[3] and catalysis.[4] The desired multifunctional interface can be achieved by controlling the chemical functionality and structural arrangement of the building blocks on a nanometer scale. For integration of functions, a polymeric material with the desired functionality and morphology can be combined with inorganic or metal nanoparticles to engineer a complex hybrid interface with structural and compositional inhomogeneity.[5–7] The precise manipulation of the physical and chemical interactions between these hybrid building blocks allows control of the interface nanomorphology and functionality of the macroscopic materials. The use of polysaccharides, such as chitosan,[8.9] amylose,[10] cellulose,[11] hyaluronic acid,[12,13] as biodegradable polymeric components for engineering multifunctional surfaces and films, is attractive because polysaccharides are natural biomacromolecules that can be chemically or biochemically modified to impart various functional properties. In particular, glycogen is a biological polysaccharidic nanoparticle found ubiquitously across the animal and plant kingdoms, serving as a vital component of the cellular energy machinery.[14,15] Glycogen nanoparticles have a dendrimer-like structure composed of repeating units of glucose connected by linear α-(1,4) glycosidic linkages with α-(1,6) branching. They have different structural properties (e.g., nanoparticle size, molecular weight, and degree of branching) depending on the source.[16] For example, phytoglycogen (PG) is a naturally abundant form of glycogen derived from sweet corn, possessing a diameter of 80 nm and a high molecular weight of 20 MDa.[16] PG nanoparticles have a highly branched, hydrated structure[17,18] and a high colloidal stability, and chemical functionalization of the polymeric chains can be performed under mild conditions using nontoxic reagents. Importantly, the reactive hydroxyl groups on glycogen can be modified to produce functional nanoparticles that remain partially biodegradable,[19] making glycogen attractive as a building block for engineering biofunctional materials and interfaces. Recently, glycogen nanoparticles with different chemical modifications and properties have been successfully exploited for drug delivery,[20–23] targeting,[24] cellular imaging,[19,25] and smart materials.[26–29]

Amine functionalities are typically introduced on glycogen to form complexes with negatively charged nucleic acids.[19–20] Octenylsuccinate hydroxypropyl PG nanoparticles were developed to improve the solubility of hydrophobic dugs.[29] The modification of glycogen with hydrophobic allyl and propargyl moieties was exploited to obtain crosslinked water-insoluble films with a fibrous or sponge-like structure. The films were used as a scaffold for growing osteoblast-like cells.[30] A stimuli-responsive hydrogel for colon-targeted drug delivery was obtained via free-radical polymerization of glycogen, modified by *N*-isopropylacrylamide moieties, with ethylene glycol dimethacrylate as a crosslinker.[31] Despite the various glycogen-based materials developed to date, the use of the adhesive properties of glycogen nanoparticles for the preparation of functional interfaces remains to be examined and exploited. The development of adhesive glycogen nanoparticles and self-assembly strategies is expected to advance this biological nanoparticle toward its use as a versatile surface coating material. We propose that the modification of PG with hydrophobic and functional moieties would endow the functionalized amphiphilic polysaccharide with unexplored adhesive properties to prepare nontoxic, biodegradable films.

In the present study, we report a rapid and robust method to form nanostructured hybrid films using lipoate-conjugated phytoglycogen (L-PG). L-PG exhibits remarkable adhesiveness to coat various substrates including organic, inorganic, and even low-surface-energy materials (e.g., polytetrafluoroethylene (PTFE)). A thin and homogenous film is rapidly formed by immersion of the substrate into an L-PG water solution. The resulting L-PG film shows negligible cytotoxicity and significant degradability, yet displays stability in various harsh environments such as strong acid. We also demonstrate that these films can be functionalized with inorganic nanoparticles (e.g., Au, Ag, and Pt nanoparticles) owing to the high affinity of disulfide bridges in the tagged lipoate to the noble metal nanoparticles. The supported Au nanoparticles (AuNPs) show catalytic activity and high stability owing to the high permeability and protection of the L-PG multilayered film. Moreover, a surface-enhanced Raman scattering (SERS) active substrate is developed by integrating Ag nanoparticles (AgNPs) into the coating, therefore producing sensing interfaces that can monitor chemical changes in the surface proximity. Overall, this study describes a rapid and facile strategy for preparing multifunctional and biodegradable interfaces for different applications including in the environmental and medical fields.

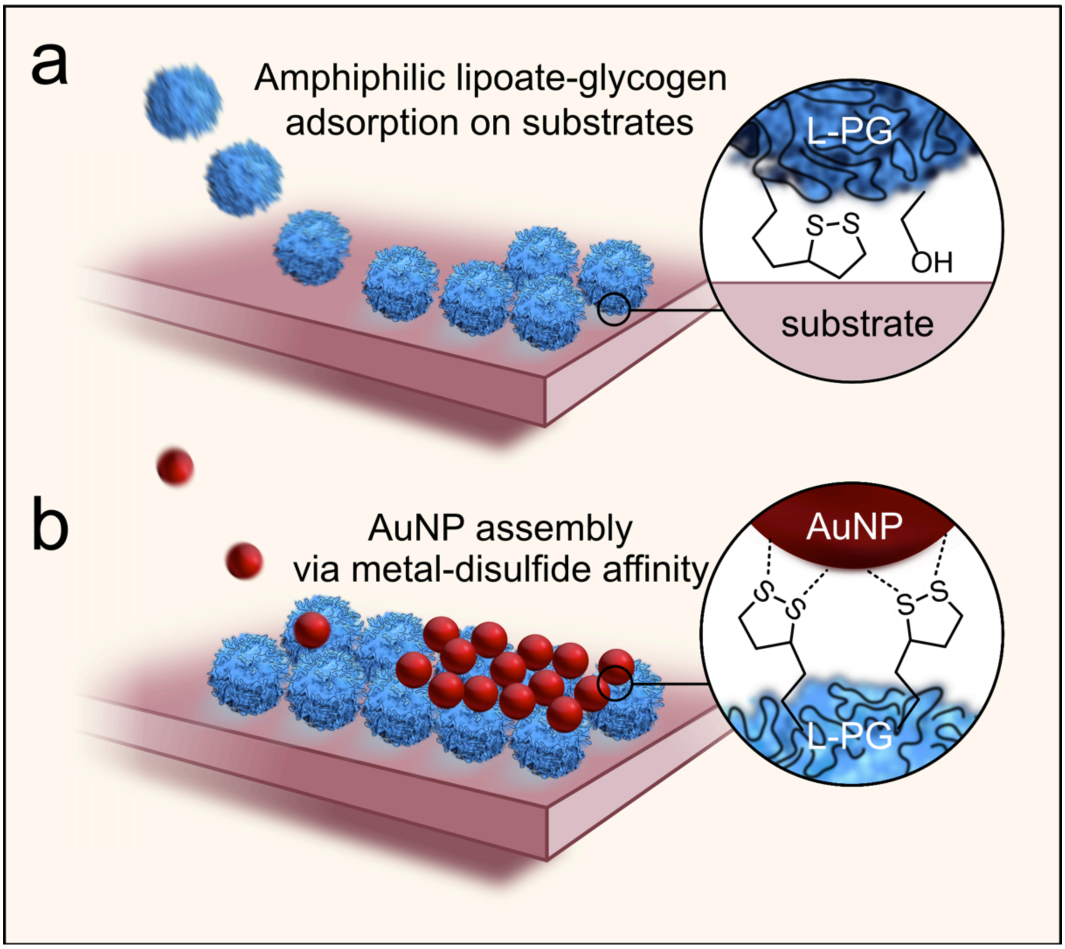

Fig. 1. (a) Schematic of the L-PG assembly on a substrate and (b) co-assembly of metal nanoparticles on the L-PG layer to obtain hybrid surfaces via LbL assembly suitable for catalysis and sensing applications.

5.1.3 Results and Discussion

5.1.3.1 Synthesis and characterization of L-PG

PG was first functionalized with a natural compound, LA, via an esterification reaction in DMSO to form L-PG (Figure S1). The resulting L-PG bears both hydrophilic and hydrophobic moieties (Figure 1a) that impart adhesion properties to the nanoparticles. In addition, the disulfide groups of lipoate are reactive toward metal nanoparticles (Figure 1b).

NMR spectra confirmed the successful preparation of L-PG, which showed distinct signals that were ascribed to the glucose repeating unit and lipoate moieties (Figure S2). The lipoate groups are likely grafted to the outermost branches of PG. Previous work has shown that glycogen inner chains that are not swollen by organic solvent (e.g., DMF and DMSO) are less accessible and reactive, leading to surface-constrained functionalization.[32]

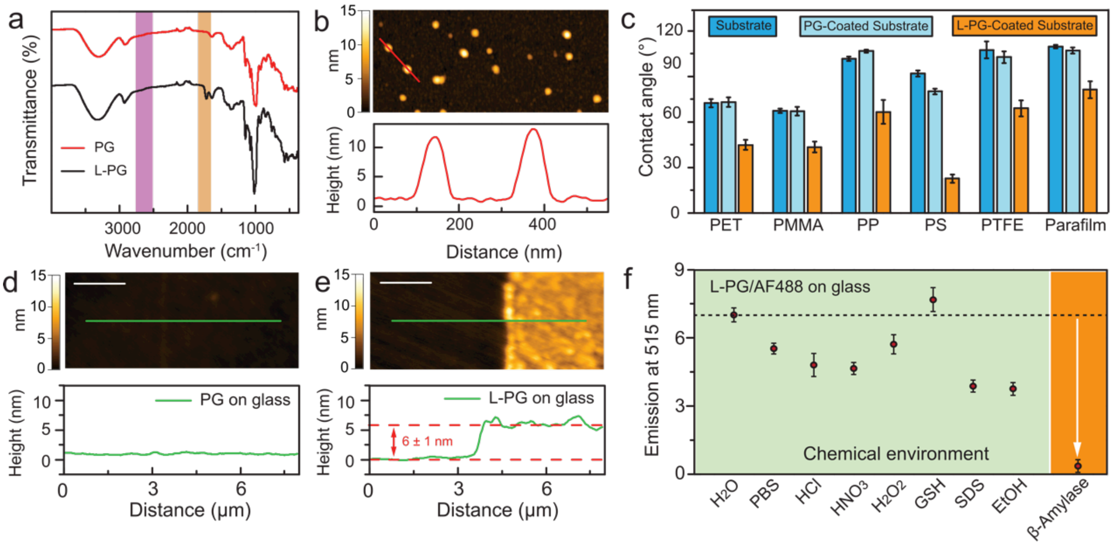

Fig. 2. Characterization and coating properties of L-PG. (a) ATR-FTIR spectra of PG and L-PG and (b) dry-state AFM image and corresponding height profile of L-PG. (c) Water contact angles of the bare, PG-, and L-PG-coated substrates. Dry-state AFM images and corresponding height profiles of (d) PG- and (e) L-PG-coated glass substrates (scale bar 2 μm). (f) Emission intensities of fluorescently labeled L-PG coatings on glass substrates after incubation in different chemical and biochemical environments. Error bars represent standard deviations.

It is noteworthy that a trade-off between hydrophilicity and hydrophobicity is vital in the design of this building block. For example, samples with a degree of functionalization higher than 2% showed poor solubility in water and DMSO owing to the high hydrophobicity (Table S1). Therefore, a degree of functionalization of 2% was considered optimal for maintaining L-PG colloidal stability in aqueous solution. The presence of lipoate groups on L-PG was further confirmed by FTIR spectroscopy. The newly formed ester bonds were observed at 1721 cm^{-1} (Figure 2a). Importantly, the 1,2-dithiolane of lipoate remained in the oxidized state during the reaction, as signals corresponding to thiol stretching bands at 2560–2570 cm^{-1} were absent.[33] The new absorbance peak observed at 290 nm in the UV–vis spectrum of L-PG further confirmed the presence of the lipoate ring (Figure S3).[34] The synthesized L-PG had a hydrodynamic diameter (90 ± 50 nm), as determined by DLS, and a ζ-potential value (−1 ± 6 mV) similar to those of unmodified PG (90 ± 40 nm; −1 ± 6 mV) (Figure S4). These results confirm that the chemical modification of PG with up to 2% hydrophobic moieties does not induce any aggregation or substantial change in the solution properties of the resulting nanoparticles relative to those of the unmodified PG. Dry-state AFM further confirmed that the L-PG nanoparticles were spherical and well dispersed, with a round flattened shape, characteristic of dehydrated spherical soft materials (Figure 2b). As measured by AFM, the L-PG nanoparticles featured an average diameter of 90 ± 20 nm and a thickness of 8 ± 2 nm.

5.1.3.2 Preparation and characterization of L-PG films

L-PG was subsequently examined for coating several planar polymeric substrates, including PET, PMMA, PP, PS, Parafilm, and PTFE. The successful coating was confirmed by contact angle measurements (Figure 2c). Specifically, the L-PG film formed on a PTFE surface featured a reduced water contact angle from 107 ± 6° (uncoated PTFE substrate) to 69 ± 5°, thus shifting the wettability of the final film from hydrophobic to hydrophilic. A similar trend was observed on other substrates (Figures 2c and S5). Conversely, when unmodified PG was used to coat these substrates, there was negligible difference in the contact angle before and after the deposition procedure (Figure 2c). This observation indicates that the unmodified PG nanoparticles show poor adhesiveness. In addition, AFM analysis revealed that, unlike unmodified PG (Figure 2d), a continuous, dense L-PG film of 6 ± 1 nm in thickness formed on the glass surface after deposition (Figure 2e).

To examine the stability of the films, L-PG was labeled with a fluorophore tag (AF488) so that the disassembly of the coating was monitored after the treatment. The L-PG coating was first incubated in different solutions for 60 min, followed by repeated washing with water. The fluorescence intensity of the substrates was then recorded to evaluate residual L-PG on the substrates. The results indicate that the L-PG coating shows moderate stability in diverse chemical environments such as in H_2O, 10 mM PBS (pH 7.4), 1 M HCl, 1 M HNO_3, 1 M H_2O_2, 10 mM GSH, 17 mM SDS, and EtOH (Figure 2f). In contrast, the L-PG film can be significantly degraded by β-amylase (Figure 2f) and the building block are not cytotoxic (Figure S6). However, the L-PG nanoparticles required a longer incubation time than the unmodified PG nanoparticles to achieve the same degree of degradation by β-amylase (Figure S7). These results show that stable aqueous suspensions of hydrophobically modified PG nanoparticles can be used to build robust but biodegradable, noncytotoxic thin films owing to the adhesiveness of L-PG that promotes the interfacial assembly of nanoparticles on substrates with different wettability.

To understand the mechanism governing the adhesion properties of L-PG, the influence of the amphiphilic nature of PG without disulfide bonds was assessed. To this end, an analogous amphiphilic PG derivative, containing 1% hydrophobic dodecane moiety (DD-PG) was synthesized (Figure S8). DD-PG displayed properties similar to those of L-PG such as hydrodynamic diameter (71 ± 40 nm) and ζ-potential (−1 ± 5 mV). The results showed that the water-soluble DD-PG also formed a film on glass similar to L-PG, with a similar thickness and surface morphology (Figure S9). These findings underline the importance of the amphiphilic characteristic of modified PG for the successful formation of coatings. Moreover, the disulfide moieties in L-PG offer an additional advantage for further functionalization of the L-PG films.

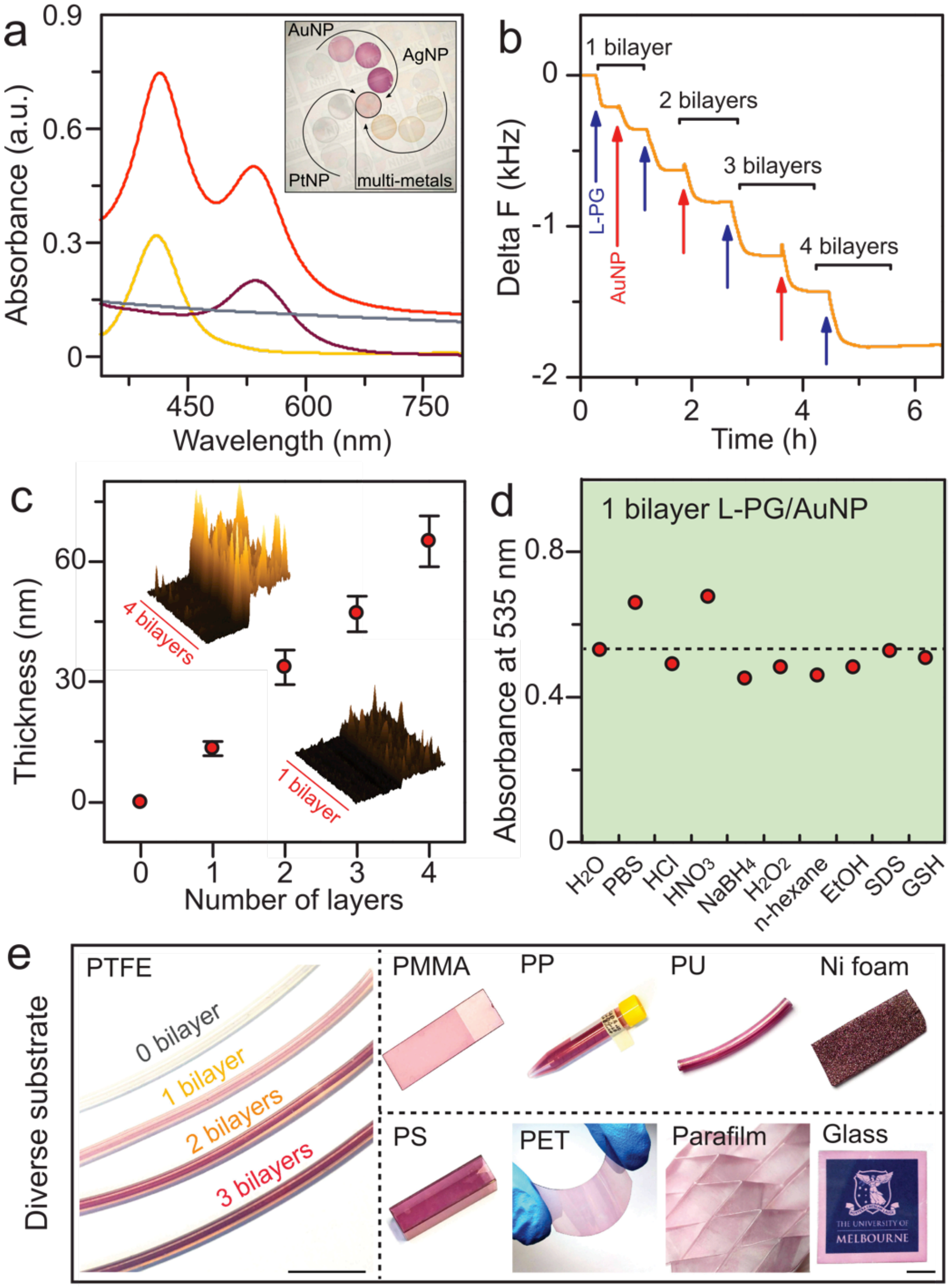

Fig. 3. Characterization of hybrid L-PG LbL assemblies with metal nanoparticles. (a) UV–Vis spectra of glass substrates coated with one bilayer of L-PG/AuNP, L-PG/AgNP and L-PG/PtNP (purple, yellow and

grey lines, respectively) and three bilayers of sequentially assembled L-PG/AuNP, L-PG/AgNP, and L-PG/PtNP (red line) and corresponding photograph (inset) of glass substrates coated with various layers of L-PG and metal nanoparticles (Au, Ag, Pt, and Au–Ag–Pt). (b) QCM-D frequency profile of an L-PG/AuNP LbL assembly on a gold chip obtained by sequential deposition of L-PG (blue arrow) and AuNPs (red arrow). (c) Dry-state AFM film thickness profile as a function of the L-PG/AuNP bilayer number and corresponding AFM images of the first and fourth bilayers (insets). (d) LSPR absorbance of glass substrates with 1 bilayer of L-PG/AuNPs after incubation in various chemical environments. (e) Photographs of L-PG/AuNP LbL assemblies on various substrates (scale bar 1 cm).

5.1.3.3 Characterization of L-PG/metal nanoparticles hybrid films

Herein, we demonstrate that glycogen–inorganic hybrid films with controlled thickness can be fabricated by LbL assembly of L-PG and metal nanoparticles, including AuNPs, AgNPs, and platinum nanoparticles (PtNPs) (Figure 3a). The assembly of the L-PG/AuNP film was monitored by measuring the (linear) increase in the intensity of the localized surface plasmon resonance (LSPR) band of the AuNPs at ~545 nm. (Figure S10). Notably, the narrow LSPR peak indicates the relatively large interparticle distance between neighboring AuNPs, suggesting that the AuNPs do not form clusters when embedded in the film and L-PG nanoparticles act as a spacer. Similar trends in relation to the increase in absorbance intensity were observed in the multilayered hybrid films containing AgNPs (LSPR at 415 nm) or PtNPs (a broad absorbance profile spanning the UV–vis region without a characteristic peak) (Figure S11). A multicomponent hybrid film with three bilayers obtained by sequential deposition of L-PG/AuNP, L-PG/AgNP, and L-PG/PtNP is also demonstrated. The resulting UV–vis spectrum exhibited a combined absorption profile comprising the typical absorbance of each metal nanoparticle assembly (Figure 3a, red line). To demonstrate the importance of disulfide moieties in coordinating the metal NPs for the successful assembly of the hybrid films, control experiments were performed using DD-PG/AuNP, unmodified PG/AuNP, and AuNPs. The deposition of these control systems on a glass slide resulted in very weak LSPR bands, indicating poor adsorption on the glass surface (Figure S12). These results highlight the importance of disulfide bonds on L-PG for the successful loading of AuNPs.

QCM-D was used to monitor the kinetics of the hybrid film assembly process by depositing sequential layers of L-PG and AuNPs. L-PG first directly adhered to the gold substrate acting as a primer layer, followed by the deposition of AuNPs on the L-PG layer to form a hybrid bilayer structure, stabilized by disulfide–gold interactions (Figure 3b).

Both L-PG and AuNP deposition reached equilibrium within 30 min of incubation. The dissipation factor increased when an L-PG layer was deposited, indicating that the L-PG layer was distorted during crystal oscillations and therefore displayed characteristics of a soft film (Figure S13). In contrast, the dissipation factor remained constant upon deposition of AuNPs, showing that the rigid AuNPs followed the oscillation of the crystal without being deformed. These results demonstrated the hybrid nature of the coating.

The film growth was also monitored by AFM measurements of the average dry thickness and roughness of the films. After the deposition of each bilayer, the dry thickness and roughness increased by 6.3 ± 0.6 and 2.4 ± 0.1 nm, respectively, indicating that the films were compact and homogeneous with a high surface coverage (Figure 3c and Figures S14, 15). Importantly, the L-PG/AuNP hybrid coatings on glass displayed excellent chemical stability up to 60 min in several harsh chemical environments such as 10 mM PBS (pH 7.4), 1 M HCl, 1 M HNO_3, 10 mM $NaBH_4$, 1 M H_2O_2, *n*-hexane, EtOH, 17 mM SDS, and 10 mM GSH (Figure 3d). Notably, the stability of the multilayered film was significantly higher than that of the single-layer L-PG film. This can be ascribed to the shielding effect of the AuNP layer,[35] which prevents the detachment and degradation of L-PG.

Remarkably, the L-PG/AuNP hybrid film formed on various materials such as rigid (PS, PMMA, PP, polyether ether ketone) and flexible (PTFE, PET, Parafilm, Viton, polyurethane) polymeric, oxide (cover glass), and metal (Ni foam) substrates (Figure 3e and Figure S16). The deposition is indicated by the change in color of the substrates upon adsorption of AuNPs mediated by interactions with the primer L-PG layer. The coating formed on the different substrates remained stable at room temperature (25 °C) for up to 6 months in dried state.

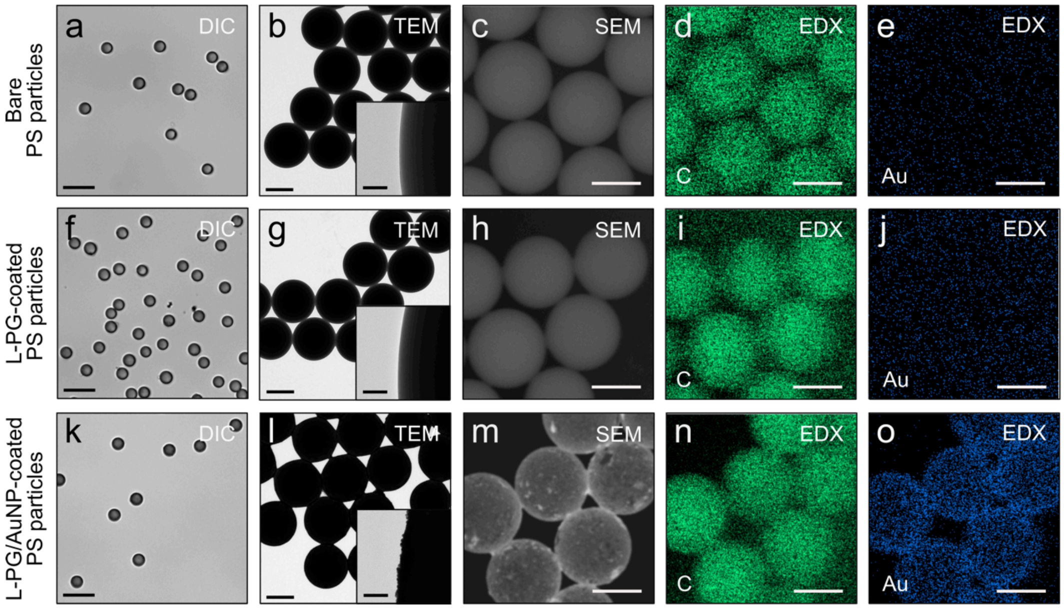

Fig. 4. PS microparticles coated with L-PG and L-PG/AuNP LbL assemblies. (a, f, k) Differential interference contrast (DIC) microscopy, (b, g, l) TEM, and (c, h, m) SEM images, and (d, i, n) C and (e, j, o) Au EDX mapping of bare PS microparticles (a–e), L-PG-coated PS microparticles (f–j), and 3-bilayer L-PG/AuNP-coated PS microparticles (k–o). Scale bars: DIC (10 µm), TEM (2 µm) and inset (100 nm), and SEM and EDX (3 µm).

To further extend the possible use of the L-PG/AuNP hybrid film to microscale objects, PS particles (3.2 µm) were successfully coated with three bilayers of L-PG/AuNP (Figure 4). Disperse bare PS microparticles (Figure 4a) displayed, a smooth particle edge (Figure 4b and inset) and a homogeneous distribution of carbon only (Figure 4c–e). The PS microparticles coated with one layer of the L-PG film did not show any aggregation (Figure 4f). Similarly to the bare PS microparticles, the L-PG-coated PS microparticles displayed a smooth particle edge (Figure 4g and inset) and a uniform distribution of carbon only (Figure 4h–j). The PS microparticles coated with three bilayers of L-PG/AuNP LbL assemblies did not show evidence of aggregation (Figure 4k). However, TEM images showed an increased contrast and roughness in the edge of the particles, compared with those of the bare PS and L-PG-coated PS microparticles, which was attributed to the presence of the dense AuNPs (Figure 4l and inset). Furthermore, the SEM images and EDX mapping showed the homogeneous presence of both carbon and gold in the coating (Figure 4m–o). These results further confirmed the presence of AuNPs and therefore the successful preparation of L-PG/AuNP LbL assemblies onto PS microparticles.

5.1.3.4 Catalytic and SERS properties of hybrid LbL assemblies

To demonstrate the applications of the tunable hybrid coatings, a chemical reactor was designed by coating the inner wall of PP tubes with L-PG/AuNP bilayers for catalysis. The catalytic activities of the hybrid films were evaluated through the $NaBH_4$-mediated reduction of methylene blue (MB) to leucomethylene blue (LMB) in the presence of metal catalysts. The reaction kinetics was monitored via UV–vis spectroscopy in real time, wherein changes in the absorption peak at 664 nm, corresponding to MB, were monitored as MB was converted to colorless LMB. When an MB solution containing $NaBH_4$ was incubated in an L-PG/AuNP-coated PP tube, the blue solution turned transparent over time, indicating the successful reduction reaction (Figure 5a). In contrast, the bare and L-PG-coated PP tubes showed no reduction of MB (Figure S17). Our results show that the catalytic efficacy of the system relies on the layers of the AuNPs coating, and faster reduction kinetics were obtained in reactors with a higher number of L-PG/AuNP bilayers (Figure 5b). Specifically, MB reduction in the reactors followed a second-order reaction with rate constants of 6.0 ± 0.8, 11.0 ± 0.8, and 20 ± 2 mM^{-1} min^{-1} for 1, 3, and 5 L-PG/AuNPs bilayers, respectively. This improvement was due to the increasing overall amount of AuNPs and easy access of small molecules into the L-PG matrix. Notably, the catalysts in the film showed high stability because of the negligible amount of AuNPs leached into the solution during the reaction (Figure 5c). The robust assembly of these hybrid films will allow defining functional coatings on various materials for catalytic purposes.

SERS can be used to detect vibrational fingerprints of chemicals with high sensitivity, wherein the Raman signals of targets are significantly augmented when located near plasmonic nanostructures (e.g., AgNPs) owing to the enhanced electromagnetic field arising from the excitation of LSPR bands. Thus, by integrating AgNPs into the coatings, we can generate a SERS-active surface on glass slides that can be used to monitor the concentration of chemical species in the surrounding. Using CV as a model, we found that the hybrid coating of three L-PG/AgNP bilayers displayed SERS activity toward the substrate (Figure 5d). The signal of CV at 1615 cm^{-1} increased with increasing CV concentration ranging from 500 nM to 10 μM (Figure S18). A limit of detection of 60 nM (signal-to-noise ratio of 3) was achieved. The facile preparation of the present hybrid coatings is expected to enable the design of “smart” SERS-active coatings on diverse substrates for sensing applications.

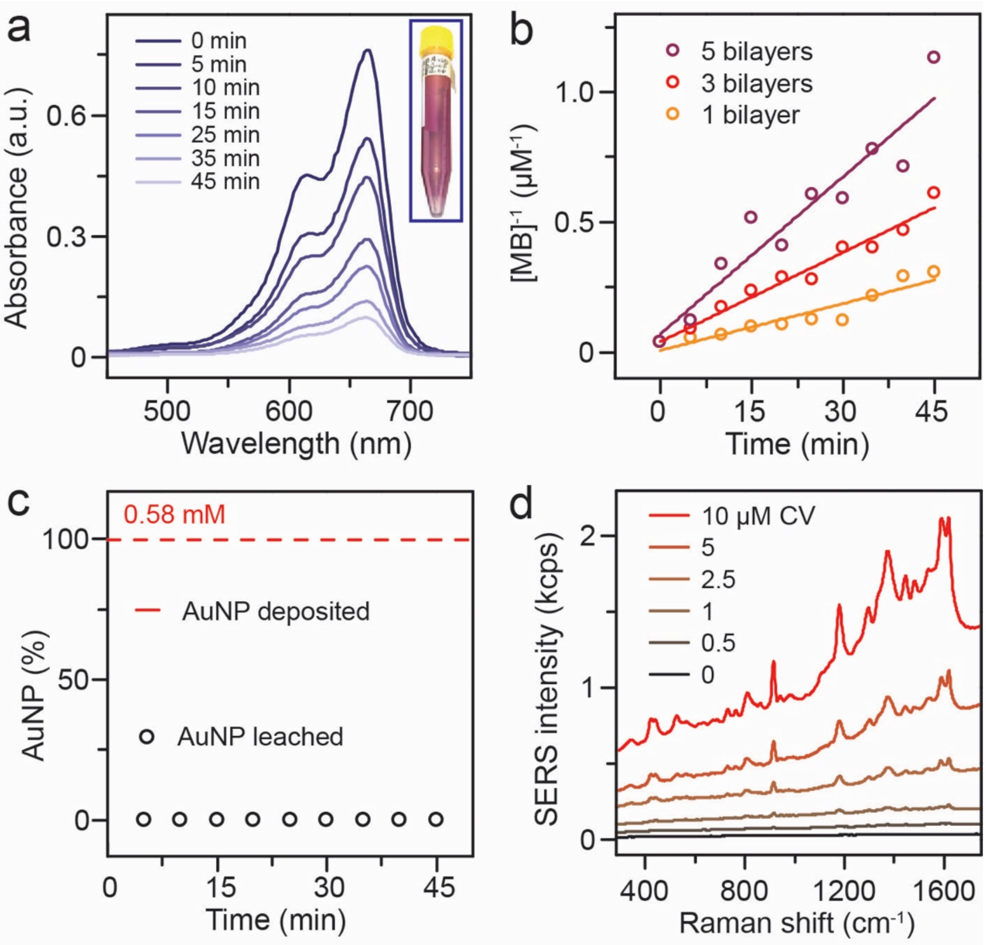

Fig. 5. Catalysis and sensing applications of L-PG/metal nanoparticles LbL assemblies. (a) UV–Vis spectra of MB recorded during its degradation via $NaBH_4$ in a 3-bilayer L-PG/AuNP-coated PP tube and photograph (inset) of the functionalized tube. (b) $NaBH_4$-mediated MB degradation kinetics in 1-, 3-, and 5-bilayer L-PG/AuNP-coated PP tubes. (c) Comparison of the amount of AuNPs leached from a 3-bilayer L-PG/AuNP-coated PP tube and the total amount of AuNPs originally deposited in the same tube. (d) SERS spectra of a 3-bilayer L-PG/AgNP-coated glass as a function of different concentrations of CV.

5.1.4 Conclusions

In the present work, adhesive glycogen nanoparticles were used as building blocks to prepare hybrid multifunctional films on various substrates, including organic and inorganic materials, in an aqueous environment. The adhesive and functional properties of L-PG are ascribed to the hydrophilic–hydrophobic interactions between the amphiphilic L-PG and the substrate. These polysaccharide-derived nano building blocks displayed negligible cytotoxicity, and the L-PG-based films were stable in harsh chemical environments but biodegradable. Furthermore, the presence of disulfide moieties onto L-PG allowed the integration of diverse metal nanoparticles to prepare multilayered films. As proof of concept, hybrid functional coatings were developed and applied for the catalysis and SERS-based detection of analytes. The PG-based coatings and multilayered films provide a versatile platform for engineering interfaces with modular functionalities and potential uses in nanomedicine, material science, catalysis, and sensing.

Conflicts of interest

There are no conflicts to declare.

5.1.5 Acknowledgements

This work was funded by an Australian Research Council (ARC) Future Fellowship (F. Cavalieri, FT140100873) and a National Health and Medical Research Council Senior Principal Research Fellowship (F. Caruso, GNT1135806) schemes. This project received funding from the European Union Horizon 2020 research and innovation program under the Marie Skłodowska-Curie grant agreement No. 690901 (“Nanosupremi”) and No. 798565 (A. Amodio “RE-IMMUNE”). This work was performed at the ARC Centre of Excellence in Convergent Bio-Nano Science and Technology (project number CE140100036) and in part at the Materials Characterization and Fabrication Platform (MCFP) at The University of Melbourne.

5.1.6 Notes and references

(1) M. Bjornmalm, K. J. Thurecht, M. Michael, A. M. Scott and F. Caruso, *ACS Nano,* 2017, **11**, 9594.

(2) M. Holzinger, A. Le Goff and S. Cosnier, *Front. Chem.,* 2014, **2**, 63.

(3) S. Goenka, V. Sant and S. Sant, *J. Controlled Rel.,* 2014, **173**, 75.

(4) D. Lu, J. Zhou, S. Hou, Q. Xiong, Y. Chen, K. Pu, J. Ren and H. Duan, *Adv. Mater.,* 2019, **31**, 1902733.

(5) X. Wang, J. Pu, B. An, Y. Li, Y. Shang, Z. Ning, Y. Liu, F. Ba, J. Zhang and C. Zhong, *Adv. Mater.,* 2018, **30**, 1705968.

(6) R. Liu, J. Zhao, Q. Han, X. Hu, D. Wang, X. Zhang and P. Yang, *Adv. Mater.,* 2018, **30**, 1802851.

(7) P. P. Tomanin, P. V. Cherepanov, Q. A. Besford, A. J. Christofferson, A. Amodio, C. F. McConville, I. Yarovsky, F. Caruso and F. Cavalieri, *ACS Appl. Mater. Interfaces,* 2018, **10**, 42786.

(8) Z. Shi, K. Neoh, E. Kang, C. Poh and W. Wang, *J. Biomed. Mater. Res., Part A,* 2008, **86**, 865.

(9) V. K. Thakur and M. K. Thakur, *ACS Sustainable Chem. Eng.,* 2014, **2**, 2637.

(10) T. Nishimura and K. Akiyoshi, *Wiley Interdiscip. Rev.: Nanomed. Nanobiotechnol.,* 2017, **9**, e1423.

(11) C. Wang, R. A. Venditti and K. Zhang, *Appl. Microbiol. Biotechnol.,* 2015, **99**, 5791.

(12) S. E. Burke and C. J. Barrett, *Biomacromolecules,* 2003, **4**, 1773.

(13) T. I. Croll, A. J. O'Connor, G. W. Stevens and J. J. Cooper-White, *Biomacromolecules,* 2006, **7**, 1610.

(14) S. G. Ball and M. K. Morell, *Annu. Rev. Plant Biol.,* 2003, **54**, 207.

(15) P. J. Roach, A. A. Depaoli-Roach, T. D. Hurley and V. S. Tagliabracci, *Biochem. J.,* 2012, **441**, 763.

(16) Q. A. Besford, F. Cavalieri and F. Caruso, *Adv. Mater.,* 2019, 1904625, DOI: 10.1002/adma.201904625.

(17) M. Grossutti and J. R. Dutcher, *Biomacromolecules,* 2016, **17**, 1198.

(18) J. D. Nickels, J. Atkinson, E. Papp-Szabo, C. Stanley, S. O. Diallo, S. Perticaroli, B. Baylis, P. Mahon, G. Ehlers and J. Katsaras, *Biomacromolecules,* 2016, **17**, 735.

(19) M. Wojnilowicz, A. Glab, A. Bertucci, F. Caruso and F. Cavalieri, *ACS Nano,* 2018, **13**, 187.

(20) M. Wojnilowicz, Q. A. Besford, Y.-L. Wu, X. J. Loh, J. A. Braunger, A. Glab, C. Cortez-Jugo, F. Caruso and F. Cavalieri, *Biomaterials,* 2018, **176**, 34.

(21) M. Perrone, A. Lopalco, A. Lopedota, A. Cutrignelli, V. Laquintana, J. Douglas, M. Franco, E. Liberati, V. Russo and S. Tongiani, *Eur. J. Pharm. Biopharm.,* 2017, **119**, 161.

(22) R. Kandimalla, S. Dash, A. C. Bhowal, S. Kalita, N. C. Talukdar, S. Kundu and J. Kotoky, *Int. J. Nanomed.,* 2017, **12**, 7025.

(23) F. Lu, A. Mencia, L. Bi, A. Taylor, Y. Yao and H. HogenEsch, *J. Controlled Rel.,* 2015, **204**, 51.

(24) Q. A. Besford, M. Wojnilowicz, T. Suma, N. Bertleff-Zieschang, F. Caruso and F. Cavalieri, *ACS Appl. Mater. Interfaces,* 2017, **9**, 16869.

(25) S. Aasen, A. Pospisilova, T. Eichler, J. Panek, M. Hruby, P. Stepanek, E. Spriet, D. Jirak, K. Skaftnesmo and F. Thorsen, *Int. J. Mol. Sci.,* 2015, **16**, 21658.

(26) Y. Zhu, W. Tong and C. Gao, *Soft Matter,* 2011, **7**, 5805.

(27) B. Macphail and M. A. Brook, *Greem Chem.,* 2017, **19**, 4373.

(28) J. Li, D. Maniar, X. Qu, H. Liu, C.-Y. Tsao, E. Kim, W. E. Bentley, C. Liu and G. F. Payne, *Biomacromolecules,* 2019, **20**, 969.

(29) Y. Xie and Y. Yao, *Carbohydr. Polym.,* 2018, **180**, 29.

(30) M. Rabyk, M. Hruby, M. Vetrik, J. Kucka, V. Proks, M. Parizek, R. Konefal, P. Krist, D. Chvatil and L. Bacakova, *Carbohydr. Polym.,* 2016, **152**, 271.

(31) P. Patra, A. P. Rameshbabu, D. Das, S. Dhara, A. B. Panda and S. Pal, *Polym. Chem.,* 2016, **7**, 5426.

(32) M. Bertoldo, G. Zampano, L. Suffner, E. Liberati and F. Ciardelli, *Polym. Chem.,* 2013, **4**, 653.

(33) T. Liebert, M. A. Hussain, M. N. Tahir and T. Heinze, *Polym. Bull.,* 2006, **57**, 857.

(34) F. Gu, C. Hu, Z. Tai, C. Yao, J. Tian, L. Zhang, Q. Xia, C. Gong, Y. Gao and S. Gao, *Sci. Rep.,* 2016, **6**, 36281.

(35) P. Thoniyot, M. J. Tan, A. A. Karim, D. J. Young and X. J. Loh, *Adv. Sci.,* 2015, **2**, 1400010.

5.2 Supplementary Information

Nanoengineering Multifunctional Hybrid Interfaces Using Adhesive Glycogen Nanoparticles

Pietro Pacchin Tomanin, Jiajing Zhou, Alessia Amodio, Rita Cimino, Agata Glab, Francesca Cavalieri, Frank Caruso

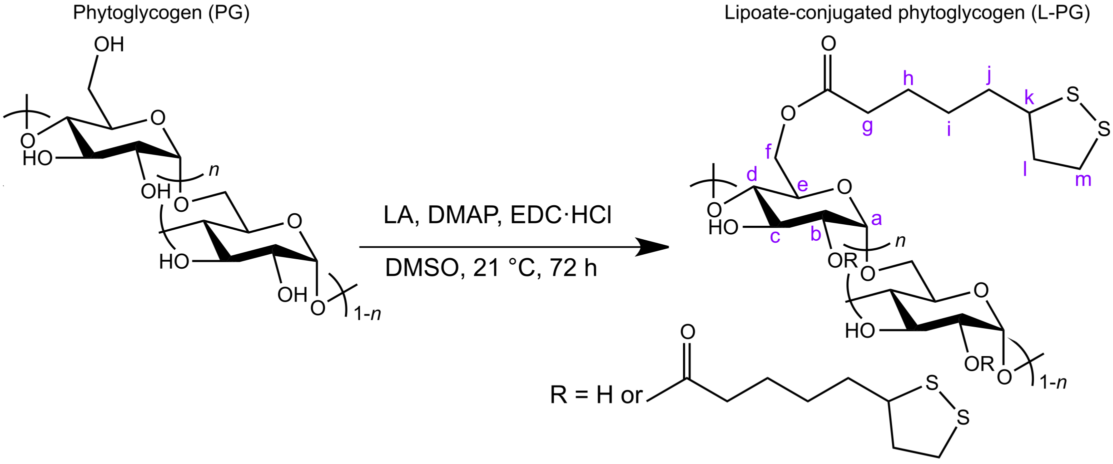

Figure S1: PG functionalization reaction with lipoic acid to obtain L-PG via Steglich esterification.

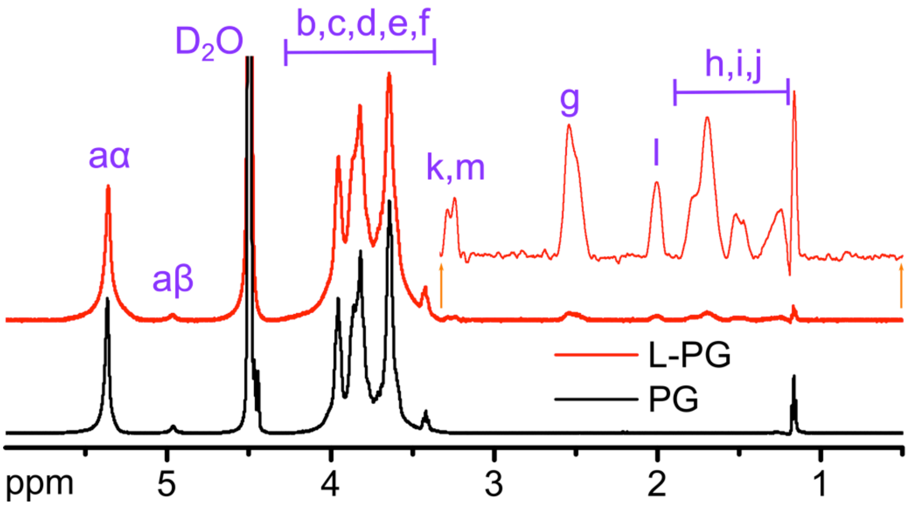

Figure S2: H-NMR spectra of L-PG and PG. The thin red line is a magnification of the lipoate peaks from 3.4 to 0.5 ppm.

Table S1: Chemical modification reactions of PG into L-PG

Type of glycogen	Targeted degree of functionalization (LA/glucose mol/mol)	Actual degree of functionalization (LA/glucose mol/mol)	Solubility
PG	30	Not measured	Non-soluble in water, EtOH, DMSO, or *n*-hexane
PG	20	Not measured	Non-soluble in water, EtOH/water (50:50), or DMSO
PG	10	2% on total glucose, 10.6% on H4 terminal	Water soluble, up to 20 mg mL^{-1}
PG	3	Below H-NMR limit of detection	Water
PG	1	Below H-NMR limit of detection	Water

PG, phytoglycogen; EtOH, ethanol; DMSO, dimethyl sulfoxide.

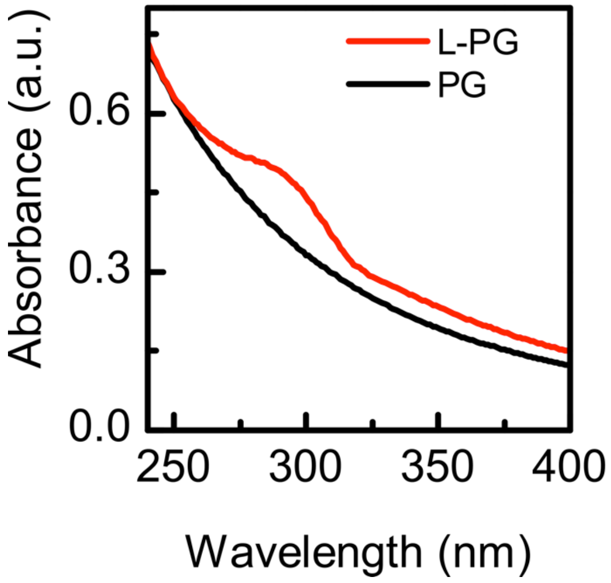

Figure S3: UV–vis spectra of L-PG and PG.

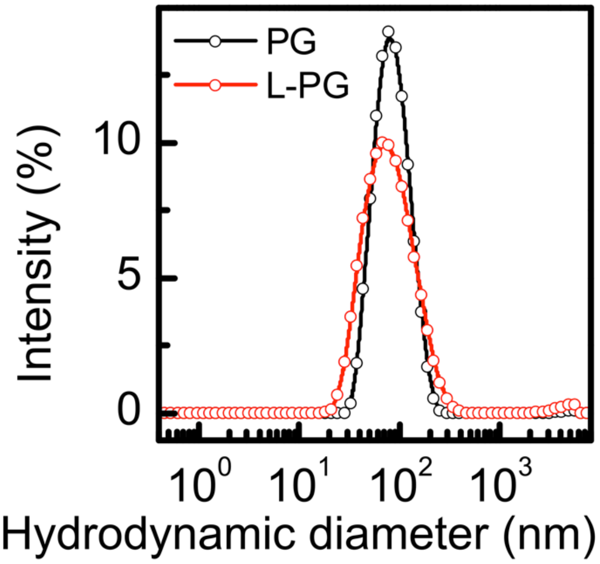

Figure S4: DLS hydrodynamic diameter populations of L-PG and PG.

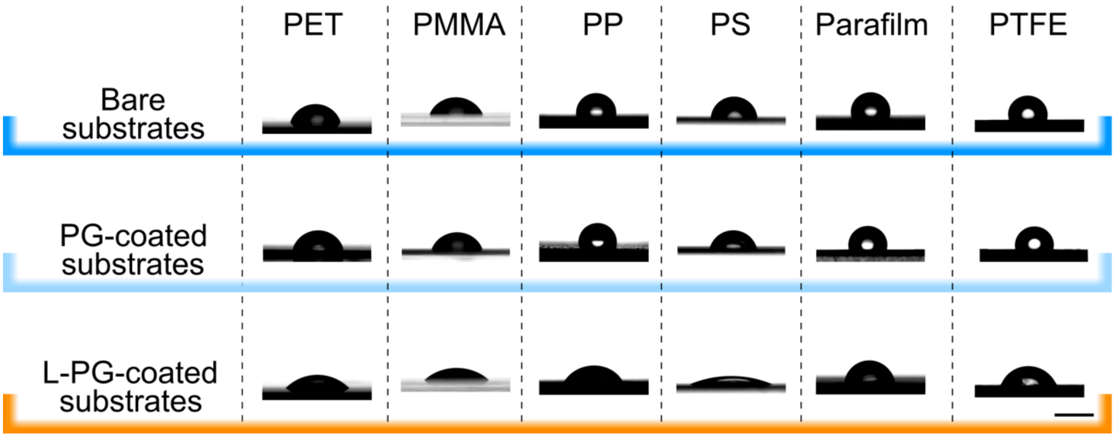

Figure S5: Photographs of water droplets on bare, PG-, and L-PG-coated substrates; the contact angle values are given in Figure 2c. Scale bar: 2 µm.

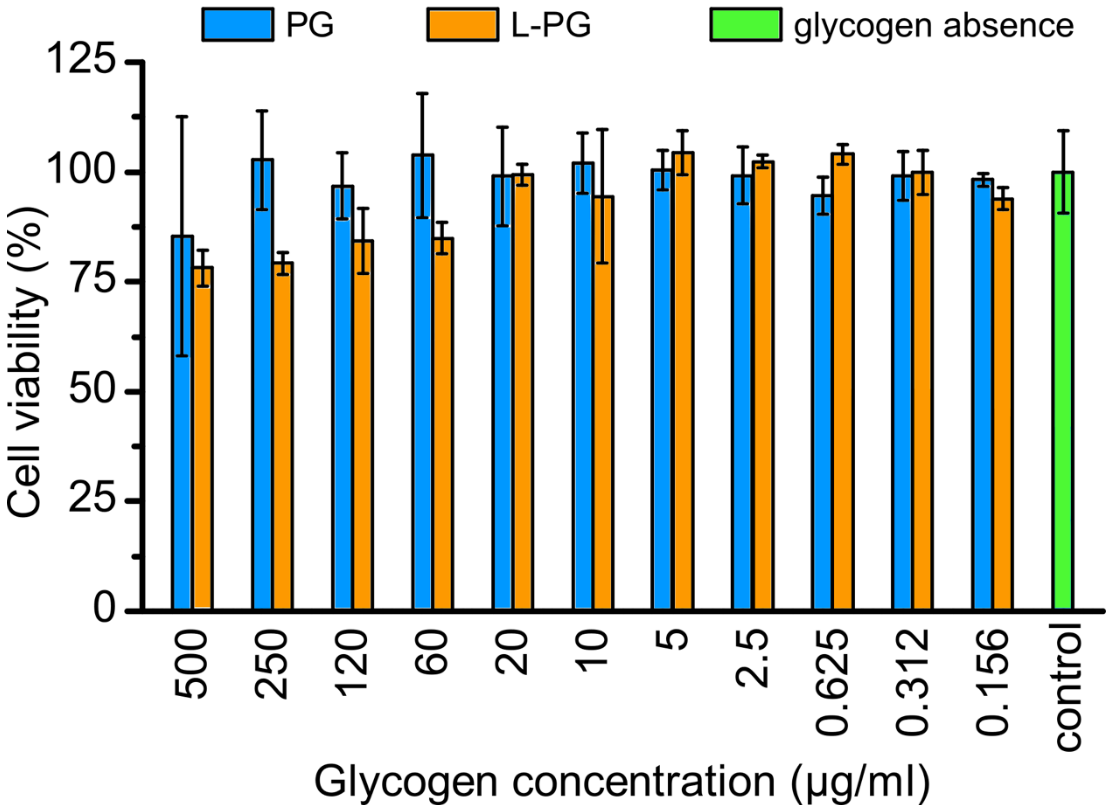

Figure S6: Cytotoxicity studies of PG and L-PG.

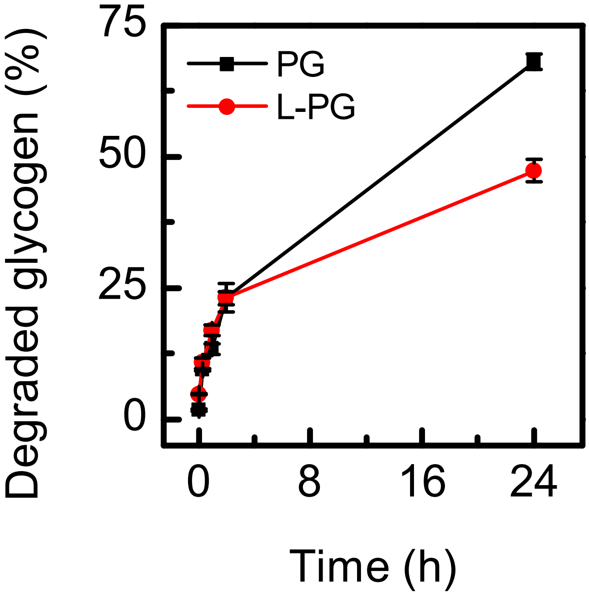

Figure S7: Enzymatic degradation of PG and L-PG.

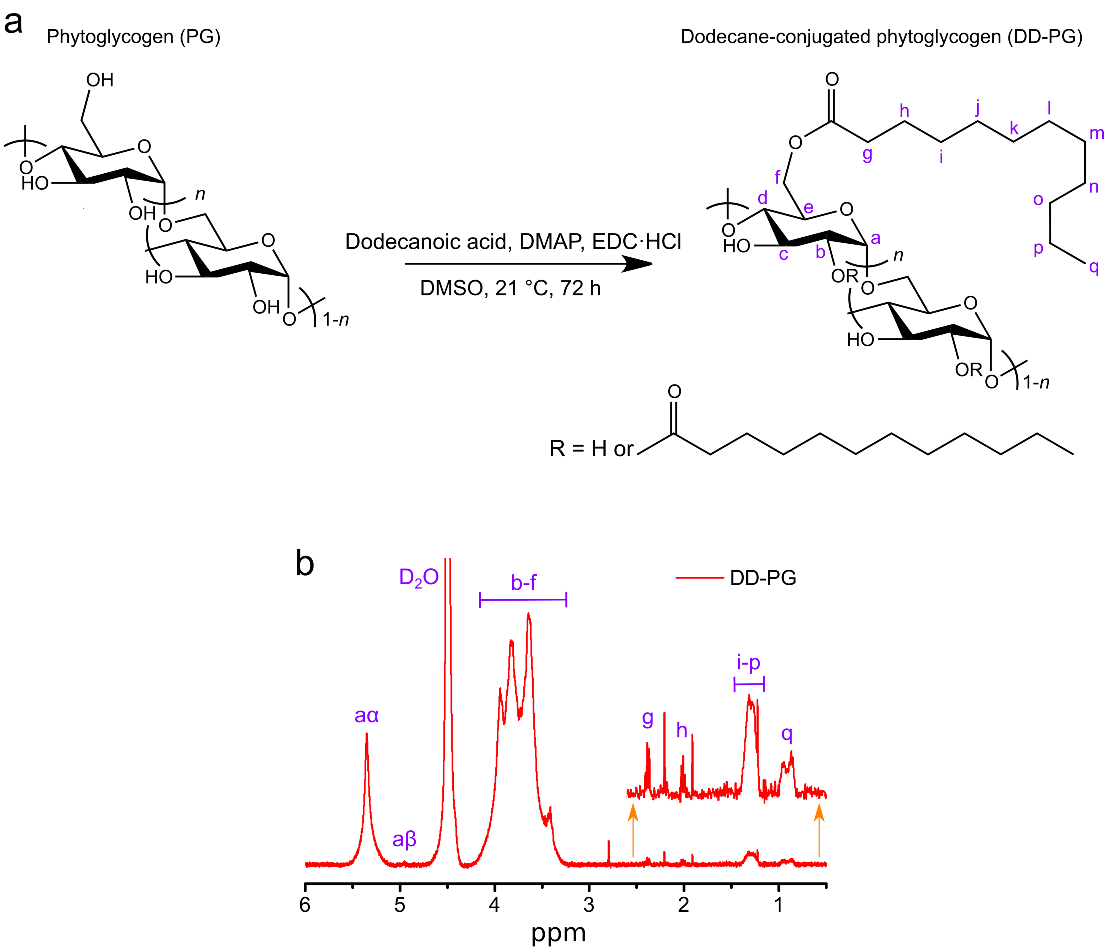

Figure S8: (a) PG functionalization reaction with dodecanoic acid to obtain DD-PG via Steglich esterification and (b) H-NMR spectra of DD-PG with magnification of the peaks corresponding to the dodecane moiety from 2.5 to 0.5 ppm.

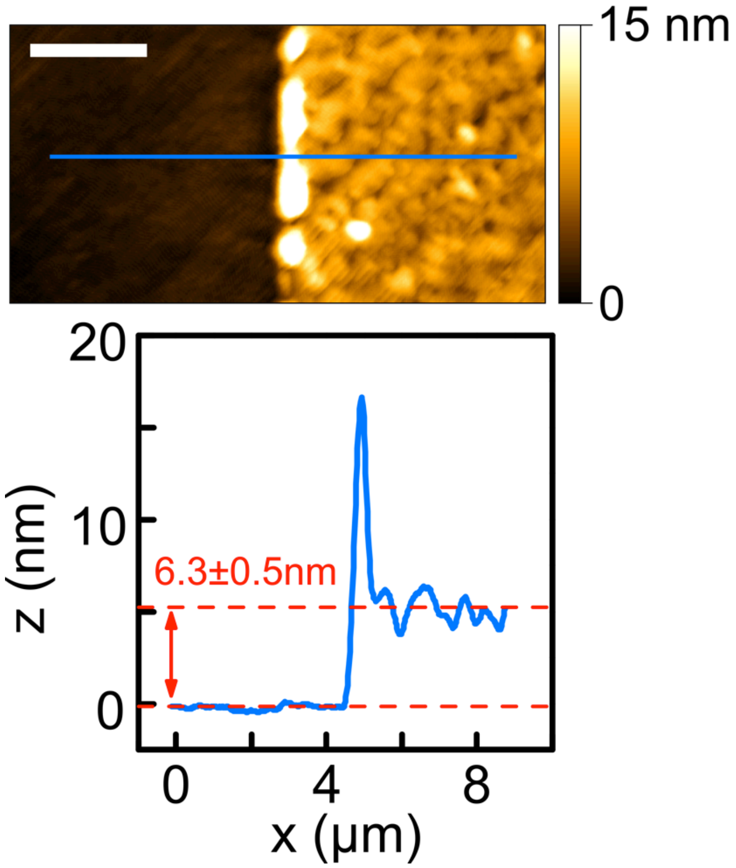

Figure S9: Dry-state AFM image and corresponding height profile of DD-PG-coated glass substrates (scale bar = 2 µm).

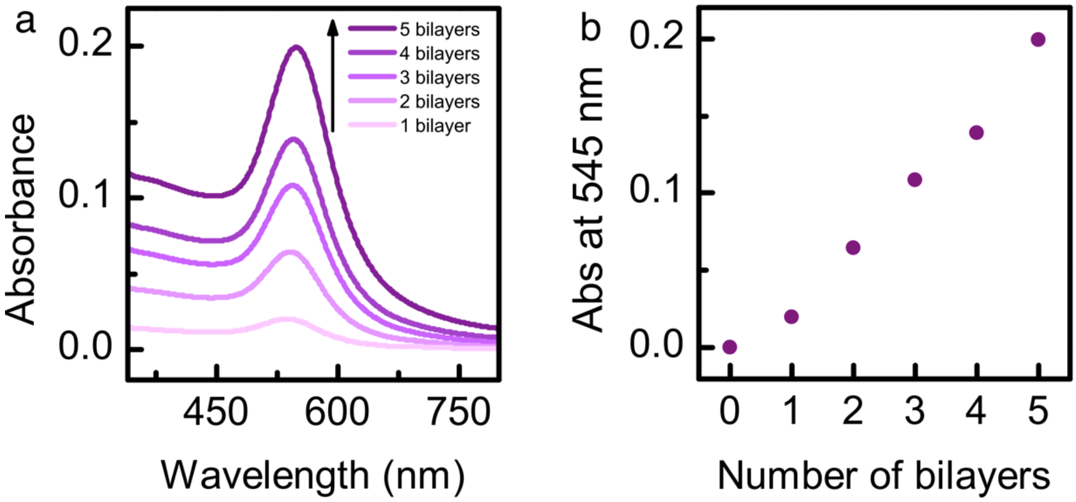

Figure S10: (a) UV–Vis spectra of glass substrates coated with increasing number of L-PG/AuNP bilayers. (b) Localized surface plasmon resonance absorbance profile at 545 nm as a function of the bilayer number.

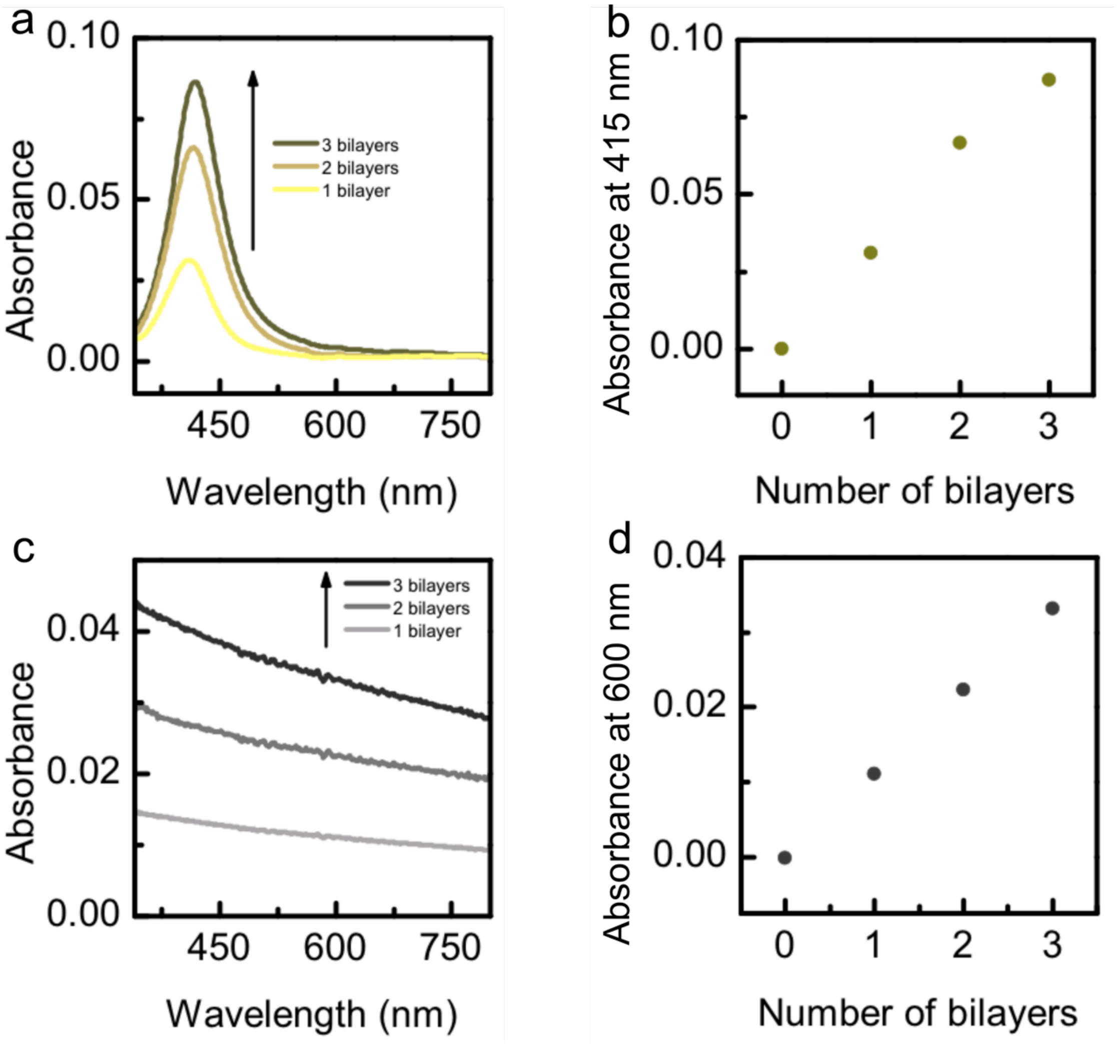

Figure S11: UV–Vis spectra of glasses coated with increasing number of (a) L-PG/AgNP and (c) L-PG/PtNP bilayers with corresponding absorbances at (b) 415 nm and (d) 600 nm as a function of the bilayer number.

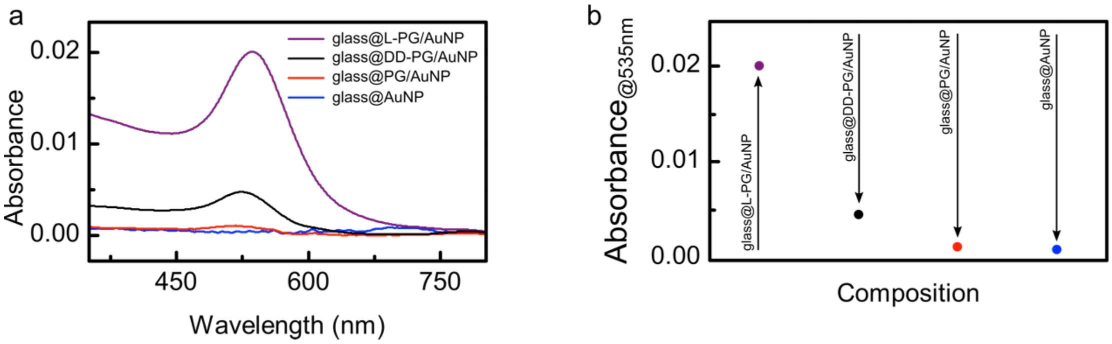

Figure S12: (a) UV–Vis spectra of glass substrates coated with L-PG/AuNP, DD-PG/AuNP, PG/AuNP assemblies or AuNPs alone and (b) corresponding absorbances at 545 nm.

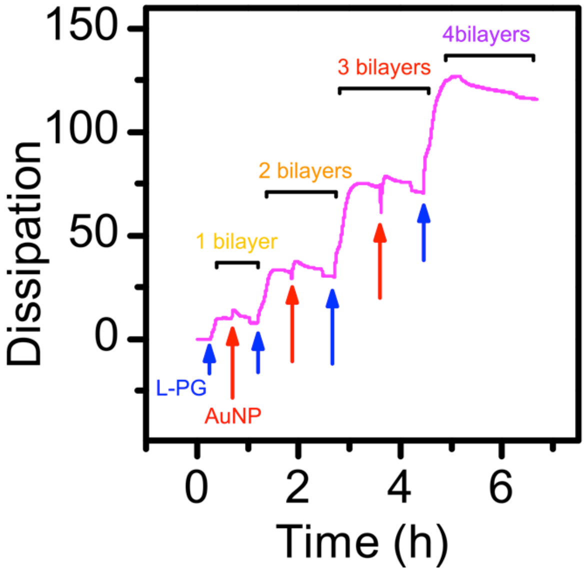

Figure S13: QCM-D dissipation profile of an L-PG/AuNP LbL assembly on gold chip obtained upon sequential deposition of L-PG (blue arrow) and AuNPs (red arrow); the corresponding QCM-D frequency profile is shown in Figure 3b.

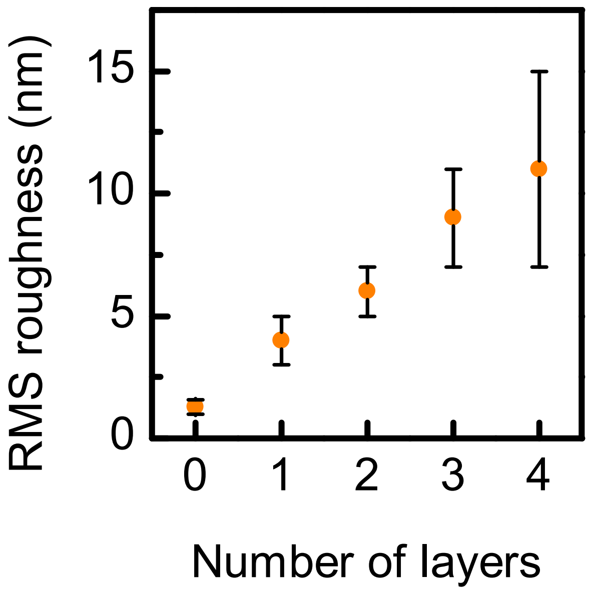

Figure S14: Root mean square (RMS) roughness of dry films as a function of the L-PG/AuNP bilayer number.

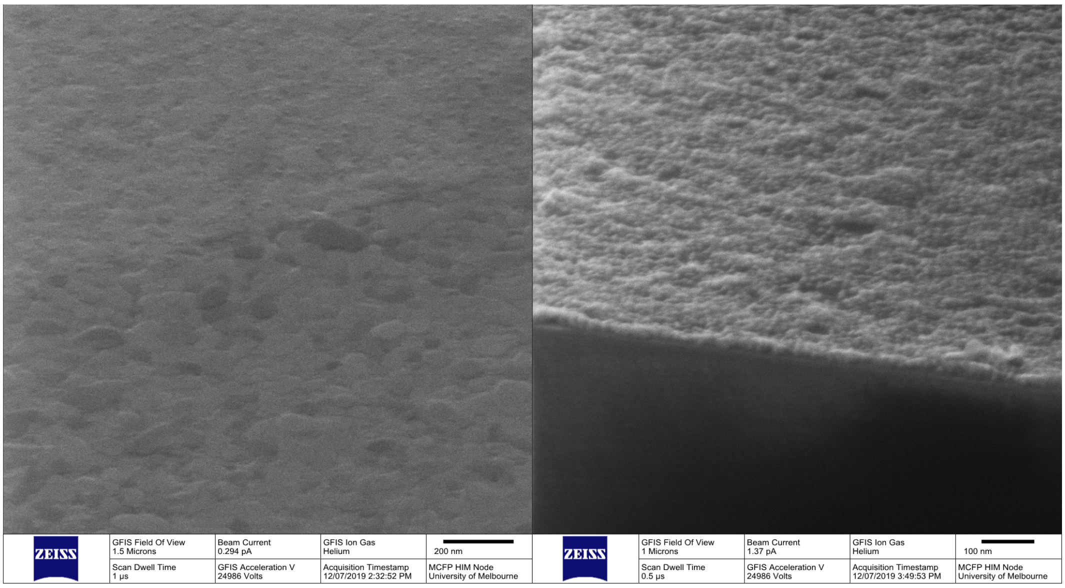

Figure S15: HIM images of L-PG/AuNP LbL assembly on glass with the final layer as L-PG (left) and AuNP (right).

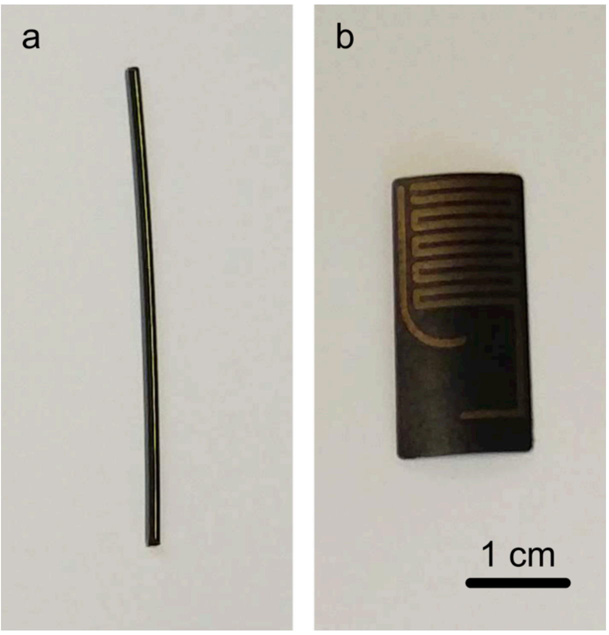

Figure S16: Photographs of L-PG/AuNP assembly on (a) polyether ether ketone and (b) Viton.

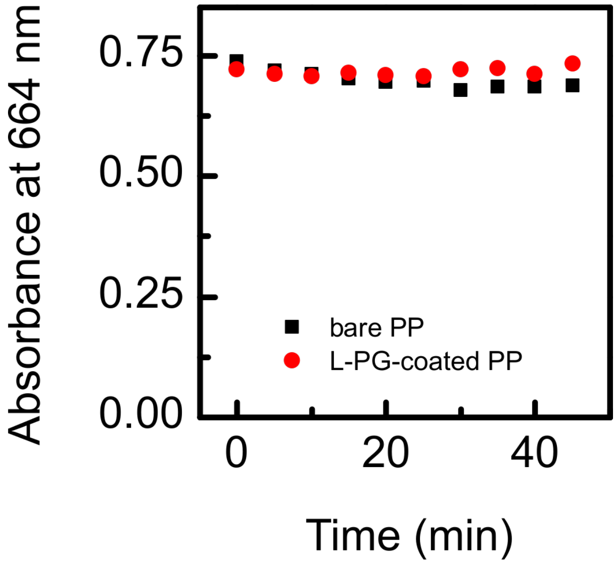

Figure S17: Degradation kinetics of MB via $NaBH_4$ on a bare PP tube and L-PG-coated PP tube. Both reaction systems do not contain AuNPs.

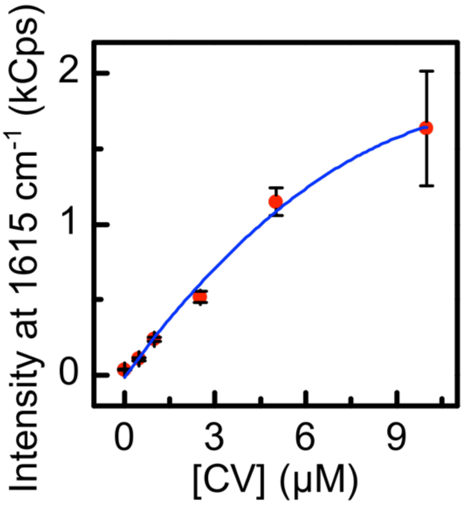

Figure S18: SERS signal intensity at 1615 cm^{-1} as a function of the concentration of the crystal violet (CV) solution; the corresponding SERS intensity profiles are shown in Figure 5d.

Chapter 6

Conclusions and Future Prospects

In summary, this research work new hybrid materials composed of organic and inorganic building blocks can be used to prepare nanostructured functional materials for sensing applications. The different synthetic strategies to prepare the studied hybrid materials, including blending, co-crystallization, and bottom-up self-assembly of nano-building blocks, allow the manipulation and tailoring of the organic and inorganic interactions to design hybrid structures with controlled chemical and physical properties. The engineering of these hybrid materials led to the development of various nanostructures with diverse electrocatalytic, catalytic, optical, functional, and adhesive properties. The newly developed hybrid materials were employed as sensors for the detection of analytes. The new results presented in this thesis can be useful for further development of advanced hybrid nanostructured materials for sensing applications, as well as for applications in drug delivery, catalysis and environmental remediation. A summary and prospects of this PhD work is provided below

In **Chapter 3**, the synthesis of electro-catalytically cobalt phosphate structures was reported via a simple crystallization strategy in mild conditions. A hybrid electrode, prepared with a ink composed of the inorganic structures together with an organic fluorinated binding polymer, displayed electrocatalytic activity toward the non-enzymatic direct oxidation of glucose, allowing the sensing of glucose in a relevant biological environment as PBS electrolyte at physiological pH of 7.4. Glucose was detected in physiological relevant concentrations from 1 to 30 mM in PBS, with a sensitivity of 7.9 nA/mM cm^2, and a limit of detection (LOD) of 0.3 mM. The system showed to be stable and specific toward the oxidation of glucose in both PBS and diluted solutions of human serum. The detection of glucose, up to 35 mM, was achieved in diluted solutions of human serum in PBS. Moreover, density functional theory experiments suggested that the optimal binding of glucose occurred at under-coordinated cobalt atoms. These findings highlight the potentials of cobalt phosphate-modified hybrid electrodes for glucose sensing in relevant biological conditions.

In **Chapter 4**, dextran sulfate-copper phosphate hybrid nanoflowers (D-NF) were reported. Optimization of crystallization parameters allows the preparation of monodisperse and hierarchically structured particles with a high volume-to-surface ratio. Furthermore, a coating process of D-NF was reported for the preparation of catalytic microreactors. The D-NF displayed non-enzymatic peroxidase-like catalytic activity that, in the presence of hydrogen peroxide (H_2O_2), promotes a chromogenic reaction, allowing the detection of H_2O_2. The sensor achieved an H_2O_2 linear detection range from 0 to 0.4 mM in PBS with a sensitivity of 28.3±0.6 kcps/mM and a LOD of 35 μM (S/N=3), and a non-linear detection up to 7 mM. Further, a glucose sensor was developed based on a hybrid enzymatic/non-enzymatic cascade reaction involving glucose oxidase (GOx) and D-NF. This system showed a linear glucose detection range from 0 to 1 mM in PBS with a sensitivity of 1180±70 cps/mM and a LOD of 35 μM, and a non-linear detection up to 6 mM. These results underline the possibility to engineer sensing platforms utilizing the catalytic properties of D-NF.

In **Chapter 5**, natural nanoparticles, i.e. phytoglycogen, were engineered, to impart adhesive and functional properties, and used as nano-building blocks to prepare hybrid multifunctional films. When lipoic acid moieties were conjugated to phytoglycogen (L-PG), these functionalized hyperbranched polysaccharidic nanoparticles could form coatings on various substrates, regardless of substrates chemical composition. It was found that the L-PG amphiphilic properties, which induced the hydrophilic–hydrophobic interactions between the nanoparticles and the substrates, were the driving force promoting the adhesion of L-PG and its self-assembly into coatings. L-PG-based coatings were stable in harsh chemical environments and yet maintain biodegradability. Moreover, these nano building blocks showed low cytotoxicity. Furthermore, the disulfide functional groups of lipoate in L-PG promoted the affinity of these structures to metal nanoparticles, allowing the preparation of multi-layered hybrid films. The properties of these hybrid nanostructures, like chemical composition, thickness, roughness, and functionality were controlled by the assembly procedure employing different metal nanoparticles and substrates. As proof of concept, hybrid functional films were prepared with gold and silver nanoparticles and applied for the catalysis and SERS-based detection of analytes, respectively. These coatings and hybrid films provide a versatile platform for engineering interfaces with modular functionalities and potential applications in nanomedicine, material science, catalysis, and sensing.

Overall, the studies performed in this thesis enabled the design of novel hybrid materials.

The studies on cobalt-based hybrid electrodes present insights into the materials preparation and its electrocatalytic properties, which will be useful to pave the way for case-specific designs of electroactive materials. In particular, non-toxic yet electroactive metals such as manganese, iron, and zinc, could be promising candidates for further developments of nanoflowers-based electrochemical biosensors.

The research work on hybrid dextran sulfate-copper phosphate nanoflowers cast light on the materials synthesis and its non-enzymatic catalytic properties. Possible future developments will involve the use of other organic and inorganic building blocks to prepare and discover unexplored kind of nanoflowers for sensing and environmental applications. For instance, hybrid nanoflowers with different morphologies could be prepared using dextran polysaccharides having different moieties that show affinity toward transition metals, like carboxyl, phosphate, amine, imine, isocyanates, thiol, and catechol functional groups. Whereas, hybrid nanoflowers with novel chemical catalytic activities could be synthesized using other inorganic phosphates based on different transition metals, such as iron, manganese, nickel, zinc, and titanium.

The studies on functionalized phytoglycogen provided knowledge into the material chemical modification and its adhesive and functional properties. Prospective research work will include the conjugation of glycogen with other hydrophobic and functional moieties, the conjugation of lipoic acid on other polysaccharides or polymers, and the coating of additional substrates. These investigations will expand the possibilities for the design of organic coatings with advanced properties. Moreover, the combination of L-PG with other inorganic nano-objects, as clays, quantum dots, as well as silica, superparamagnetic, and metal nanoparticles can be a scientific area to explore for the preparation of new glycogen-based hybrid materials. Notwithstanding a few examples of promising applications of L-PG-based hybrid assemblies were proposed in this thesis, diverse other directions can be studied more in details. For instances, the capability of L-PG to coat intricate geometries as the inside of tubes can be used, utilizing gold and silver nanoparticles respectively, to prepare catalytic microfluidic reactors or antibacterial catheter.

Appendix

Self-Assembly of a Metal–Phenolic Sorbent for Broad-Spectrum Metal Sequestration

Md Arifur Rahim, Gan Lin, **Pietro Pacchin Tomanin**, Yi Ju, Anders Barlow, Mattias Björnmalm, Frank Caruso

ACS Appl. Mater. Interfaces 2020, 12, 3, 3746-3754
https://doi.org/10.1021/acsami.9b19097

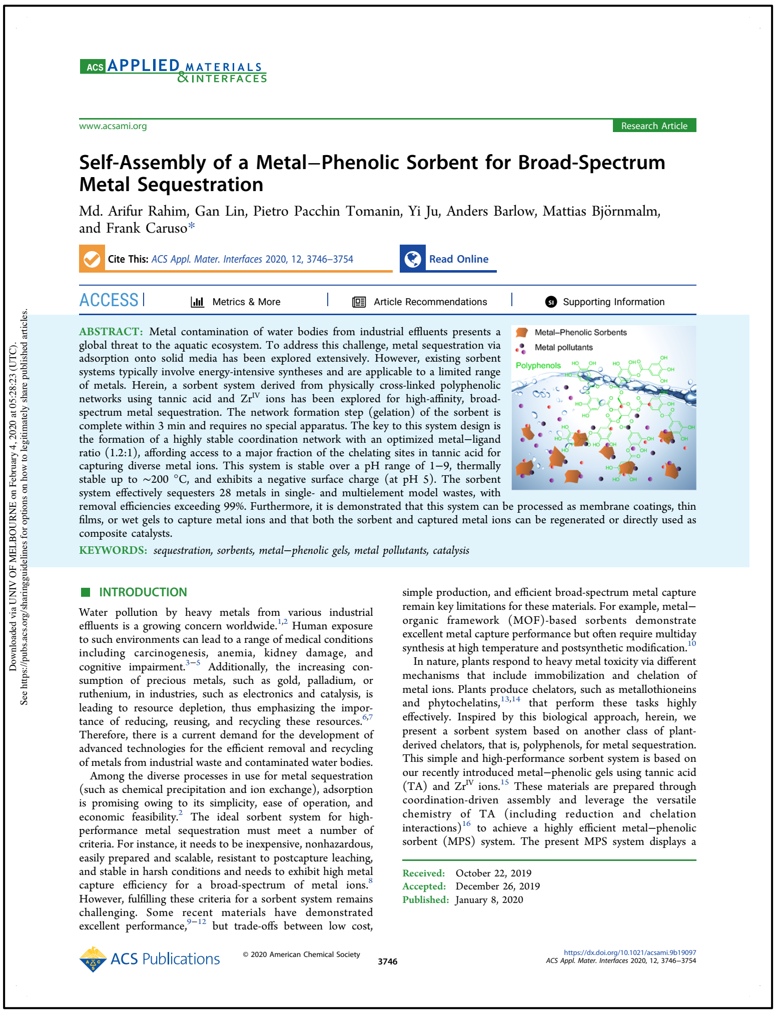

ACS APPLIED MATERIALS & INTERFACES
www.acsami.org Research Article

Self-Assembly of a Metal−Phenolic Sorbent for Broad-Spectrum Metal Sequestration

Md. Arifur Rahim, Gan Lin, Pietro Pacchin Tomanin, Yi Ju, Anders Barlow, Mattias Björnmalm, and Frank Caruso*

Cite This: *ACS Appl. Mater. Interfaces* 2020, 12, 3746−3754 Read Online

ACCESS | Metrics & More | Article Recommendations | Supporting Information

ABSTRACT: Metal contamination of water bodies from industrial effluents presents a global threat to the aquatic ecosystem. To address this challenge, metal sequestration via adsorption onto solid media has been explored extensively. However, existing sorbent systems typically involve energy-intensive syntheses and are applicable to a limited range of metals. Herein, a sorbent system derived from physically cross-linked polyphenolic networks using tannic acid and Zr^{IV} ions has been explored for high-affinity, broad-spectrum metal sequestration. The network formation step (gelation) of the sorbent is complete within 3 min and requires no special apparatus. The key to this system design is the formation of a highly stable coordination network with an optimized metal−ligand ratio (1.2:1), affording access to a major fraction of the chelating sites in tannic acid for capturing diverse metal ions. This system is stable over a pH range of 1−9, thermally stable up to ∼200 °C, and exhibits a negative surface charge (at pH 5). The sorbent system effectively sequesters 28 metals in single- and multielement model wastes, with removal efficiencies exceeding 99%. Furthermore, it is demonstrated that this system can be processed as membrane coatings, thin films, or wet gels to capture metal ions and that both the sorbent and captured metal ions can be regenerated or directly used as composite catalysts.

KEYWORDS: *sequestration, sorbents, metal−phenolic gels, metal pollutants, catalysis*

■ INTRODUCTION

Water pollution by heavy metals from various industrial effluents is a growing concern worldwide.[1,2] Human exposure to such environments can lead to a range of medical conditions including carcinogenesis, anemia, kidney damage, and cognitive impairment.[3−5] Additionally, the increasing consumption of precious metals, such as gold, palladium, or ruthenium, in industries, such as electronics and catalysis, is leading to resource depletion, thus emphasizing the importance of reducing, reusing, and recycling these resources.[6,7] Therefore, there is a current demand for the development of advanced technologies for the efficient removal and recycling of metals from industrial waste and contaminated water bodies.

Among the diverse processes in use for metal sequestration (such as chemical precipitation and ion exchange), adsorption is promising owing to its simplicity, ease of operation, and economic feasibility.[2] The ideal sorbent system for high-performance metal sequestration must meet a number of criteria. For instance, it needs to be inexpensive, nonhazardous, easily prepared and scalable, resistant to postcapture leaching, and stable in harsh conditions and needs to exhibit high metal capture efficiency for a broad-spectrum of metal ions.[8] However, fulfilling these criteria for a sorbent system remains challenging. Some recent materials have demonstrated excellent performance,[9−12] but trade-offs between low cost, simple production, and efficient broad-spectrum metal capture remain key limitations for these materials. For example, metal−organic framework (MOF)-based sorbents demonstrate excellent metal capture performance but often require multiday synthesis at high temperature and postsynthetic modification.[10]

In nature, plants respond to heavy metal toxicity via different mechanisms that include immobilization and chelation of metal ions. Plants produce chelators, such as metallothioneins and phytochelatins,[13,14] that perform these tasks highly effectively. Inspired by this biological approach, herein, we present a sorbent system based on another class of plant-derived chelators, that is, polyphenols, for metal sequestration. This simple and high-performance sorbent system is based on our recently introduced metal−phenolic gels using tannic acid (TA) and Zr^{IV} ions.[15] These materials are prepared through coordination-driven assembly and leverage the versatile chemistry of TA (including reduction and chelation interactions)[16] to achieve a highly efficient metal−phenolic sorbent (MPS) system. The present MPS system displays a

Received: October 22, 2019
Accepted: December 26, 2019
Published: January 8, 2020

https://dx.doi.org/10.1021/acsami.9b19097
ACS Appl. Mater. Interfaces 2020, 12, 3746−3754

ACS APPLIED MATERIALS & INTERFACES

www.acsami.org Research Article

Self-Assembly of a Metal–Phenolic Sorbent for Broad-Spectrum Metal Sequestration

Md. Arifur Rahim, Gan Lin, Pietro Pacchin Tomanin, Yi Ju, Anders Barlow, Mattias Björnmalm, and Frank Caruso*

Cite This: ACS Appl. Mater. Interfaces 2020, 12, 3746–3754 Read Online

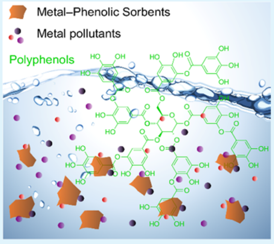

ABSTRACT: Metal contamination of water bodies from industrial effluents presents a global threat to the aquatic ecosystem. To address this challenge, metal sequestration via adsorption onto solid media has been explored extensively. However, existing sorbent systems typically involve energy-intensive syntheses and are applicable to a limited range of metals. Herein, a sorbent system derived from physically cross-linked polyphenolic networks using tannic acid and Zr^{IV} ions has been explored for high-affinity, broad-spectrum metal sequestration. The network formation step (gelation) of the sorbent is complete within 3 min and requires no special apparatus. The key to this system design is the formation of a highly stable coordination network with an optimized metal–ligand ratio (1.2:1), affording access to a major fraction of the chelating sites in tannic acid for capturing diverse metal ions. This system is stable over a pH range of 1−9, thermally stable up to ~200 °C, and exhibits a negative surface charge (at pH 5). The sorbent system effectively sequesters 28 metals in single- and multielement model wastes, with removal efficiencies exceeding 99%. Furthermore, it is demonstrated that this system can be processed as membrane coatings, thin films, or wet gels to capture metal ions and that both the sorbent and captured metal ions can be regenerated or directly used as composite catalysts.

KEYWORDS: *sequestration, sorbents, metal–phenolic gels, metal pollutants, catalysis*

INTRODUCTION

Water pollution by heavy metals from various industrial effluents is a growing concern worldwide.[1,2] Human exposure to such environments can lead to a range of medical conditions including carcinogenesis, anemia, kidney damage, and cognitive impairment.[3−5] Additionally, the increasing consumption of precious metals, such as gold, palladium, or ruthenium, in industries, such as electronics and catalysis, is leading to resource depletion, thus emphasizing the importance of reducing, reusing, and recycling these resources.[6,7] Therefore, there is a current demand for the development of advanced technologies for the efficient removal and recycling of metals from industrial waste and contaminated water bodies.

Among the diverse processes in use for metal sequestration (such as chemical precipitation and ion exchange), adsorption is promising owing to its simplicity, ease of operation, and economic feasibility.[2] The ideal sorbent system for high-performance metal sequestration must meet a number of criteria. For instance, it needs to be inexpensive, nonhazardous, easily prepared and scalable, resistant to postcapture leaching, and stable in harsh conditions and needs to exhibit high metal capture efficiency for a broad-spectrum of metal ions.[8] However, fulfilling these criteria for a sorbent system remains challenging. Some recent materials have demonstrated excellent performance,[9−12] but trade-offs between low cost, simple production, and efficient broad-spectrum metal capture remain key limitations for these materials. For example, metal–organic framework (MOF)-based sorbents demonstrate excellent metal capture performance but often require multiday synthesis at high temperature and postsynthetic modification.[10]

In nature, plants respond to heavy metal toxicity via different mechanisms that include immobilization and chelation of metal ions. Plants produce chelators, such as metallothioneins and phytochelatins,[13,14] that perform these tasks highly effectively. Inspired by this biological approach, herein, we present a sorbent system based on another class of plant-derived chelators, that is, polyphenols, for metal sequestration. This simple and high-performance sorbent system is based on our recently introduced metal–phenolic gels using tannic acid (TA) and Zr^{IV} ions.[15] These materials are prepared through coordination-driven assembly and leverage the versatile chemistry of TA (including reduction and chelation interactions)[16] to achieve a highly efficient metal–phenolic sorbent (MPS) system. The present MPS system displays a

Received: October 22, 2019
Accepted: December 26, 2019
Published: January 8, 2020

https://dx.doi.org/10.1021/acsami.9b19097
ACS Appl. Mater. Interfaces 2020, 12, 3746–3754

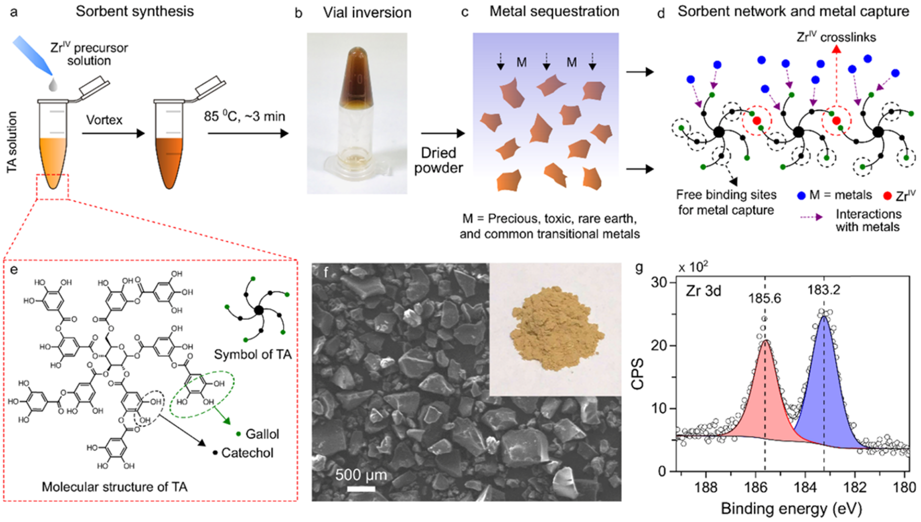

Figure 1. (a−c) Schematic illustration of the preparation of the MPS and subsequent application for metal sequestration. (d) Molecular view of the MPS network and metal sorption via interaction with free catechol and/or gallol groups of TA in the sorbent. (e) Molecular structure and schematic representation of TA. (f) Scanning electron microscopy image and photograph (inset) of the MPS powder. (g) Core-level X-ray photoelectron spectroscopy pattern of Zr^{IV} in the MPS.

combination of attributes: (i) it can sequester 28 metals both in single- and multielement model wastes (a more diverse set than that of previously reported sorbents); (ii) its performance is on par or exceeds current high-performance systems (including capture efficiencies exceeding 99%, distribution coefficients (K_d) exceeding 4×10^5 mL g^{-1}, and maximum sorption capacities ranging from 400 to >1000 mg g^{-1} for key metals such as Au, Pb, and Hg); and (iii) it can be assembled quickly (<3 min), easily (no special apparatus needed), and inexpensively (using low-cost, off-the-shelf components). In addition to this set of attributes, the MPS system can be engineered into membrane coatings, thin films, or wet gels to further facilitate its application in diverse areas. Finally, the MPS system (and the captured metals) can be easily regenerated or directly used as composite catalysts for the decomposition of organic pollutants.

■ RESULTS AND DISCUSSION

Synthesis and Characterization. The fabrication of the MPS is based on a rapid sol−gel process that does not require intensive energy input or any special apparatus. Both constituents of the sorbent system are inexpensive, highly biocompatible, and abundant: TA is a ubiquitous plant polyphenol (Figure 1e),[16] and the concentration of Zr^{IV} in the Earth's crust is ~0.02%.[17] The preparation of the MPS system is schematically presented in Figure 1a,b. After mixing the ligand (TA) and metal solutions, the TA/Zr^{IV} sol turned into a transparent gel within 3 min at 85 °C (at room temperature (25 °C), the gelation time was observed to be ~10 min). The MPS sorbent powders obtained (Figure 1f) from the dried TA/Zr^{IV} gels were subsequently examined for metal sequestration (Figure 1c,d). In contrast to our previous work on the gelation behavior of a TA/Zr^{IV} system at a molar ratio of 1:5,[15] the present MPS system was optimized with a TA/Zr^{IV} molar ratio of 1:1.2, which allowed a major fraction (~80%) of the binding sites (i.e., catechol and gallol groups, Figure 1e) in TA to be available (i.e., non-cross-linked by Zr^{IV}) for the capture of incoming metals in the sorbent network (Figure 1d).

The gelation of the MPS system was confirmed by the vial inversion test (Figure 1b) and rheological measurements (Figure S1). The in situ gelation (at room temperature, ~25 °C) was monitored by dynamic oscillatory rheology experiments—both the storage modulus (G') and loss modulus (G'') profiles displayed an increase with time and overlapped (Figure S1). The sol−gel transition occurred when $G' > G''$ after the G'/G'' crossover point. After the drying and washing steps, the resulting MPS powder was subjected to further characterization. The Fourier transform infrared spectra of pure TA and the MPS (Figure S2) revealed notable differences. For example, the characteristic vibrational peaks of TA, that is phenolic C═O stretching at 1703.78 cm^{-1}, phenolic C−O stretching at 1533.40, 1444.63, 1310.05, and 1082.40 cm^{-1}, and phenolic O−H in-plane bending at 1179.76 cm^{-1}[18,19] were shifted to 1696.62, 1504.77, 1441.77, 1314.34, 1186.92, and 1060.92 cm^{-1}, respectively, in the MPS, indicating the coordination interactions involving Zr^{IV} and the catechol and/or gallol groups of TA in the sorbent network. The survey X-ray photoelectron spectroscopy (XPS) pattern revealed the presence of C 1s, O 1s, and Zr 3p and 3d peaks (Figure S3), which are consistent with the sorbent constituents. The Zr 3d peaks at binding energies (BEs) of 183.2 (3d$_{5/2}$) and 185.6 (3d$_{3/2}$) eV were detected in the core-level XPS pattern (Figure 1g) with a spin−orbit separation of 2.4 eV. Relative to the characteristic Zr 3d peaks for ZrO$_2$ at 182.3 (3d$_{5/2}$) and 184.7 (3d$_{3/2}$) eV,[20,21] the shift to the higher binding energies (~1.1 eV) in the MPS suggested the presence of catechol− and/or gallol−Zr^{IV} coordination bonding in the network; it is known that the BE of a central atom increases with increasing electronegativity of the attached atoms or groups.[22,23] Similar BE shifts for Zr-based coordination compounds, such as Zr^{IV}/

https://dx.doi.org/10.1021/acsami.9b19097
ACS Appl. Mater. Interfaces 2020, 12, 3746−3754

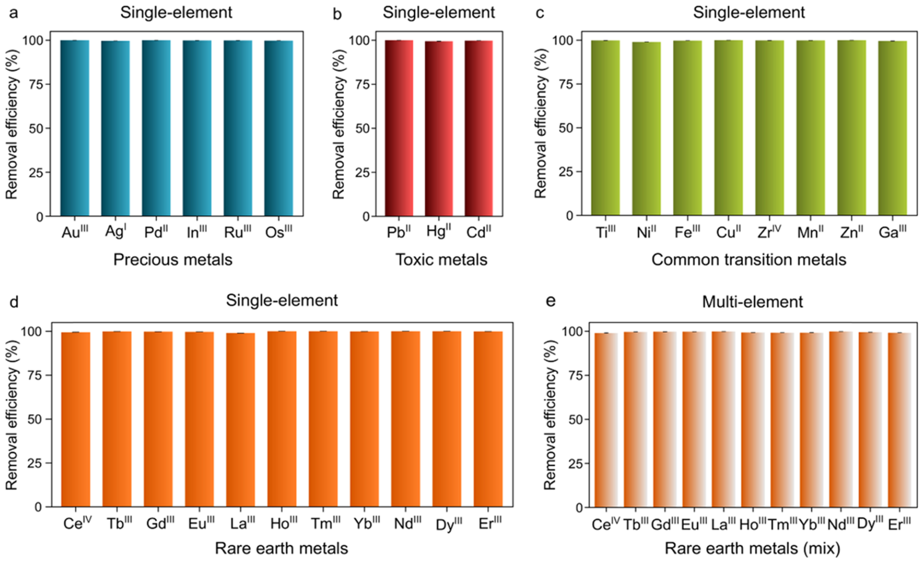

Figure 2. (a−d) Efficiency of the MPS system for the removal of different classes of metals from a single-element model waste. (e) Example of nonselective removal of rare earth metal ions from a multielement rare earth metal mixture by the MPS. Conditions: single-element study, MPS = 0.010 g; concentration of each metal ion = 10 ppm; volume = 10 mL; pH 7 for Cu^{II}, Ni^{II}, and Zn^{II}, and pristine pH (4.8−5.8) for the remaining metal ions; multielement study, MPS = 0.11 g; concentration of each metal ion = 10 ppm; volume = 10 mL; pristine pH of the mixture was ∼5.1.

phytic acid complexes, have been reported.[24] From analysis of the scanning electron microscopy image shown in Figure 1f, the particle size of the MPS ranged from 0.3 to 1.2 mm, and the particles exhibited no macro- and/or microporous structures, suggesting that the sorbents are nanoporous in nature. ζ-Potential measurements performed on the sorbents suggest a negative surface charge for the MPS at pH 5 (−33.1 ± 1.5 mV) as expected, whereas the point of zero charge (determined from ζ-potentials recorded over the pH range of 2−6) was estimated to be pH ∼2, which is in agreement with a previous report.[25] Thermogravimetric analyses suggested the thermal stability of the sorbents to be around 200 °C (Figure S4). The MPS system was stable in the pH range of 1−9, as evident from the flat spectral lines observed in the UV−visible absorption spectra (Figure S5) of the supernatant after 24 h, suggesting that there is no leaching of TA from the MPS (characteristic absorbance peaks of TA are found in the range of 220−400 nm[26]). Leaching of Zr^{IV} was also absent (simultaneously determined from the supernatant as above), as confirmed by inductively coupled plasma mass spectrometry (ICP-MS) analyses (data not shown). The high stability of the TA/Zr^{IV} bulk network over the wide pH range (1−9) can be attributed to the strong catechol− and/or gallol−Zr^{IV} cross-links stemming from the high Lewis acidity and oxidation state of Zr.[15,27] This is also consistent with the higher stability observed for Zr^{IV}/gallic acid MOFs when compared with the conventional Zr^{IV}/carboxylate MOFs.[16,27] High stability of a sorbent system, particularly in acidic conditions, is important: (i) as metal-contaminated wastewater is typically acidic in nature;[6,8] (ii) to prevent secondary pollution via leaching;[8] and (iii) as it offers the possibility to regenerate the sorbent via pH regulation[10] (see also Regeneration and Catalysis).

Single- and Multielement Metal Capture Efficiency. To investigate the capture efficiency of the MPS system, the sorption experiments involved a library of metal ions that can be classified into four general categories: precious, toxic, rare earth, and common transition metals (Table S1). The metal ion concentrations before and after sorption tests were determined using ICP-MS. As shown in Figure 2a−d and Table S2, the MPS sequestered all 28 metal ions studied—precious metals (Au^{III}, Ag^{I}, Pd^{II}, In^{III}, Ru^{III}, and Os^{III}), toxic metals (Pb^{II}, Hg^{II}, and Cd^{II}), common transition metals (Ti^{III}, Ni^{II}, Fe^{III}, Cu^{II}, Zr^{IV}, Mn^{II}, Zn^{II}, and Ga^{III}), and rare earth metals (Ce^{IV}, Tb^{III}, Gd^{III}, Eu^{III}, La^{III}, Ho^{III}, Tm^{III}, Yb^{III}, Nd^{III}, Dy^{III}, and Er^{III})—in single-element model wastes, with removal efficiencies exceeding 99%. Note that the sorption experiments for all metal ions were performed at their pristine solution pH (4.8−5.8) except for Cu^{II}, Ni^{II}, and Zn^{II}. Initial sorption experiments with Cu^{II}, Ni^{II}, and Zn^{II} at their pristine pH (∼4.5−4.8) resulted in removal efficiencies of 80−85%, which improved to >99% at pH 7. The higher removal efficiency is likely due to the higher deprotonated state of TA at the higher pH, which facilitates coordination interactions (see Sorption Mechanism for more details).[16,26] Thus, the results obtained at pH 7 for these three metals are reported in Figure 2c.

For metal sequestration, the affinity of a sorbent for a target metal ion can be expressed by K_d defined as follows:[28]

$$K_d = \frac{(C_i - C_f)}{C_f} \frac{V}{m}$$

where C_i and C_f are the initial and final equilibrium metal ion concentrations, respectively, V is the volume of the treated solution (mL), and m is the mass of the sorbent (g). Sorbent materials possessing K_d values of 1×10^4 mL g^{-1} are considered "very good", and values exceeding 1×10^5 mL g^{-1} are considered "excellent".[28,29] The K_d values determined for the MPS system for the 28 metal ions studied were within the range of 4×10^5 to 1×10^6 mL g^{-1}. To our knowledge, such

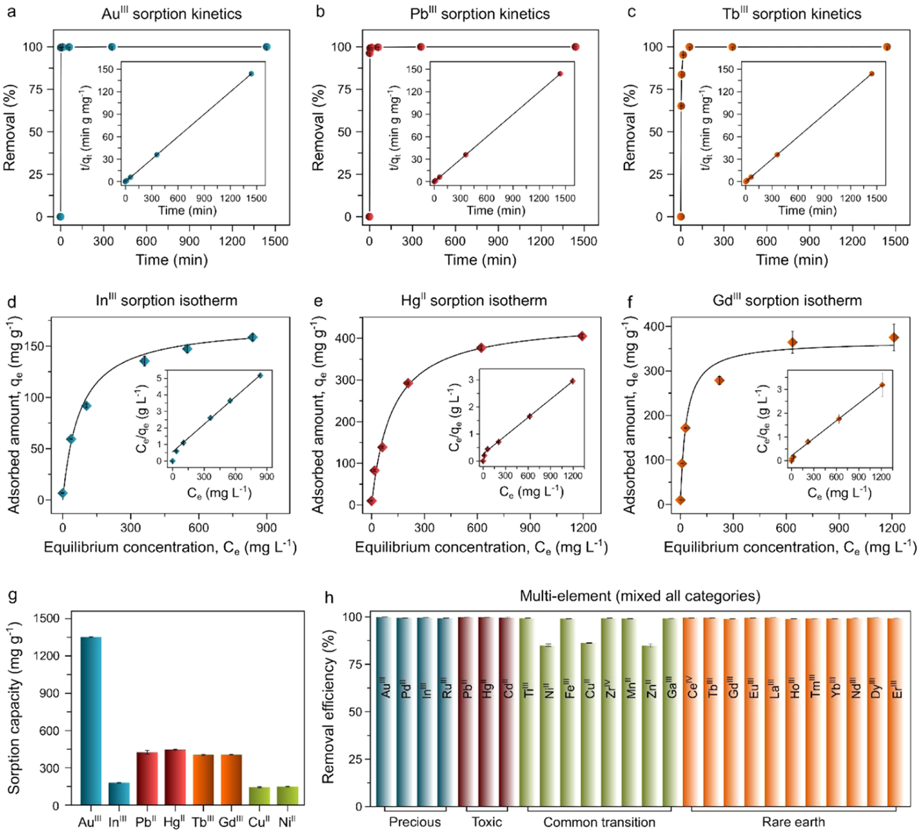

Figure 3. (a–c) (Au^{III}, Pb^{II}, and Tb^{III}) sorption kinetics of the MPS; insets show the linear pseudo-second-order kinetics fit of the data. (d–f) (In^{III}, Hg^{II}, and Gd^{III}) sorption isotherms of the MPS; insets show the linear fit of the Langmuir adsorption model. (g) Maximum sorption capacity calculated from the sorption model-fitted data for the representative metal ions. (h) Simultaneous removal of metals from multielement model waste containing 26 metal ions by the MPS (conditions: MPS = 0.13 g; concentration of each metal ion in the mixture = 5 ppm; volume = 10 mL; pH ≈ 5).

values (above excellent in classification) for a diverse set of metals as reported herein have not been reported for other sorbent systems.

In addition to achieving high removal efficiency, it is important to consider the residual concentration of highly toxic metals in the treated water. According to the U.S. Environmental Protection Agency, the acceptable limit of Pb^{II} and Hg^{II} in drinking water is <2 ppb.[10,29,30] After treatment with the MPS, the concentrations of Pb^{II} and Hg^{II} in the model waste were reduced from 5 ppm (typical median concentration found in industrial effluents and wastewater)[10,31] to 0.4 (removal efficiency of ~99.99%) and 1.4 ppb (removal efficiency of ~99.97%), respectively, indicating the potential of the MPS system.

Similar removal efficiency levels (>99%) were also achieved in the multielement sorption tests performed with the rare earth and precious metals (Figures 2e and S6), highlighting the broad-spectrum metal ion-capturing ability of the MPS system, which can be attributed to the abundant catechol and gallol groups in the system that can form metal chelate/redox complexes (see Sorption Mechanism for more details).

Sorption Kinetics and Isotherm. Sorption kinetics and maximum sorption capacity are metrics that are also used to assess the performance of a sorbent. For convenience, Au^{III} and In^{III}, Pb^{II} and Hg^{II}, Tb^{III} and Gd^{III}, and Cu^{II} and Ni^{II} were selected as representatives of precious, toxic, rare earth, and common transition metals, respectively. Regardless of the metal category studied, the MPS showed fast sorption kinetics (Figures 3a–c and S7–S11), where the removal efficiency exceeded 90% within ~15 min and 99% after equilibrium at 2–4 h. The experimental data were fitted with the pseudo-second-order kinetic model[32] (Experimental Section) with high correlation coefficients of >0.99 (Table S3). The fast sorption kinetics (e.g., activated carbon typically requires 72 h to reach equilibrium)[33] of the MPS further suggests that the rate-determining step for the sorption of metal ions onto the sorbent is mainly chemical in nature (see Sorption Mechanism for more details).

The sorption isotherms for the above representative metals were also measured, and the experimental data were fitted with the Langmuir adsorption model[34] (Figures 3d–f and S12–S16; Table S3). The maximum sorption capacities (Figure 3g) determined from the sorption model for these metal ions were

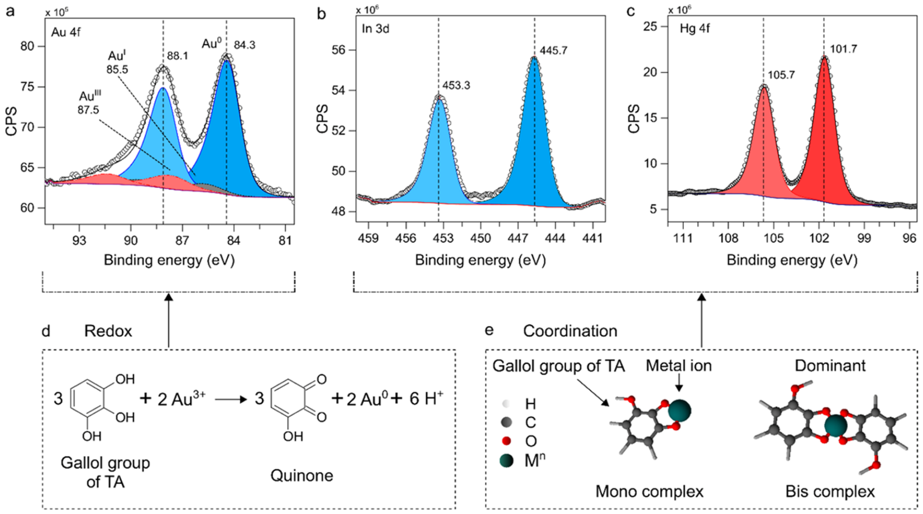

Figure 4. Core-level XPS spectra of (a) Au 4f, (b) In 3d, and (c) Hg 4f. Proposed sorption mechanisms for the metals onto the MPS system: (d) redox interactions and (e) coordination interactions.

approximately 1350, 180, 424, 446, 404, 406, 135, and 149 mg g^{-1} for Au^{III}, In^{III}, Pb^{II}, Hg^{II}, Tb^{III}, Gd^{III}, Cu^{II}, and Ni^{II}, respectively. These values are higher than those achieved by many other sorbents and competitive with some of the highest-performing sorbents in the field (Table S4). Also note that, unlike the MPS, the high sorption capacities displayed by most sorbents in the literature are generally applicable to specific metal ions (rather than a range of metal ions).

Contaminated water bodies are typically multifarious in nature, that is, they contain multiple metal pollutants. Based on the applicability of the MPS to a wide range of metals (Figure 2e), the simultaneous removal efficiency of the MPS was studied for all four categories of metal ions. A mixture containing a total of 26 metal ions was used. Ag^{I} and Os^{III} were omitted because of the observed precipitation in the mixture (see Experimental Section for details). As shown in Figure 3h, the MPS system simultaneously captured 23 of the 26 metal ions studied with efficiencies above 99%. The removal efficiencies for Ni^{II}, Cu^{II}, and Zn^{II} were lower (~80%), as expected (and mentioned above), as the pristine pH of the mixture was ~5.

Sorption Mechanism. XPS was used to probe the chemical interactions occurring during the sorption of various metal ions onto the MPS. The analyses provided two broad scenarios for the different metal categories studied. In the precious metal category, two distinct types of interactions were observed. The core-level Au 4f XPS spectra, as shown in Figure 4a (survey spectra are provided in Figure S17), revealed the BEs of Au 4f$_{7/2}$ and Au 4f$_{5/2}$ peaks at 84.3 and 88.1 eV, respectively, with a spin−orbit separation of 3.8 eV, which can be assigned to elemental Au^{0}.[35,36] Minor contributions from the ionic forms of Au^{I} (BE at 85.5 eV)[37] and Au^{III} (BE at 87.5)[37] were also observed, where the former is possibly caused by the incomplete reduction of some Au^{III} ions and the latter originates from the direct coordination with catechol and/or gallol binding sites. The redox interactions of TA with precious metals (e.g., Au^{III} and Ag^{I}) are well documented in the literature and are generally attributed to the redox potential matching of TA with these metals, leading to the reduction of the metal ions with the concomitant oxidation of gallol and/or catechol groups to quinones (Figure 4d).[38] In contrast, in the same category, In^{III} was captured within the MPS network via coordination to the catechol and/or gallol binding sites (Figures 4b and S17), as confirmed by the appearance of BE peaks at 445.7 (3d$_{5/2}$) and 453.3 (3d$_{3/2}$) eV (cf. In^{0} at 443.8 (3d$_{5/2}$) and In^{III} in In$_2$O$_3$ at 444.7 (3d$_{5/2}$) eV).[39,40] Similarly, BE peaks of Hg 4f at 101.7 (4f$_{7/2}$) and 105.7 (4f$_{5/2}$) eV, with a spin−orbit separation of 4 eV (Figure 4c), can be attributed to Hg^{II} species (as referenced to Hg^{0} at 99.9 and Hg^{II} in HgO at 100.5 eV)[41,42] coordinated to catechol/gallol groups from TA in the MPS. For the other metal categories, coordination interactions were observed to be dominant (Figures S18−S28). For example, the BEs for Pb^{II}; Tb^{III} and Gd^{III}; and Cu^{II} and Ni^{II} from the toxic, rare earth, and common transition-metal categories, respectively, as detected from their XPS core-level spectra confirmed that their oxidation states could be assigned to their corresponding coordination complexes with the catechol and/or gallol binding sites in the MPS (see relevant discussions in Figures S18−S28).

Additionally, considering the TA/Zr molar composition (1:1.2) of the MPS system, the total amount of binding sites (catechol and/or gallol groups) available for metal capture in 1 g of the MPS is about 4 mmol. For metals captured via coordination, if the mono-type coordination mode (i.e., each metal ion is attached to one catechol or gallol group, Figure 4e) dominates, the maximum sorption capacity values are expected to be approximately 459 (In^{II}), 829 (Pb^{II}), 802 (Hg^{II}), 636 (Tb^{III}), 629 (Gd^{III}), 254 (Cu^{II}), and 235 (Ni^{II}) mg g^{-1}. However, the maximum sorption capacities determined experimentally were roughly half of these values (Figure 3g and Table S4), suggesting that these metals were captured into the MPS via the bis-type coordination mode (bis complex), wherein each metal ion is attached to two catechol or gallol groups, as shown in Figure 4e.

Processing Flexibility. Processing flexibility is another important aspect to consider in realizing the full potential of a sorbent system, as the metal sequestration medium may be required in different forms, such as thin films on solid surfaces or support membranes, depending on the application. Most of the current sorbent systems are intrinsically limited in this criterion and require additional materials (e.g., polymers) to process as thin films. Examples include MOFs, zeolites, and ion-exchange resins that are typically synthesized as solid particles[10,43,44] and as such are difficult to be processed as thin films without polymer excipients and additional processing steps. In contrast, the preparation of the present MPS system is based on a sol−gel route, possessing intrinsic solution processability, that enables the system to be processed as thin films on solid surfaces. Sorption experiments performed on the MPS-coated commercial filter membranes or glass substrates (film thickness of ∼200 nm as measured by atomic force spectroscopy; Figure S29) with Ti^{III}, Fe^{III}, and Au^{III} as representative examples are shown in Figure 5. The color changes detected upon metal sorption were due to the characteristic ligand-to-metal charge transfer (LMCT) bands of Ti^{III}− and Fe^{III}−catechol/gallol complexes[15,45,46] and the surface plasmon resonance of Au^0 nanoparticles.[38]

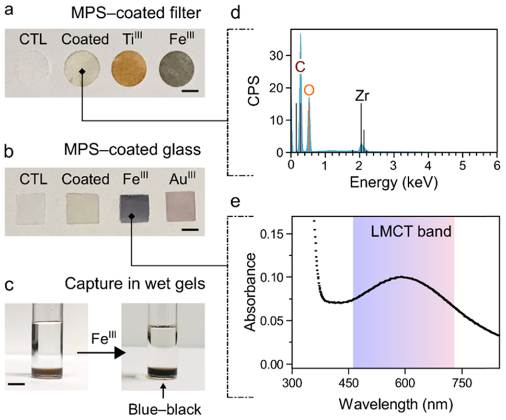

Figure 5. (a, b) Photographs illustrating the processing flexibility of the MPS system engineered into the MPS-coated commercial filter membranes or glass substrates and their subsequent use for metal sequestration. CTL, control. (c) Photograph showing the sequestration of Fe^{III} by the MPS gel. Scale bars are 5 mm. (d) Energy-dispersive X-ray spectroscopy pattern showing the presence of Zr^{IV} in the MPS-coated filter. (e) Characteristic absorbance spectrum after sorption of Fe^{III} onto the MPS-coated glass substrate.

Furthermore, there has been recent interest in using supramolecular gels for environmental remediation owing to their highly solvated structure, which can provide high surface area and intimate contact with liquid phases containing pollutants and their rapid diffusion into the gel matrix.[2,3] Taking this into account, we demonstrate the use of the wet MPS gel (the pristine gel was subjected to a solvent-exchange step with water) for metal ion removal. During the capture of Fe^{III} ions into the gel matrix (Figure 5c), the gel turned blue-black owing to the characteristic LMCT band originating from the Fe^{III}−catechol/gallol complex formation.

Regeneration and Catalysis. Regeneration of sorbent materials is essential for durability and cyclic use. When the MPS sorption mechanism proceeds via coordination, the MPS sorbent system can be easily regenerated by washing in 0.1 M HCl. This leads to desorption of the adsorbed metal ions through destabilization of their coordination interactions with the MPS matrix, without perturbation of the TA−Zr^{IV} cross-links. However, for sorption occurring via redox interactions, a different desorption solution was necessary, that is, thiourea 1 M in 0.1 M HCl solution.[47,48] The MPS sorbent could undergo a series of sorption−desorption cycles without loss in efficiency. For example, In^{III} and Tb^{III} (sorption via coordination) captured by the MPS were regenerated in four consecutive cycles (Figure 6a,b) without any detectable loss in efficiency when the sorption experiments were performed at a low metal concentration of 10 ppm. At a higher metal ion concentration (700 ppm; to reach the maximum sorption capacity of the MPS for each metal ion), the sorption capacity of the MPS could be retained, with minimal loss in efficiency (<2%), in four consecutive sorption−desorption cycles. However, for precious metals, such as Au^{III} captured via redox interactions, the MPS system showed a slightly lower regeneration efficiency—the removal efficiency of the MPS decreased from ∼95 to ∼88% after three consecutive sorption−desorption cycles (Figure S30). This reduced efficiency can be attributed to some irreversible structural changes in TA within the MPS via the formation of quinones and their intermediates during the redox interactions.

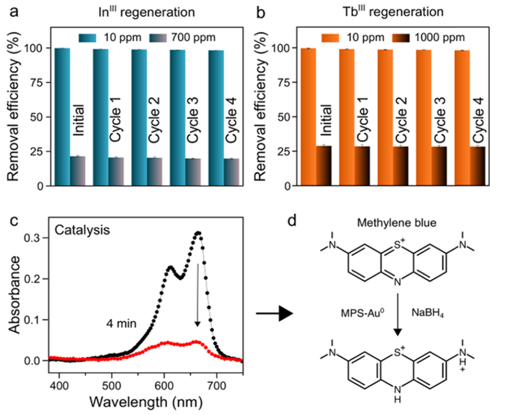

Figure 6. Regeneration of the MPS system, as investigated by the sorption−desorption cycles of (a) In^{III} and (b) Tb^{III} at different initial metal ion concentrations. UV−visible absorbance spectra (c) of the catalytic degradation of methylene blue in the presence of MPS−Au^0 (d).

We hypothesized that the capture of precious metals from water via redox-mediated formation of metallic species (as observed for some precious metals, e.g., Au^0 species after Au^{III} sorption in the MPS) could endow the sorbents with catalytic properties. Such properties may be useful for different and complementary applications including the decontamination of toxic organic pollutants. To test this hypothesis, the catalytic activity of the sorbents (MPS−Au^0 and MPS−Ag^0) toward the degradation of methylene blue (MB) and 4-nitrophenol (4-NP), respectively, was assessed after confirming the capture of precious metals and formation of the corresponding nanoparticles within the MPS network. MPS−Au^0 degraded MB

(Figure 6c,d) and catalyzed the conversion of 4-NP into 4-aminophenol (4-AP) (Figure S31).

■ CONCLUSIONS

A robust sorbent system using tannic acid and Zr^{IV} with high sequestration performance was reported. The MPS sorbent system displayed distribution coefficients exceeding 4×10^5 mL g^{-1} with removal efficiencies of >99% for 28 metal ions studied. Considering the multifarious nature of polluted water streams, the simultaneous removal of 23 metals in multielement model waste with high efficiency was also demonstrated. The sorbent system, of which the preparation is simple, rapid, and involves naturally abundant and inexpensive starting components, features high stability, high sorption capacity, fast sorption kinetics, and easy regeneration, making it potentially suitable for environmental remediation and precious metal recovery. Moreover, following the capture of precious metals, the resulting sorbent was demonstrated to perform as composite catalysts for the degradation of organic pollutants. We are currently investigating the use of the MPS system for the sequestration of metalloid (such as arsenic) pollutants.

■ EXPERIMENTAL SECTION

Synthesis of the MPS. In a typical synthesis, aliquots of TA solution (300 μL, 60% w/v in ethanol, 600 mg mL^{-1}), tetrahydrofuran (THF) (120 μL), and Zr^{IV} precursor solution (180 μL, 0.735 M in 1:1 v/v of water/THF mixture) were mixed in a tube under vortex to achieve a TA/Zr^{IV} molar ratio of 1:1.2. The mixture was immediately placed in a preheated oven at 85 °C, and gelation occurred within 3 min as confirmed from the vial inversion test (at room temperature, 25 °C, the gelation time was ~10 min). The obtained gel samples were dried in a fume hood for 6 h and ground (~3 g sample) in a commercial micronizer (XRD-Mill McCrone, MEP Instruments) set at 50 W for 5 min. The ground powder samples were washed three times in water and freeze-dried to obtain the final sorbent samples.

Stability Tests for the MPS. The MPS (0.005 g) samples were added to 1.5 mL tubes containing aqueous solutions (1 mL) of different pHs ranging from 1 to 9, and the tubes were kept on a rotating wheel (~40 rpm) for 24 h. The dispersions were filtered through 0.22 μm membrane filters, and the filtrates were analyzed by UV−visible spectroscopy and ICP-MS to assess the leaching of TA and Zr^{IV} ions, respectively.

Metal Sorption from Single-Element Model Waste Systems. For the metal sorption experiments in single-element model waste systems, stock solutions of the metal ions were first prepared by dissolving the relevant metal salts (Table S1) in Milli-Q water. Then, in a typical sorption experiment, the MPS (0.010 g) was added into a 15 mL tube containing stock solution (10 mL) of the metal ion (10 ppm) and the tube was kept on a rotating wheel (~40 rpm) for 24 h. After the adsorption process, the mixture was filtered through a 0.22 μm membrane filter to separate the MPS from the metal ion solution, and the filtrate was analyzed by ICP-MS to determine the metal concentration in the supernatant. The adsorption experiments were conducted at the intrinsic pH of the metal ion solution (10 ppm)—precious metals, 4.8−5.2; toxic metals, 5.5−5.8; rare earth metals, 5.2−5.5; and common transition metals, 4.5−5.1—except for the experiments involving Cu^{II}, Ni^{II}, and Zn^{II}, which were conducted at pH 7. The removal efficiency for each metal ion studied was calculated using the following equation:

$$\text{removal efficiency (\%)} = (C_i - C_f)/C_i \times 100$$

where C_i is the initial metal ion concentration and C_f is the final equilibrium metal ion concentration after adsorption onto the MPS.

Conducting sorption experiments with Cu^{II}, Ni^{II}, and Zn^{II} at their pristine pH (~4.5−4.8, 10 ppm) resulted in removal efficiencies of 80−85%, which improved to >99% at pH 7 (bis−tris buffer, 10 mM). Thus, only the results obtained from sorption experiments performed at pH 7 are reported.

Metal Sorption from Multielement Model Waste Systems. For the metal sorption experiments in multielement model waste systems, stock solutions of the metal ions were prepared by dissolving the relevant metal salts (Table S1) in Milli-Q water. For each metal ion category studied, the metal stock solutions were mixed to obtain a final stock of 10 ppm for each metal ion. Then, for a given category, the MPS (0.11 g for rare earth and 0.04 g for precious metal categories) was added into a 15 mL tube containing stock solution (10 mL) of the mixed metal ions and the tube was kept on a rotating wheel (~40 rpm) for 24 h. Note that data for the precious metal category, Os^{III} and Ag^{I} (due to the presence of metal chloride-based salts that lead to the formation of AgCl, which is insoluble in water) were omitted because of the occurrence of precipitation in the mixture. Subsequently, the mixture was filtered through a 0.22 μm membrane filter to separate the MPS from the metal ion solution, and the filtrate was analyzed by ICP-MS to determine the metal ion concentration.

Experiments involving all metal ion categories (a total of 26 metals, as Ag^{I} and Os^{III} were omitted as mentioned above) were also performed (MPS 0.13 g) as above with mixed metal ions at a concentration of 5 ppm for each.[10]

Sorption Kinetics Measurements. The MPS (0.010 g) was added into a 15 mL tube containing a solution (10 mL) of the metal ion (10 ppm). The mixture was kept on a rotating wheel (~40 rpm) at room temperature (~25 °C) for 24 h. During the sorption period, aliquots of the suspension (300 μL) were filtered at specific time intervals through a 0.22 μm membrane filter, and the filtrates were analyzed by ICP-MS to determine the remaining metal content. The experimental data thus obtained were fitted with the pseudo-second-order kinetic model according to the following equation:[29]

$$t/q_t = 1/kq_e^{\,2} + t/q_e$$

where q_t (mg g^{-1}) and q_e (mg g^{-1}) are sorption amounts of the metal ions at time t (min) and at equilibrium, respectively, and k (g mg^{-1} min^{-1}) is the rate constant for the pseudo-second-order equation.

Sorption Isotherm Tests. The MPS (0.010 g) was added into a 15 mL tube containing a solution (10 mL) of the metal ion with varying concentrations from 10 to 2000 ppm. The mixture was kept on a rotating wheel (~40 rpm) at room temperature (~25 °C) for 24 h. Subsequently, the mixture was filtered through a 0.22 μm membrane filter to separate the MPS from the metal ion solution, and the filtrate was analyzed by ICP-MS to determine the remaining metal concentration. The experimental data were fitted with the Langmuir isotherm model described by the following equation:[10]

$$c_e/q_e = 1/K_L q_m + c_e/q_m$$

where q_e (mg g^{-1}) is the amount of metal ions adsorbed onto the sorbent at equilibrium, c_e (mg L^{-1}) is the metal ion concentration at equilibrium, q_m (mg g^{-1}) is the maximum sorption capacity at monolayer coverage, and K_L is the Langmuir constant.

Preparation of the MPS Films. To obtain the MPS films coated on a glass substrate, aliquots of TA solution (300 μL, 60% w/v in ethanol, 600 mg mL^{-1}), THF (120 μL), and Zr^{IV} precursor solution (180 μL, 0.735 M in 1:1 v/v water/THF mixture) were mixed in a tube under vortex for 15 s to achieve a TA/Zr^{IV} molar ratio of 1:1.2. The mixture was immediately diluted (2-fold) under vortex by ethanol, and an aliquot of this mixture (50 μL) was spread onto a standard microscope glass slide using a cell scrapper and allowed to dry. For the MPS membrane preparation, cellulose filter papers were dipped into the above mixture for 2 min and allowed to dry.

Before the sorption experiments, the MPS-coated membranes or glass substrates were washed twice in Milli-Q water. Sorption experiments were performed using 50 ppm of the desired metal salt solutions (10 mL, pH 3.5−4.5) and dipping the substrates into the metal solutions for 6 h.

Regeneration of the MPS. The MPS (0.010 g) was added into a 15 mL tube containing a solution (10 mL) of the metal ion (In$^{\mathrm{III}}$, Tb$^{\mathrm{III}}$, or Au$^{\mathrm{III}}$). The mixture was kept on a rotating wheel (~40 rpm) at room temperature (~25 °C) for 24 h. Subsequently, the mixture was filtered through a 0.22 μm membrane filter to separate the MPS from metal ion solutions, and the filtrate was analyzed by ICP-MS to determine the remaining metal concentration. The In$^{\mathrm{III}}$- and Tb$^{\mathrm{III}}$-captured MPS samples were then treated with 0.1 M HCl (5 mL) for 6 h (desorption step) and washed three times with water before the next sorption step. This process was repeated for four cycles (sorption−desorption) for the metal ion studied. For the sorption steps, two sets of experiments with different concentrations for In$^{\mathrm{III}}$ (10 and 700 ppm) and Tb$^{\mathrm{III}}$ (10 and 1000 ppm) were performed. For Au$^{\mathrm{III}}$, the concentration used for Au$^{\mathrm{III}}$ was 1000 ppm, and after each desorption step (thiourea 1 M in 0.1 M HCl solution, 5 mL), the MPS samples were treated with 1 mM of NaBH$_4$ (5 mL, for 5 min) to reduce the quinones back to gallol and catechol groups. The sorption−desorption cycle was repeated three times.

Catalysis Experiments. The Au$^{\mathrm{III}}$- and Ag$^{\mathrm{I}}$-captured MPS samples (MPS−Au^0 and MPS−Ag^0, respectively) obtained from the sorption experiments with 10 ppm metal concentrations (0.01 g MPS) were washed with water several times, and their catalytic activity toward the degradation/reduction of MB was evaluated.

An MB solution (2 mL, 100 μM) containing freshly prepared NaBH$_4$ (20 μM) (reducing agent) was added to the washed pellets of MPS−Au^0, and the absorbance of the MB solution at ~665 nm was measured over time. The MB solution turned colorless within 5 min. A 4-NP solution (2 mL, 0.4 mM) containing freshly prepared NaBH$_4$ (40 mM) (reducing agent) was added to the washed pellets of MPS−Ag^0, and the absorbance of the 4-NP solution at ~400 nm was measured over time. Along with the decrease in the peak intensity at ~400 nm, a peak at ~300 nm appeared over time, suggesting the formation of 4-AP. For the control experiments, which were conducted in the absence of the MPS-based samples, no change in absorbance (that correlates to the catalytic activity) was observed.

ASSOCIATED CONTENT

Supporting Information

The Supporting Information is available free of charge at https://pubs.acs.org/doi/10.1021/acsami.9b19097.

> Materials and characterization; additional characterization data for the MPS sorbents, including rheology, XPS, FTIR, and UV−vis absorbance; additional data regarding removal efficiency, sorption kinetics, sorption isotherm, and sorption mechanisms (XPS) for different metals; AFM film thickness and catalysis experimental data (PDF)

AUTHOR INFORMATION

Corresponding Author

Frank Caruso − *The University of Melbourne, Parkville, Australia;* orcid.org/0000-0002-0197-497X;
Email: fcaruso@unimelb.edu.au

Other Authors

Md. Arifur Rahim − *The University of Melbourne, Parkville, Australia*
Gan Lin − *The University of Melbourne, Parkville, Australia*
Pietro Pacchin Tomanin − *The University of Melbourne, Parkville, Australia*
Yi Ju − *The University of Melbourne, Parkville, Australia;* orcid.org/0000-0003-0103-1207
Anders Barlow − *The University of Melbourne, Parkville, Australia*
Mattias Björnmalm − *The University of Melbourne, Parkville, Australia;* orcid.org/0000-0002-9876-7079

Complete contact information is available at:
https://pubs.acs.org/10.1021/acsami.9b19097

Notes

The authors declare no competing financial interest.

ACKNOWLEDGMENTS

This research was conducted and funded by the Australian Research Council (ARC) Centre of Excellence in Convergent Bio-Nano Science and Technology (Project Number CE140100036) and an ARC Discovery Project (DP170103331). F.C. acknowledges the award of a National Health and Medical Research Council Senior Principal Research Fellowship (GNT1135806). This work was performed in part at the Materials Characterisation and Fabrication Platform (MCFP) at The University of Melbourne and the Victorian Node of the Australian National Fabrication Facility. The authors acknowledge the use of facilities within the Monash X-ray Platform and Dr. Andrew Mitchell (MCFP, The University of Melbourne) for the helpful discussions regarding the inductively coupled plasma mass spectrometry studies.

REFERENCES

(1) Bilal, M.; Shah, J. A.; Ashfaq, T.; Gardazi, S. M. H.; Tahir, A. A.; Pervez, A.; Haroon, H.; Mahmood, Q. Waste Biomass Adsorbents for Copper Removal from Industrial Wastewater − A Review. *J. Hazard. Mater.* **2013**, *263*, 322−333.

(2) Okesola, B. O.; Smith, D. K. Applying Low-Molecular Weight Supramolecular Gelators in an Environmental Setting − Self-Assembled Gels as Smart Materials for Pollutant Removal. *Chem. Soc. Rev.* **2016**, *45*, 4226−4251.

(3) Alizadehgiashi, M.; Khuu, N.; Khabibullin, A.; Henry, A.; Tebbe, M.; Suzuki, T.; Kumacheva, E. Nanocolloidal Hydrogel for Heavy Metal Scavenging. *ACS Nano* **2018**, *12*, 8160−8168.

(4) Lee, J.-C.; Son, Y.-O.; Pratheeshkumar, P.; Shi, X. Oxidative Stress and Metal Carcinogenesis. *Free Radicals Biol. Med.* **2012**, *53*, 742−757.

(5) Liu, J.; Du, X. Fast Removal of Aqueous Hg(II) with Quaternary Ammonium-Functionalized Magnetic Mesoporous Silica and Silica Regeneration. *J. Mater. Chem.* **2011**, *21*, 6981−6987.

(6) Das, N. Recovery of Precious Metals through Biosorption — A Review. *Hydrometallurgy* **2010**, *103*, 180−189.

(7) Dodson, J. R.; Parker, H. L.; García, A. M.; Hicken, A.; Asemave, K.; Farmer, T. J.; He, H.; Clark, J. H.; Hunt, A. J. Bio-Derived Materials as a Green Route for Precious & Critical Metal Recovery and Re-Use. *Green Chem.* **2015**, *17*, 1951−1965.

(8) Bacelo, H. A. M.; Santos, S. C. R.; Botelho, C. M. S. Tannin-Based Biosorbents for Environmental Applications − A Review. *Chem. Eng. J.* **2016**, *303*, 575−587.

(9) Bolisetty, S.; Mezzenga, R. Amyloid−Carbon Hybrid Membranes for Universal Water Purification. *Nat. Nanotechnol.* **2016**, *11*, 365−371.

(10) Peng, Y.; Huang, H.; Zhang, Y.; Kang, C.; Chen, S.; Song, L.; Liu, D.; Zhong, C. A Versatile MOF-Based Trap for Heavy Metal Ion Capture and Dispersion. *Nat. Commun.* **2018**, *9*, No. 187.

(11) Mahmoud, M. E.; Amira, M. F.; Seleim, S. M.; Mohamed, A. K. Amino-Decorated Magnetic Metal-Organic Framework as a Potential Novel Platform for Selective Removal of Chromium (VI), Cadmium (II) and Lead (II). *J. Hazard. Mater.* **2020**, *381*, No. 120979.

(12) Mahmoud, M. E.; El-Said, G. F.; Rashedy, I. R. K.; Abdelfattah, A. M. Assembly and Implementation of an Eco-Friendly Marine Nanosediment for Adsorptive Removal of Heptavalent Manganese:

Supporting Information

Self-Assembly of a Metal–Phenolic Sorbent for Broad-Spectrum Metal Sequestration

Md. Arifur Rahim,[†,§] *Gan Lin,*[†] *Pietro Pacchin Tomanin,*[†] *Yi Ju,*[†] *Anders Barlow,*[‡] *Mattias Björnmalm,*[†] *and Frank Caruso*[*,†]

[†]ARC Centre of Excellence in Convergent Bio-Nano Science and Technology, and the Department of Chemical Engineering, The University of Melbourne, Parkville, Victoria 3010, Australia

[‡]Materials Characterisation and Fabrication Platform, The University of Melbourne, Parkville, Victoria 3010, Australia

[§]Present address: School of Chemical Engineering, University of New South Wales (UNSW), Sydney Campus, NSW 2052, Australia

*Corresponding author. E-mail: fcaruso@unimelb.edu.au

Materials

Tannic acid (TA), zirconium(IV) oxychloride octahydrate ($ZrOCl_2\cdot 8H_2O$), thiourea, sodium borohydride ($NaBH_4$), bis-tris, 4-nitrophenol (4-NP), and methylene blue were purchased from Sigma-Aldrich and used as received. Ethanol and tetrahydrofuran were purchased from Chem-Supply. High-purity (Milli-Q) H_2O with a resistivity of 18.2 MΩ cm was obtained from an inline Millipore RiOs/Origin H_2O purification system. The metal salts used for the metal sorption experiments are listed in Table S1 with their respective sources.

Table S1. Metal salts used for the metal sorption experiments

No	Metal ion	Salt used	Formula	Source
Precious metals				
1	Au^{III}	Gold(III) chloride trihydrate	$HAuCl_4\cdot 3H_2O$	Sigma-Aldrich
2	Ag^{I}	Silver(I) nitrate	$AgNO_3$	Sigma-Aldrich
3	Pd^{II}	Sodium tetrachloropalladate(II)	Na_2PdCl_4	Sigma-Aldrich
4	Ru^{III}	Hexaammineruthenium(III) chloride	$[Ru(NH_3)_6]Cl_3$	Sigma-Aldrich
5	In^{III}	Indium(III) nitrate hydrate	$InNO_3\cdot xH_2O$	Sigma-Aldrich
6	Os^{III}	Osmium(III) chloride hydrate	$OsCl_3\cdot H_2O$	Fisher Scientific
Toxic metals				
7	Pb^{II}	Lead(II) nitrate	$Pb(NO_3)_2$	Sigma-Aldrich
8	Hg^{II}	Mercury(II) chloride	$HgCl_2$	Sigma-Aldrich
9	Cd^{II}	Cadmium(II) chloride	$CdCl_2$	Sigma-Aldrich
Rare earth metals				
10	Ce^{IV}	Cerium(IV) ammonium nitrate	$(NH_4)_2Ce(NO_3)_6$	Sigma-Aldrich
11	Tb^{III}	Terbium(III) chloride hexahydrate	$TbCl_3\cdot 6H_2O$	Sigma-Aldrich
12	Gd^{III}	Gadolinium(III) chloride hexahydrate	$GdCl_3\cdot 6H_2O$	Sigma-Aldrich
13	Eu^{III}	Europium(III) chloride hexahydrate	$EuCl_3\cdot 6H_2O$	Sigma-Aldrich
14	La^{III}	Lanthanum(III) chloride heptahydrate	$LaCl_3\cdot 7H_2O$	Sigma-Aldrich
15	Ho^{III}	Holmium(III) chloride hexahydrate	$HoCl_3\cdot 6H_2O$	Alfa Aesar
16	Tm^{III}	Thulium(III) chloride hexahydrate	$TmCl_3\cdot 6H_2O$	Sigma-Aldrich
17	Dy^{III}	Dysprosium(III) chloride hexahydrate	$DyCl_3\cdot 6H_2O$	Alfa Aesar
18	Nd^{III}	Neodymium(III) chloride hexahydrate	$NdCl_3\cdot 6H_2O$	Alfa Aesar
19	Yb^{III}	Ytterbium(III) chloride hexahydrate	$YbCl_3\cdot 6H_2O$	Alfa Aesar
20	Er^{III}	Erbium(III) chloride hexahydrate	$ErCl_3\cdot 6H_2O$	Sigma-Aldrich
Common transition metals				
21	Ti^{III}	Titanium(III) chloride in HCl (≥12% $TiCl_3$ basis)	$TiCl_3$	Sigma-Aldrich
22	Ni^{II}	Ni(II) chloride	$NiCl_2$	Sigma-Aldrich
23	Cu^{II}	Copper(II) chloride dihydrate	$CuCl_2\cdot 2H_2O$	Sigma-Aldrich
24	Zn^{II}	Zinc(II) nitrate hexahydrate	$Zn(NO_3)_2\cdot 6H_2O$	Sigma-Aldrich
25	Zr^{IV}	Zirconium(IV) oxychloride octahydrate	$ZrOCl_2\cdot 8H_2O$	Sigma-Aldrich
26	Mn^{II}	Manganese(II) chloride tetrahydrate	$MnCl_2\cdot 4H_2O$	Sigma-Aldrich
27	Fe^{III}	Ammonium iron(III) citrate	$C_6H_8O_7\cdot xFe^{3+}\cdot yNH_3$	Sigma-Aldrich
28	Ga^{III}	Gallium(III) nitrate hydrate	$Ga(NO3)_3\cdot H_2O$	Sigma-Aldrich

Characterization

Fourier transform infrared (FTIR) spectra were collected using a TENSOR II (Bruker) attenuated total reflectance FTIR spectrometer. UV-Visible absorption spectra were recorded on a Specord 250 plus UV-Vis spectrophotometer. Rheological experiments were performed at 25 °C on a twin drive rheometer MCR 702 (Anton Paar) with a cone and plate geometry. Initially, the linear viscoelastic region (LVR) of the gels was determined by frequency sweep (0.1–100 Hz) and strain sweep (1–1000%) tests. Storage moduli and loss moduli of the metal–phenolic sorbent (MPS) gel were determined at a frequency of 1 Hz and 1% strain (within the predetermined LVR). ζ-Potential measurements were performed on a Zetasizer Nano-ZS (Malvern Instruments, UK). Thermogravimetric analysis (TGA) was carried out on a TG 209F1 Libra (NETZSCH) from 35 to 700 °C with a heating rate of 2 K min^{-1}. Atomic force microscopy (AFM) experiments were carried out with a JPK NanoWizard II BioAFM instrument. Typical scans were recorded in tapping mode with MikroMasch silicon cantilevers (HQ:NSC15/CR-AU BS). The MPS film sample on a glass slide was scratched with a razor blade and the scratched area was imaged to obtain the height profile. Scanning electron microscopy (SEM) images were obtained on a Hitachi FlexSEM 1000. Energy-dispersive X-ray spectroscopy (EDX) was performed at 15 kV using a Bruker Quantax 80 EDX unit attached to the SEM instrument. The metal ion concentrations were measured by inductively coupled plasma mass spectrometry (ICP-MS; NexION 2000 ICP Mass Spectrometer, Perkin Elmer). X-ray photoelectron spectroscopy (XPS) was performed on a Thermo Scientific Nexsa spectrometer equipped with a hemispherical analyzer. The incident radiation was monochromatic Al Kα X-rays (1486.6 eV) at 72 W (6 mA and 12 kV, 400 × 800 μm^2 spot). Survey (wide) and high-resolution (narrow) scans were recorded at analyzer pass energies of 200 and 50 eV, respectively. Survey scans were performed with a step size of 1.0 eV and a dwell time of 10 ms. High-resolution scans were obtained within a 20-eV binding energy range with a step size of 0.1 eV and dwell time of 50 ms. The base pressure in the analysis chamber was less than 5.0×10^{-9} mbar. A low-energy dual-beam (ion and electron) flood gun was used to compensate for surface charging. All data were processed using CasaXPS software (version 2.3.19) and the energy calibration was referenced to the low binding energy component of the C 1s peak in TA at 284.7 eV.

Supplementary Figures S1–S31 and Tables S1–S4

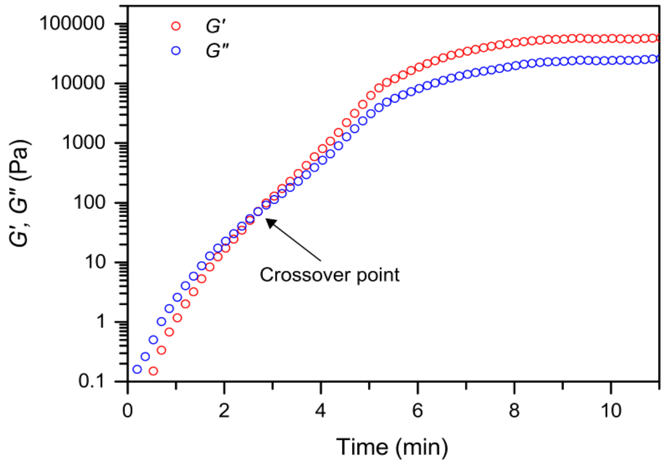

Figure S1. Rheological measurements showing the gelation behavior of the MPS system.

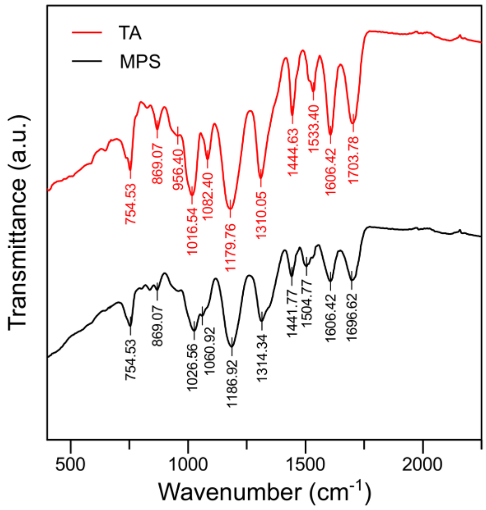

Figure S2. FTIR spectra of TA and the MPS system.

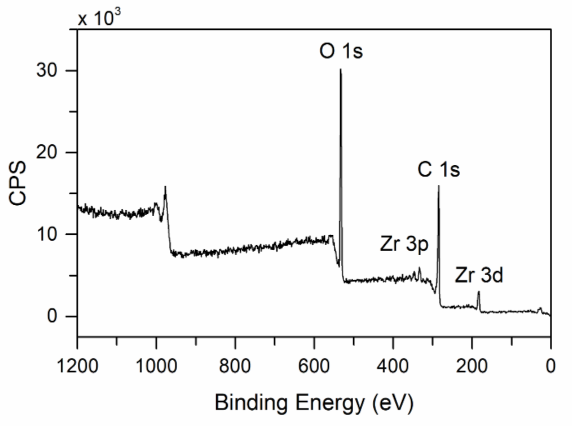

Figure S3. XPS survey spectrum showing the elemental composition of the MPS system.

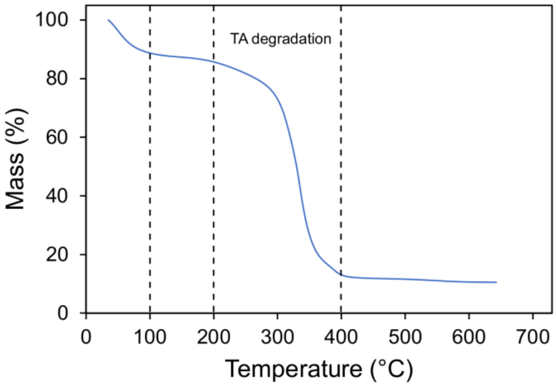

Figure S4. TGA analysis of the MPS sorbents. The mass loss up to 120 °C is due to the water content in the sample, which is close to 10% of the initial total mass. From 200 to 400 °C, there is a steep decrease in mass due to the decomposition of tannic acid.[1] After 400 °C, the mass reaches a plateau, possibly due to the formation of ZrO_2.[2]

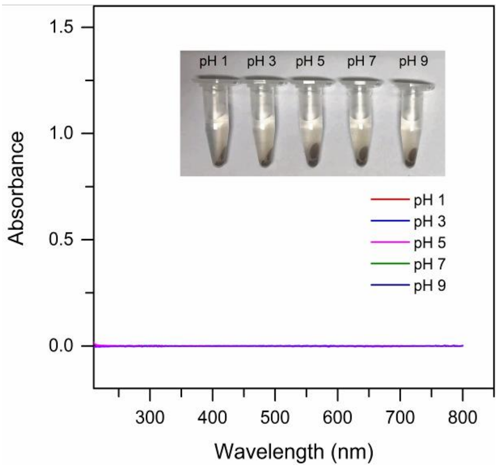

Figure S5. UV-Visible absorbance of the filtrates obtained from the MPS dispersions in aqueous solutions of pH 1–9. Flat spectral lines suggest that there is no leaching of TA from the MPS (absorbance of TA is generally found in the range of 220–400 nm).[3] Photographs (inset) demonstrate the stability of the MPS in the corresponding aqueous solutions with different pH values. In addition, the absence of Zr^{IV} in the filtrate was confirmed by ICP-MS.

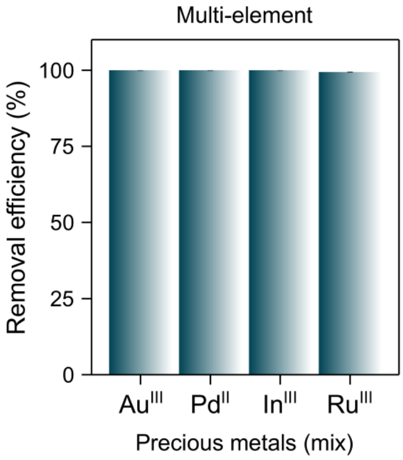

Figure S6. Multi-element sorption test conducted within the precious metal category. The removal efficiency of these metals in the mix was >99%.

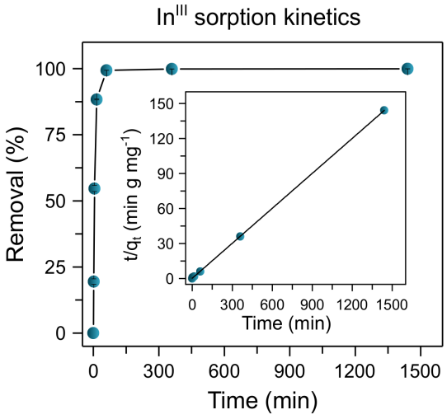

Figure S7. Sorption kinetics of In^{III} ions onto the MPS. Inset shows the linearity (correlation coefficient >0.99) of the data fitted with the pseudo-second-order-kinetic model.

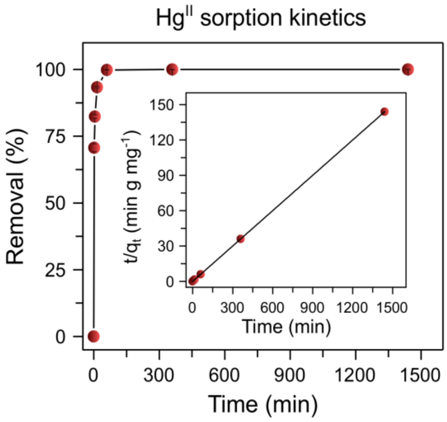

Figure S8. Sorption kinetics of Hg^{II} ions onto the MPS. Inset shows the linearity (correlation coefficient >0.99) of the data fitted with the pseudo-second-order kinetic model.

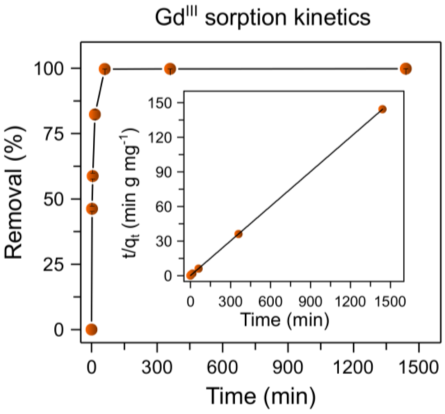

Figure S9. Sorption kinetics of Gd^{III} ions onto the MPS. Inset shows the linearity (correlation coefficient >0.99) of the data fitted with the pseudo-second-order kinetic model.

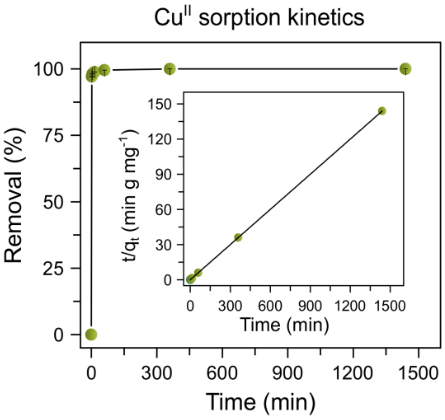

Figure S10. Sorption kinetics of Cu^{II} ions onto the MPS. Inset shows the linearity (correlation coefficient >0.99) of the data fitted with the pseudo-second-order kinetic model.

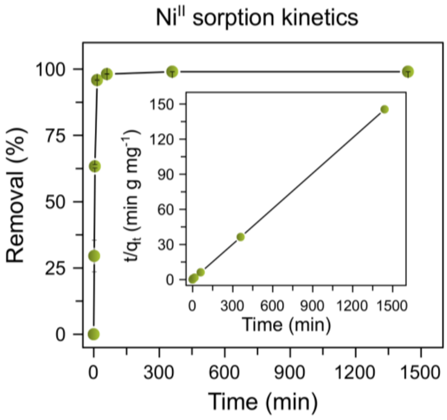

Figure S11. Sorption kinetics of Ni^{II} ions onto the MPS. Inset shows the linearity (correlation coefficient >0.99) of the data fitted with the pseudo-second-order kinetic model.

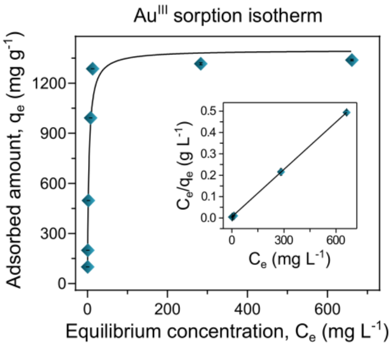

Figure S12. Sorption isotherm of Au^{III} ions onto the MPS. Inset shows the linearity (correlation coefficient >0.99) of the data fitted with the Langmuir adsorption model.

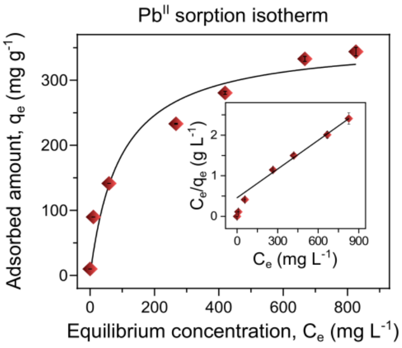

Figure S13. Sorption isotherm of Pb^{II} ions onto the MPS. Inset shows the linearity (correlation coefficient >0.99) of the data fitted with the Langmuir adsorption model.

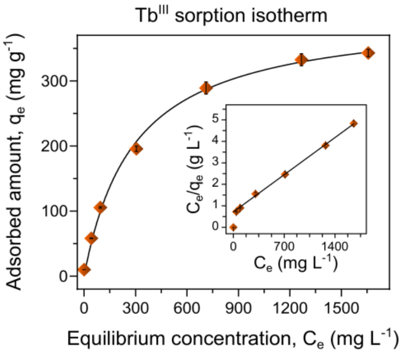

Figure S14. Sorption isotherm of Tb^{III} ions onto the MPS. Inset shows the linearity (correlation coefficient >0.98) of the data fitted with the Langmuir adsorption model.

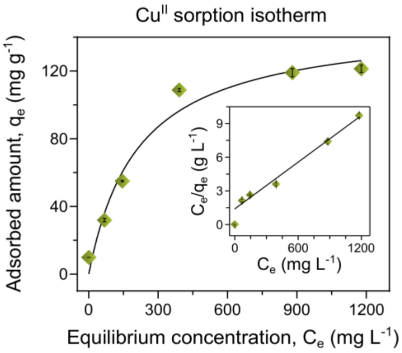

Figure S15. Sorption isotherm of Cu^{II} ions onto the MPS. Inset shows the linearity (correlation coefficient >0.97) of the data fitted with the Langmuir adsorption model.

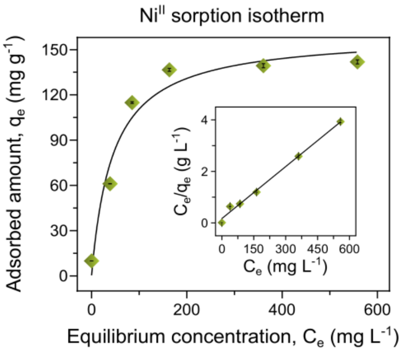

Figure S16. Sorption isotherm of Ni^{II} ions onto the MPS. Inset shows the linearity (correlation coefficient >0.99) of the data fitted with the Langmuir adsorption model.

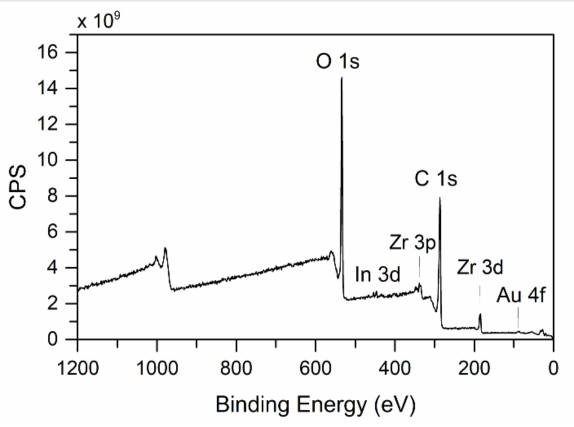

Figure S17. XPS survey spectrum of the Au^{III}- and In^{III}-captured MPS system showing the presence of Au^{III} and In^{III}. The metals were simultaneously captured from a mixed metal ion solution.

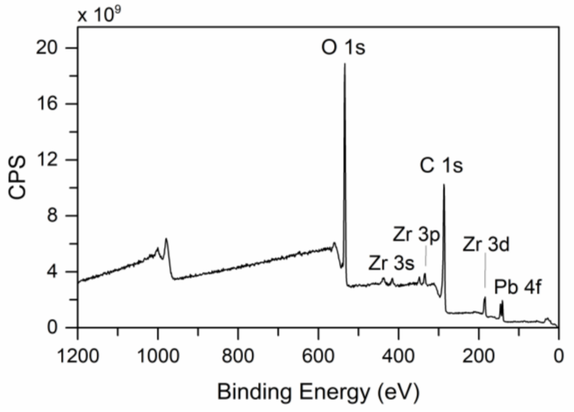

Figure S18. XPS survey spectrum of the Pb^{II}-captured MPS system showing the presence of Pb^{II}.

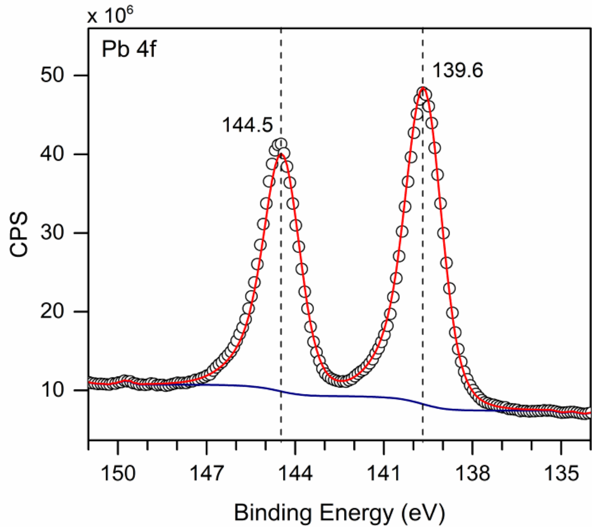

Figure S19. Core-level XPS spectra (Pb 4f) of the Pb^{II}-captured MPS system. Two Pb 4f peaks were detected at 139.6 ($4f_{7/2}$) and 144.5 ($4f_{5/2}$) eV, with a spin-orbit separation of 4.9 eV. This implied that Pb in the MPS existed in a divalent state. The peak shifts to higher binding energies (BEs) for Pb $4f_{7/2}$ in the MPS (relative to Pb^0 at 136.8 eV ($4f_{7/2}$) and Pb^{II} in PbO at 137.8 eV ($4f_{7/2}$))[4,5] can be attributed to the coordination of Pb^{II} species to the catechol and/or gallol groups in the MPS.

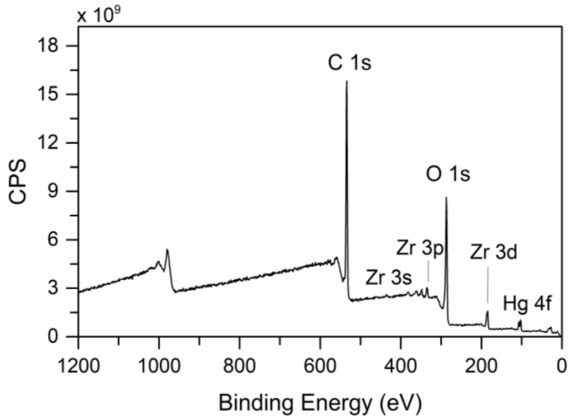

Figure S20. XPS survey spectrum of the Hg^{II}-captured MPS system showing the presence of Hg^{II}.

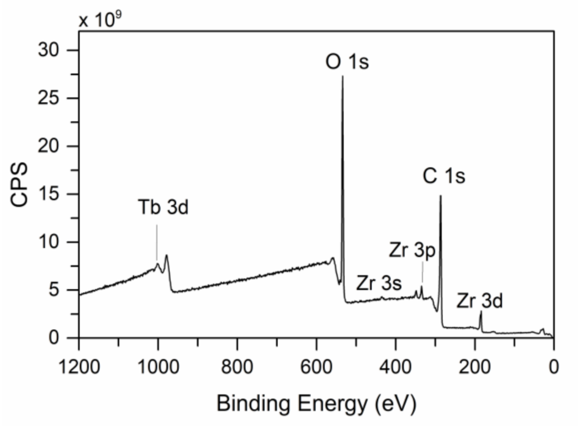

Figure S21. XPS survey spectrum of the Tb^{III}-captured MPS system showing the presence of Tb^{III}.

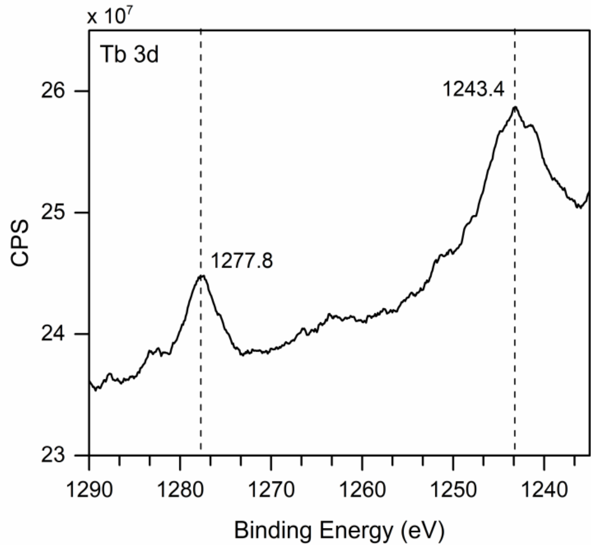

Figure S22. Core-level XPS spectrum (Tb 3d) of the Tb^{III}-captured MPS system. The photoelectron emission peaks of Tb 3d were detected at 1243.4 ($3d_{5/2}$) and 1277.8 ($3d_{3/2}$) eV, with a spin-orbit separation of 34.4 eV. The peak shifts to higher BEs for Tb 3d in the MPS, relative to Tb^{III} in Tb_2O_3 at 1240.1 ($3d_{5/2}$) and 1275.1 ($3d_{3/2}$) eV,[6,7] can be attributed to the coordination of Tb^{III} species to the catechol and/or gallol groups in the MPS.

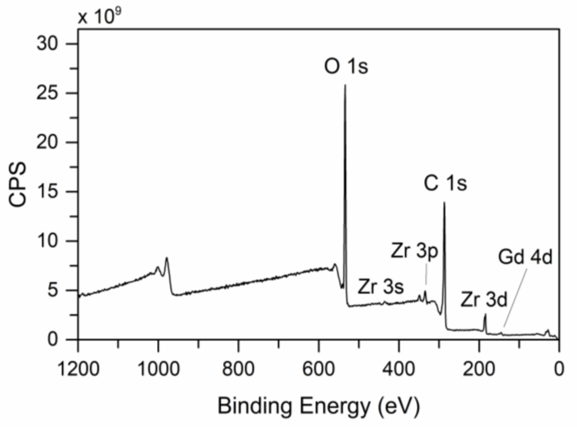

Figure S23. XPS survey spectrum of the Gd^{III}-captured MPS system showing the presence of Gd^{III}.

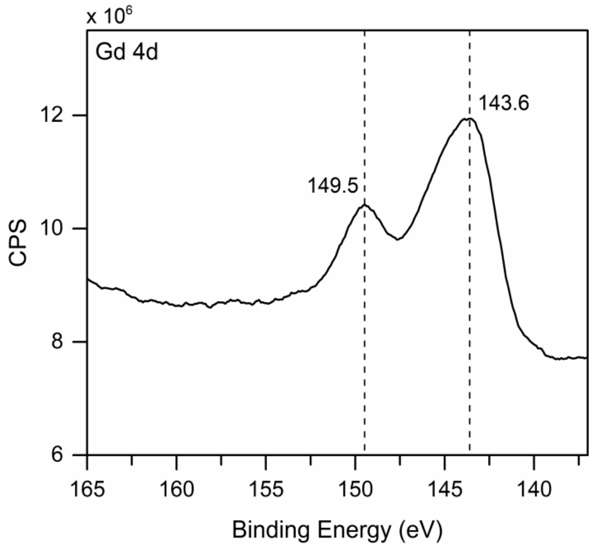

Figure S24. Core-level XPS spectrum (Gd 4d) of the Gd^{III}-captured MPS system. The photoelectron emission peaks of Gd 4d were detected at 143.6 ($4d_{5/2}$) and 149.5 ($4d_{3/2}$) eV, with a spin-orbit separation of 5.9 eV. The peak shifts to higher BEs for Gd 4d in the MPS, relative to metallic Gd at 141.4 ($4d_{5/2}$) eV, and Gd^{III} in Gd_2O_3 at 142.5 ($4d_{5/2}$) and 148.1 ($4d_{3/2}$) eV,[8,9] can be attributed to the coordination of Gd^{III} to the catechol and/or gallol groups in the MPS.

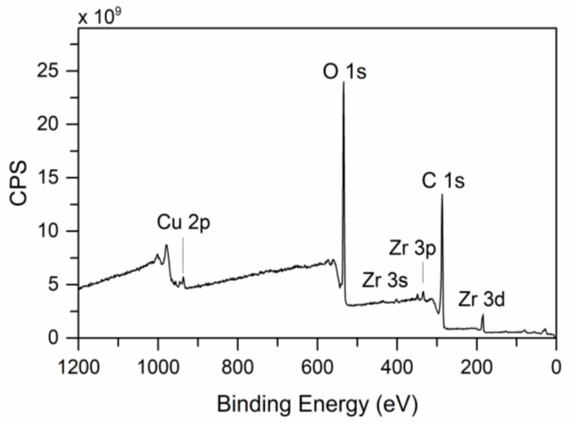

Figure S25. XPS survey spectrum of the Cu^{II}-captured MPS system showing the presence of Cu^{II}.

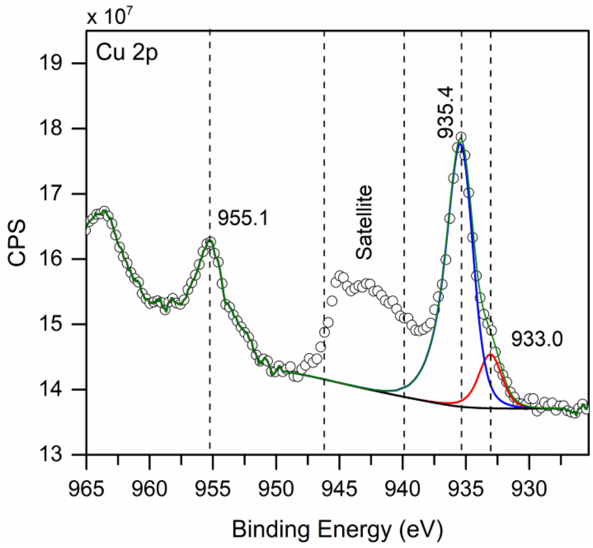

Figure S26. Core-level XPS spectra (Cu 2p) of the Cu^{II}-captured MPS system. The photoelectron emission peaks of Cu 2p were detected at 955.1 (2p$_{1/2}$) and 935.4 (2p$_{3/2}$) eV, respectively, with a spin-orbit separation of 19.7 eV. The peak positions along with the appearance of satellite peaks imply that the dominant Cu species in the MPS is in divalent state.[10] Furthermore, the peak shifts to higher BEs for Cu 2p in the MPS, relative to metallic Cu at 952.6 (2p$_{1/2}$) eV and Cu^{II} in CuO at 953.7 (2p$_{1/2}$) eV,[11,12] can be attributed to the coordination of Gd^{III} to the catechol and/or gallol groups in the MPS. However, a small contribution of Cu^{I} (peak position at BE 933.0 eV) species in the fitted spectra was also noted that suggests the occurrence of redox interactions to a small extent in the MPS.

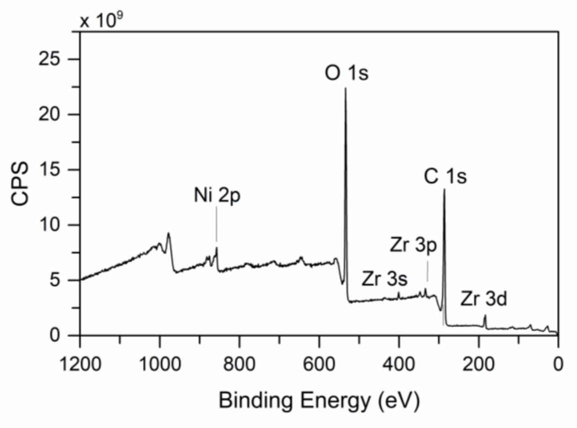

Figure S27. XPS survey spectrum of the Ni^{II}-captured MPS system showing the presence of Ni^{II}.

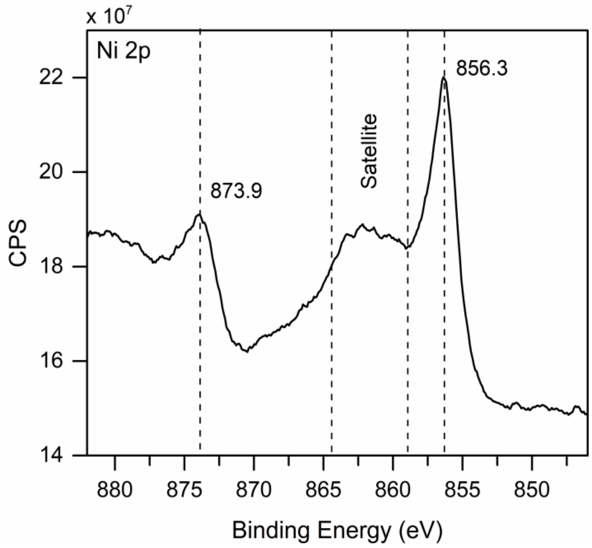

Figure S28. Core-level XPS spectrum (Ni 2p) of the Ni^{II}-captured MPS system. The photoelectron emission peaks of Ni 2p were detected at 873.9 ($2p_{1/2}$) and 856.3 ($2p_{3/2}$) eV, with a spin-orbit separation of 17.6 eV. The peak positions along with the appearance of satellite peaks imply that the dominant Ni species in the sorbent is in divalent state.[13,14] Furthermore, the peak shifts to higher BEs for Ni 2p in the MPS, relative to metallic Ni at 870 ($2p_{1/2}$) eV, and Ni^{II} in NiO at 871.9 ($2p_{1/2}$) and 854.1 ($2p_{3/2}$) eV,[14-18] can be attributed to the coordination of Ni^{II} to the catechol and/or gallol groups in the MPS.

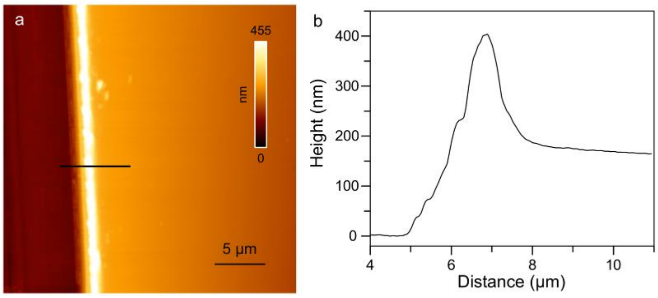

Figure S29. (a) AFM image showing the thickness of an MPS film coated on a glass substrate and (b) the corresponding height profile.

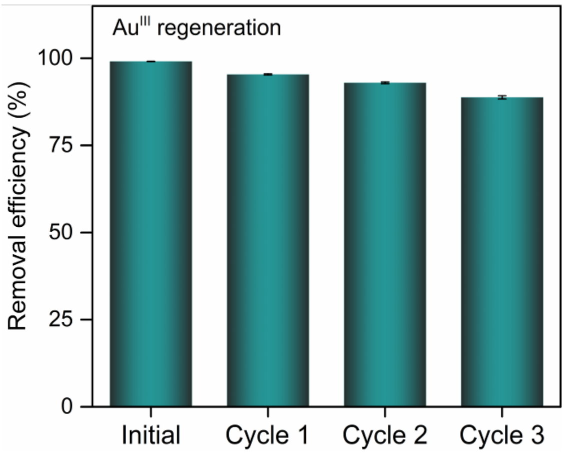

Figure S30. Removal efficiency of Au^{III} by the MPS as a function of sorption–desorption cycle number.

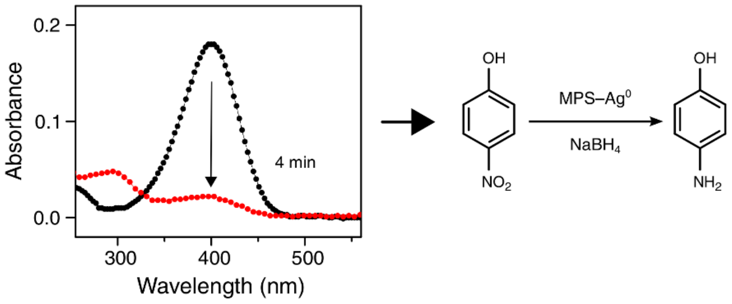

Figure S31. Degradation of 4-NP to 4-AP by MPS–Ag^0 catalyst as monitored by UV-visible absorption spectroscopy.

Table S2. Removal efficiency of the MPS sorbents for different metals in single- and multi-element model wastes[a]

No	Metal ion	Removal efficiency (%) (Single-element)	Removal efficiency (%) (Multi-element)[b]
Precious metals			
1	$\mathrm{Au^{III}}$	100.00	99.98
2	$\mathrm{Ag^{I}}$	99.67	NA
3	$\mathrm{Pd^{II}}$	99.95	99.45
4	$\mathrm{Ru^{III}}$	99.92	99.61
5	$\mathrm{In^{III}}$	99.93	99.38
6	$\mathrm{Os^{III}}$	99.77	NA
Toxic metals			
7	$\mathrm{Pb^{II}}$	100.00	99.85
8	$\mathrm{Hg^{II}}$	99.45	99.81
9	$\mathrm{Cd^{II}}$	99.78	99.53
Rare earth metals			
10	$\mathrm{Ce^{IV}}$	99.46	99.46
11	$\mathrm{Tb^{III}}$	99.87	99.47
12	$\mathrm{Gd^{III}}$	99.80	99.00
13	$\mathrm{Eu^{III}}$	99.67	99.45
14	$\mathrm{La^{III}}$	98.96	99.62
15	$\mathrm{Ho^{III}}$	99.95	99.02
16	$\mathrm{Tm^{III}}$	99.96	99.16
17	$\mathrm{Dy^{III}}$	99.92	99.11
18	$\mathrm{Nd^{III}}$	99.99	99.24
19	$\mathrm{Yb^{III}}$	99.97	99.58
20	$\mathrm{Er^{III}}$	99.94	99.22
Common transition metals			
21	$\mathrm{Ti^{III}}$	99.84	99.34
22	$\mathrm{Ni^{II}}$	99.01	85.02
23	$\mathrm{Cu^{II}}$	99.77	99.09
24	$\mathrm{Zn^{II}}$	99.98	86.23
25	$\mathrm{Zr^{IV}}$	99.85	99.34
26	$\mathrm{Mn^{II}}$	99.90	99.11
27	$\mathrm{Fe^{III}}$	99.96	84.86
28	$\mathrm{Ga^{III}}$	99.52	99.17

[a] The values reported represent the average of triplicates. From an analysis of the standard deviations of the triplicates, the errors in the values are <1%

[b] Mixed all categories – refers to Figure 3h

Table S3. Parameters of the pseudo-second order kinetic and Langmuir adsorption isotherm models for the MPS

Metal ion	Kinetic model (pseudo second order)			Sorption model (Langmuir)		
	k (g mg^{-1} min^{-1})	q_e (mg g^{-1})	R^2	q_m (mg g^{-1})	K_L (L mg^{-1})	R^2
$\mathrm{Au^{III}}$	5.00	10.0	0.99	1350	0.255	0.99
$\mathrm{In^{III}}$	0.04	10.0	0.99	180	0.018	0.99
$\mathrm{Pb^{II}}$	1.58	10.0	0.99	424	0.013	0.98
$\mathrm{Hg^{II}}$	0.17	10.0	0.99	446	0.013	0.99
$\mathrm{Tb^{III}}$	0.19	10.0	0.99	404	0.005	0.98
$\mathrm{Gd^{III}}$	0.06	10.0	0.99	406	0.026	0.99
$\mathrm{Cu^{II}}$	0.93	10.0	0.99	135	0.008	0.97
$\mathrm{Ni^{II}}$	0.06	9.9	0.99	149	0.041	0.99

Table S4. Comparison of the sorption capacity of the MPS and sorbents reported in the literature

Sorbent	Maximum sorption capacity (mg g^{-1})								Ref.
	$\mathrm{Au^{III}}$	$\mathrm{In^{III}}$	$\mathrm{Pb^{II}}$	$\mathrm{Hg^{II}}$	$\mathrm{Tb^{III}}$	$\mathrm{Gd^{III}}$	$\mathrm{Cu^{II}}$	$\mathrm{Ni^{II}}$	
Activated carbon	493[19]	NA	147[20]	300[21]	300[22]	NA	18[22]	40[23]	19–23
Zeolites	NA	NA	120[24]	12[25]	6.1[26]	6.5[27]	13[24]	61[24]	24–27
MOFs[a]	~600[28]	NA	313[29]	~200[30]	NA	NA	155[29]	155[29]	28–30
Tannin resin	642–1200[31]	NA	139[31]	210[31,32]	NA	NA	44[33]	NA	31–33
PDA[b]	NA	NA	166[34]	467	NA	NA	113[35]	NA	34,35
Chitosan	78[36]	NA	35[37]	375[38]	NA	NA	222[36]	159[39]	36–39
MPS	**1350**	**180**	**424**	**446**	**404**	**406**	**135**	**149**	**This work**

[a]MOFs, metal–organic frameworks; [b]PDA, Polydopamine.

References

[1] Zhang, N.; Luo, J.; Liu, R.; Liu, X. Tannic Acid Stabilized Silver Nanoparticles for Inkjet Printing of Conductive Flexible Electronics. *RSC Adv.* **2016**, *6*, 83720–83729.

[2] Al-Hazmi, M. H.; Choi, Y.; Apblett, A. W. Preparation of Zirconium Oxide Powder Using Zirconium Carboxylate Precursors. *Adv. Phys. Chem.* **2014**, *2014*, 1–8.

[3] Rahim, M. A.; Ejima, H.; Cho, K. L.; Kempe, K.; Müllner, M.; Best, J. P.; Caruso, F. Coordination-Driven Multistep Assembly of Metal–Polyphenol Films and Capsules. *Chem. Mater.* **2014**, *26*, 1645–1653.

[4] Malitesta, C.; Sabbatini, L.; Zambonin, P. G.; Bicelli, L. P.; Maffi, S. Analytical Characterization of Electrode Surface by X-ray Photoelectron Spectroscopy. β-PbO_2-based Cathode in Voltage-Compatible Lithium Cells. *J. Chem. Soc., Faraday Trans. 1* **1989**, *85*, 1685–1696.

[5] Li, Y.; Zhao, R.; Chao, S.; Sun, B.; Wang, C.; Li, X. Polydopamine Coating Assisted Synthesis of MnO_2 Loaded Inorganic/Organic Composite Electrospun Fiber Adsorbent for Efficient Removal of Pb^{2+} from Water. *Chem. Eng. J.* **2018**, *344*, 277–289.

[6] Padalia, B. D.; Lang, W. C.; Norris, P. R.; Watson, L. M.; Fabian, D. J.; Price W. C. X-ray Photoelectron Core-Level Studies of the Heavy Rare-Earth Metals and their Oxides. *Proc. R. Soc. London, Ser. A* **1977**, *354*, 269–290.

[7] Sohn, Y. Structural and Spectroscopic Characteristics of Terbium Hydroxide/Oxide Nanorods and Plates. *Ceram. Int.* **2014**, *40*, 13803–13811.

[8] Puppin, E.; Lindau, I.; Abbati, I. Photoemission Core Level Shifts in Gd Silicides. *Solid State Commun.* **1991**, *77*, 983–986.

[9] Raiser, D.; Deville, J. P. Study of XPS Photoemission of some Gadolinium Compounds. *J. Electron. Spectrosc. Relat. Phenom.* **1991**, *57*, 91–97.

[10] Parmigiani, F.; Sangaletti, L. The Cu2p X-Ray Photoelectron Core-Lines in Copper Oxide Based High Temperature Superconductors. *J. Electron. Spectrosc. Relat. Phenom.* **1994**, *66*, 223–239.

[11] Mansour, A. N. Copper Mg Kα XPS Spectra from the Physical Electronics Model 5400 Spectrometer. *Surf. Sci. Spectra* **1994**, *3*, 202–210.

[12] Jolley, J. G.; Geesey, G. G.; Hankins, M. R.; Wright, R. B.; Wichlacz, P. L. Auger Electron and X-Ray Photoelectron Spectroscopic Study of the Biocorrosion of Copper by Alginic Acid Polysaccharide. *Appl. Surf. Sci.* **1989**, *37*, 469–480.

[13] Venezia, A. M.; Bertoncello, R.; Deganello, G. X-Ray Photoelectron Spectroscopy Investigation of Pumice-Supported Nickel Catalysts. *Surf. Interface Anal.* **1995**, *23*, 239–247.

[14] Mansour, A. N. Characterization of NiO by XPS. *Surf. Sci. Spectra* **1994**, *3*, 231–238.

[15] Li-Shing, H.; Williams, R. S. Electronic-Structure Study of the Ni–Ga and the Ni–In Intermetallic Compounds using X-Ray Photoemission Spectroscopy. *J. Phys. Chem. Solids* **1994**, *55*, 305–312.

[16] Miller, A. C.; Simmons, G. W. Nickel by XPS. *Surf. Sci. Spectra* **1992**, *1*, 312–317.

[17] Lian, K.; Thorpe, S. J.; Kirk, D. W. Electrochemical and Surface Characterization of Electrocatalytically Active Amorphous Ni–Co Alloys. *Electrochim. Acta* **1992**, *37*, 2029–2041.

[18] Mansour, A. N. Nickel Mg Kα XPS Spectra from the Physical Electronics Model 5400 Spectrometer. *Surf. Sci. Spectra* **1994**, *3*, 211–220.

[19] Zalupski, P.; McDowell; Dutech. The Adsorption of Gold, Palladium, and Platinum from Acidic Chloride Solutions on Mesoporous Carbons. *Solvent Extr. Ion Exch.* **2014**, *32*, 737–748.

[20] Li, Y.; Du, Q.; Wang, X.; Zhang, P.; Wang, D.; Wang, Z.; Xia, Y. Removal of Lead from Aqueous Solution by Activated Carbon Prepared from *Enteromorpha Prolifera* by Zinc Chloride Activation. *J. Hazard. Mater.* **2010**, *183*, 583–589.

[21] Hadi, P.; To, M.-H.; Hui, C.-W.; Lin, C. S. K.; McKay, G. Aqueous Mercury Adsorption by Activated Carbons. *Water Res.* **2015**, *73*, 37–55.

[22] Dodson, J. R.; Parker, H. L.; Muñoz García, A.; Hicken, A.; Asemave, K.; Farmer, T. J.; He, H.; Clark, J. H.; Hunt, A. J. Bio-derived Materials as a Green Route for Precious and Critical Metal Recovery and Re-use. *Green Chem.* **2015**, *17*, 1951–1965.

[23] Anoop Krishnan, K.; Sreejalekshmi, K. G.; Baiju, R. S. Nickel(II) Adsorption onto Biomass Based Activated Carbon Obtained from Sugarcane Bagasse Pith. *Bioresour. Technol.* **2011**, *102*, 10239–10247.

[24] Wang, S.; Peng, Y. Natural Zeolites as Effective Adsorbents in Water and Wastewater Treatment. *Chem. Eng. J.* **2010**, *156*, 11–24.

[25] Chojnacki, A.; Chojnacka, K.; Hoffmann, J.; Górecki, H. The Application of Natural Zeolites for Mercury Removal: From Laboratory Tests to Industrial Scale. *Miner. Eng.* **2004**, *17*, 933–937.

[26] Vasylechko, V. O.; Gryshchouk, G. V.; Zakordonskiy, V. P.; Patsay, I. O.; Len, N. V.; Vyviurska, O. A. Sorption of Terbium on Transcarpathian Clinoptilolite. *Microporous Mesoporous Mater.* **2013**, *167*, 155–161.

[27] Vasylechko, V.; Stechynska, E. T.; Stashkiv, O. D.; Gryshchouk, G. V.; Patsay, I. Sorption of Neodymium and Gadolinium on Transcarpathian Clinoptilolite. *Acta Phys. Pol., A* **2018**, *133*, 794–797.

[28] Mon, M.; Ferrando-Soria, J.; Grancha, T.; Fortea-Pérez, F. R.; Gascon, J.; Leyva-Pérez, A.; Armentano, D.; Pardo, E. Selective Gold Recovery and Catalysis in a Highly Flexible Methionine-Decorated Metal–Organic Framework. *J. Am. Chem. Soc.* **2016**, *138*, 7864–7867.

[29] Peng, Y.; Huang, H.; Zhang, Y.; Kang, C.; Chen, S.; Song, L.; Liu, D.; Zhong, C. A Versatile MOF–Based Trap for Heavy Metal Ion Capture and Dispersion. *Nat. Commun.* **2018**, *9*, 187.

[30] Li, B.; Zhang, Y.; Ma, D.; Shi, Z.; Ma, S. Mercury Nano-trap for Effective and Efficient Removal of Mercury(II) From Aqueous Solution. *Nat. Commun.* **2014**, *5*, 5537.

[31] Bacelo, H. A. M.; Santos, S. C. R.; Botelho, C. M. S. Tannin-Based Biosorbents for Environmental Applications – A review. *Chem. Eng. J.* **2016**, *303*, 575–587.

[32] Yee, K.-K.; Reimer, N.; Liu, J.; Cheng, S.-Y.; Yiu, S.-M.; Weber, J.; Stock, N.; Xu, Z. Effective Mercury Sorption by Thiol-Laced Metal–Organic Frameworks: in Strong Acid and the Vapor Phase. *J. Am. Chem. Soc.* **2013**, *135*, 7795–7798.

[33] Şengil, İ. A.; Özacar, M.; Türkmenler, H. Kinetic and Ssotherm Studies of Cu(II) Biosorption onto Valonia Tannin Resin. *J. Hazard. Mater.* **2009**, *162*, 1046–1052.

[34] Zhang, Q.; Yang, Q.; Phanlavong, P.; Li, Y.; Wang, Z.; Jiao, T.; Peng, Q. Highly Efficient Lead(II) Sequestration Using Size-Controllable Polydopamine Microspheres with Superior Application Capability and Rapid Capture. *ACS Sustainable Chem. Eng.* **2017**, *5*, 4161–4170.

[35] Yu, Y.; Shapter, J. G.; Popelka-Filcoff, R.; Bennett, J. W.; Ellis, A. V. Copper Removal Using Bio-Inspired Polydopamine Coated Natural Zeolites. *J. Hazard. Mater.* **2014**, *273*, 174–182.

[36] Babel, S.; Kurniawan, T. A. Low-Cost Adsorbents for Heavy Metals Uptake From Contaminated Water: A Review. *J. Hazard. Mater.* **2003**, *97*, 219–243.

[37] Ngah, W. S. W.; Fatinathan, S. Pb(II) Biosorption Using Chitosan and Chitosan Derivatives Beads: Equilibrium, Ion Exchange and Mechanism Studies. *J. Environ. Sci.* **2010**, *22*, 338–346.

[38] Vieira, R. S.; Beppu, M. M. Dynamic and Static Adsorption and Desorption of Hg(II) Ions on Chitosan Membranes and Spheres. *Water Res.* **2006**, *40*, 1726–1734.

[39] Pivarčiová, L.; Rosskopfová, O.; Galamboš, M.; Rajec, P. Sorption of Nickel on Chitosan. *J. Radioanal. Nucl. Chem.* **2014**, *300*, 361–366.